Results from the Laser-wire at ATF2 and Development of a Fibre Laser for its Upgrade

Laurence James Nevay

Wolfson College, Oxford

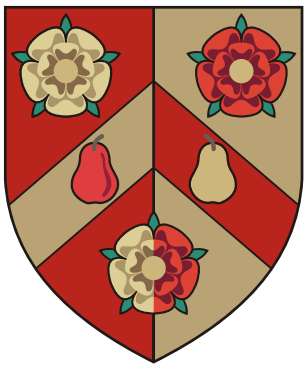

Thesis submitted in partial fulfilment of the requirements for the degree of Doctor of Philosophy at the University of Oxford

Trinity Term, 2011

Abstract

The commissioning and development of a laser-wire transverse electron beam profile monitor at the Accelerator Test Facility 2 in Japan is presented. The experimental setup used including a gigawatt laser system is detailed and characterised. Results from data taking in December 2010 are presented detailing the use of the laser-wire to tune the electron beam.

In conjunction with this, the use of a fibre-based laser system as a suitable laser source for a laser-wire is discussed. A test bed fibre laser system was constructed to investigate the suitability of fibre lasers and the results are presented demonstrating high efficiency and excellent spatial quality. From this, a laser system capable of high resolution and high repetition intra-train scanning for demonstration at the Accelerator Test Facility 2 was designed, constructed and characterised. A commercial fibre laser system was extended using a photonic crystal fibre where periodic amplification designed to match the duty cycle of an accelerator was used advantageously to achieve higher than normal pulse energies. The results and techniques developed to measure them are presented.

Acknowledgements

I would like to start by thanking my supervisors, Roman Walczak and Laura Corner, for their tireless guidance and support throughout my studies. This work would not have been possible without them nor as enjoyable. I would also like to thank the other members of the laser-wire group, in particular Stewart Boogert, Alex Aryshev and Lawrence Deacon who have not only helped and guided me with work at the ATF2, but also been great friends. The many long nights spent at the ATF2 as well as by the coffee vending machine were a pleasure.

I would like to thank the ATF2 collaboration and staff for the time provided to our experiment and the huge amount of support required to keep the accelerator operational. Thank you to Glen White and Mark Woodley, the ATF2 tuning task force, for their support and help in creating a suitable electron beam for our experiment. Thanks also to YoungIm Kim who has been a great friend and always made me smile. However, the disappearance of many laser-wire RF components has yet to be explained.

When not at the ATF2 or in the lab in Oxford, the Wolfson common room has provided many hours of relief with badly completed crosswords containing many new and unheard-of words. Many thanks to the friends there who were always willing to listen or play an emergency game of croquet. I'd also like to thank the Wolfson rowing club for their ability to step in when any distraction was needed and for providing me with many great memories.

Last, but by no means least, I'd like to thank my mum for her support throughout my studies and her ability to listen to me ramble on and on about my research.

Contents

List of Figures

List of Tables

Glossary

ADC Analogue-to-digital converter. Samples an analogue input signal giving a digitised readout.

AFG Arbitrary function generator.

AOM Acouto-optic modulator. Spatially deflects a laser beam from its path using the diffraction grating effect from a periodic density fluctuation induced by a sound wave in a crystal.

APD Avalanche photodiode. An amplified photodiode capable of detecting very low intensity pulses of light.

ASE Amplified spontaneous emission.

ATF Accelerator Test Facility.

ATF2 Accelerator Test Facility 2 - the upgraded and extended ATF.

CAMAC Computer automated measurement and control is a standard card bus for data acquisition and control used in nuclear and particle physics experiments as well as in industry. The bus allows data exchange between plug-in modules and a crate controller, which then interfaces to a computer.

CW Continuous wave. A laser with a constant output is called continuous wave as opposed to a pulsed laser that produces discrete pulses of light.

DAQ Data acquisition system.

DDG Digital delay generator.

DOLP Degree of linear polarisation.

EOM Electro-optic modulator. Rotates the polarisation of a laser beam in a controllable fashion, which is typically used in combination with a polarising beam splitter to modulate the intensity of a laser beam.

EPICS Experimental physics and industrial control system. Database software developed specifically for controlling large-scale physics experiments and industrial machinery.

FWHM Full-width at half-maximum.

HWP Half-wave plate. Rotates the linear polarisation of a laser beam for a specified wavelength.

ILC International Linear Collider. A proposed future linear electron-positron collider.

IP Interaction point.

KEK The Japanese National High Energy Physics Research Organisation, which is based in Tsukuba, Japan.

LWIP Laser-wire interaction point.

MOPA Master oscillator power amplifier. A laser system that uses a master oscillator followed by a single or series of amplifiers.

MOFA Master oscillator fibre amplifier. Similar to a MOPA system, but with the amplifier(s) based on fibre laser technology.

ND Neutral density. A neutral density filter is one that uniformly attenuates all wavelengths of light within a certain range, typically the visible part of the spectrum.

NIM Nuclear instrument module. A modular hardware standard specifically designed for experimental particle physics. Modules are placed in a container ('crate') that powers and controls the modules and interfaces with a computer.

OTR Optical transition radiation. The radiation emitted when a relativistic charged particle crosses the boundary between two regions of different dielectric constant, i.e. different materials.

PCF Photonic crystal fibre. An optical fibre where the light is guided by an array of microscopic air holes in a single piece of silica.

PBS Polarising beam splitter.

PMT Photo-multiplier tube.

QCW Quasi-continuous wave. A laser beam consisting of a continuous stream of high repetition rate pulses that are temporally unresolvable by the human eye.

QWP Quarter-wave plate.

SPM Self-phase modulation. An optical nonlinearity of a medium introduced by the high intensity of a single pulse of light, which leads to spectral broadening.

UV Ultra-violet.

VI Virtual Instrument. A program created in the LabView programming environment.

XPM Cross-phase modulation. An optical nonlinearity of a medium produced by the interaction of two intense light sources, which leads to spectral broadening.

Yb Ytterbium. A quasi-three level laser ion that is commonly used in fibre amplifiers.

Chapter 1

Introduction

1.1 High Energy Particle Accelerators

Over the last 50 years, particle accelerators and their applications have developed significantly. Particle colliders used to study the nature of matter have attained higher and higher centre of mass energies in search of new fundamental particles. Accelerator applications are wide ranging from industrial applications such as lithography and ion implantation to medical treatment.

High energy particle colliders are typically circular with two counter-propagating particle beams that are made to overlap and collide at certain points. At these points the particles that collide produce new particles with masses and momenta summing to the energy of the collision. By accelerating the particles to higher energies, particles with a greater mass can be created and characterised.

The particle beams produced in such colliders typically consist of discrete short duration bunches and when they collide only a fraction of the particles collide with each other because of their low interaction cross-section. To reach the required high energies, the bunches of particles are successively accelerated on each pass around the ring in a circular collider. Furthermore, the remaining particles that don't collide can be recirculated until they do.

It is for these reasons that circular colliders are advantageous for both acceleration and collisions.

However, several limits prevent a circular collider from indefinitely accelerating particles to higher and higher energies. Firstly, as the energy and hence momenta of the particles increases, stronger magnetic fields are required to maintain the same orbital radius and hence trajectory of the particles. The dipole electromagnets used to bend the trajectory of the particles are typically made from various alloys of iron, which have a magnetic saturation point of approximately 1.6 T that proves to be the limit of the magnetic field they can generate. Superconducting magnets allow higher fields of up to 15 T to be generated [1]. The Large Hadron Collider (LHC) at CERN in Geneva, Switzerland is the largest current use of superconducting dipoles and the field strength of the dipoles there is 8.33 T [2]. To reach higher collisions energies using available magnets, larger circumference colliders are required, although the 27 km circumference of the LHC is already reaching the practical limit.

Secondly, the emission of synchrotron radiation provides another limit on the achievable energy in a circular collider. When the trajectory of a charged particle is bent by a magnetic field, the particle will release synchrotron radiation [3]. The power radiated by a single particle is described by

$$P = \frac{q^2 c}{6\pi\epsilon_0}\frac{\gamma^4}{\rho^2} \tag{1.1}$$

where q is the charge of the particle, γ the Lorentz factor and ρ its bending radius. In a circular collider, the energy lost to synchrotron radiation must be at least replaced each turn. As the synchrotron radiation increases with the fourth power of the energy of the charged particle, eventually a point is reached when the energy lost per revolution cannot be replaced by the accelerator. Despite further acceleration, the maximum energy of the particle saturates. As the synchrotron power lost is also inversely proportional to the fourth power of the particle's rest mass, therefore the power radiated by an electron will be $\sim 10^{13}$

times greater than that from a proton.

Being hadrons, the energy of a proton in a collider is distributed amongst the quarks and gluons that constitute it. During a collision the constituents collide with each other and a large range of energy distributions is possible. Therefore, in proton-proton collisions, a multitude of different particles are produced with a range of energies. In contrast, electrons are point-like particles with no constituents, so the collision energy is more precisely defined and known. The LHC is currently the highest energy particle accelerator in the world, however, it is envisioned that an electron-positron collider would follow this for further investigation [4].

Because of the much greater emission of synchrotron radiation from an electron or positron, a linear collider without bends would be required to reach the necessary high energies. However, in a linear collider the bunches of particles pass through the accelerating structure only once and collide only once. To produce enough collisions per particle bunch to achieve experimental results within a suitable timescale of several years, the electron and positron bunches must be compressed to a very small size to increase the probability of collision. Furthermore, the accelerating gradient must be sufficiently high to keep the footprint of the accelerator within reasonable limits.

For a general collider, collision rate (luminosity) $\mathcal{L}$ is defined by

$$\mathcal{L} = \frac{N_b N_e^2 f_t}{4\pi\sigma_x\sigma_y} \times H_D \tag{1.2}$$

where N_b and N_e are the number of particle bunches and the number of electrons or positrons per bunch and f_t is the bunch train repetition rate [5, 6]. $\sigma_{x,y}$ are the horizontal and vertical beam sizes at the interaction point of both particle bunches (assumed the same here), and H_D is a disruption parameter for either the mutual attraction or repulsion between the colliding bunches caused by their charge. It can be seen that for a given number of particle bunches the luminosity can be increased by making the size of the bunches as small as possible at the interaction point. The size of the particle beam σ is described by

$$\sigma = \sqrt{\epsilon\beta} \tag{1.3}$$

Here it can be seen that the size of the particle beam depends on two parameters. Firstly, ϵ, the emittance is a property of the beam itself and secondly, β which is a parameter derived from the lattice of magnets in the accelerator at the interaction point. These are both explained in greater detail in Section 1.2. The β function of the accelerator is easily calculated from knowledge of the magnets used and their layout, however, the emittance must be measured directly. The emittance is typically measured by measuring the size of the particle beam σ at various points in the accelerator where the β function is known. Imperfections in alignment and magnet strengths can cause the emittance to grow [7], and so accurate measurements are required to control this.

Two proposed linear colliders are the International Linear Collider (ILC) [4] and the Compact Linear Collider (CLIC) [8]. The ILC consists of two $\sim$ 15 km linacs accelerating electrons and positrons to an energy of 250 GeV each using cryogenic superconducting accelerating cavities to produce the high accelerating gradient necessary. To achieve the smallest focussed electron beam possible, diagnostics are required that can measure each of the intense 250 GeV electron beams that have a size of approximately $\sigma = 1$ μm before they are focussed for collision [9].

CLIC on the other hand, aims to accelerate electrons and positrons to an energy of 1.5 TeV each. Instead of cryogenic superconducting accelerating cavities, normal conducting high frequency copper cavities are the proposed accelerating method. A second high current, low energy drive electron beam parallel to the main beam will be used by local power extracting structures to transfer energy from the drive beam to the main high energy beam. Although quite different from the ILC, CLIC also requires diagnostics to measure the intense full energy electron and positron beams before they are focussed at the collision point.

In recent years, the synchrotron radiation emitted by electrons has been put to use as a light source. Special devices called wigglers and undulators have been designed and built

that consist of alternating magnetic fields which in effect act like a series of bends to the trajectory, maximising the amount of synchrotron radiation produced. In this case, the peak frequency of the synchrotron radiation emission spectrum is given approximately by

$$\omega_c = \frac{3}{2}\frac{c}{\rho}\gamma^3 \tag{1.4}$$

where ρ is the bending radius of the magnets used and γ is the relativistic γ. As the spectrum of the emitted synchrotron radiation depends on the relativistic γ and therefore the energy of the particles, the spectrum can be tuned to suit a particular application. Light sources based on synchrotron radiation can provide high intensities over a broad range of frequencies making them highly sought after sources for many scientific and industrial applications.

In light sources such as these, the emittance of the electron beam defines the angular spread of the synchrotron radiation and therefore how small a spot size it can be focussed to. A low emittance is desirable as this produces high brilliance synchrotron radiation reducing the time required for users of the light source. The electron beams in synchrotron light sources typically have very small transverse sizes making accurate measurement of the emittance difficult.

A number of high energy particle accelerators and modern light sources have high charge particle beams with small sizes that no current diagnostics can characterise. In this thesis, an investigation of a non-invasive high resolution transverse beam profile monitor - a laser-wire - is presented, which could be applied to the ILC, CLIC and both current and future light sources.

1.2 Motion of a Charged Particle

In a particle accelerator, charged particles are guided and contained using magnetic fields. The derivation of the motion of a charged particle in an accelerator follows the description given by [10, 11]. Electromagnets used in accelerators have a number of poles that is a

multiple of two. A magnet with two poles is called a dipole and a magnet with four poles, a quadrupole. The equation of motion of a particle with charge e moving with velocity $\mathbf{v}$ perpendicularly to a uniform magnetic field $\mathbf{B}$ is given by

$$e\mathbf{v} \times \mathbf{B} = \frac{d\mathbf{p}}{dt} \tag{1.5}$$

Here $\frac{d\mathbf{p}}{dt}$ is the rate of change of relativistic momentum. The particle momentum can be described by

$$\frac{d|\mathbf{p}|}{dt} = |\mathbf{p}|\frac{d\theta}{dt} = \frac{|\mathbf{p}|}{\rho}\frac{ds}{dt} \tag{1.6}$$

as the particle's trajectory changes by angle θ at bending radius ρ. This can be used in conjunction with the case of a particle where the magnetic field is normal to the plane of motion to derive

$$B\rho = \frac{p}{e} \tag{1.7}$$

where $B\rho$ is called the magnetic rigidity, which describes the motion of a particle in a uniform magnetic field that is orthogonal to its trajectory. The particle will move in a curved path for as long as it is within the magnetic field. A dipole generates such a field and so they are normally used to change the trajectory of a particle in one dimension.

In addition to dipoles, quadrupoles are used that consist of four alternating magnetic poles in a symmetric distribution about the trajectory of a particle passing through it. These produce a non-uniform magnetic field that is zero on the axis of the device but rises linearly with distance from the axis. The quadrupole therefore acts like the restoring force of a spring in one dimension, where the force towards the axis of the device is proportional to the distance from the axis. In the other dimension, the quadrupole acts in the opposite way where the particle experiences a force away from the axis of the device.

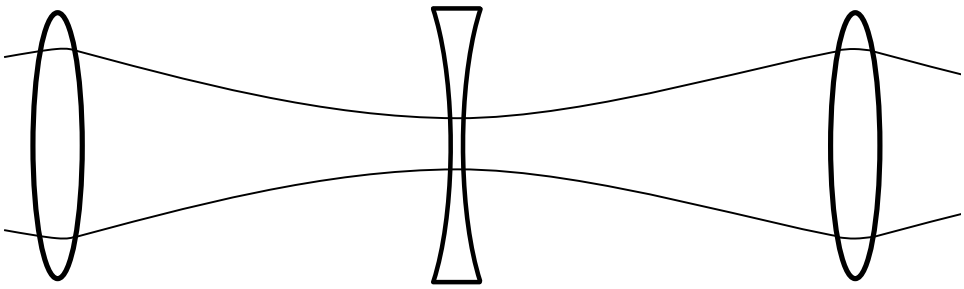

Figure 1.1: Diagram showing the particle beam envelope for a single dimension through a series of focussing and defocussing quadrupole magnets, here represented by thin lenses.

For a bunch consisting of a large number of particles, a quadrupole focusses the bunch in one dimension and defocusses it in the other. Successive combinations of quadrupoles can be used to contain and focus a particle beam. The strength k of a quadrupole is dependent on its gradient $\frac{dB_y}{dx}$ normalised to the magnetic rigidity

$$k = \frac{1}{B\rho}\frac{dB_y}{dx} \tag{1.8}$$

Under the assumption of a short quadrupole of length l, the focal length of the quadrupole along the focussing dimension is given by

$$f = -\frac{1}{kl} \tag{1.9}$$

In this manner a series of quadrupoles can be used to contain the beam. At the focus of the particles in, for example, the horizontal plane, a quadrupole with the opposite polarity can be placed to focus the divergent vertical dimension. The horizontal dimension will be defocussed by this quadrupole however, the effect is small as the horizontally focussed beam experiences little force near the axis of the quadrupole. This is shown schematically for one dimension in Figure 1.1.

This pattern of quadrupoles is repeated to contain and focus a beam of particles and is referred to as a FODO lattice as it consists of alternating focussing and defocussing quadrupoles. For a repeating FODO lattice, the angular deflection of a particle passing

through a quadrupole of strength k and length ds is

$$dx' = -kx\ ds \tag{1.10}$$

where x' is dx/ds. This represents a restoring force that returns the particle to zero displacement. From this, a differential equation describing the particle motion in the vertical plane can be deduced

$$x'' + k(s)x = 0 \tag{1.11}$$

where s is the distance along the axis of the lattice. This is called Hill's Equation. This equation of motion can be solved in a similar fashion to a harmonic oscillator assuming an infinitely repeating FODO lattice. A known solution to Hill's equation is

$$x = \sqrt{(\beta(s)\epsilon)}\, cos(\phi(s) + \phi_0) \tag{1.12}$$

where $\beta(s)$ represents an amplitude variation with distance s to represent the changing focussing strength, ϵ and ϕ_0 are constants that depend on initial conditions and $\phi(s)$ is the phase advance. Plotting x' as a function of x for a family of different particles with arbitrary phases we find an ellipse called the phase ellipse with semi-axis $\sqrt{\beta\epsilon}$ in x and $\sqrt{\beta/\epsilon}$ in x'. The phase ellipse has an area $\pi\epsilon$ where ϵ is referred to as the emittance.

Liouville's Theorem states that the area of phase space ellipse is conserved, however its orientation will change throughout the FODO lattice. A matrix formalism can be used to describe the solution to Hill's equation using the following substitutions

$$w = \sqrt{\beta} \qquad \alpha = -\frac{\beta'}{2} \qquad \gamma = \frac{1+\alpha^2}{\beta} \tag{1.13}$$

which are described fully by E. Wilson [11]. α, β and γ are referred to as the Twiss parameters

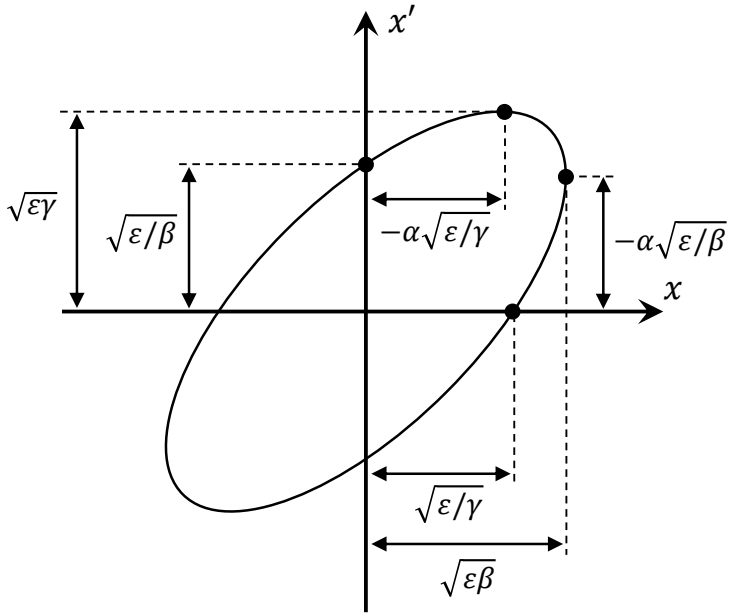

Figure 1.2: A diagram showing the phase space ellipse of a particle beam described by the Twiss parameters, α, β and γ.

of the matrix formalism, and using these a phase space ellipse at an arbitrary point in the FODO lattice as shown in Figure 1.2 is described by the equation

$$\gamma x^2 + 2\alpha x x' + \beta x'^2 = \epsilon \tag{1.14}$$

Each element of an accelerator lattice including dipoles, quadrupoles and drift spaces can be represented by a transfer matrix. The Twiss parameters describing the evolution of the particle beam can then be propagated to any point in the lattice by multiplying the matrices of all the preceding components with the matrix describing the initial conditions

Emittance describes the extent the particle beam occupies in phase space and the β function is a property of the accelerator lattice. Although Hill's Equation was solved for an infinitely repeating FODO lattice, the matrix formalism allows these solutions to be extended to any unique non-repeating lattice given initial conditions. This is the basis of MAD software which is commonly used to simulate and design accelerators [12].

The maximum extent of this projection is described by $\sqrt{\beta\epsilon}$, so with knowledge of the β function at the location of the transverse profile measurement, the emittance can be

calculated. It is common to measure several points in one dimension for a higher degree of accuracy, which can be achieved either by varying the β function at the point in the lattice where the beam profile is measured or by using several beam profile measurements at various locations with different β functions. The former can prove difficult as the magnet strengths have to be changed, which affects the propagation of the particle beam throughout the accelerator. The latter is more common as the electron beam optics can remain static.

The formulation up until now has considered a mono-energetic beam. In a typical particle bunch in an accelerator, there is a distribution of momenta about the design value. As shown in Equation 1.7, the deflection of a particle in a magnetic field depends on its momentum p, and so particles with different momenta will behave differently throughout an accelerator lattice [13]. This effect is called dispersion and adds in quadrature to the beam size described by Equation 1.3. The resultant beam size is described by

$$\sigma(s)_e = \sqrt{\beta(s)\epsilon + D(s)^2 \left(\frac{\Delta p}{p}\right)^2} \tag{1.15}$$

where $D(s)$ is the dispersion function at that point in the lattice and $\Delta p/p$ is the momentum spread of the particle bunch.

Additionally, as the particles are accelerated, their forward momentum vector increases but their transverse momentum vector doesn't, which has the effect of lowering the emittance. This can be accounted for by using the normalised emittance

$$\epsilon_n = \epsilon \left(\gamma \frac{v}{c}\right) \tag{1.16}$$

where γ here is the Lorentz relativistic gamma, v is the velocity of the particle and c is the speed of light. Various nonlinear effects introduced by imperfections in magnets and improper alignment can lead to emittance growth in an accelerator leading to an increased focussed beam size. The beam must therefore be well characterised to avoid this. Furthermore, the emission of synchrotron radiation lowers the emittance and 'cools' the beam.

It can be seen that for a given lattice and hence β function, the size of the beam will depend on the emittance and the dispersion of the particle beam. To achieve the small focus necessary in a linear collider, a particle beam with a low emittance is desirable.

Furthermore, the emission of synchrotron radiation in an accelerator used as a light source has the effect of damping the transverse motion of the electron beam being used and lowering its emittance. As the electron beams in lights sources are typically stored for many hours, the beam can have a very low emittance and consequently a very small transverse size that can be difficult to measure.

1.3 Measurement of Small Electron Beams

A conventional method for measuring the transverse size of a particle beam in an accelerator is a phosphorescent coated screen that is placed at an angle into the beam. The visible light given off by the phosphors creates an image of the beam that can be used in real time to observe its size and shape. This method has many disadvantages. Firstly, the beam is scattered by the screen and therefore cannot be used for further experiments or collisions. Secondly, screens have a resolution limited by the size of the phosphor grains of approximately 20 μm [14].

Another common technique to measure the transverse size of a particle beam is to use a wire scanner. This consists of a fine wire that is translated across the particle beam. As it intersects the beam it produces a shower of bremsstrauhlung radiation and scattered electrons proportional to the overlap of the wire and the particle beam. By scanning it across the beam, and with knowledge of the exact size of the wire, the beam profile can be extracted [15]. The resolution of a wire scanner is limited by the width of the wire and so by decreasing its width a greater resolution can be achieved. However, as the width of the wire is decreases, so does its strength and wires below 10 μm are often destroyed by the particle beam [16]. Wires as small as 4 μm have been demonstrated but only with low charge electron beams [15]. It is not possible to use wire scanners to measure the profile of a high charge

particle beam at high energies that would normally be present immediately before the final focus optics of a collision point in a linear electron or positron collider, as they would be destroyed [9]. Wire scanners, like screens, are destructive monitors and additionally, take many particle bunches to scan the beam. They often provide an over estimate of the beam size because of the bunch to bunch spatial jitter.

A more recent profile measurement technique is to use optical transition radiation (OTR). Transition radiation is produced when a relativistic particle passes through the surface of a conductor. The beam profile can be measured by imaging the broadband radiation covering the visible part of the spectrum. Typically, a screen with a thin metal coating is placed into the beam at an angle and an imaging system used to record the backward OTR. The resolution of OTR monitors is limited to several micrometres by the opening angle of the OTR which is inversely dependent on the Lorentz gamma factor of the particles. Additionally, the thin metal coating on the screen is damaged by the high charge density of a small electron or positron beams [17] and therefore could not be used to measure the beam profile of the nominal beam before collision in an electron or positron linear collider.

Screens, wire scanners and OTR monitors are the most typical beam profile measurement techniques and are widely used as diagnostics in many accelerators. However, as they are all destructive, they are susceptible to damage with small high intensity electron beams that would typically be found immediately before the particle beam optics before a collision point. A recent development in beam profiling is to use a laser in place of a wire [15]. Compton scattered photons from the electron beam propagate near parallel to the original electron bunch and can be separated from the beam and measured downstream of the interaction point. The laser beam can be scanned across the electron bunch in the same fashion as a wire scanner and this technique is therefore referred to as a laser-wire.

A laser-wire has many advantages over conventional profiling techniques with the most obvious that the laser beam is an indestructible target. A greater resolution can be achieved as the size of the focussed laser beam is limited by the wavelength of light used and so it is possible to measure electron beams of sizes down to $\sim$ 400 nm [18].

A further technique is to use the interference pattern of two laser beams to scan the electron beam. The interference pattern can be much smaller than the normally limiting wavelength of the light. By scanning the interference pattern across the electron beam the number of Compton scattered photons is modulated and with knowledge of the interference fringe spacing, the size of the electron beam can be measured. This can potentially measure electron beams with a theoretical maximum resolution of 10 nm [19].

1.4 Laser-wire Interaction

In a laser-wire profile monitor, a laser beam is focussed and scanned across a particle beam at 90^o. For the remainder of this thesis, an electron beam is considered. The photons in the laser beam collide with the passing electrons and a fraction are Compton scattered. As the photons from typical high power laser sources have a wavelength in the visible part of the spectrum, their momentum is considerably less than that of the ultra-relativistic electrons they scatter from. Due to conservation of momentum, the photons are scattered parallel to the electron beam and can be detected further along the accelerator when the electrons are deflected by a dipole magnet. In the case where the scattered photon has greater energy than the original photon, the process is referred to as inverse Compton-scattering.

By moving the laser across the electron beam the number of scattered photons is modulated corresponding to the density of the laser and the electron beams. If the transverse intensity profile of the laser is known, the profile of the electron bunch can therefore be extracted.

More quantatively, the number of scattered photons N_γ per collision event is

$$\langle N_\gamma \rangle = \mathcal{L}\sigma \tag{1.17}$$

where $\mathcal{L}$ is the luminosity of the collision and σ is the interaction cross-section. The luminosity of the collision is defined by

$$\mathcal{L} = N_e N_L \int\int\int_{-\infty}^{+\infty} \rho_e(x,y,z)\rho_L(x,y,z)\, dx\, dy\, dz \tag{1.18}$$

where N_e and N_L are the number of electrons and photons respectively and $\rho_{e,L}(x,y,z)$ are the probability distribution functions of the electron bunch and the laser pulse [6]. The interaction cross-section, the Compton cross-section σ_C, is related to the Thomson cross-section σ_T, given by

$$\sigma_T = \frac{8\pi}{3}\left(\frac{q^2}{4\pi\epsilon_0 mc^2}\right)^2 \tag{1.19}$$

where q and m are the charge and mass of particle respectively and ϵ_0 is the vacuum permittivity. In the case of an electron, the Thomson cross-section is $6.6528 \times 10^{-29}\mathrm{m}^2$. The Compton cross-section σ_C is related to the Thomson cross-section by

$$\frac{\sigma_C}{\sigma_T} = \frac{3}{4}\left\{\frac{1+\epsilon_1}{\epsilon_1^3}\left[\frac{2\epsilon_1(1+\epsilon_1)}{1+2\epsilon_1} - \ln(1+2\epsilon_1)\right] + \frac{1}{2\epsilon_1}\ln(1+2\epsilon_1) - \frac{1+3\epsilon_1}{(1+2\epsilon_1)^2}\right\} \tag{1.20}$$

where $\epsilon_1 \equiv \gamma h\nu_0/m_e c^2$ is the normalised energy of the laser photons in the electron rest frame, and γ here is the Lorentz factor.

Figure 1.3 shows a simulation of the ratio of the Compton cross-section to the Thomson cross-section calculated using Equation 1.20. Common high power laser wavelengths of 1064nm, 532nm and 266nm were used which cover the near-infra-red, the visible and ultra-violet parts of the spectrum respectively. Additionally, an electron was used as the particle in the simulation.

As the laser wavelength decreases, so does the Compton cross-section. Also, as the energy of the electrons increases beyond a few GeV, the Compton cross-section drops sharply. The Compton cross-section continues to decrease above 100 GeV but at a much slower rate. The energy spectrum of the scattered photons is described by

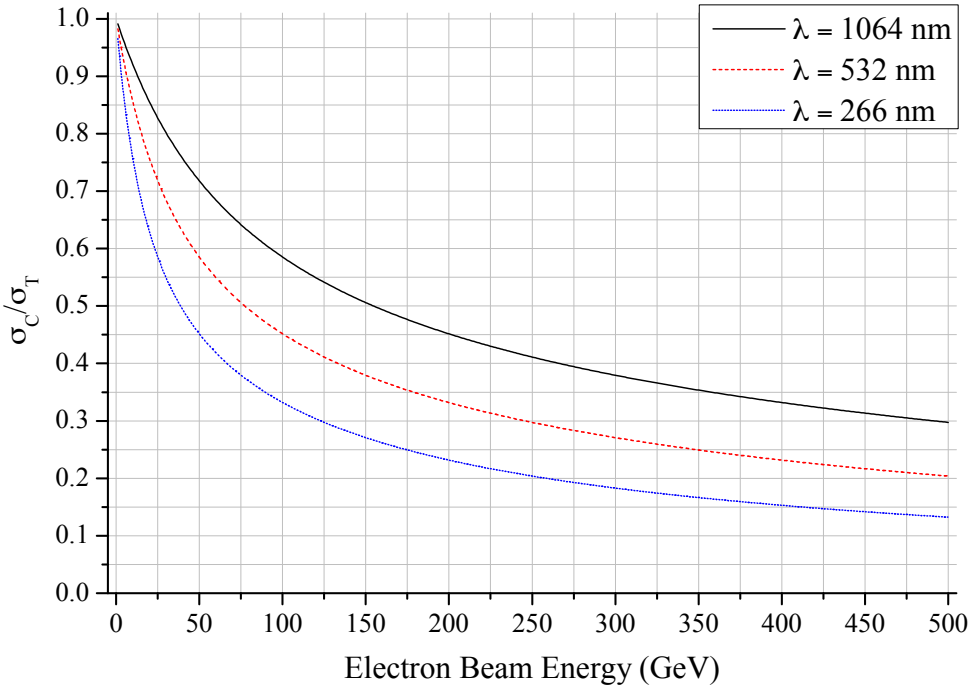

Figure 1.3: Simulation of the ratio of the Compton cross-section to the Thomson cross-section using common high power laser wavelengths for different electron energies.

$$\frac{d\sigma_C/\sigma_0}{dw} = \frac{3}{8\epsilon_1}\left\{\frac{1}{1-w} + 1 - w + \left[\frac{w}{\epsilon_1(1-w)}\right]^2 - \frac{2w}{\epsilon_1(1-w)}\right\} \tag{1.21}$$

where $w \equiv \frac{h\nu_\gamma}{E_e}$ is the energy of the scattered photon normalised to the electron energy and the maximum energy of the scattered photons is given by Equation 1.22.

$$h\nu_{max} = \frac{2E_e\epsilon_1}{(1+2\epsilon_1)} \tag{1.22}$$

Using Equation 1.21 with the cut-off at the maximum scattered photon energy defined by Equation 1.22, the scattered photon energies for three common high power laser wavelengths are shown in Figure 1.4 for two different electron beam energies. The two cases shown are for a low energy scaled test facility ($E_e = 1.3$ GeV)described in Chapter 2 and the aforementioned ILC ($E_e = 250$ GeV). The spectrum is both cases is broad with a sharp peak at the maximum scattered photon energy. In the low energy case, there is also a greater proportion of low energy scattered photons. In the low electron beam energy case, the scattered photon energy is a low fraction of the incoming electron energy, however, in

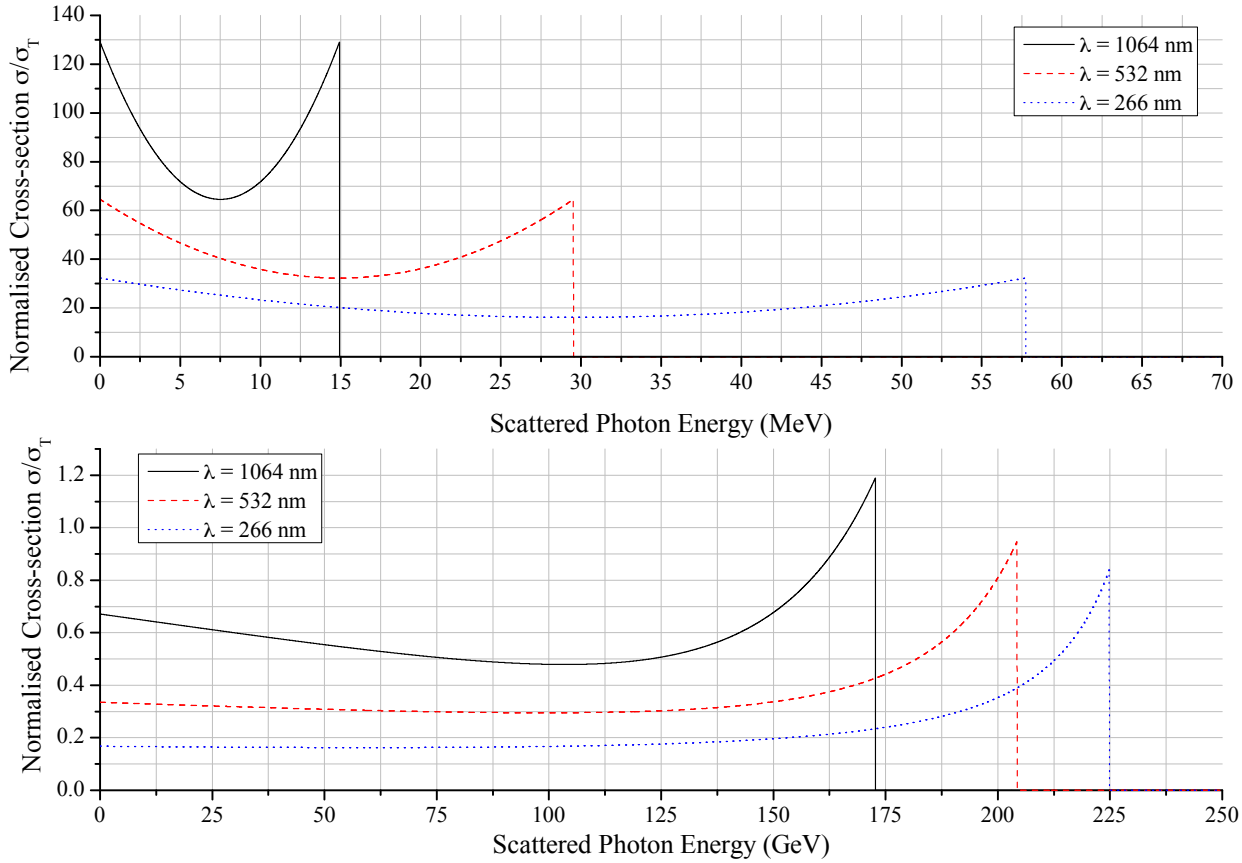

Figure 1.4: Energy spectrum of scattered photons from a 1.3 GeV (top) and 250 GeV (bottom) electron beam. In each case, three common high power laser wavelengths are shown.

the high electron beam energy case, it is a much higher fraction.

This difference may determine the detection method used. In the low energy case, the electrons that the photons have scattered experience only a small degradation in their energy and will continue to be transported by the accelerator and therefore it would be logical to build a detector for the inverse-Compton scattered photons. However, in the high energy case the electrons with a considerably different energy will not be contained within the accelerator and therefore it may be simpler to detect the ejected electrons close to the interaction point [15].

Using Equation 1.17, Equation 1.18 and σ_C from Equation 1.20, the expected number of inverse-Compton scattered photons N_γ is

$$\langle N_\gamma \rangle = N_e \frac{P_L \lambda}{hc} \sigma_C \int\int\int_{-\infty}^{+\infty} \rho_e(x,y,z)\rho_L(x,y,z)\, dx\, dy\, dz \tag{1.23}$$

where P_L is the instantaneous power of the laser pulse. Here it assumed that the laser pulse is considerably longer than the electron bunch and therefore the intensity of the laser is essentially constant. Furthermore, by assuming Gaussian probability distribution functions for the remaining dimensions of the laser beam and for the electron beam and that only displacement in the y axis between the two beams is considered, Equation 1.23 can be simplified to

$$\langle N_\gamma \rangle = N_e \frac{P_L \lambda}{hc} \sigma_C \frac{1}{\sqrt{2\pi}\sigma_s} exp\left(-\frac{\delta y^2}{2\sigma_s^2}\right) \tag{1.24}$$

where $\delta y = y_L - y_e$ is the vertical difference between the centres of the electron and laser beams and $\sigma_s = \sqrt{\sigma_L^2 + \sigma_e^2}$ is the sum in quadrature of the vertical size of each beam.

This model assumes that the sizes of both beams are unchanging throughout the interaction point, however this is not always the case and if the electron beam is large enough in the horizontal dimension x that the laser beam varies in size, the full integral of Equation 1.23 with the appropriate distributions will have to be used.

1.5 Development of a Laser-wire

Herein, the development of a laser-wire and a suitable laser system are described. The first laser-wire was successfully demonstrated at the Stanford Linear Collider (SLC) interaction point [18], which consisted of an ultra-violet (UV) laser source that was focussed using a spherical mirror. This laser-wire successfully demonstrated a minimum electron beam width of $\sigma_y = 376 \pm 17$ nm, however significant difficulties were encountered.

The reflective focussing geometry was used as the short wavelength of light prohibits transmissive optics. The spherical mirror did not perform well when offset from the laser

beam during scanning and therefore the electron beam was instead moved to the laser-wire. For a laser-wire, either the laser beam or the electron beam can be scanned across the other, but if the laser-wire is being used for high energy particle beams it will be more advantageous to move the laser beam instead of the particle beam. Furthermore, it was not possible to measure the focussed spot size of the laser without interrupting the incoming laser beam to the spherical mirror. The laser-wire in this case was therefore calibrated using a 4 μm carbon wire scanner with low charge electron bunches. Additionally, Ross et al. [18] found that laser-induced optical component damage from the UV light was common if traces of chemical contaminants were present and so the laser system and transport line were required to be kept in an ultra-clean environment.

To allow for easy scanning and calibration, transmissive focusing optics, a lens, is considered. The focussed spot size of a laser beam with a Gaussian transverse intensity profile is described by

$$w_0 = \frac{M^2 f \lambda}{\pi w_i} \tag{1.25}$$

where w_0 is the focussed beam width (2σ) of the Gaussian beam, w_i is the input beam width, f is the focal length of the lens used, λ is the wavelength of the light and M^2 is a scaling factor describing the spatial quality of the beam which would ideally have a value of 1 [20] (described in Section 4.7).

To achieve the best laser-wire resolution, the smallest focussed spot size of the laser beam is desired. Generally speaking, a larger lens and input beam size will produce a smaller focussed spot size. However, larger lenses are more difficult to manufacture and more expensive. Additionally, a minimum focal length is imposed by radiation-induced damage from the particle beam. Therefore, from Equation 1.25, a shorter wavelength and a better spatial quality beam will produce a smaller focussed spot size.

As future large scale accelerators using laser-wires would require between 10 and 100 laser-wires, a laser-wire system at the ATF2 was developed that could be scanned using a

lens over a greater range without manipulating the electron beam. A longer wavelength in the visible part of the spectrum was used instead of UV due to the aforementioned low transmission of conventional optical components.

The goal of the laser-wire at the ATF2 is to demonstrate a laser-wire capable of reliably and accurately measuring $\sigma = 1$ μm electron beams using a visible wavelength laser focussed by a lens. The experimental setup and results are discussed in Chapter 2 and Chapter 3 respectively.

In addition to this, the development of an efficient laser source with the excellent spatial quality needed to achieve the best resolution possible with the longer visible wavelength was investigated. In Chapter 4, fibre lasers are considered. A test bed system was used to determine the suitability of fibre lasers in Chapter 5 and a laser system developed for demonstration at the ATF2 is described in Chapter 6.

Chapter 2

A Laser-wire at ATF2

In this chapter, the experimental setup and methods used for the commissioning of a laser-wire at the ATF2 in Japan are described. The basic geometry of the accelerator and the experiment is described in Section 2.1 followed by the details of the laser system used in Section 2.3. The hardware involved in the interaction region is then described as well as the properties of the electron beam at that position in the accelerator. After this, the detection of the scattered photons is discussed in Section 2.6 and finally, the timing systems and alignment strategy necessary for collisions are discussed along with the scanning procedures and the software used to accomplish this.

2.1 The ATF2

To demonstrate a laser-wire and investigate micrometre level transverse profile measurements, a laser-wire was constructed at the Accelerator Test Facility 2 (ATF2) at the Japanese National High Energy Physics Research Organisation (KEK) in Tsukuba, Japan. The ATF2 is an upgrade of the ATF that extends the extraction line with a scaled test bed system of the proposed ILC, which requires a beam size at the collision point of ~ 7 nm vertically [9]. The goal of the ATF2 is to create a focussed electron beam with a vertical size of $\sigma_y = 37$ nm [21] before proceeding to smaller sizes. The major components of the laser-wire described here were used from a successfully demonstrated laser-wire at the ATF [22, 23].

The ATF2 consists of a 1.28 GeV electron linac followed by a damping ring to produce a

very low emittance electron beam. After remaining in the damping ring for between 100,000 and 500,000 revolutions, the electron beam is extracted into the extraction line. Various diagnostics including the laser-wire measure the electron beam as it passes along the linear extraction line to the final focus region where a special set of electron beam optics are being developed to create a focussed electron beam with a vertical size of $\sigma_y = 37$ nm. The full layout of the machine is illustrated in Figure 2.1 and the extraction line in particular is shown in Figure 2.2.

The goal of the laser-wire experiment is to measure the vertical transverse profile of the electron beam with sub-micrometre resolution as required to make a high precision emittance measurement in the beam delivery system between the linac and the final focussing system of a future collider such as the ILC [9]. This is necessary to fully characterise the accelerated beam and match it into the final focus electron beam optics. In practice, this translates to demonstrating a vertical transverse profile of $\sigma_y \sim 1$ μm that is the typical predicted size of the fully accelerated electron or positron beam before the final focus section.

2.2 Experimental Setup

The laser-wire experiment consists of a laser laboratory above the accelerator where the laser system and electronics can be operated in a radiation-safe and temperature-controlled environment. The laser is mounted on an optical table that has sufficient space to manipulate the size and divergence of the laser beam as well as for the necessary laser diagnostics.

The laser beam is transported into the radiation-hard accelerator environment using a periscope through a hole (radius $\sim$ 7 cm) in the concrete radiation shielding below the laser table in the laser laboratory. Two enclosed optical tables beside the accelerator beam line contain the optics necessary to relay the laser beam along the accelerator enclosure to the laser-wire interaction point (LWIP). Here the necessary optics for alignment, delivery and diagnostics are mounted on a further optical table surrounding the LWIP vacuum chamber. Due to the high power nature of the laser system used, the laser system is in an interlocked

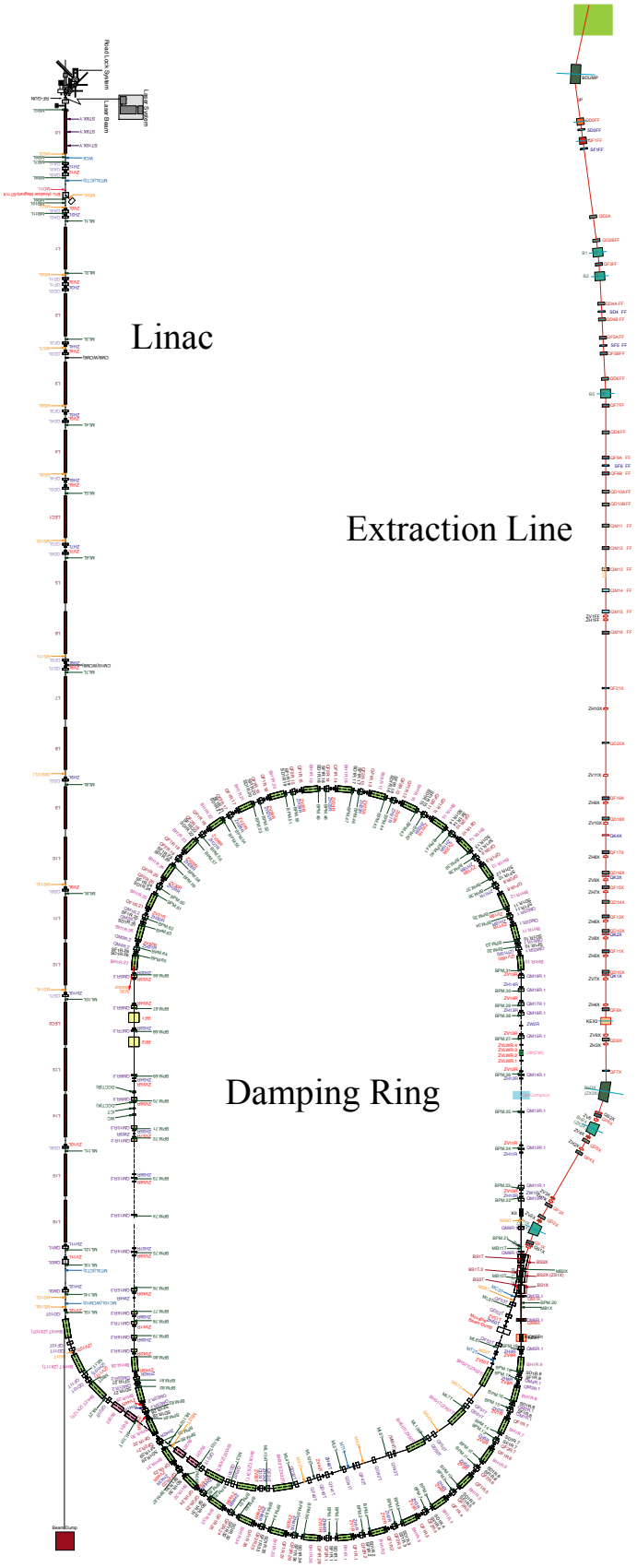

Figure 2.1: Schematic layout of the ATF2 showing in order: the linac, the damping ring and finally the extraction line.

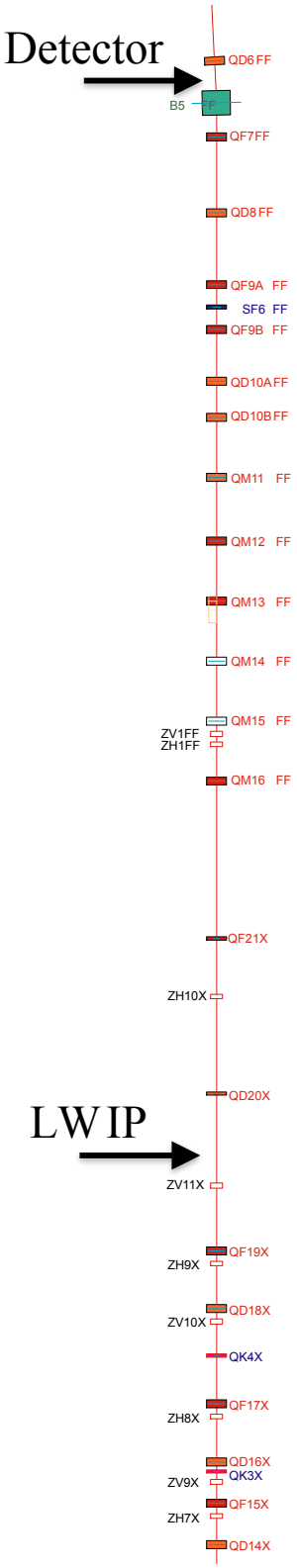

Figure 2.2: Location of the laser-wire interaction point in the extraction line as well as the position of the detector. The electron beam proceeds from bottom to top. LWIP is the laser-wire interaction point and the laser-wire detector is marked further along the beam line after the B5FF dipole magnet.

room and the beam path outside the laser laboratory is entirely encased for safety.

At the interaction point, a custom made fused-silica lens [23] is used to focus the laser beam through a fused-silica vacuum window. The majority of the photons in the laser pulse are transmitted through the electron bunch and pass out of a similar fused-silica vacuum window on the other side of the interaction chamber where a f = 100 mm plano-convex collimating lens and several mirrors direct the laser beam onto an energy meter providing pulse by pulse energy normalisation.

The inverse-Compton scattered photons proceed from the LWIP near parallel to the electron beam and are detected by the laser-wire detector further along the extraction line after the B5FF dipole magnet. Here, the direction of electron beam is changed by the magnet leaving the unaffected photons to pass straight through the magnet and the 300 μm thick aluminium vacuum window into the laser-wire detector.

The laser-wire lens is fixed to the vacuum chamber and the whole vacuum chamber is moved using a two axis x-y mover system. This moves the laser-wire lens by the same amount and hence the focus of the laser beam allowing the laser focus to be scanned across the electron beam. Scanning the vertical position of the vacuum chamber and hence the focussed laser spot is the principal method of performing a laser-wire scan and profiling the electron beam. The laser system, interaction point and detection are among the various parts of the experiment described in the following sections.

2.3 Laser System

The laser system used consists of a seed laser followed by three amplification stages, providing laser pulses of length $\sigma \approx 150$ ps with an energy of up to 400 mJ. The wavelength of the output pulse is 532 nm. The layout of the laser system is shown schematically in Figure 2.3.

The seed laser is a Time-Bandwidth Neodynium-doped vanadate (Nd:VAN - chemical formula Nd^{3+}:YVO_4) passively-modelocked laser that produces a beam of pulses at $\sim$ 357 MHz

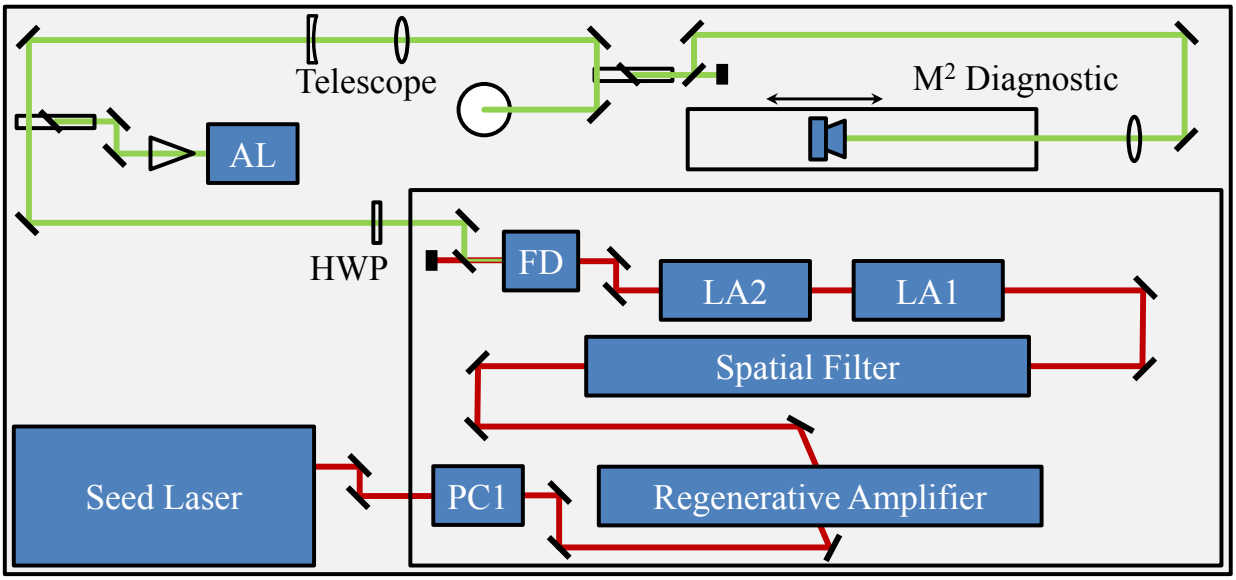

Figure 2.3: Schematic of the laser system used. PC1 is the first EOM that modulates the beam, LA1,2 are the linear amplifiers and FD is the frequency doubling crystal. The red line represents the path of the laser beam before FD and the green line represents the frequency doubled light afterwards. AL is the low power CW alignment laser and HWP is a half-wave plate.

with a typical output power of 500 mW. The wavelength of the laser light from the seed laser is 1064 nm. One of the mirrors in the seed laser cavity is mounted on a piezo-driven actuator that allows the position of the mirror and hence the cavity length to be controlled electronically. This is used along with feedback from a photodiode in the laser enclosure to lock the laser frequency to the frequency of the accelerator.

The laser beam from the seed laser is directed into the main laser system containing the three stages of amplification. Two electro-optic modulators (EOMs) are used in conjunction to isolate a single laser pulse from the continuous stream of pulses from the seed laser at 1.56 Hz, the repetition rate of the extraction line in the ATF2. The single pulse is amplified in a regenerative amplifier which passes the same laser pulse many times through a laser gain medium providing a high level of amplification. A third EOM is used to extract the pulse once it has reached the maximum possible pulse energy in the regenerative amplifier. The second and third EOMs are contained within the cavity of the regenerative amplifier and are not shown in Figure 2.3.

The laser gain medium in the regenerative amplifier is a flash lamp pumped Neodynium-

doped Yttrium Aluminium Garnet (ND:YAG - chemical formula $Nd^{3+}:Y_3Al_5O_{12}$) rod. Due to the transient nature of the light from the flash lamps, the gain in the regenerative amplifier is also short-lived and the timing of the pulse injection and extraction to the regenerative amplifier is precisely controlled using external electronics. The flash lamps although transient provide a very high intensity pump source for the laser gain medium. The pulse remains in the regenerative amplifier for approximately 15 round trips of the cavity before the gain decreases and it is favourable to extract the laser pulse.

After the regenerative amplifier, the laser pulse is transported through a spatial filter that is designed to alter the near Gaussian transverse intensity profile from the regenerative amplifier into a top-hat profile. The spatial filter was opened up so as not to affect the intensity profile and preserve the Gaussian profile, which would therefore provide a smaller focussed spot size and better laser-wire resolution. Following this are two single-pass linear amplifiers that contain flash-lamp pumped Nd:YAG laser gain media. These provide a high level of amplification due to the high power flash lamps and their large volume. The pulse energy after exiting the regenerative amplifier is approximately 15 mJ which is increased to nearly 900 mJ after the two linear amplifiers.

The timing of the flash lamps in the linear amplifiers can be varied manually with respect to the timing of the regenerative amplifier. By increasing the delay of the linear amplifier flash lamps the flash lamps fire later and the laser pulse that passes through experiences a lower gain. In this way the gain and hence the final output pulse energy of the laser system can be controlled.

After the linear amplifiers, a nonlinear potassium titanyl phosphate (KTP - chemical formula $KTiOPO_4$) crystal is used to double the frequency and hence halve the wavelength of the light. This halves the minimum focussed spot size achievable with the laser beam and although approximately 40 % efficient, is necessary for the factor of two gain in resolution required to achieve micrometre resolution. Here, the input wavelength of 1064 nm therefore becomes 532 nm. Two filters separate the 532 nm wavelength light from the residual unconverted 1064 nm light before the beam exits the laser system.

The change of wavelength also affects the Compton cross-section as described by Equation 1.20. However, the decrease in Compton cross-section is ~ 1 % at the electron energy of 1.28 GeV at the ATF2. At the design energy of 250 GeV for the ILC, the Compton cross-section would be reduced by ~ 10 %. In either case, this decrease can be accommodated by the available pulse energy of the laser system.

After the laser system, various CVI 3" diameter mirrors coated for a high reflectivity (> 99.6 %) at 532 nm, as well as a high damage threshold are used to direct the laser beam towards the periscope that transports the laser beam into the accelerator environment. A half-wave plate placed immediately after the exit port of the laser system rotates the output linear polarisation into the plane of incidence of the mirrors for a higher reflectivity from each mirror.

A telescope consisting of a plano-concave lens followed by a plano-convex lens before the periscope manipulates the size and divergence of the laser beam to give the appropriate sized beam at the LWIP. Additionally, two extra mirrors mounted on linear translation stages allow both a low power alignment laser (AL) to be inserted into the main laser beam path as well as for the main laser beam to be extracted for diagnostic purposes.

An optical relay line ~ 17 m long was constructed in the laser laboratory above the accelerator to simulate the full path length of the laser beam from the exit aperture of the laser system to the LWIP. This was used to make various diagnostic measurements easily within the laser laboratory and did not require access to the accelerator, which is inaccessible during its continuous operation periods.

2.4 Interaction Point

The laser beam and electron beam meet at the laser-wire interaction point (LWIP), which consists of a custom made vacuum chamber with circular fused-silica vacuum windows on either side to allow the laser beam to pass through. A custom made fused-silica doublet lens of focal length 56.6 mm was mounted to the side of the vacuum chamber to focus the laser

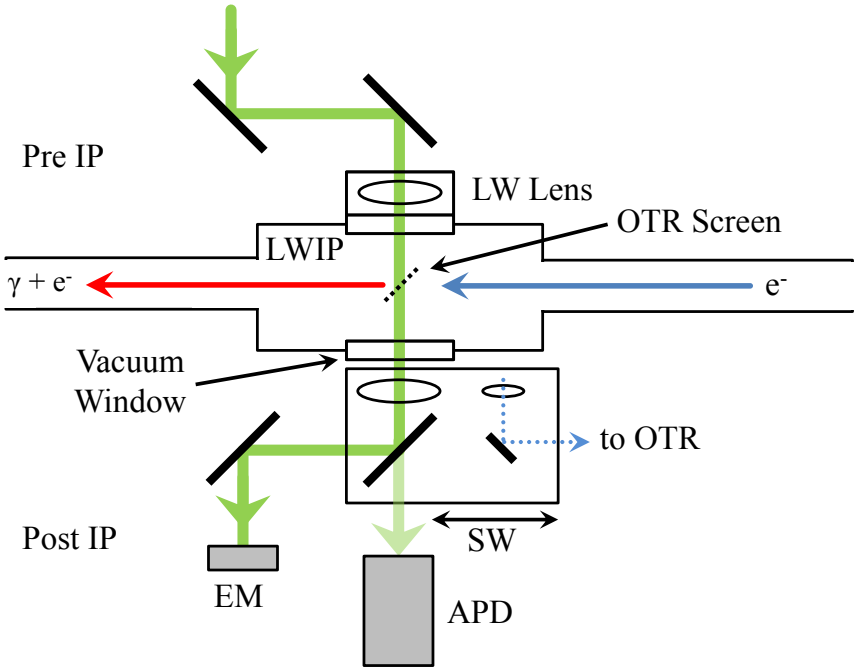

Figure 2.4: Plan view of the LWIP where the electron beam is moving from right to left. The laser beam (green) enters from the top and is directed to the LWIP by mirrors where it is focussed by the LW lens which is mounted to the vacuum chamber. Post IP, a moveable stage (SW) is used to switch between the LW and OTR optics (set to LW here). The main laser beam is dumped after the IP into the energy meter (EM). The OTR screen can be raised above the IP and is shown here as a dashed line.

beam on to the electron beam. A plan view of the LWIP is shown in Figure 2.4.

The lens is made of fused-silica as this is the only material that will not darken with the radiation from the electron beam as is common with normal types of glass [23]. As the refractive index of the fused-silica is dependent on the wavelength of the light passing through it, different spectral components will focus at different distances from the lens. This chromatic aberration causes the lens to produce a larger focussed spot size for a input beam with a broad spectral input than it would for a monochromatic source. Commonly, lenses can be designed to be chromatically corrected by constructing the lens from two pieces of glass with different compositions and hence different refractive indices. However, as only a single suitable material that is radiation resistant exists, the lens has a bandwidth acceptance of 2 nm.

The LW lens consists of three pieces of fused-silica. Two pieces are mounted together in a threaded holder and the third is the uniform thickness vacuum window. The vacuum

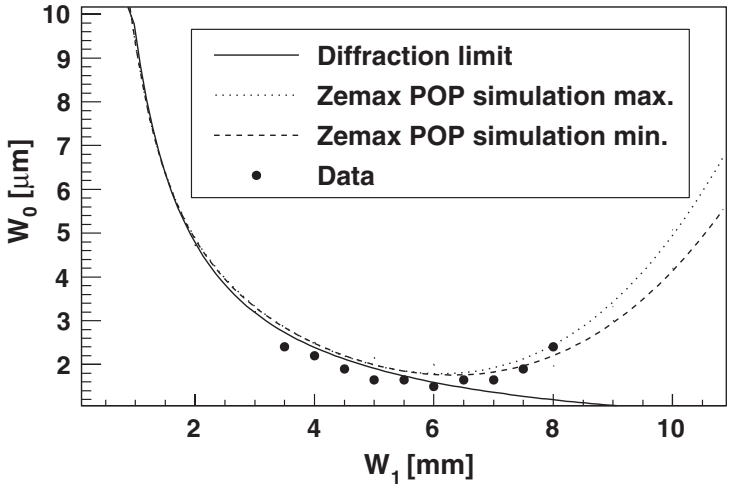

Figure 2.5: Lens simulation using ZEMAX software showing the predicted focussed spot size. Measurements of a high spatial quality CW laser focussed by the lens are overlaid.

window had to be taken into account during the lens design if the minimum focussed spot size was to be achieved. Simulations by S. Boogert and data recorded by M. Newman are shown in Figure 2.5 [23] that depict the size of the focussed spot w_0 as a function of input beam size w_1. In both cases w is the beam radius which is equivalent to 2σ for a beam with a Gaussian transverse intensity profile.

For increasing input beam sizes $w_1 < 4$ mm, the focussed spot size decreases as would be expected from Equation 1.25. However, beyond this point, the finite size of the lens acts as an aperture that causes the focussed beam size to increase. When the laser-wire was first demonstrated at the ATF, these simulations and measurements had not been performed and a larger input beam size was used. The divergence of the laser beam from the laser system was not adjusted in any way in the laser-wire at the ATF and so this was required at the ATF2 to provide the correct input beam size to the LW lens.

It was also envisioned that if this was adjustable during accelerator operation, the input beam size could be adjusted to empirically achieve the smallest laser-wire scan demonstrating the best resolution. From Figure 2.5 it is clear that the optimum input beam size is 6 mm, which corresponds to a 4σ diameter (more commonly measured) of 12 mm. For this input beam size, the focussed spot size is predicted to be $\sigma = 2.03$ μm [23]. The distance over which the laser focus will stay approximately constant is ~ 80 μm which is explained in

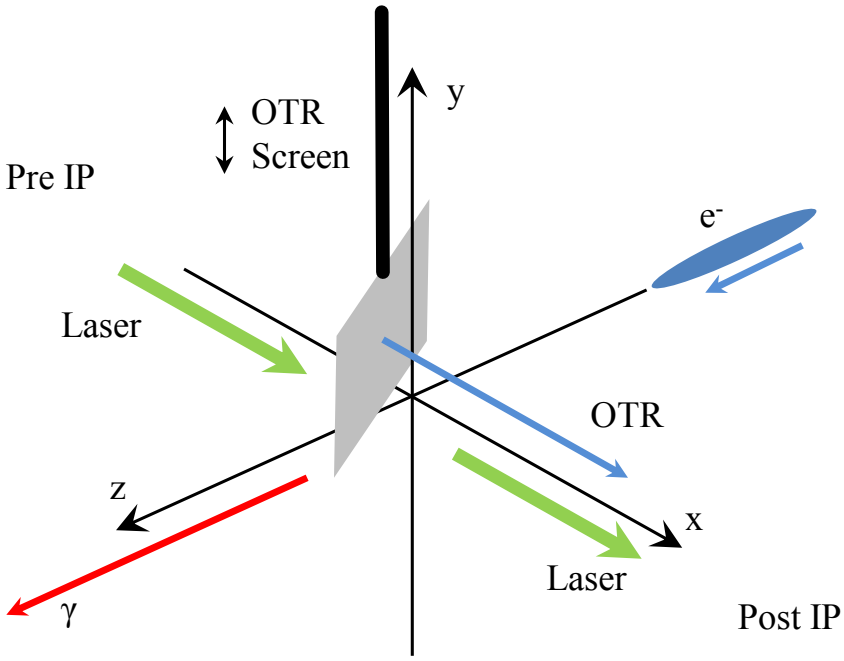

Figure 2.6: The x, y and x axes of the LW interaction with the electron beam. The OTR screen is shown here above the LWIP (0,0,0) for clarity. Laser photons scatter off the electron beam travelling parallel to the electron beam (γ).

greater detail in Section 4.7.

The geometry of the interaction is shown in Figure 2.6 where the axes of the interaction are defined as well as the direction of the laser beam, electron beam, inverse-Compton scattered photons and OTR are illustrated. A rotated isometric projection of the LWIP is shown in Figure 2.7 where the post LWIP side of the vacuum chamber as well as the recollimating lens have been removed.

As can be seen in Figure 2.7, a vacuum manipulator arm mounted above the interaction point inside the vacuum chamber holds an aluminium coated 300 μm thick silicon screen. This screen served as an alignment aid for the laser-wire but also as an OTR screen that could be used along with special optics external to the vacuum chamber to image the beam directly. The manipulator arm could be translated vertically (y) and rotated about the vertical axis by computer control. Additionally, two micrometers allowed manual adjustment of the manipulator arm position along both the laser axis and the electron beam axis (x and z respectively).

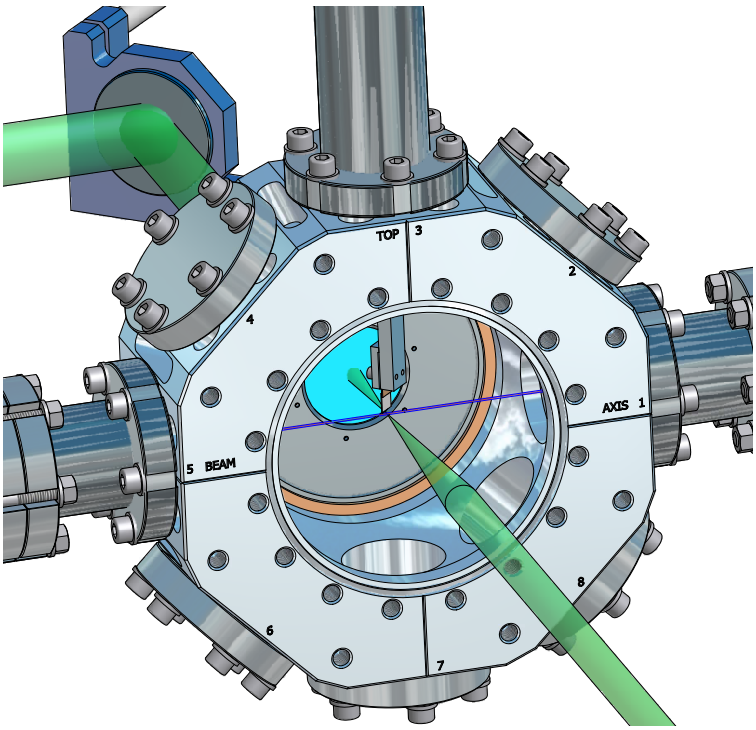

Figure 2.7: Schematic of the laser-wire interaction point with both the post IP side of the vacuum chamber and recollimating lens removed.

Figure 2.8a shows a photograph of the laser-wire lens mounted in a kinematic lens mount on the side of the vacuum chamber, and Figure 2.8b shows a photograph of the LWIP from the post-IP side. The electron beam passes from right to left in Figure 2.8b, passing through the LWIP vacuum chamber, which can be seen in the centre. The laser beam transport (grey pipe) and the second enclosed relay box (black) can be seen behind the LWIP. The mover system for the OTR screen mounted on the manipulator arm can be seen protruding from the top of the LWIP enclosure.

After post-LWIP recollimation of the laser, the laser beam is directed onto a Gentec-EO QE25LP-S-MB energy meter. Behind the first mirror after recollimation, light collection optics collect and focus the small amount of transmitted laser light from the mirror into a fibre bundle, which carries the light to an avalanche photodiode (APD) below the accelerator beam line. The APD is used to detect both the laser light and the OTR, and is therefore used for temporal alignment of the laser and electron beams. Because of the high sensitivity of the APD, a ceramic shield is moved into place by a translation stage to cover the entrance to the light collecting optics during normal laser-wire operation where the high power laser

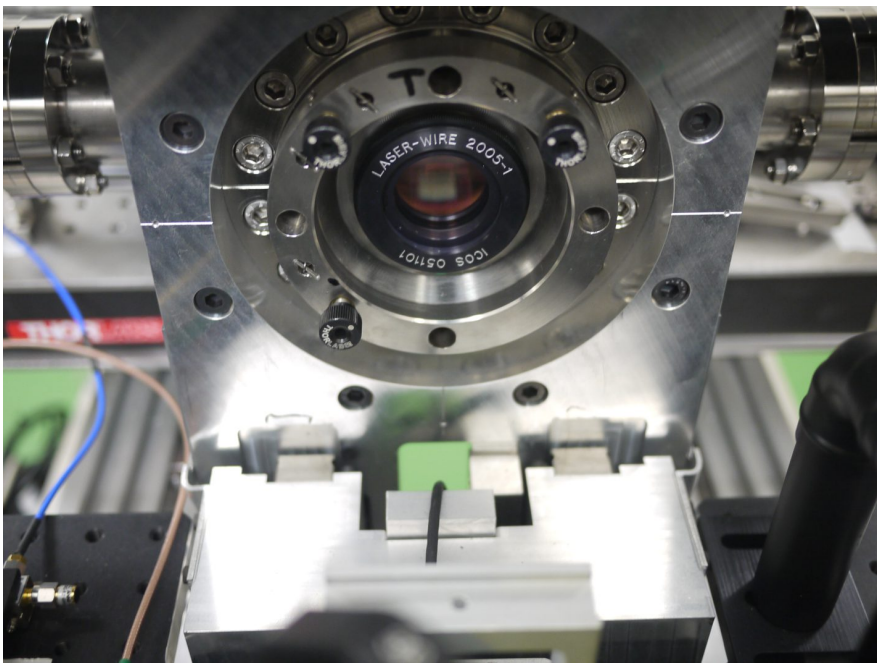

(a) Photograph of the LW lens mounted to the vacuum chamber.

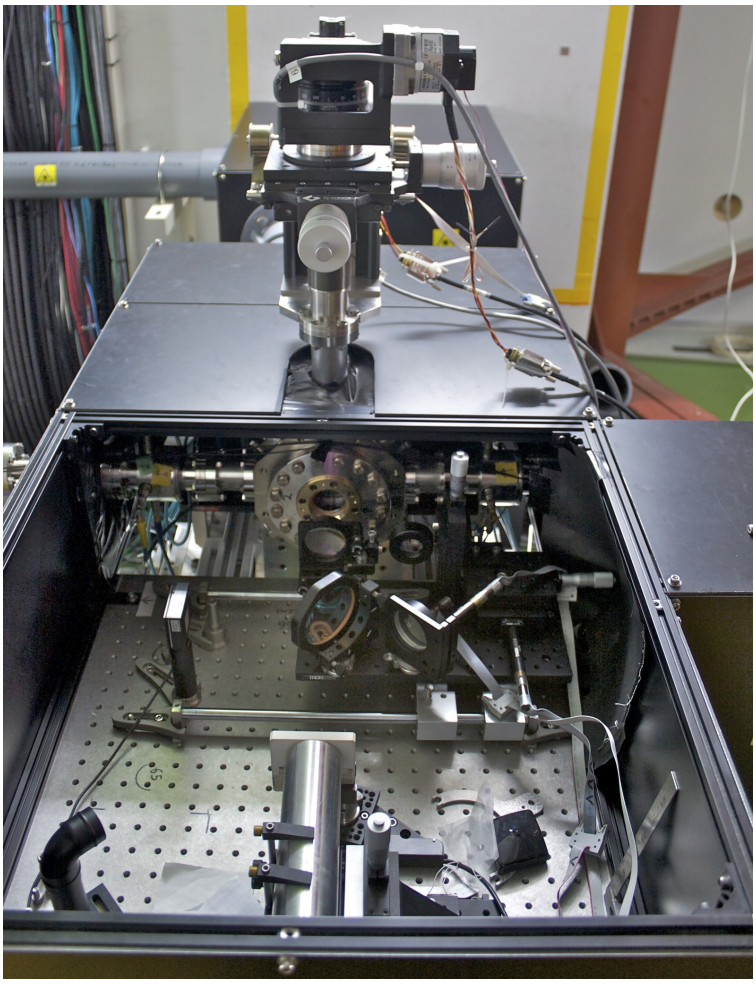

(b) Photograph of the LWIP from the post-IP side.

Figure 2.8: Photographs of the laser-wire interaction point showing (a) the laser-wire lens mounted to the side of the chamber and (b) the post interaction side of the vacuum chamber. Here, the electron beam passes from right to left and the laser is coming out of the page.

light would damage it.

Both the recollimating lens and the turning mirror are mounted on top of a moveable bread-board that can be moved parallel to the electron beam remotely by computer control. This allows a different recollimating lens and optical beam path to be used for observing the OTR and using it as a monitor of the electron beam size at the LWIP.

The LWIP vacuum chamber is moveable both along the laser axis (x) and vertically (y) using remotely controlled geared stepper motors, which are geared down by a ratio of 200:1. An optical position readout gives a position accuracy of $\pm$ 50 nm. By moving the vacuum chamber along the x axis, the laser focus is also moved along the x axis. Moving the chamber vertically in the y axis moves the laser focus vertically with respect to the electron beam.

2.5 Electron Beam Optics

The nominal ATF2 electron beam optics are designed to produce a 37 nm vertical focus at the ATF2 IP at the end of the extraction line [21]. To achieve such a small vertical electron beam size, the electron beam behaviour, the magnets used and their settings must all be thoroughly characterised. The extraction line contains a diagnostic section containing four wire scanners and four experimental OTR monitors before the final focus section, which consists of the electron beam optics designed to produce the small vertical electron beam size. 41 high resolution cavity BPMs are placed throughout the extraction line providing accurate position information [24].

The square root of the β functions of the nominal ATF2 electron beam optics around the LWIP is shown in 2.9a. The β functions have values of $\beta_x = 8.167$ m and $\beta_y = 5.786$ m in the horizontal and vertical respectively at the LWIP. The electron beam optics of the ATF2 accelerator lattice in this chapter were developed using MAD software by M. Woodley. The nominal values of horizontal and vertical dispersion at this point in the extraction line are 0.5×10^{-8} m and 0 m respectively. The horizontal and vertical emittances are also nominally 1.2 nm-rad and 12 pm-rad in the extraction line. Substituting these values into

Equation 1.15, the expected beam size at the LWIP using the standard ATF2 electron beam optics is 99.0 μm horizontally and 8.33 μm vertically.

To fully demonstrate the ability of a laser-wire to scan 1 μm electron beams, a special set of electron optics were developed by L. Deacon and M. Woodley, which were designed to produce a smaller vertical beam size at the LWIP. Additionally, the optics were matched back to the nominal ATF2 electron beam optics for the remainder of the accelerator to ensure containment, low background and compatibility with other users of the facility. The square root of the β functions using these LW electron beam optics around the LWIP is shown in Figure 2.9b. In a similar fashion to conventional optics, a large input beam size to a lens, or magnet in this case, produces a smaller focussed spot size, and so the electron beam is first allowed to expand by reducing the strength of the magnets before the two quadrupoles immediately before the LWIP that then strongly focus the electron beam.

Using the LW electron beam optics, the β functions at the LWIP calculated using MAD are $\beta_x = 0.461$ m and $\beta_y = 0.300$ m. Using Equation 1.15, the predicted size of the electron beam is 23.5 μm horizontally and 1.9 μm vertically.

Figure 2.10a shows the square root of the β functions beyond the LWIP for the nominal ATF2 electron beam optics. As in Figure 2.9a, these have a relatively constant and low value throughout the LWIP region before reaching the start of the final focus section of the lattice where the vertical beta function (dashed line) characteristically increases as part of the final focus optics design.

In contrast, Figure 2.10b shows the same part of the accelerator lattice using the LW electron beam optics. Here much greater changes in the vertical and horizontal β functions can be seen before and after the LWIP at approximately $s = 42$ m. However, the β functions were successfully matched going into the final focus section of the lattice as can be seen by the characteristic rise of β_y at $s = 60$ m.

The integrated magnet focussing strengths for both the normal ATF2 electron beam optics and the LW optics are shown for comparison in Table 2.1. The letter Q in the magnet

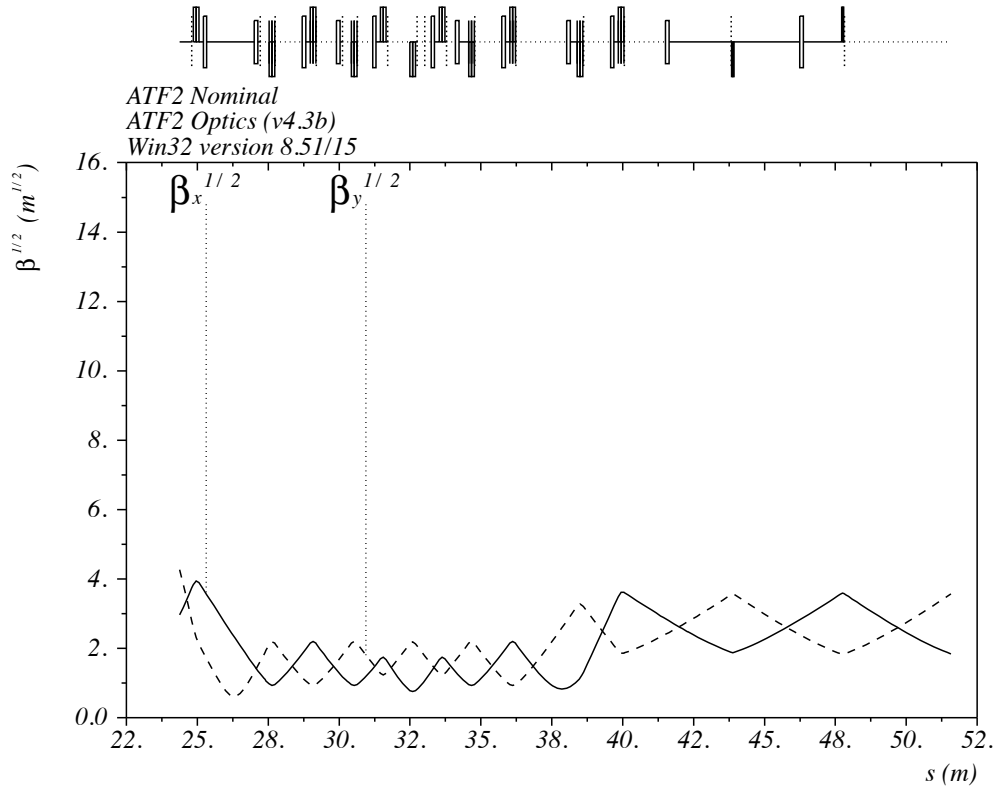

(a) ATF2 Optics Beta Functions

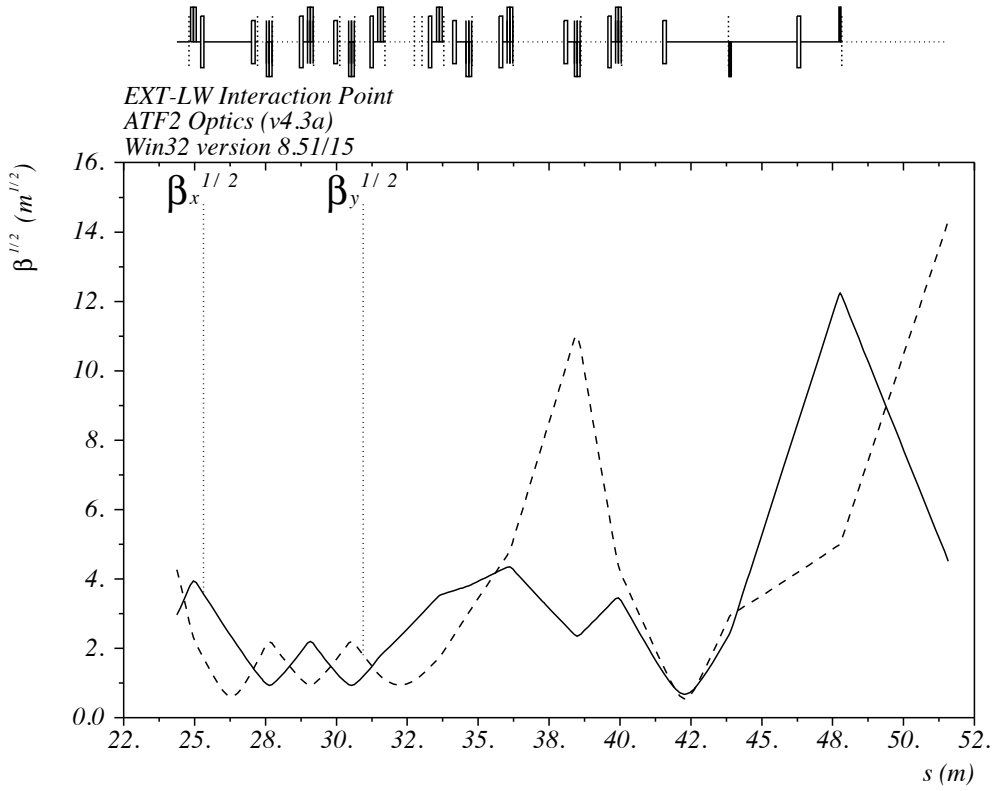

(b) LW Optics Beta Functions

Figure 2.9: The horizontal (solid line) and vertical (dashed line) $\sqrt{\beta}$ functions at the LWIP for both (a) the nominal ATF2 electron beam optics and (b) the laser-wire optics. The electron beam is moving from left to right and the laser-wire interaction is at approximately $s = 42$ m.

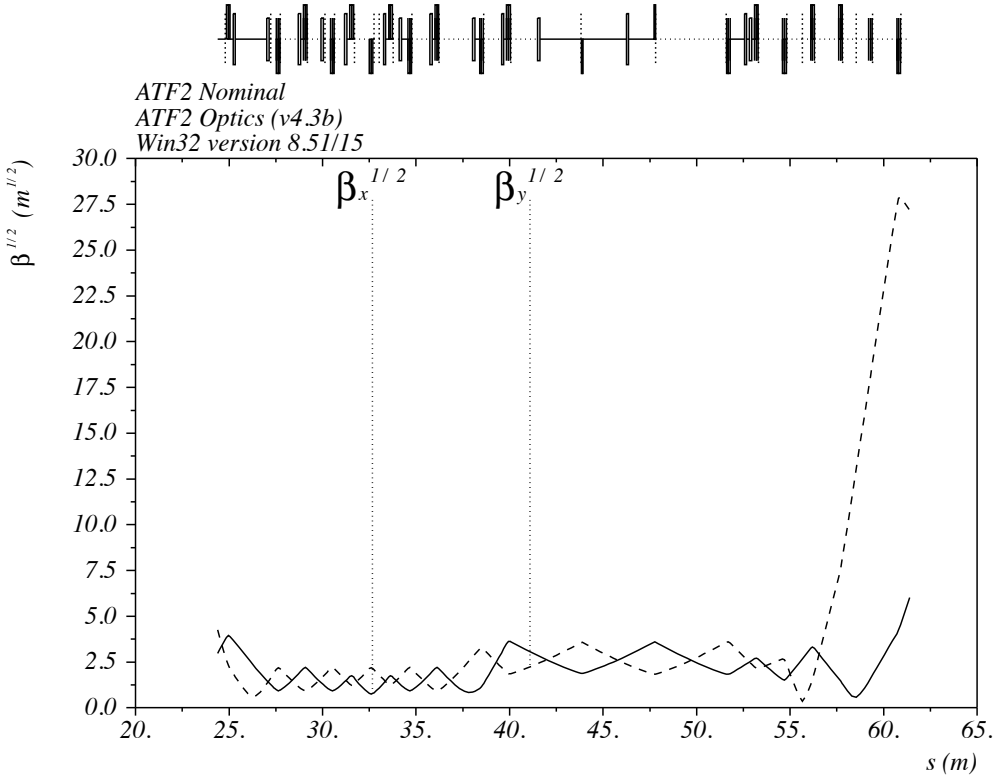

(a) ATF2 Optics Beta Functions Final Focus

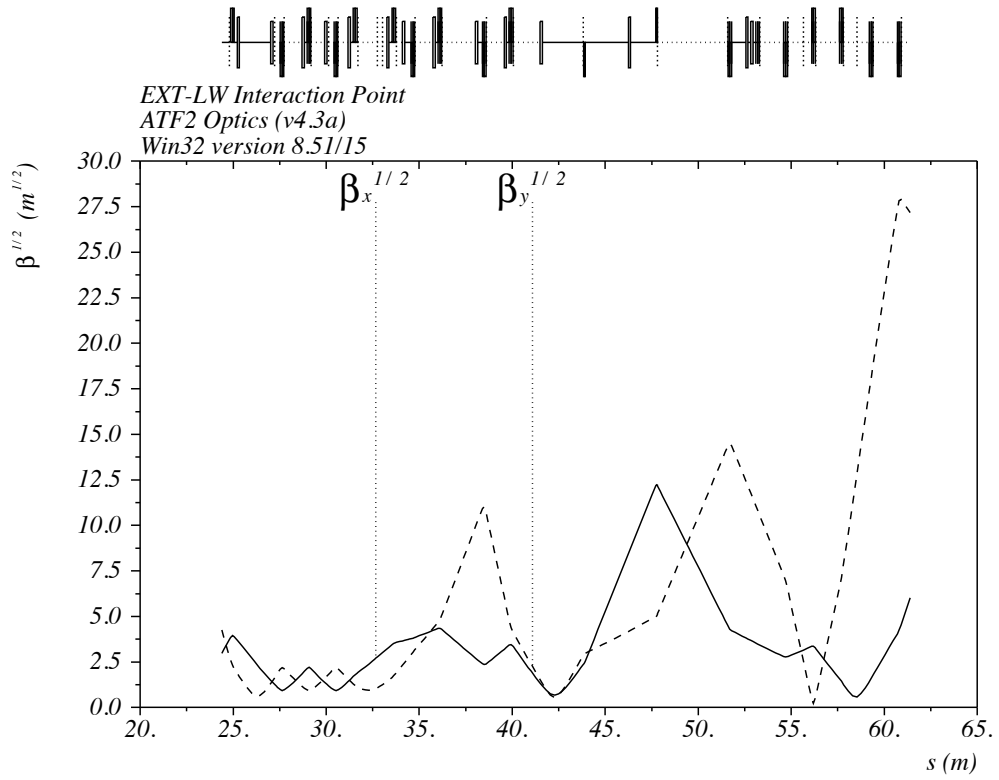

(b) LW Optics Beta Functions Final Focus

Figure 2.10: The horizontal (solid line) and vertical (dashed line) $\sqrt{\beta}$ functions entering the final focus section for both (a) the nominal ATF2 electron beam optics and (b) the laser-wire optics. The electron beam is moving from left to right and the laser-wire interaction is at approximately $s = 42$ m.

Table 2.1: Integrated magnet focussing strengths for normal ATF2 electron beam optics and the laser-wire optics with the electron beam passing through the elements from the top of the table to the bottom.

Magnet	k (m^{-1}) Normal ATF2 Optics	k (m^{-1}) Laser-wire Optics	Δk (m^{-1})
QD8X	-0.5696	-0.5696	0
QF9X	0.7933	0.7933	0
QD10X	-1.2420	-1.2420	0
QF11X	1.0233	1.0233	0
QD12X	-1.0233	-1.0233	0
QF13X	1.3682	0.1810	-1.1872
QD14X	-1.0154	0.0000	+1.0154
QF15X	1.3682	0.1810	-1.1882
QD16X	-1.0233	-0.0315	+0.9918
QF17X	1.0233	0.3006	-0.7227
QD18X	-0.6860	-0.6809	+0.0051
QF19X	0.6551	0.6693	+0.0142
LWIP			
QD20X	-0.3023	-0.4458	-0.1435
QF21X	0.3014	0.3746	+0.0732
QM16FF	-0.4420	-0.3443	+0.0977
QM15FF	0.5942	0.000	-0.5942
QM14FF	-1.2291	-0.3111	+0.9180
QM13FF	0.7977	0.5393	-0.2584
QM12FF	0.3410	0.3056	-0.0360
QM11FF	0.0000	-0.0155	-0.0155
QD10FF	-0.2900	-0.2900	0
QF9FF	0.3787	0.3787	0
QD8FF	-0.6044	-0.6044	0
QF7FF	0.5502	0.5502	0
QD6FF	-0.6023	-0.6023	0

name indicates the magnet is a quadrupole, F or D whether it is a focussing or defocussing magnet, M if it is a magnet designed to match into the final focus and the number its point in the lattice. The suffix represents whether its location is in the extraction line (X) or in the final focus (FF) section. Here the skew quadrupoles used for correcting x-y coupling are omitted as these are nominally turned off and only used at small values to make online corrections. The dipoles in the final focus section are also omitted as their value would not affect the size of the electron beam, nor can they be changed. In Table 2.1, the electron beam proceeds from the top of the table to the bottom.

2.6 Detection

A detector developed by Boogert et al. [23] was modified and used for the laser-wire experiment and consisted of a 6 mm thick sheet of lead on top of a 40 mm × 40 mm × 40 mm piece of SP-15 Aerogel (density 60 kgm^{-3} and refractive index 1.015). The high energy inverse-Compton scattered photons from the LWIP generate high momentum electron-positron pairs in the lead, which in turn produce Cherenkov radiation as they pass through the Aerogel. The Cherenkov radiation is guided to a Hamamatsu R877 photomultiplier tube (PMT) by an aluminium-coated-Mylar lined pipe. The voltage generated by the PMT was digitised using a gated 14-bit analogue-to-digital converter (ADC) that represents the input signal as a value between 1 and 16836.

Given the new location of the laser-wire at the ATF2 with respect to the laser-wire at the ATF, as well as the space available, the detector was rebuilt with the same head but with a new geometry of light pipe allowing the insertion of the detector immediately behind the window from the vacuum chamber and before the next magnet in the lattice. The geometry of the detector is shown schematically in Figure 2.11.

A theoretical investigation undertaken by L. Deacon has shown that the maximum inverse-Compton scattered photon energy detectable using this Cherenkov detector is 30 MeV and that the detectable threshold is 2.9 MeV [22]. Using Equation 1.21, the spectrum of the scattered photons is shown in Figure 2.12 where the maximum energy of the scattered photons is 29.4 MeV. The electron-positron pairs, that produce the detectable Cherenkov radiation in the Aerogel scintillator, will only be produced in the lead sheet if the photon energy exceeds 1.022 MeV, the sum of the rest masses of the electron and positron. Given the spectrum in Figure 2.12, the majority of the inverse-Compton scattered photons are within the bandwidth of the detector.

Additionally, using Equation 1.4 and the bending radius of 16 m [21] of the dipole immediately before the detector, the peak frequency of the synchrotron radiation emission spectrum is $\tilde{0}.3$ keV, which is below the threshold for electron-positron pair production.

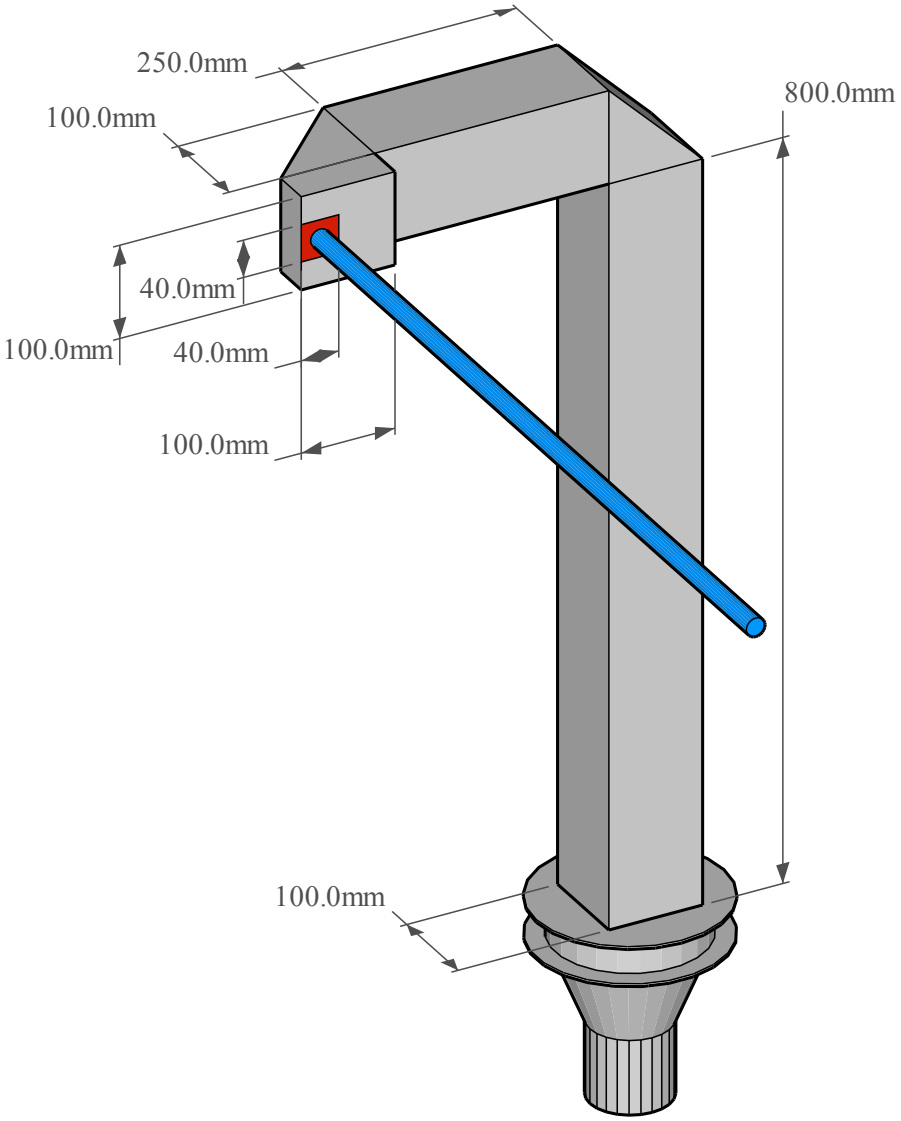

Figure 2.11: Schematic of the detector used. The active area is shown on the face of the detector in red. The blue cylinder represents the incoming photon trajectory.

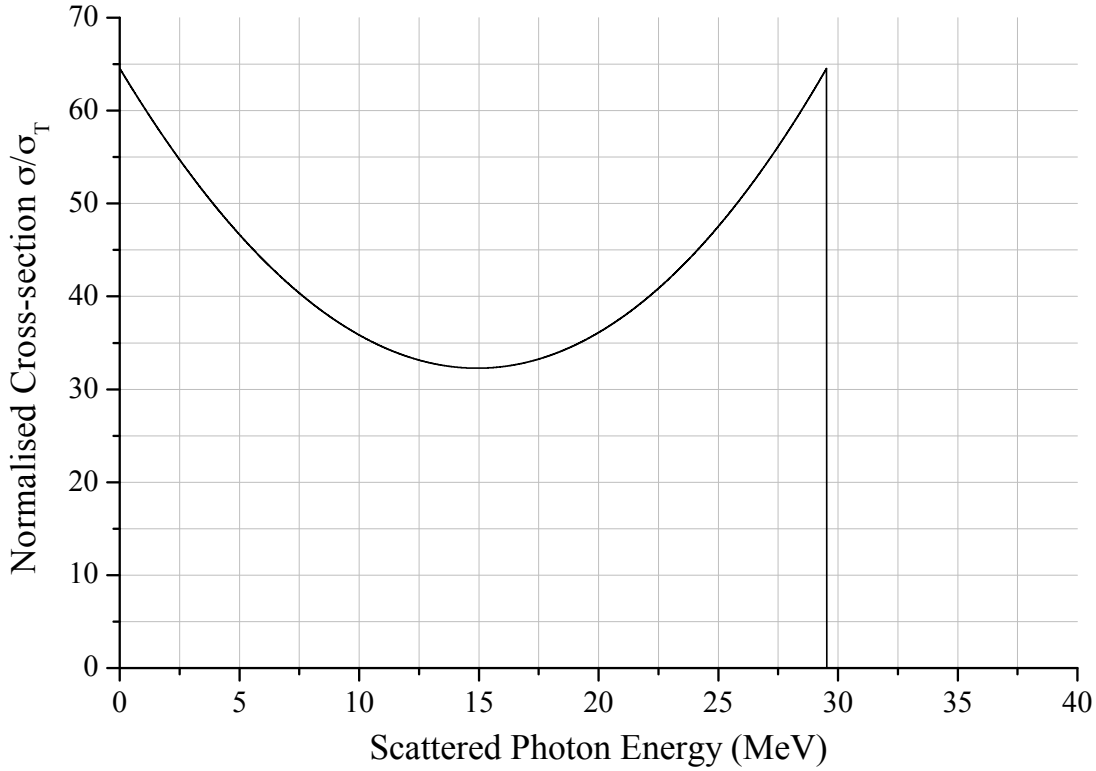

Figure 2.12: Calculated energy spectrum of the scattered photons from the laser-wire at the ATF2 with an electron energy of 1.28 GeV and a photon wavelength of 532 nm.

Therefore, the synchrotron radiation will not provide a background signal in the detector.

The gain of the PMT is controlled by its supply voltage and a high voltage power supply was used to provide the required operating voltage of 1250 V, with which the gain of the PMT was determined to be 5.0×10^5 [22]. The ADC is gated by a gate signal from the main electronics. During accelerator operation, the background signal was observed along with the gate signal on an oscilloscope and the width and timing of the gate were adjusted to only encompass the signal from the PMT. Furthermore, the ADC output was recorded with no input connected as a background reading that was subtracted using software detailed in Section 2.9. The ADC is integrated into a CAMAC crate which provides the computer interface necessary for integration into the main data acquisition software (DAQ). Additionally, a variable attenuator that could provide combinations of -1, -2, -4 and -8 dB of attenuation was used before the ADC to avoid saturation.

L. Deacon has shown using an light emitting diode as a light source, that with -22 dB of attenuation (typical of operation) that the digitised PMT signal is linear with the number

of input photons to the PMT [22].

2.7 Timing

To collide 150 ps long laser pulses with 30 ps long electron bunches (σ in both cases) stably, an accurate timing system is required that ensure the correct arrival time of the laser pulse with respect to the electron bunch.

The master oscillator of the ATF2 has a frequency of 1.427989 GHz from which all timing signals are derived. A 10 MHz reference signal from this master oscillator is carried across the accelerator building by a coaxial cable to the laser laboratory above the LWIP. Here, a local signal generator is used to generate the operating frequency of 356.99 MHz of the ATF2 extraction line, which is a quarter of the master oscillator frequency. Generating the required frequency locally in the laser laboratory ensures that the signal is of sufficient quality and stability that it can be used to frequency lock the laser system as well as triggering the data acquisition system (DAQ). If the master oscillator changed frequency, the local oscillator frequency had to be recalculated and updated.

Trigger signals for various components of the laser system as well as the DAQ are generated using TD2 digital delay modules in a nuclear instrumentation module (NIM) standard crate. These count a programmable number of clock cycles from an input clock signal which is started by an input trigger signal. After the desired number of clock cycles has passed, an output pulse is produced. Multiple copies of the same output pulse are available from one delay module.

To ensure there is sufficient time for the laser system to amplify a seed pulse and for the pulse to reach the LWIP, the pre-extraction kicker trigger signal is used. This trigger signal primes the high voltage power supply of the extraction kicker and happens a fixed number of damping ring clock cycles before the extraction trigger signal fires the extraction kicker.

The locally generated 356.99 MHz signal is passed through a voltage controlled phase

shifter before it is distributed as a clock source for the laser-wire laser and DAQ allowing the laser and electron beams to be precisely temporally aligned.

2.8 Alignment

To repeatedly collide an ideally 1 μm laser beam and electron beam at 90° when the pulse lengths are on the order of picoseconds requires precise and accurate temporal and spatial alignment. In the following sections, the methods used to achieve this alignment are detailed.

2.8.1 Temporal Alignment

To align the laser pulse and the electron bunch temporally, OTR from the OTR screen generated by the electron beam and laser light transmitted beneath the screen are simultaneously observed using the APD. The signal from this is observed using an oscilloscope and the timing of the laser adjusted to match the electron beam. The master trigger for the laser system is controlled using a TD2 NIM delay module that counts a programmable number of 357 MHz clock cycles before triggering the laser system. By adjusting the delay of the TD2 module and then the control voltage of the phase shifter, the laser pulses and electron bunches can be overlapped temporally.

2.8.2 Spatial Alignment

To align the laser-wire vertically, the edge of the OTR screen is placed at the reference position of the laser focus in the vacuum chamber with the laser set to its minimum intensity so as not to damage the OTR screen. The vacuum chamber and hence the laser focus is then scanned vertically until the electron beam is encountered as evidenced by the large background signal detectable when the OTR screen is placed in the electron beam.

The LW vacuum chamber is aligned like all other components of the ATF2 using a laser theodolite to within $\pm$ 100 μm in any dimension of the desired position on the accelerator

axis. The vacuum chamber can therefore be set to its zero horizontal position and the laser focus should be sufficiently close to the electron beam to generate detectable collisions that can then be optimised by performing horizontal and vertical laser-wire scans. The OTR screen is then removed and the laser energy increased to achieve collisions.

2.9 Data Acquisition System

Normal operation of the ATF2 and the laser-wire is carried out in the ATF2 control room which is in a separate building from the accelerator as the accelerator is a radiation-hard environment that cannot be accessed during operation. For this reason the laser-wire system is operated remotely using a software interface. To control various devices part of the laser-wire, read, record and analyse data a DAQ system is used comprising of several pieces of software.

- Experimental Physics and Industrial Control System (EPICS)
- LabView
- Python
- Extensible Display Manager (EDM)

An EPICS database created by S. Boogert that I developed allows values to be stored under variables that can be easily accessed from any computer on the ATF2 computer network. Any EPICS variable can either be written to, which replaces its old value with the new supplied one, or read from the database. The structure of the DAQ system is shown schematically in Figure 2.13.

All devices in the laser-wire system are controlled by a piece of software that reads and writes to the EPICS database. LabView is a graphical programming environment that most device manufacturers provide software drivers for, which most devices in the laser-wire system are controlled by. The virtual instrument programs ('VIs') created in LabView are

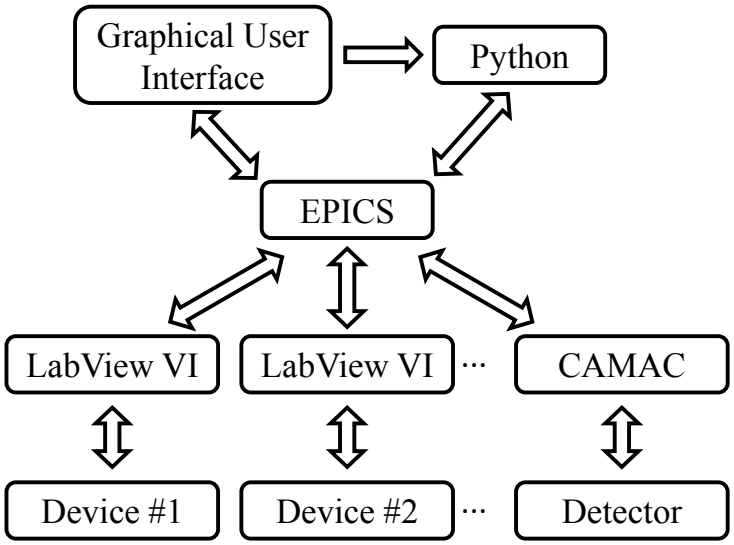

Figure 2.13: Schematic of the data acquisition system built where individual devices are controlled by an independent piece of software, typically a LabView program, which then interacts the EPICS database. A graphical user interface is used to monitor and control the system using python programs for automation.

compiled into simple executable files that stand alone and do not require the LabView environment on the computer they are deployed on to run. This greatly reduces the operational load on any one computer allowing multiple devices to be controlled simultaneously with a high degree of reliability.

The ADC however is installed in a computer automated measurement and control (CAMAC) crate that has its own Linux computer built into it. This runs its own custom built input-output controller software designed by the staff of the ATF2. The CAMAC crates updates all its EPICS variables when it is externally triggered by a gate signal from the main electronics system.

A graphical user interface (GUI) used to monitor and control the laser-wire system from the control room was built using Extensible Display Manager (EDM) software which provides full integration with EPICS and the ability to easily create interfaces. The GUI can display or set numeric values of EPICS variables as well as display them graphically. A screenshot of the GUI is shown in Figure 2.14. This can be accessed from any computer in the ATF2 irrespective of the operating system which allowed the vacuum chamber to be controlled from both the laser laboratory above the accelerator when temporally aligning the laser to

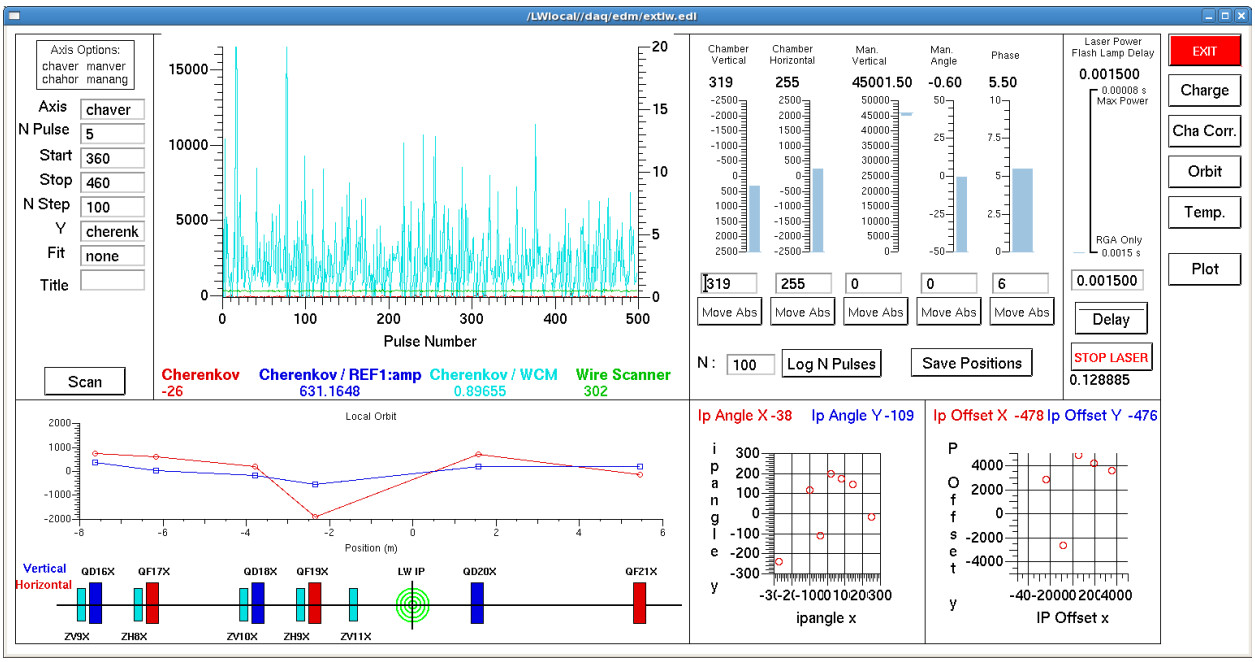

Figure 2.14: The graphical user interface built using EDM software. The BPM positions through the section of the accelerator surround the LWIP are shown in the bottom left quadrant. The detector signals are shown in the graph at the top and the vacuum chamber positions in the top right quadrant.

the electron beam and the control room for normal operation.

A number of small programs created using the python programming language are used to record, analyse and display data taken by the laser-wire as well as perform a number of intermediate steps between the user interface and the database. The python software created to perform a fully automated laser-wire scans is such a piece of software.

2.9.1 Scanning and Analysis Software

When making a laser-wire scan, a number of scan parameters are required to be entered into the GUI. These input fields write the values to intermediate EPICS variables, which contain parameters such as the start and stop positions of position scans, the number of positions between these to stop at and the number of samples at each location. Once the scan parameters are entered, a Python program is executed by clicking the scan button in the GUI. The Python program reads these intermediate EPICS variables and prepares a set of chamber positions for the scan. It then updates the appropriate EPICS variables

commanding the vacuum chamber to move to a specified position, during which the chamber position is monitored until it has reached is destination. The specified number of data samples are recorded and stored in a custom file format developed by S. Boogert. This is repeated until the prepared list of positions and hence the scan is completed.

Each scan is stored in its own time-stamped file on the network with information detailing the scan performed. In each data file, every variable from the laser-wire system available is recorded, which was possible given the relatively low number of variables as well as data samples. The parameters recorded in each data file are

- Extraction line orbit X & Y
- Detector signal
- Chamber vertical position
- Chamber horizontal position
- OTR screen vertical position
- OTR screen angular position
- Phase shifter voltage
- ATF2: linac charge
- ATF2: damping ring charge
- ATF2: extraction line charge
- BPM extraction line charge
- Temperatures around laser lab

After completion of the scan, the Python program uses other specially written python programs to extract the appropriate data from the new data file, analyse it and display the results graphically. The raw data is filtered to exclude any points where the ATF2 did not produce an electron bunch and then normalised to the recorded electron beam charge. The mean and standard deviation of the data at each chamber position are then calculated. The laser-wire scans were fitted to

$$y = y_0 + \frac{A}{\sqrt{2\pi}\sigma} exp\left(-\frac{(x - x_{centre})^2}{2\sigma^2}\right) \tag{2.1}$$

which is a modified version of Equation 1.24. Here y_0 represents the background, A is a scaling constant, x_{centre} is the x value the scan is centred about and σ is the width of the

scan.

This software provides immediate analysis of the recorded data allowing greater progress to be made in the limited time available for using the ATF2. Additional analysis can be performed by accessing the library of Python programs from any computer in the ATF2 network.

Chapter 3

Results of Laser-wire at ATF2

In this chapter, the results from the commissioning of the laser-wire at the ATF2 are presented. The results of the laser characterisation are presented in Section 3.1, after which the results from the alignment procedure as well as improvements to it are detailed in Section 3.2. In spring 2010, the laser-wire was operated but no collisions between the laser and the electron beam were observed. Modifications to the alignment and the detector that successfully overcame these difficulties are reported in Section 3.3. The results achieved after these improvements during the operation of the ATF2 in December 2010 are presented in Section 3.4, followed by a discussion of the possible electron beam size in Section 3.6.

3.1 Laser Characterisation

Before laser-wire operation using the accelerator, the laser system was characterised and tuned for optimal performance. In the following sections, the results of the basic characterisation are shown.

In all cases, the seed laser was allowed to stabilise before being frequency locked to locally synthesised 357 MHz signal. The frequency of the master oscillator of the accelerator was checked at the beginning of each shift and the frequency of the local signal generator updated accordingly. The frequency of the accelerator's master oscillator is occasionally changed throughout the seasons according to the expansion and contraction of the damping ring. Additionally, the flash lamps for both the regenerative amplifier and the two linear

amplifiers were turned on several hours before use to allow the system to thermally stabilise. This is key as the thermal lensing produced by the amplifiers is an integral part of the optical design and the without it the optical arrangement within the laser system would not produce a collimated output beam. The flash lamps are fired at the original design frequency of 6.24 Hz despite the lower multiple of the laser pulses passing through the system (1.56 Hz) to maintain the thermal load and hence thermal lensing.

3.1.1 Power and Energy Measurements

After the system had warmed up, the output power of the seed laser was measured to be approximately 530 mW. This varied over time but the power was maintained above 500 mW. At times when the output power dropped, it was often recovered by cleaning the cavity mirrors. As high as possible seed power is required for the passive modelocking process in the laser that provides the pulsed output.

The timing of the EOMs was adjusted to amplify a single pulse in the regenerative amplifier. Initially only EOM #1 was switched on and the signal from a photodiode permanently situated behind one of the two regenerative amplifier cavity mirrors was observed using an oscilloscope. In this regime, a broad series of laser pulses could be seen to increase in amplitude over time and then decay representing the initial amplification of the pulses as they oscillate in the cavity followed by their eventual absorption as the transient gain in the amplifier decayed. The timing of EOM #1 which allows pulses into the regenerative amplifier was adjusted using a dedicated delay module with a resolution of 0.25 ns for the three EOMs to give the highest intensity pulses.

After this, EOM #3 was turned on and its delay adjusted until only a single pulse is amplified. This is achieved when a clean oscilloscope trace of single pulses is observed as opposed to the multiple pulses with only EOM #1 turned on. If the delay of EOM #3 is made too short, no laser pulses are allowed into the cavity and no pulse build up is observed on the oscilloscope.

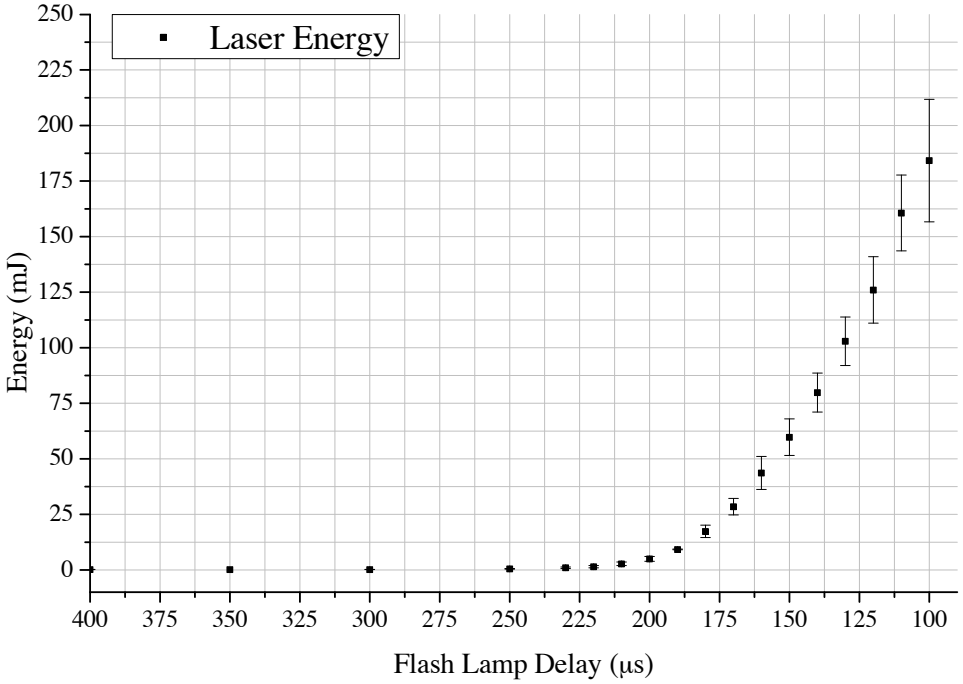

Figure 3.1: Laser pulse energy of the frequency doubled output measured at the exit aperture of the laser system for various linear amplifier flash lamp delays. The gain in the media is inversely proportional to the flash lamp delay and so the flash lamp delay is plotted in reverse order.

Finally, EOM #2 is used to extract a pulse from the cavity. The delay of this EOM is adjusted so that the maximum intensity pulse is extracted from the cavity. The regenerative amplifier output energy was regularly measured to be approximately 14 mJ, however at the time of the laser-wire data presented in the remainder of this chapter, the output pulse energy was measured to be 9.31 $\pm$ 1.69 mJ.

Similarly, the pulse energy measured immediately after the two linear amplifiers was measured at the start of the Autumn 2010 operation period to be approximately 850 mJ. However, the performance of the linear amplifiers decreased during this operation period and the output pulse energy was measured to be 483 $\pm$ 55 mJ at the time of the data presented here. This was deemed to be sufficient for laser-wire operation.

After the linear amplifiers, the light is frequency doubled in a nonlinear crystal. This process is approximately 40 % efficient and the measured laser pulse energies at the exit aperture of the laser after this are shown in Figure 3.1.

The pulse energies are shown as a function of the linear amplifier flash lamp delay. By decreasing the flash lamp delay the gain they generate in the linear amplifiers occurs closer to the time when the laser pulse passes through producing a greater amplification and hence higher pulse energy. The laser here produces a maximum output pulse energy of 184.2 ± 27.6 mJ. The approximately 15 % jitter of the laser pulse energy is higher than previous measured values of 5 % jitter. It is unclear why this is and future work remains to improve the stability of the laser system. The pulse energy jitter was accounted for by measuring the laser pulse energy whilst performing laser-wire scans and normalising the detected signal.

3.1.2 Spatial Quality

In order to model the propagation of the laser beam it is necessary to characterise its spatial quality. This is quantified using the dimensionless M^2 parameter that describes the measured propagation of a laser beam compared to that of one with a Gaussian transverse intensity profile. This is discussed in greater detail in Section 4.7, however it is useful to note that an ideal Gaussian beam would have an M^2 of 1 and that the spot size of the focussed laser beam scales with M^2.

The M^2 of the laser system was determined by measuring the transverse size of the laser beam using a WinCamD camera at various points through a focus generated using a lens. Figure 3.2 shows the recorded 4σ widths of the laser beam around a focus created using a 2" plano-convex lens with a focal length of 1 m. This focal length was chosen so as not to introduce spherical aberrations that may increase the M^2.

The laser beam was found to be generally elliptical and at an angle to the laboratory frame. The major and minor axes of the elliptical beam were found to focus at different distances from the lens (astigmatism) and so the profiles recorded on the camera were analysed along the major and minor axes of the ellipse at an angle of 35°, which was chosen manually by looking at the profiles. The M^2 was found by fitting the data to the M^2 model described in Section 4.7 giving values of 2.54 ± 0.13 and 1.98 ± 0.10 along the major and minor axes

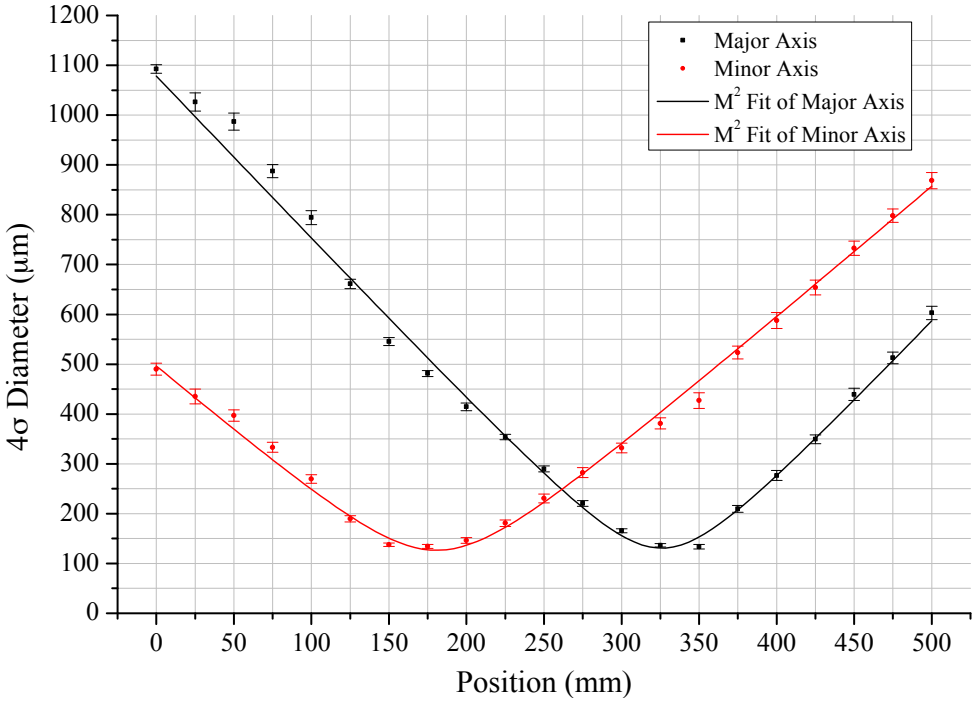

Figure 3.2: M^2 measurement of the laser output showing an astigmatic beam where the two independent propagation dimensions focus at different positions along the optical axis.

of the laser beam respectively. When the laser is scanned across the electron beam at the LWIP it will be the vertical projection of the focus laser beam that contributes to the size of the laser-wire scan and not the size of the laser beam along the major or minor axes. However, the M^2 model is ideally used along each of the independent axes of the beam.

A WinCamD camera was placed at the end of the optical relay line to observe the laser beam as it would be at the LW lens. The centroid of the intensity distribution on the camera was recorded for 1200 laser pulses using the DataRay software provided with the WinCamD camera. The DataRay software provides both the size and the centroid of the laser beam in micrometres with reference to the centre of the camera. The recorded centroids are shown in Figure 3.3 with the average subtracted.

The standard deviation of the measured centroids is 233 μm and 321 μm for the horizontal and vertical in the laboratory frame of reference respectively. The pointing jitter measured here will be the same at the lens at the LWIP. This scales with the size of the laser beam and so the expected spatial jitter of the focussed laser beam at the LWIP is 248 nm horizontally and 341 nm vertically.

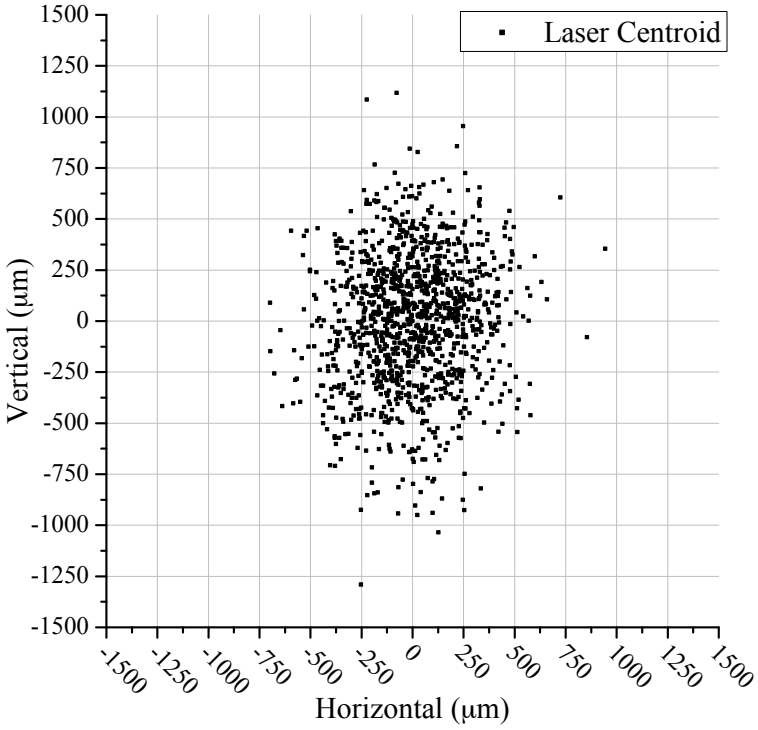

Figure 3.3: The centroid of the laser observed on a camera at the same distance from the laser system as the laser-wire lens.

This is smaller than either the focussed laser beam and the focussed electron beam, but it is not insignificant and should smaller electron and laser beam sizes be attained, this may either have to be improved or accounted for.

Although the transverse intensity profile of the laser beam is not Gaussian or symmetric as would be ideal, the M^2 values can be used to approximately predict the size of the focussed laser beam. Using the larger M^2 of the major axis as an upper limit, the focal length of the laser-wire lens of 56.6 mm and the input beam 4σ diameter of 12 mm, the focussed spot size should have a 4σ diameter of 12.75 μm and hence a σ of 3.19 μm.

A typical transverse intensity profile of the laser is shown in Figure 3.4, where the rotated asymmetry of the beam is clear. It can also be seen that the transverse intensity profile is not Gaussian and therefore the M^2 model which uses a superposition of Hermite-Gaussian modes has limited validity in accurately predicting the focussed spot size of this laser beam.

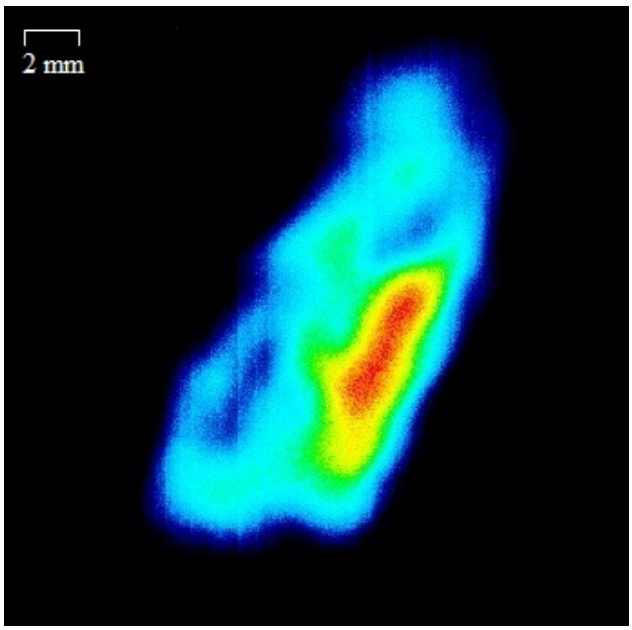

Figure 3.4: A typical transverse intensity profile of the ATF2 laser system showing its rotated asymmetry.

3.1.3 Pulse Duration

Although the laser pulse energy had been regularly measured, the pulse length had not. It was thought that the laser pulse length was approximately $\sigma \sim 150$ ps and therefore, the laser intensity was essentially constant over the much shorter $\sigma \sim 30$ ps electron bunch. Additionally, knowing both the pulse energy and pulse length, the peak power of the laser can be calculated which would feed into the development of further laser-wires. To measure the laser pulse length, an intensity autocorrelator was built with the layout shown in Figure 3.5.

An autocorrelator consists of a interferometer that splits the laser beam into two equal parts and then recombines the reflected beams in a frequency doubling crystal. The length of one arm of the interferometer is varied, delaying one of the copies of the laser pulse and therefore modulating the intensity of the frequency doubled light which depends on the overlap between the two pulses. The change in length of the arm of the interferometer is precisely provided by a translation stage which can then be converted into a temporal delay. The autocorrelation signal is the convolution of the two pulses and so it must be deconvoluted by making an assumption about the pulse shape [25].

This apparatus was constructed to measure the laser pulse length and the deconvoluted

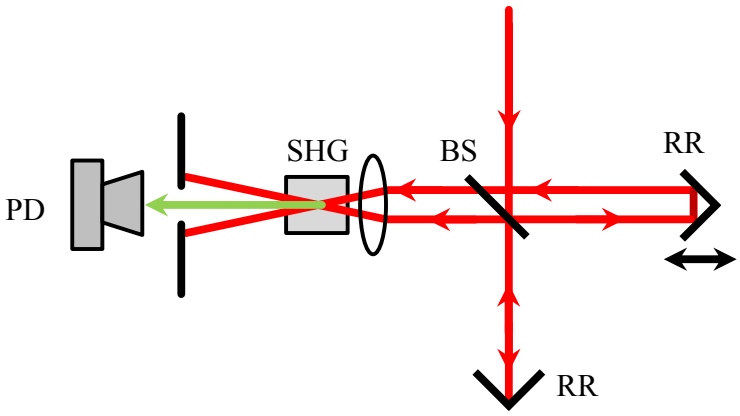

Figure 3.5: Layout of intensity autocorrelator used to measure laser pulse length. BS is a 50:50 beamsplitter, RR is a retroreflector which relfects the beam back antiparallel to the incoming beam, SHG is a second harmonic generating crystal and PD is a photodiode.

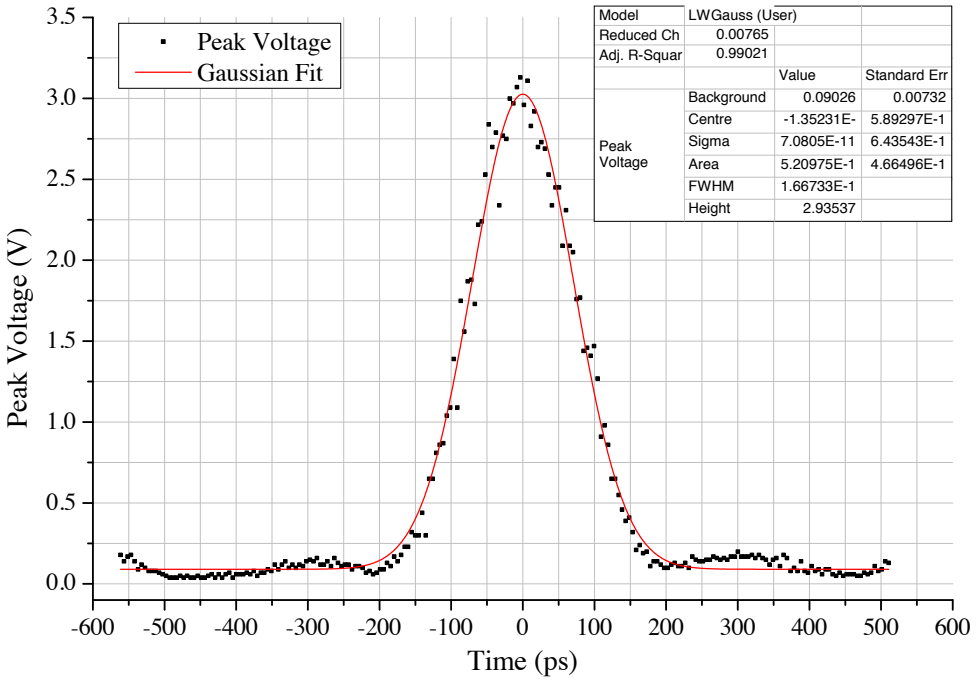

Figure 3.6: Intensity autocorrelation of the laser output showing the pulse length.

intensity autocorrelation is shown in Figure 3.6. For the purposes of the deconvolution, the pulse shape was assumed to be Gaussian as this model was judged to fit well with the data. In this case the width of the autocorrelation is divided by the deconvolution factor of $\sqrt{2}$. From the autocorrelation, the σ of the pulse is 70.8 $\pm$ 0.6 ps and therefore the more quotable FWHM is 166.7 $\pm$ 1.4 ps.

With a maximum output pulse energy measured to be 184.2 $\pm$ 27.6 mJ and the above FWHM, Equation 3.1 can be used to calculate the peak power of the pulse which is 1.10 $\pm$ 0.3 GW.

$$P_p = \frac{E}{t_{FWHM}} \tag{3.1}$$

Although this is the maximum peak power this laser system can provide, the minimum pulse energy and hence peak power required for an observable laser-wire signal is of interest for development of a laser-wire or a laser system for a laser-wire. Agapov et al. have shown that a peak power of 50 MW would be sufficient for a laser-wire similar to this one for the ILC [6].

3.1.4 Telescope Calibration

The Galilean type telescope consisted of a plano-concave lens followed by a plano-convex lens. The lenses were mounted in a kinematic lens mount on a three axis (x,y,z) translation stage providing three axes of position and two axes of angular allowing precise alignment.

The plano-convex lens was placed so that the two focal points of the lenses overlapped and the telescope should simply magnify the size of the laser beam [26].

To align the lenses to the level laser beam, a mirror was first used in each of the kinematic lens mounts to align the lens mounts. The angle of each lens mount was adjusted to overlap the reflected laser beam with the incident laser beam several metres before the telescope. After this, an iris was placed in each lens mount and the position of the lens mount adjusted so that the laser beam passed through the centre of the iris. These steps ensured that the

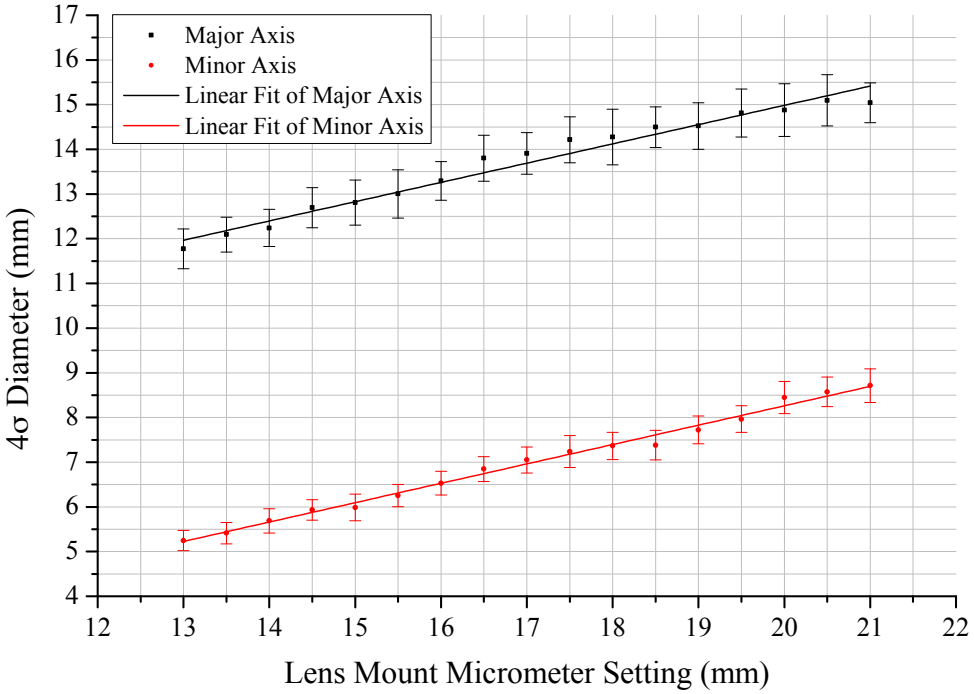

Figure 3.7: The 4σ diameters of the major and minor axes of the laser beam measured at the same distance from the laser system as the laser-wire lens. Here, a larger micrometer setting corresponds to the separation of the two lenses in the telescope decreasing.

lens were perpendicular to the incident laser beam and that it was passing through the centre of each lens, which in turn ensured that any aberrations introduced by the lenses would be minimised. The lenses were then placed in the mounts.

A WinCamD camera was used to observe the beam at the end of the optical relay at the same distance the LW lens was from the laser system. The position of the plano-convex lens along the optical axis was then varied by manually adjusting the micrometer and images of the laser beam were recorded using the WinCamD camera at the end of the optical relay line, providing the size of the laser beam at the laser-wire lens. The camera files were then analysed to provide 4σ diameters along the major and minor axes of the laser beam as shown in Figure 3.7.

As expected, increasing the separation of the lenses (lower micrometer settings in Figure 3.7) causes the plano-convex lens to focus the laser beam and decrease the size of the laser beam at the end of the optical relay line. Similarly decreasing the separation of the lenses provides a larger laser beam size at the end of the optical relay line. It is difficult to

accurately predict the size of the focussed spot size of the laser beam given its transverse intensity distribution and astigmatism. Therefore, a micrometer setting of 18 mm was chosen as the vertical projection of the laser beam at this setting was approximately the desired input 4σ diameter of 12 mm. It was intended that a person would be able to manipulate the input beam size to the LW lens without having to shutdown the accelerator to make changes to the optics and without affecting the alignment of the laser beam.

3.2 Alignment

3.2.1 Laser Alignment

The first stage of aligning the laser-wire was to align the laser beam through the optical transport line to the LWIP. This was achieved using a Crystal Laser 25 mW continuous wave (CW) laser with the same wavelength of 532 nm as the main laser system. The output beam from this was expanded using a 10x beam expander making it less divergent and similar in size and divergence to the main laser beam. Various neutral density (ND) filters were used to attenuate the output to be eye-safe. Because of the large geometrical distances involved in the laser alignment, both myself and L. Corner performed these tasks.

The alignment laser was overlapped with the main laser beam by adjusting the angle of the two mirrors immediately before the alignment laser insertion point into the main laser beam path. Both laser beams were observed one after the other on the WinCamD camera at fixed points immediately after the telescope and at the end of the optical relay line. The two camera locations provided a near and far reference respectively to ensure the two beams were overlapped over a long distance.

During the shutdown periods of the ATF2 in both spring and summer of 2010, the AL beam was aligned along the optical transport line and through the vacuum chamber at the LWIP. The laser beam had to be aligned to the centre of the LW lens and so the LW vacuum chamber was first set to its zero position in both the horizontal and vertical dimensions. The

lens was initially removed from the vacuum chamber and the reflection of the alignment laser from the uncoated fused-silica vacuum chamber window was observed using semi-transparent optical tissue at the first optical relay table in the accelerator enclosure $\sim$ 11 m from the LWIP. The fused-silica vacuum window is an integral part of the optical design of the lens and therefore the laser beam must be aligned perpendicular to it to provide the smallest focussed spot size. The angle of incidence of the laser beam on the vacuum chamber was then adjusted using the turning mirror immediately before the LWIP so that the backwards reflection was overlapped with the incoming laser beam.

A mirror with an adjustable iris on top of it was fitted into the kinematic LW lens mount on the side of the vacuum chamber. The reflection from the mirror was observed again at the first relay table and made to overlap with the original laser beam ensuring that optical axis of the lens would be parallel to the normal of the vacuum window.

After this the iris was used to centre the laser beam on the lens mount and hence the lens. The iris was closed from a fully open position slowly until scattered light from the alignment laser was observed on any side of the aperture of the iris. The laser beam was then centred on the iris using the two turning mirrors before the LWIP. This of course adjusted the angle of the incoming laser beam as well as the position and so the reflection from the mirror was observed again at the first relay table. This process was repeated iteratively to ensure the laser beam was both central on the LW lens mount and perpendicular to both the lens and the vacuum chamber window. This alignment process ensured that the lens performs optimally and should produce its designed focussed spot size.

To allow the alignment process detailed in Section 2.8, the position of the laser focus was also referenced using the OTR screen detailed in Section 2.4 which was set at its nominal angle of 45° to both the electron beam and the laser beam. The OTR screen was lowered into the vacuum chamber from its home position of 50,000 μm until it encountered the laser beam, which was observed by looking at the transmitted beam through the chamber with the recollimating post-LWIP lens in place. The OTR screen was lowered further until the laser beam was fully obscured. This distance was initially measured to be $\sim$ 60 μm. The

position of the manipulator arm and hence the OTR screen was then adjusted along the optical axis of the laser (x) using the manual micrometer until the distance required for the OTR screen to travel to fully obscure the laser beam was minimised to ~ 5 μm, which ensured that the pre-IP side of the OTR screen was at the focus of the laser. Note that the screen is 300 μm thick and that the size of the laser beam will change over this distance. It is therefore the first edge of the OTR screen to encounter the laser that is aligned to the laser focus. The vertical position of the OTR screen at the laser focus in the coordinate system of the manipulator arm was found to be 9456 μm, which was noted as a reference point.

Before performing laser-wire scans of the electron beam during accelerator operation, the laser-beam was aligned with respect to the electron beam both spatially and temporally.

3.2.2 Temporal Alignment

During accelerator operation, the OTR screen was placed 50 μm above the referenced laser focus position. The flash lamps for the linear amps were switched off providing only the output of the regenerative amplifier. The laser intensity was further attenuated by adding various 2" neutral density (ND) filters in the path of the laser beam in the laser laboratory. The vacuum chamber was then lowered vertically so that the electron beam hit the OTR screen producing OTR. The signal from the APD showing both the laser light and the OTR was observed using a Tektronix TDS 684C oscilloscope in the laser laboratory displaying the signal from the APD using the sum signal from a stripline BPM immediately before the LWIP as a stable trigger.

The laser system was aligned temporally using the main laser TD2 NIM delay module to within one 357 MHz clock cycle of the detected OTR. After this, the control voltage to the phase shifter was adjusted until the maximum overlap between the two signals was found.

The laser pulse was known to have a temporal length of $\sigma = 70.8 \pm 0.6$ ps and the electron beam $\sigma \sim 30$ ps [21]. The APD however, produces output pulses no shorter than 1 ns and so it is not possible to accurately resolve the temporal profile of either the laser

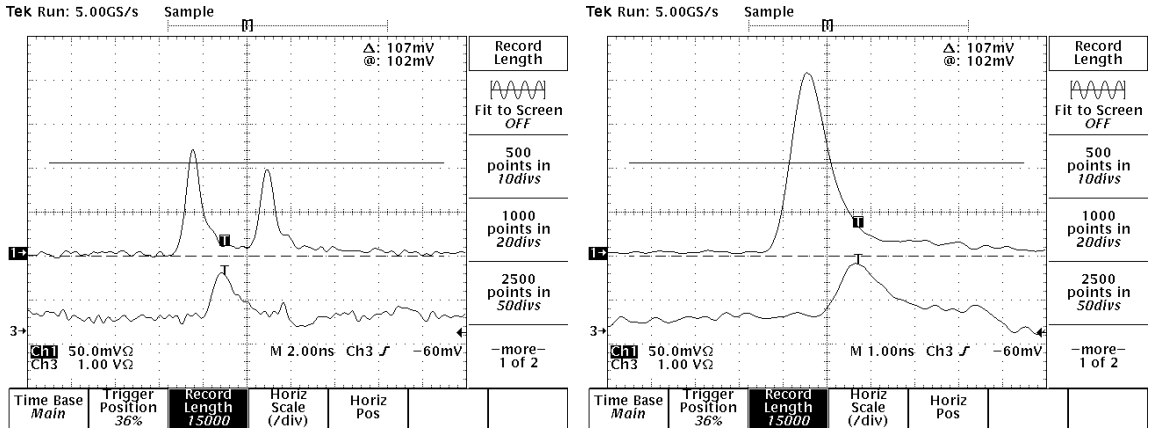

(a) Poor temporal alignment. (b) Good temporal alignment.

Figure 3.8: Oscilloscope traces (top) of the signal from the avalanche photodiode showing (a) both the laser and the OTR from the electron beam arriving at different times and (b) the phase of the laser system adjusted to overlap the two pulses. The bottom trace is the rectified BPM signal from a stripline BPM immediately before the LWIP used to trigger the oscilloscope.

pulse or the electron bunch. Furthermore, the oscilloscope available had an input bandwidth of 1 GHz which would act as a low pass filter to short pulses containing frequencies higher than this. Therefore, despite the short pulse lengths of both the laser and electron beam, both were represented as $\sim$ 1 ns long pulses on the oscilloscope.

These were aligned by adjusting the intensity of the laser such that it matched that of the OTR. The laser timing was adjusted by changing the number of counts on the TD2 delay module to align them within 1 period of 357 MHz. At this point a voltage controlled phase delay was used to adjust the phase of 357 MHz frequency of the laser system slowly as the overlap between the laser and electron beam was observed on the oscilloscope. The phase delay was controlled by a voltage between 0 V and 10 V with a 0.01 V resolution providing a timing resolution of $\sim$ 2.8 ps. For temporal overlap, the electron beam and laser beam had to be aligned within the laser pulse length (the longer of the two) of $\sim$ 167 ps which corresponds to a phase control voltage of 0.6 V. It was possible to determine the temporal overlap to within $\pm$ 0.1 V.

Figure 3.8 shows two screenshots from the oscilloscope of firstly the misaligned laser and electron beams and secondly, the overlap between the two when aligned. The two were

deemed to be aligned when the resultant signal had reached exactly double the intensity of the electron bunch OTR and the equal laser pulse.

3.2.3 Spatial Alignment

After temporal alignment, the laser beam was spatially aligned to overlap with the electron beam using the referenced vertical position of the laser focus. The OTR was placed at the laser focus with the laser beam still heavily attenuated and the vertical chamber position was scanned until the electron beam was encountered. As the OTR screen approaches the electron beam, the halo as well as the disturbed electron beam produces a signal in the laser-wire detector. When the OTR screen transits the electron beam this rises sharply. This rise in detector signal was used to judge where to set the vacuum chamber vertically. After this, the OTR screen was removed from the LWIP, the ND filters were removed from the laser beam path and the laser pulse energy increased to its maximum to achieve collisions.

However, during laser-wire operation in September 2010, the OTR screen was accidentally left at the reference position of the laser focus when the laser pulse energy was increased to search for collisions. This destroyed a large part of the OTR screen as shown in Figure 3.9. The OTR screen originally had a horizontal edge that allowed precise vertical alignment.

Figure 3.9 was produced by illuminating the OTR screen with a low power alignment laser along the electron beam line. The OTR imaging system was then used to record the image. The bright spot in the lower left quadrant is the partially occluded laser-wire laser beam. Although it does not appear to be touching the edge of the OTR screen, the shape of the laser beam was noticeably affected at this vertical position of the OTR screen indicating the pre-LWIP side of the OTR screen, which is not illuminated here is touching the laser beam.

This large hole in the screen however, allowed both the normal vertical alignment and additionally, accurate horizontal alignment of the laser focus with respect to the electron beam that was not possible before. Without this notch, the alignment strategy required

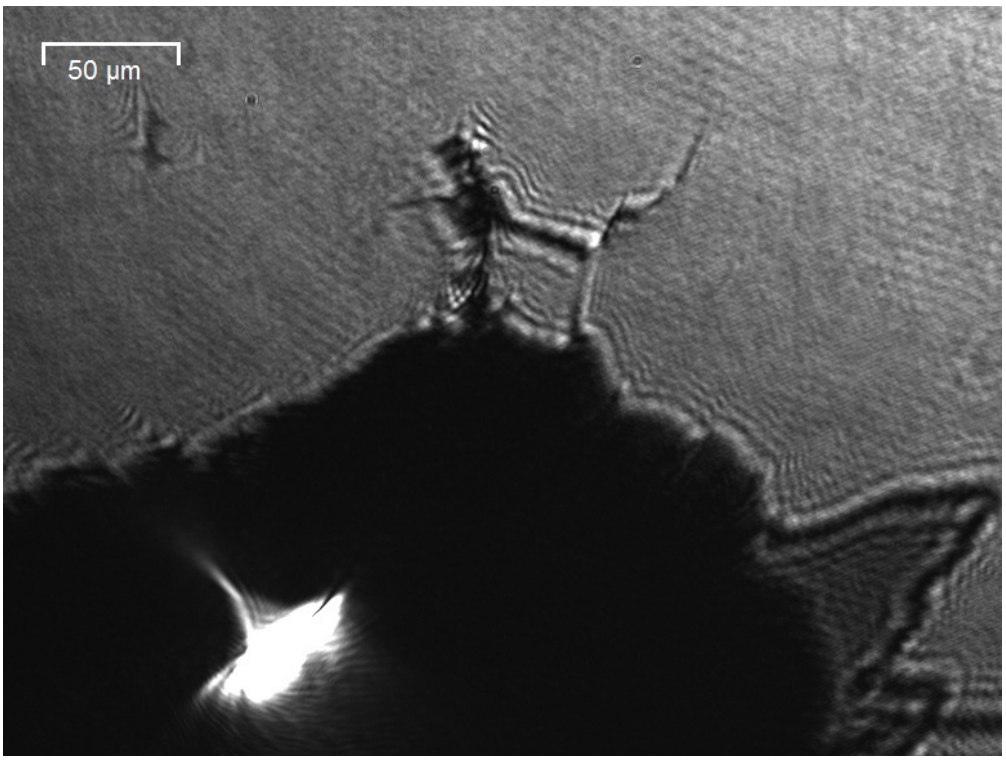

Figure 3.9: Image of the OTR screen at the LWIP illuminated by the OTR alignment laser along the electron beam path and imaged by the OTR imaging system. The large indent caused by the high power laser pulses is clearly visible.

that both the temporal and vertical dimensions be aligned to find collisions and the larger acceptance range in the horizontal would be inconsequential.

For subsequent laser-wire operation, the alignment procedure was repeated as normal but with the addition of horizontal alignment by scanning the vacuum chamber horizontally and observing the minima in signal as the electron beam passed through the notch. The vacuum chamber was placed horizontally at the centre of this minima.

3.3 Detector Relocation and Alignment

Despite the accurate alignment procedure used, no laser-wire signal was observed from collisions between the laser and the electron beam during laser-wire operation in spring 2010. During the 2010 summer shutdown of the ATF2, this was investigated and I identified several problems that were solved with consultation with A. Aryshev, S. Boogert and L. Corner. Again, due to the large geometrical distances involved in the alignment and referencing

procedures in this section, it was necessary that both myself and L. Corner conduct these experiments.

3.3.1 Laser-wire Signal Window

It was discovered that the electron beam pipe in the B5FF was not in a fixed position and was free to move with the surrounding vacuum bellows. The vacuum flange at the end of this section of beam pipe contains the window for the laser-wire signal and so if the window is not aligned with the straight section of the ATF2 extraction line, the LW signal would be blocked.

To remedy this, a low power CW Helium-Neon alignment laser along the electron beam pipe was used. The laser beam was inserted into the beam pipe between ZH4X and ZV7X, ~ 14 m before the LWIP, using a mirror (the insertion mirror) mounted at 45° on a pneumatic arm inside the vacuum beam pipe.

The vacuum bellows on either side of the section of electron beam pipe through B5FF were removed including the vacuum flange with the LW signal window. The two external mirrors before the insertion mirror were used to align the laser beam from approximately the centre of the insertion mirror in the vacuum chamber (by visual inspection) to the centre of the beam pipe before the B5FF dipole, which was ~ 41 m away. The position of the beam pipe in the B5FF dipole was then aligned to the alignment laser beam and fixed in position using adjustable screw mounts attached to the B5FF dipole.

When the vacuum flange and bellows were replaced, the bellows showed a deviation from the original position of the beam pipe of approximately 10 mm, which is almost half of the window diameter of 26 mm

3.3.2 Laser-wire Detector Position

During the operation of the laser-wire in spring 2010, the original detector developed by S. Boogert [23] was used and it was placed behind the quadrupole immediately after the B5FF dipole. It was envisioned that the scattered photons from the laser-wire would, after exiting the electron beam pipe from the LW signal window, pass between the poles of the quadrupole before reaching the detector.

However, during the alignment of the electron beam pipe in the B5FF dipole, it was noted that the small divergence angle between the diverted electron beam and the scattered photons from the laser-wire made it likely that the scattered photons were hitting both the vacuum flanges necessary for the vacuum bellows approximately 100 mm from the LW signal window and the copper cavity BPM mounted within the poles of the quadrupole. The detector was originally placed here as this was not anticipated and there was only space for the detector after the quadrupole.

It was for this reason that the detector was rebuilt to fit within in the space available immediately after the LW signal window. The surface of the PMT was cleaned and the aluminium-coated-Mylar lining of the light pipe was replaced. Furthermore, the area of both lead on the front face of the detector as well as the Aerogel inside it was reduced from 100 mm $\times$ 100 mm to 40 mm $\times$ 40 mm with the intention of reducing the detector background signal. The rebuilt detector is shown in Figure 2.11.

After the improvements were made to the detector, it was mounted immediately behind the LW signal window.

3.3.3 Electron Beam Angle

In addition to these issues, it was realised that the typical angle of the electron beam with respect to the axis of the accelerator at the LWIP was large enough that the scattered photons from the laser-wire travelling essentially parallel to the electron beam would not reach the LW signal window without hitting the side of the electron beam pipe.

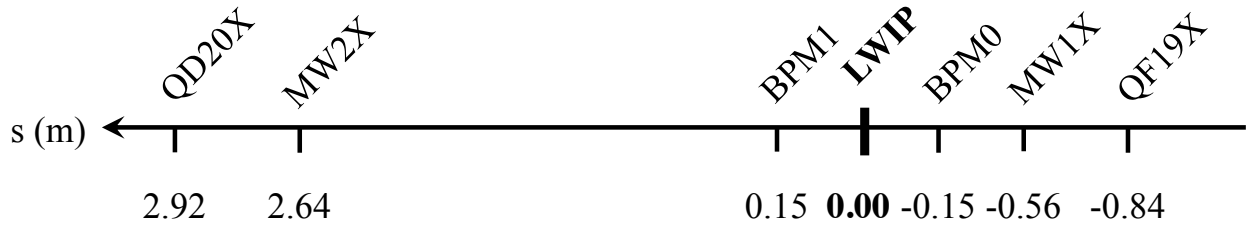

Figure 3.10: The distance from the laser-wire interaction point to the surrounding components. The distance s is the distance from the beginning of the extraction line (not to scale).

It was therefore necessary to ensure that the electron beam was not at a significant angle at the LWIP and that the vector of the electron beam was pointing towards the detector. To calculate the vector of the electron beam, its position at two points needs to be accurately known. The cavity BPMs throughout the extraction line provide accurate position information with respect to the quadrupole they are in but not in a unified coordinate frame. For this reason, they cannot be used to accurately measure the electron beam vector.

However, surrounding the LWIP between the two nearest quadrupoles are two wire scanners (MW1X and MW2X), which are normally used to measure the size of the electron beam. In doing so, they also provide the centre of the electron beam in their own coordinate frame. During the summer shutdown of the ATF2 in 2010, the electron beam pipe surrounding the wire scanners was opened by myself and L. Corner. The alignment laser discussed in Subsection 3.3.1 was used to reference the position of the wires in MW1X and MW2X, linking their coordinate frames and allowing the electron beam vector to be measured using the wire scanners.

The separation between the LWIP, wire scanners and surrounding quadrupoles is shown schematically in Figure 3.10.

Each wire scanner consists of several different wires mounted at different angles in a single yoke that moves along a linear translation stage. The yoke is moved to the appropriate position to use a single wire for a transverse electron beam profile scan.

As the laser beam was several millimetres in diameter and the wires in the wire scanners were either 50 μm or 10 μm in diameter (for the horizontal and vertical dimensions respec-

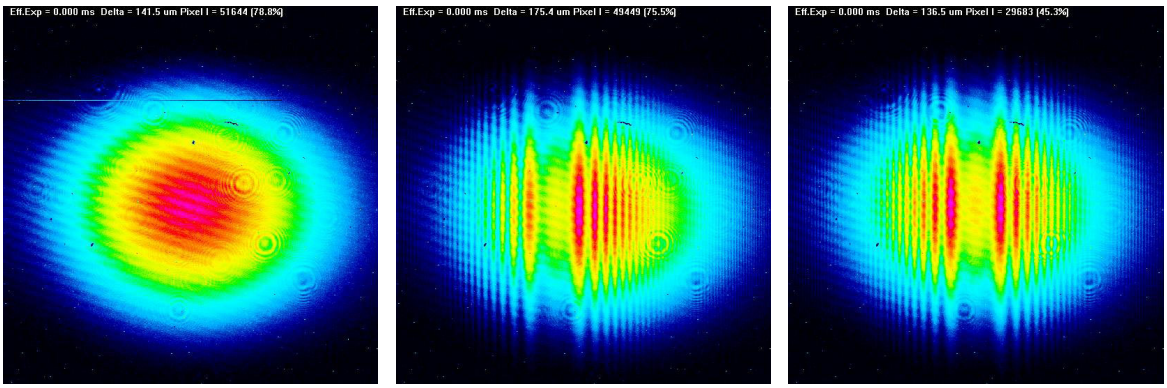

(a) Alignment Laser (b) Off-centre MW1X X (c) Centred MW1X X

Figure 3.11: Images of the alignment laser used during alignment. (a) the unobstructed alignment laser beam, (b) the diffraction pattern caused by the misaligned horizontal dimension wire and (c) the centred horizontal dimension wire. Note a vertical wire is used to scan the horizontal dimension of the electron beam.

tively), the diffraction pattern produced by them was observed rather than a clear shadow. Figure 3.11 shows the images of the alignment laser recorded using a WinCamD camera.

The camera was placed immediately after each wire scanner to record the image and the wire in the wire scanner was moved until the diffraction pattern appeared to be centred on the image of the laser beam. It was possible to align each wire to within $\pm$ 50 μm which corresponds to an angular uncertainty of $\pm$ 31.3 μrad each using the separation of the wire scanners of 3.18 m. Given the detector is 22.3 $\pm$ 0.1 m from the LWIP, this translates to a position uncertainty at the detector of $\pm$ 0.7 mm, which is less than the 40 mm height and width of the detector and the predicted $\sim$1 cm γ-ray beam width. Therefore, this method was judged to be sufficiently accurate. Furthermore, although the detector is 40 mm $\times$ 40 mm in area, the vacuum window before it has a radius of 13.5 mm. This hard aperture at a distance of 22.3 m corresponds to an angular acceptance of 605 μrad.

During accelerator operation, wire scanner measurements were made using MW1X and MW2X to determine both the size and position of the beam. Steering magnets ZH9X and ZV10X were adjusted by approximately $\pm$ 0.2 A to adjust the trajectory of the electron beam to be parallel to the vector defined by the reference measurements. It was not necessary to align the electron beam to the exact same position as the laser measurements, but merely parallel. The final wire scanner results are shown in Table 3.1 as well as the reference

Table 3.1: Results of the wire scan measurements made using MW1X and MW2X.

Wire Scanner	σ_x	σ_y	μ_x	μ_y
MW1X	146.5 ± 14.8 μm	37.4 ± 8.3 μm	20.76 ± 0.01 mm	53.16 ± 0.01 mm
MW1X Ref	N.A.	N.A.	23.40 ± 0.05 mm	52.50 ± 0.05 mm
$\Delta\mu_{MW1X}$	N.A.	N.A.	2.64 ± 0.01 mm	-0.66 ± 0.01 mm
MW2X	68.2 ± 4.0 μm	11.7 ± 0.7 μm	34.13 ± 0.01 mm	62.16 ± 0.01 mm
MW2X Ref	N.A.	N.A.	37.15 ± 0.05 mm	61.30 ± 0.05 mm
$\Delta\mu_{MW2X}$	N.A.	N.A.	3.02 ± 0.01 mm	-0.86 ± 0.01 mm

measurements made using the OTR alignment laser.

The wire scanner measurements were taken by sampling 3 electron bunches at each position and recording 25 positions. The software then provides a Gaussian fit to the averaged data indicating the standard deviation σ and the mean μ of the fit. The mean is as previously discussed in the coordinate frame of the individual wire scanner and are not the same between wire scanners. Therefore, the difference $\Delta\mu_{MW\#X}$ is used to compare the measured position of the electron beam with respect to the laser reference measurements. The separation of the two wire scanners is 3.18 m from Figure 3.10.

With respect to the reference vector using the OTR alignment laser and the wire scanners, the angle of the electron beam was calculated to be 119 ± 3 μrad and 63 ± 2 μrad in the horizontal and vertical respectively which is less than the 605 μrad angular acceptance of the detector.

After making these improvements during the 2010 summer shutdown and ensuring the electron beam vector at the LWIP was pointing towards the detector, the normal laser-wire alignment procedure was performed during laser-wire operation. When the laser pulse energy was increased to its maximum value, the laser-wire detector signal immediately doubled and collisions were detected.

With collisions detected the electron beam orbit as described by the cavity BPMs in each quadrupole was recorded and is shown in Figure 3.12.

These show the angle of the electron beam to be 68.9 μrad and -28.3 μrad at the LWIP which is different from that of the wire scanners. The cavity BPMs are aligned to the

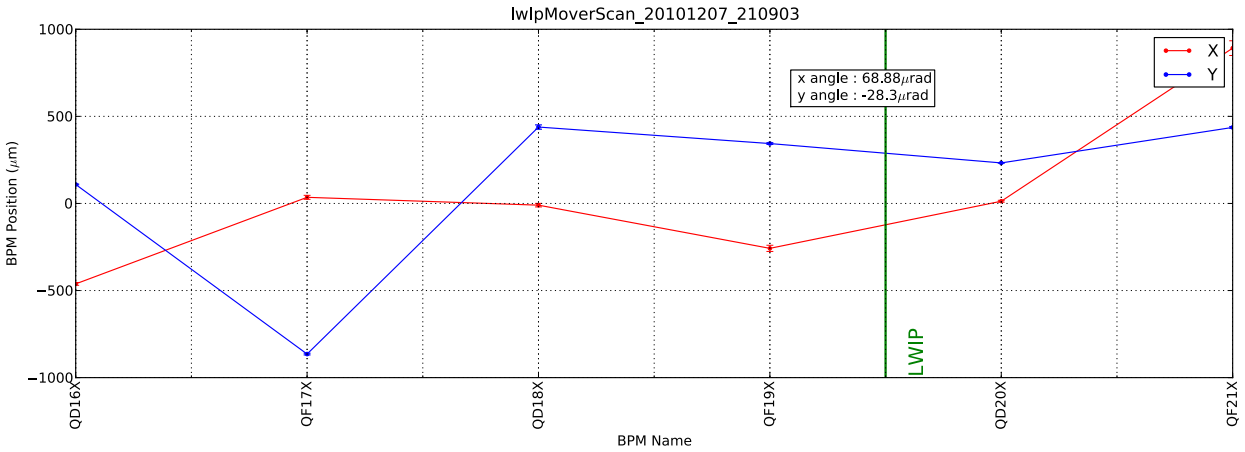

Figure 3.12: The mean cavity BPM positions illustrating the electron beam orbit recorded when collisions between the laser beam and the electron beam were observed. The standard deviations are also plotted, but are too small to see.

magnetic centres of the quadrupoles and the quadrupoles have been aligned using beam-based alignment, therefore it is to be expected that the cavity BPMs provide a different but not too dissimilar vector from the wire scanners.

The cavity BPMs were used after this to check and correct the alignment of the electron beam through the LWIP as they provide the position bunch by bunch, are non-destructive and give more accurate position measurements (within their own coordinate frame).

3.4 Laser-wire Results

The results presented here pertain to data recorded on the 7^{th} and 8^{th} of December 2010, during which myself, A. Aryshev, L. Corner operated the laser-wire experiment together. G. White and M. Woodley assisted in the operation of the accelerator and its tuning. Although a collaborative effort, I performed all of the laser-wire scans shown in this section as well as their analysis. Both myself and L. Corner operated the laser system during laser-wire shifts. During these laser-wire shifts the following tasks were performed in order

1. Reverse polarity of QM16FF

2. Load laser-wire electron beam optics

3. Tune magnets for low background signal

4. Perform temporal alignment

5. Perform spatial alignment

6. Iteratively scan phase, y and x to optimise collisions

For the LW electron beam optics, both QM16FF and QM11FF required their polarities to be changed. It was noted however that the value of QM11FF determined by the MAD software simulation was below the minimum output of the power supply and so this magnet was turned off and its polarity left intact. After this, the LW electron beam optics were loaded.

After loading the LW optics, the LW detector was initially saturated by a very large background signal. Over the course of several hours, the settings of individual quadrupoles as well as the vertical and horizontal steering magnets were adjusted iteratively to reduce the background by myself, A. Aryshev, G. White and M. Woodley. During this period, it was discovered that several magnet power supplies had not changed their values due to a fault with the accelerator control software. Correcting this significantly reduced the background levels. The minimum background level achieved was approximately 3000 - 4000 ADC counts out of a potential maximum 16384 with no attenuation used.

After successive iterations of magnet settings the background level could not be lowered any further and so the laser-wire alignment procedure was performed. Because of the alignment referencing in Section 3.3 and by actively adjusting the angle of the electron beam at the LWIP using ZH10X and ZV11X corrector magnets located immediately before the LWIP, collisions were immediately observed after the normal spatial and temporal alignment procedure. After achieving detectable collisions between the laser and electron beams several laser-wire scans were performed to optimise the alignment and then to use the laser-wire as a diagnostic to tune the electron beam optics.

During this operation period, the supplied software for the Gentec energy meter repeatedly caused the computer it was running on to crash. This computer also controlled the

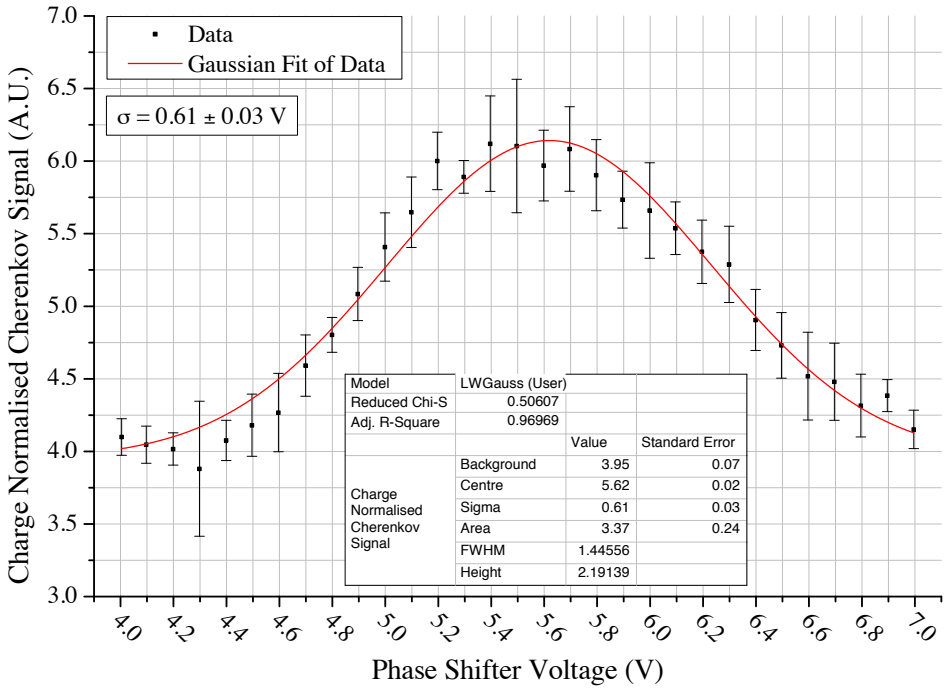

Figure 3.13: The laser-wire signal as function of the phase shifter control voltage that controls the phase of the laser pulse within one period of the 357 MHz clock.

movement of the LW vacuum chamber and the OTR equipment. For this reason, the energy meter could not be used to measure the laser energy and all of the results presented in the remainder of this chapter are without laser pulse energy normalisation. The laser pulse energy jitter was measured to be approximately 15 % in Subsection 3.1.1 and so it was expected that there would be at least this level of jitter in the laser-wire signal.

Additionally, the OTR camera hardware failed and it was not possible to replace it at that time. Because of this, the electron beam size was unknown and the laser-wire data presented here are the raw convoluted scans.

After collisions were achieved, a phase scan was performed to more accurately align the laser pulse and the electron bunch temporally. Figure 3.13 shows the charge normalised laser-wire signal for this scan. Using this scan, the phase shifter voltage was set to 5.62 V for the maximum signal.

The charge of each electron bunch was measured using the digitised amplitude of the REF1 cavity BPM that is highly linear with charge and is located very close to the LWIP [27]. The digitised value is 0 when no electron bunch is present and ranges approximately between

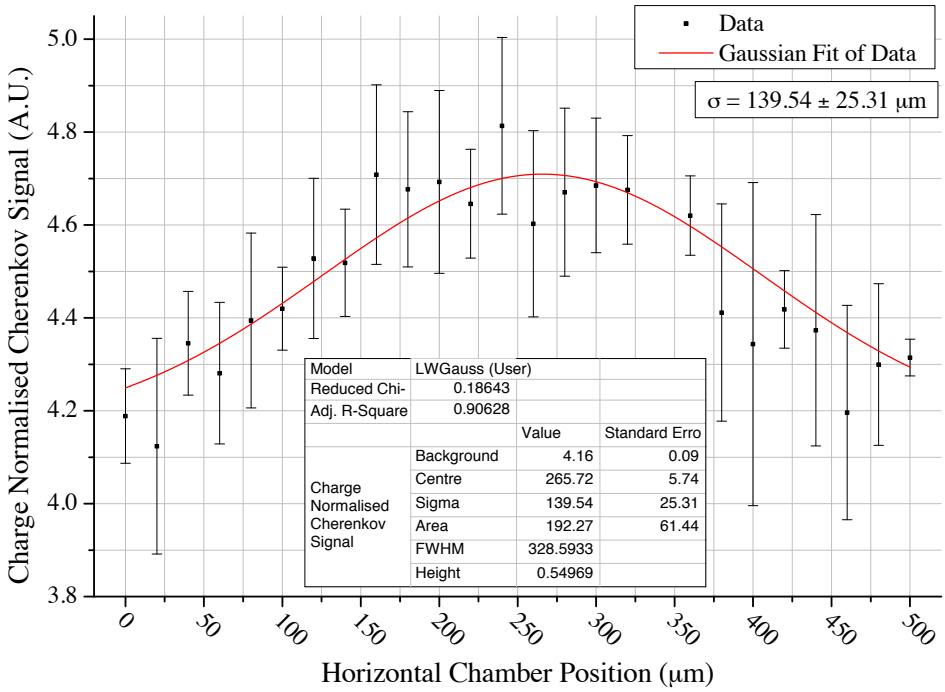

Figure 3.14: The initial horizontal laser-wire scan of the electron beam.

1200 and 2000 for the nominal charge per bunch at the ATF2 of 1×10^9 e to 10×10^9 e.

The phase scan is dominated by the laser pulse profile which is several times longer than the electron bunch length. Fitting this to a Guassian distribution, the standard deviation of the fitted distribution is 0.61 ± 0.04 V. As the ± 10 V control range of the phase shifter corresponds to 1 period of 357 MHz (2.8 ns), this shows the convoluted length of the laser and electron bunches to be $\sim 84.0 \pm 4.1$ ps. The measured 70.8 ± 0.6 ps laser pulse length will add in quadrature to the specified electron bunch length of 30 ps to give a theoretical convoluted size of 76.9 ±3.7 ps. This agrees well with the measured $\sim$ 84.0 ± 4.1 ps distribution. A recent and accurate electron bunch length measurement does not exist to confirm this. Also, a laser-wire phase scan covering a larger voltage range would help improve the accuracy of the determination of the electron bunch length.

After the phase scan, a horizontal chamber scan was performed to ensure that the laser focus was aligned to the electron beam. The chamber was scanned over 500 μm recording 5 samples at each of the 25 points in the scan. This data is shown in Figure 3.14 along with a fit to a Gaussian model.

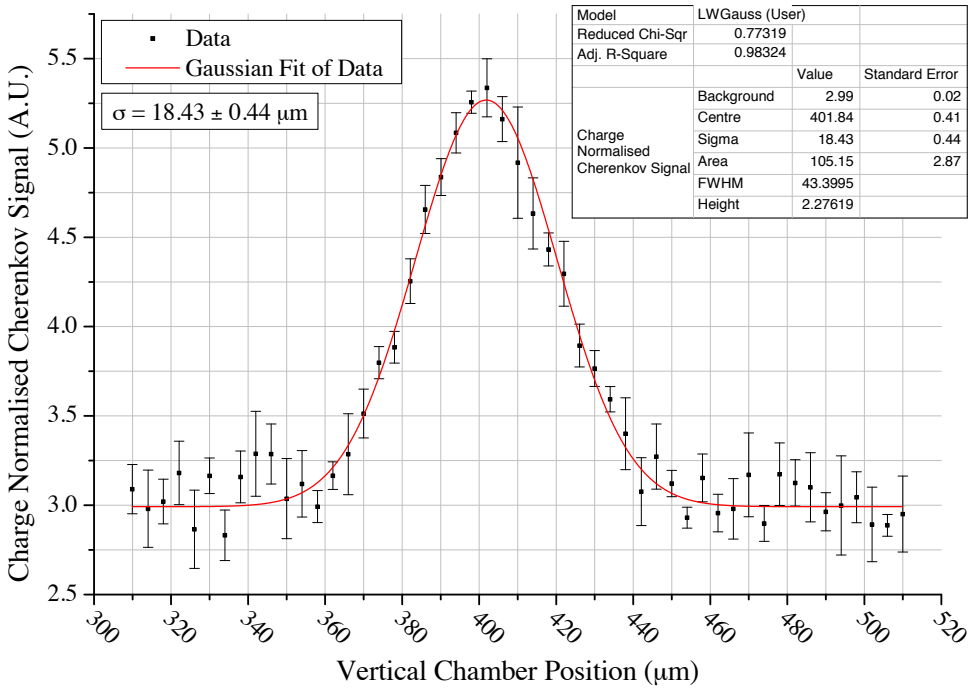

Figure 3.15: The initial vertical laser-wire scan of the electron beam.

The electron beam width of $\sigma_x = 139.5 \pm 25.3$ μm was larger than expected and the scan does not show its full extent. Additionally, the jitter of the laser pulse energy is clearly visible in the large standard deviation of each averaged data point in the scan. The chamber was positioned at 266 μm where the peak signal was observed.

After this, a vertical chamber scan was performed. Similarly, 5 samples were recorded at each location and averaged. This data is shown in Figure 3.15 where the data was fitted to a Gaussian.

The convoluted size was found from the fit to be $\sigma_y = 18.4 \pm 0.4$ μm, which is considerably larger than expected and after A. Aryshev and G. White checked the electron beam optics, it was found that the current of QF19X, the quadrupole directly before the LWIP, was at a lower value than desired. This was corrected by A. Aryshev and I repeated the vertical laser-wire scan. At this point, the laser-wire signal dropped in intensity and so a horizontal scan was performed first. This revealed that the electron beam had moved horizontally by approximately 60 μm indicating imperfect alignment of the electron beam through the accelerator lattice. With the horizontal position optimised once more the vertical scan was

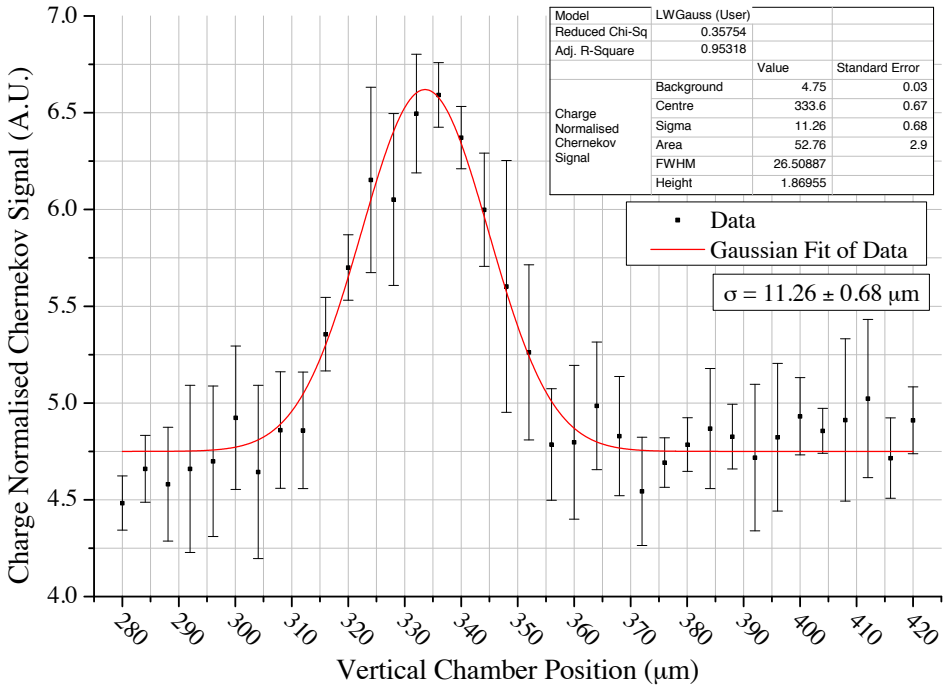

Figure 3.16: The first vertical laser-wire scan performed after correcting the current of QF19X.

repeated as before and the data is shown in Figure 3.16.

Here, the σ of the convoluted laser-wire scan is 11.3 $\pm$ 0.7 μm which is considerably smaller than the previously measured σ_y = 18.4 $\pm$ 0.4 μm. With the current of QF19X at its correct and higher value than the vertical scan shown in Figure 3.15, the vertical focus of the electron beam is expectedly smaller and closer to the quadrupole as shown by the smaller convoluted beam profile in Figure 3.16.

Following this, G. White and M. Woodley made a dispersion measurement by varying the frequency of the damping ring by $\pm$ 2 kHz in 1 kHz steps. The electron beam position reported by each cavity BPM in the extraction line was recorded and the difference in position at each location in the lattice used to calculate the dispersion function. This measurement showed that there was residual vertical dispersion at the LWIP from x-y coupling and G. White used skew quadrupoles at the beginning of the extraction line to minimise coupling and hence the residual vertical dispersion. From G. White's computer model, the residual vertical dispersion at the LWIP was calculated to be 1.1 $\pm$ 0.5 mm and 0.06 $\pm$ 0.09 mm in the horizontal and vertical respectively. The vertical laser-wire scan shown in Figure 3.17

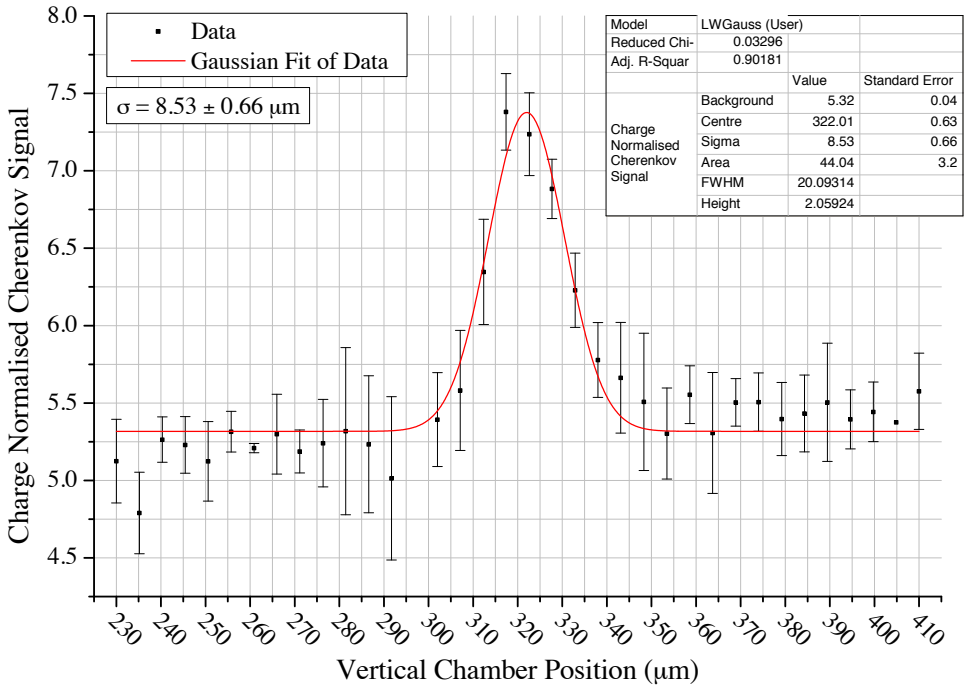

Figure 3.17: Vertical laser-wire scan recorded after a dispersion correction was made.

was made after the dispersion correction.

It can be seen from Figure 3.17 that the dispersion correction has decreased the convoluted laser-wire scan size from $\sigma_y = 11.3 \pm 0.7$ μm in Figure 3.16 to $\sigma_y = 8.53 \pm 0.66$ μm. After dispersion, G. White and M. Woodley then used the OTR#0 in the SLAC OTR system [28] to observe the electron beam between QD18X and QF19X. The electron beam was observed to be coupled between the horizontal and vertical. M. Woodley adjusted QK1X, a skew quadrupole, from 0 A to -15.5 A until the electron beam appeared uncoupled on the OTR #0 screen. A further vertical laser-wire scan was performed as shown in Figure 3.18.

The convoluted beam size was measured to be $\sigma_y = 8.07 \pm 0.35$ μm. After these measurements and corrections to the electron beam optics, several vertical laser-wire scans made whilst successively making small adjustments to various magnets. However, no smaller convoluted vertical laser-wire scan than Figure 3.18 was achieved within the time available to use the accelerator. There was also insufficient time to perform a long range horizontal scan to full observe the width of the electron beam at the LWIP.

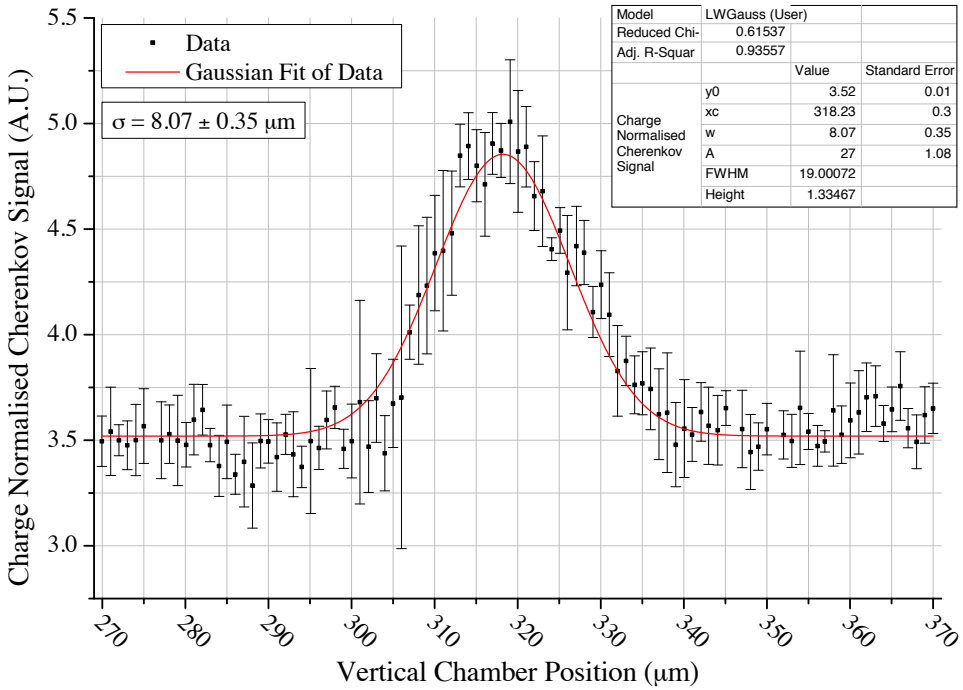

Figure 3.18: Vertical laser-wire scan performed after a coupling correction was made with a convoluted size of $\sigma_y = 8.07 \pm 0.35$ μm. This was the smallest convoluted laser-wire scan demonstrated in this operational period.

3.5 Signal Linearity

The dependence of the laser-wire signal with laser pulse energy and electron bunch charge were investigated to verify the laser-wire model and the experimental setup. Firstly, the charge dependence was investigated by recording the laser-wire signal whilst decreasing the charge of the electron bunches. The electron bunch charge was controlled by altering the power of the laser used to produce electrons at the photo-cathode at the start of the accelerator. The data is shown in Figure 3.19 with a linear fit to the data.

The electron bunch charge is nonlinearly related to the laser system power control making recording and averaging data at discrete levels impractical. Additionally, the electron bunch charge was not stable at the time of operation also preventing discrete data points being recorded. The laser-wire signal would appear to have a linear relationship with electron bunch charge as expected from Equation 1.24 however, the large jitter in the laser-wire signal makes it ambiguous. The jitter is most likely due to the known jitter of the laser pulse energy.

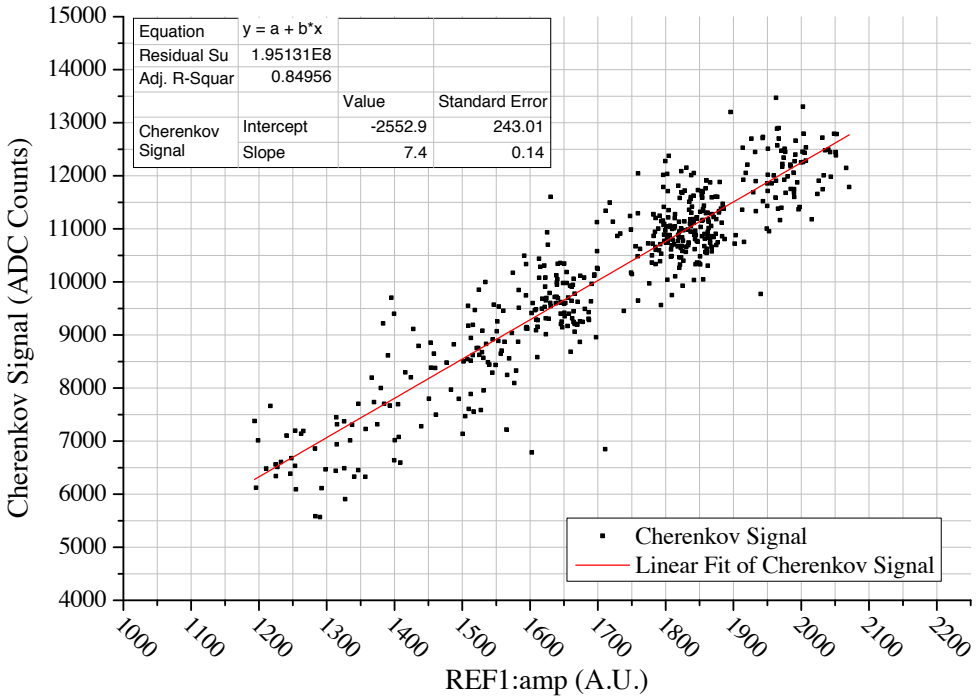

Figure 3.19: The laser-wire signal recorded as the charge of the electron bunch was decreased.

The electron bunch charge was returned to its normal value and the dependence of the laser-wire signal with laser pulse energy investigated. The delay of the main amplifier flash lamps was adjusted to change the laser pulse energy. This was changed in discrete steps, but the jitter of the laser pulse energy was too large to calculate discrete average data points.

As this was investigated at the end of the laser-wire operation period, the Gentec Energy meter was briefly used to measure the laser pulse energy. The data recorded is shown in Figure 3.20 as well as a linear fit to the data.

Similar to Figure 3.19, the laser-wire signal would appear to have a linear dependence with the laser pulse energy but the jitter of the signal obscures this.

At this point, the laser pulse energy was decreased by increasing the delay of the flash lamps in the linear amplifiers. The pulse energy was then modulated by repeatedly increasing the flash lamp delay to a large value and then returning it to its previous value. This modulated the laser-wire signal to judge visually what the minimum laser pulse energy required for observable signal was with the current conditions. This was found to be ~ 20 mJ, which corresponds to a peak laser power of ~ 120 MW. Although another laser source could

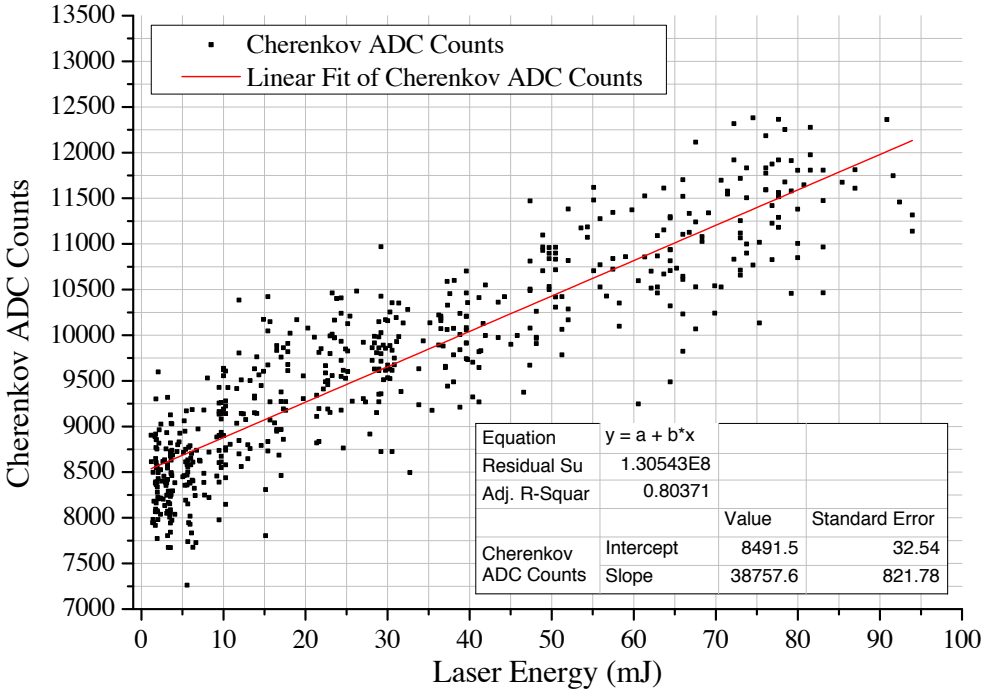

Figure 3.20: The laser-wire signal recorded as a function of the laser pulse energy.

be used with a different pulse length, the peak power required would be the same.

This measurement was specifically performed to aid the laser development discussed in further chapters however, there was no laser pulse energy or electron beam charge normalisation which would have reduced the jitter of the laser-wire signal and therefore the minimum laser pulse energy required for a resolvable difference in detector signal.

3.6 Electron Beam Size

Although a laser-wire is designed to provide an accurate measurement of the electron beam size, several issues prevented the electron beam size from being determined by the laser-wire at the ATF2.

Firstly, it is not possible to accurately determine the size of the laser focus directly. Commercially available slit profilers that are capable of measuring a laser focus of a similar size to a micrometre are physically incompatible with a low repetition pulsed laser system such as the one being used. Another common experimental technique is to scan a knife

edge across the laser focus and measure the transmitted pulse energy however, the means for this were not available at the ATF2. The very small focus makes this technique difficult to accurately accomplish. Lastly, the M^2 model cannot be used with the high degree of accuracy required given the non-Gaussian transverse intensity profile of the laser beam shown in Subsection 3.1.2.

This problem was known at the outset of the experiment and it was expected to accurately measure the size of the electron beam using the OTR monitor and thus determine the size of the focussed laser beam. This in turn would provide information about the validity of the M^2 model for this laser beam. However, the failure of the high sensitivity camera used for the OTR prevented this. The size of the electron beam can however be estimated from information already known about the accelerator.

The β functions at the LWIP are predicted to be $\beta_x = 0.461$ m and $\beta_y = 0.300$ m by the MAD software simulation. From G. White's measurements, the dispersion functions are $D_x = 1.1 \pm 0.5$ mm and $D_y = 0.06 \pm 0.09$ mm. The energy spread of the electron beam is specified as 0.08% [21]. An accurate measurement of the emittance was not available at this point and an attempt by M. Woodley [29] to measure the emittance using the wire scanners provided an estimate of 29 pm-rad in the vertical which is over double the nominal vertical emittance of 12 pm-rad. The horizontal emittance from the same measurement was approximately 1.7 nm-rad which is also considerably larger than the design value of 1.2 nm-rad.

Using these numbers, the predicted electron beam size is $\sigma_x = 28.0$ μm and $\sigma_y = 3.0$ μm. As discussed in Subsection 3.1.2, using the larger M^2 value from the laser characterisation as a predicted upper limit, the predicted size of the laser beam at the focus is $\sigma = 3.19$ μm. Adding both of the predicted electron beam and laser beam sizes in quadrature as described by Equation 1.24, the predicted convoluted beam size is $\sigma_y = 4.4$ μm, which is approximately half of the minimum convoluted vertical beam size of $\sigma_y = 8.07 \pm 0.35$ μm.

There are several possible reasons for the larger measured convoluted laser-wire scan size. Given the large number of small adjustments made to a large number of magnets

whilst attempting to minimise the electron beam size at the LWIP and the background signal, the β functions of the accelerator may be different from those predicted by the MAD model. The current required in the skew quadrupole to correct the x-y coupling of the beam was quite high and whilst this may have rotated the beam at the location of OTR #0 , it does not preclude coupling elsewhere in the lattice or at the LWIP. The two dimensions of the electron beam are considerably different and even a small amount of coupling from the horizontal into the vertical would significantly increase the measured vertical electron beam size using the laser-wire. If the prediction of the focussed laser spot size is correct, this would infer that the electron beam has a size of $\sigma_y \sim 7.9$ μm.

Moreover, the size of the focussed laser beam is unknown and whilst the M^2 model provides an estimate and therefore limits on the size of the laser beam, there is an ambiguity in the correct input laser beam size to the laser-wire lens required to produce this optimal focus. It was intended to scan through various input laser beam sizes to the laser-wire lens to empirically find the smallest focussed laser beam, but there was insufficient time for this experiment.

3.7 Summary

The results presented here show the successful installation and operation of a laser-wire at the ATF2. A new alignment technique using wire scanners to reference an alignment laser allowed the alignment of the electron beam and hence the inverse-Compton scattered photons to the detector and hence detectable collisions. The laser system was fully characterised providing the information necessary for development of a new laser system for laser-wire. Collisions were regularly achieved quickly with the alignment procedure developed and the laser-wire was used on several occasions as a diagnostic for the ATF2 extraction line. Although not calibrated, the convoluted laser-wire scan size does depend on the size of the electron beam and provides a mean to tune the accelerator.

The research presented in this chapter represents the commissioning of the laser-wire

and it was intended to return after the operating period this research was conducted during for further experimentation. However, a fire in the klystron gallery damaged parts of the accelerator that took several months to repair. Not long after the recovery of the accelerator, the 2011 Tohoku earthquake and tsunami prevented any further operation of the ATF2 or visits to Japan within the scope of this research.

Chapter 4

Fibre Lasers

This chapter presents the motivation for development of a suitable laser source for laser-wire. Fibre lasers are investigated and the basic properties of optical fibres are outlined in Section 4.2. How these are modified by adding laser dopants is then described in Section 4.4 followed by the typical architecture of such a laser system in Section 4.5. In Section 4.8, amplification regimes are explored and related to the achievable peak powers. The ramifications of nonlinear effects evident in optical fibres are considered in Section 4.6.

4.1 Requirements

A laser system for a laser-wire must produce laser pulses with at least megawatt peak powers for a similar duration and at a similar frequency to the particle bunches being measured. In the case of a laser-wire at the ATF2 where there are nominally 10^{10} electrons per bunch, a peak power of 50 MW would be required for an accurate laser-wire scan [6]. In addition to this, the laser source must have the excellent spatial quality required to provide the smallest focussed spot size and hence the greatest resolution possible [15]. Furthermore, as mentioned in Chapter 2, the lens used to focus the laser beam for laser-wire has a narrow bandwidth acceptance. Exceeding this will lead to a larger focussed spot size due to the chromatic aberrations introduced by the lens, in turn reducing the resolution of the laser-wire. To make an emittance measurement of a particle beam without changing the electron beam optics, many laser-wire scans would have to be performed at different points along the

Table 4.1: Beam parameters of the ILC and ATF2

Parameter	Units	ILC	ATF2
Particles / Bunch	10^{10}	2	0.5
Bunch Repetition Rate	MHz	2.7	357
Number of Bunches	Bunches / Train	2625	1
Bunch Train Repetition Rate	Hz	5	1.5
Typical Dimensions	h (μm) $\times$ v (μm)	100 $\times$ 1	100 $\times$ 1
Bunch Duration	ps	1	30

accelerator lattice [6]. Therefore, a laser system that is efficient, distributable and scalable would make a considerable difference to initial and maintenance costs.

Specifically considered in this research is the development of a high resolution laser-wire for an electron or positron accelerator. Typical parameters for both a future linear electron positron collider, the ILC, and the aforementioned test facility, the ATF2, are outlined in Table 4.1. Although a laser-wire is suitable for many different accelerators, these are the two that are specifically considered for this laser development research. The ATF2 is currently the most suitable test facility for a high resolution laser-wire and if a new laser system were to be developed, it would most likely be tested here.

The energy per laser pulse required to achieve this peak power depends on the pulse length by the common relation shown in Equation 4.1.

$$P = \frac{E}{t} \tag{4.1}$$

A further consideration is the repetition rate of the laser pulses. Within certain limits, the pulse energy from a laser can be increased by lowering the repetition rate of the pulses, redistributing the average power of the system amongst fewer pulses [30]. To make a two-dimensional emittance measurement by precisely measuring the transverse particle beam size at several points in the accelerator lattice requires a large amount of time at the typical bunch train repetition rates of several Hertz. To make the emittance measurement within a useful time to allow iterative tuning of the accelerator, intra-train scanning that utilises the thousands of particle bunches within a train is necessary [6]. However, this involves

performing laser-wire scans at the megahertz repetition rates within a particle bunch train.

In this scenario a laser-wire could either complete the full transverse profile measurement within one train requiring a fast, precise and accurate scanning mechanism or use the large number of bunches within a train to provide sufficient statistics so that the number of trains required for an accurate emittance measurement is reduced.

High repetition rate intra-train scanning considerably increases the power requirements of the laser system for the laser-wire. If the laser were to produce pulses similar to those mentioned in Chapter 3 (20 mJ, 358 ps) at 2.7 MHz as specified in Table 4.1 for the ILC, the average laser power would be approximately 56 kW. Although the laser would only have to produce this average power for approximately 1ms, this is still an unfeasibly high average power as the electrical power required would be considerably higher than this.

A common technique used to attain high peak powers from megawatts to terawatts is to reduce the pulse duration as much as possible (typically tens of femtoseconds) to increase the peak power for a given pulse energy. However, in the case of laser-wire this is not a suitable solution because if the laser pulse is considerably shorter than the electron bunch the collision luminosity will decrease. Therefore a pulse length of a similar order of magnitude is required. This could potentially be slightly shorter than the electron bunch to achieve a higher peak power. For example, a laser producing 1 ps pulses with 50 MW peak power at 2.7 MHz would require an average power of 135 W, which is non-trivial but feasible. In this case, the energy required per pulse is 50 μJ.

As discussed in Chapter 1, the minimum achievable focussed spot size of the laser beam and hence the limit of the laser-wire resolution is dependent on the wavelength of light used as described by Equation 1.25. By using a shorter wavelength, a smaller focussed spot size, and therefore a better resolution, can be achieved. Most high-power pulsed laser systems produce light in the infra-red part of the spectrum as producing high energy pulses at shorter wavelengths is often difficult and cannot reach as high pulse energies. A more common technique is to double the frequency of the high power infra-red laser light either once or successively using nonlinear crystals accessing shorter and shorter wavelengths of

light. Frequency doubling however, is typically $\sim$ 50 % efficient at most and therefore successive frequency doubling results in considerably lower output pulse energies.

To use nonlinear crystals in this fashion, the infra-red source must also have a high degree of linear polarisation. For a final achievable pulse energy of 50 μJ already discussed, an initial pulse of at least 100 μJ would be required of infra-red light before frequency doubling to the visible.

To provide the greatest laser-wire resolution, the laser beam must have high spatial quality so that it can be focussed to the smallest possible spot size. Although the energy and pulse duration demands of a laser-wire can be met with typical bulk laser technology, simultaneously achieving these whilst also having a high spatial quality can be difficult. High pulse energy lasers often have poor spatial quality because of the macroscopic nature of the gain media used and the thermal gradients present at high pumping levels introduce aberrations and distortions. High peak power laser systems often require the laser pulses to pass many times through the same gain medium which can cumulate these effects. This is a limit of current technology and not one that is easily avoided purely because of the macroscopic nature of the gain media used and the methods of exciting the lasing ions for amplification. For these reasons, other laser technologies were considered.

It should be noted that although the specifications in Table 4.1 specify a repetition rate of 2.7 MHz for the ILC, this parameter has evolved since the outset of this research. At the time this research was undertaken, this frequency was approximately 6 MHz and the repetition rate chosen for a developmental laser system was 6.49 MHz as this matched the 154 ns bunch spacing of the ATF2 where this laser system would be demonstrated [21]. The repetition rate was similar to the ILC parameters and so a demonstration for these parameters would also show that the laser system was suitable for the ILC.

Research was undertaken towards a new laser system for a laser-wire. Fibre lasers were the chosen technology for this research and in the following sections, the physics behind them, their advantages compared to conventional bulk lasers systems and some of the achievable parameters are considered.

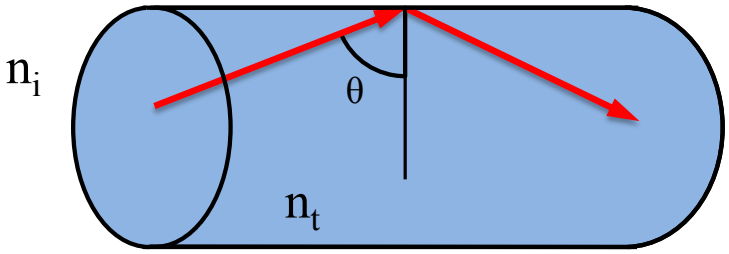

Figure 4.1: A typical fibre consisting of a cylindrical waveguide demonstrating total internal reflection.

4.2 Fibre Lasers

Fibre lasers have many desirable properties including high spatial quality, high efficiency, compactness and simpler thermal management compared to conventional bulk laser systems capable of the required high peak powers. Fibre lasers replace the macroscopic ('bulk') gain media with a doped fibre waveguide. Although the area of fibre core which is the gain medium is much smaller than a macroscopic crystal, the fibre can be many metres long and being flexible can be coiled for compactness.

The most basic fibre is a cylindrical waveguide made from glass as shown in Figure 4.1. Using a simple ray-optics approach, a ray passing through the cylinder will be totally internally reflected if its angle of incidence θ, (measured from the normal of the surface) is greater than the critical angle θ_c [26] as described in Equation 4.2 where n_i and n_t are the refractive indices of the incident and transmitting media respectively. In the case of Figure 4.1, the transmitting medium would be the air surrounding it.

$$sin\,\theta_c = \frac{n_t}{n_i} \tag{4.2}$$

However, if anything were to touch the fibre other than air its refractive index would most likely be higher than air and the light in the fibre may not be totally-internally reflected. To avoid this another layer called the cladding is placed around the core. This is usually made from glass again but with a different composition that is engineered to have a lower refractive index than the core as depicted in Figure 4.2b. The lower refractive index ensures

total internal reflection irrespective of anything touching the cladding of the fibre.

The above ray optics description of total internal reflection - with rays traversing the waveguide - is valid only when the diameter of the fibre is much greater than the wavelength of the light used. In the case where the waveguide is of the same order of magnitude as the wavelength of the light being used, Maxwell's Equations must be used to determine the propagation of the light [31].

Using Maxwell's Equations, it can be found that only certain unchanging transverse electro-magnetic distributions ('modes') are guided by the fibre [25]. For a given wavelength of light the number of modes supported increases as the diameter of the guiding core increases. When multiple modes are supported a superposition of different modes is possible and as the number of modes increases to a high number, the transverse mode pattern becomes more homogeneous.

A useful parameter is the normalised frequency V as defined in Equation 4.3 where a is the radius of the core; λ is the wavelength of the light and n the refractive index of the appropriate part of the fibre [31]. This is commonly referred to as the V-number.

$$V = \frac{2a\pi}{\lambda}\sqrt{n_{core}^2 - n_{cladding}^2} \tag{4.3}$$

A parameter which is often specified with commercially manufactured optical fibres is the numerical aperture of the core. This is defined in Equation 4.4 where n is the refractive index of the core or cladding. This assumes that the light incident on the fibre is entering from air ($n_{air} \sim 1.000$) [25].

$$NA = \sqrt{n_{core}^2 - n_{cladding}^2} \tag{4.4}$$

The V number can then be more conveniently be written using the often quoted numerical aperture.

$$V = \frac{2a\pi}{\lambda} NA \tag{4.5}$$

The modes supported in the fibre are described by a series of modified Bessel functions. The cut-off V-number V_c can be calculated for any given mode, below which that mode will not be supported. After the lowest-order mode, the cut-off V number for the next highest mode is 2.405. A fibre with a V number lower than this will only support the lowest order mode. This is commonly referred to as single mode fibre.

Although a modified Bessel function, the lowest order mode can be very well approximated by a Gaussian which is simpler to use in calculations [25]. Single mode fibres are therefore the most desirable if high spatial quality is important as is the case of a laser-wire. For a given lens and fixed input beam size, a Gaussian transverse intensity profile will also produce the smallest focussed spot size [26].

Using a typical infra-red wavelength of 1.1 μm; a typical NA of 0.13 [32] and $V_c = 2.405$ for single mode operation, a single mode fibre core radius could therefore be no greater than 3.2 μm. This is appreciably smaller than a macroscopic crystal used in a conventional bulk laser system which may be several to tens of millimetres across and the laser beam within it hundreds of micrometres. Looking at Equation 4.5 the diameter of the fibre will have to decrease as the wavelength does to maintain the same V number and hence number of modes. Therefore a single mode fibre for the visible part of the spectrum would need to be only a few micrometres in diameter.

To make the fibre more than a passive waveguide, the core can be doped with a lasing ion. For lasing to occur the ion must be excited or 'pumped' to a higher energy state. The lasing ions can be pumped from the side [33] but this isn't very efficient and more commonly the pump source is launched into the fibre along with the input beam or 'seed' to be amplified. In this case the pump is also typically a high power laser source itself.

However, few high power pump sources exist with a sufficiently high spatial quality to be efficiently launched or 'coupled' into the fibre core. A common pump source is a diode

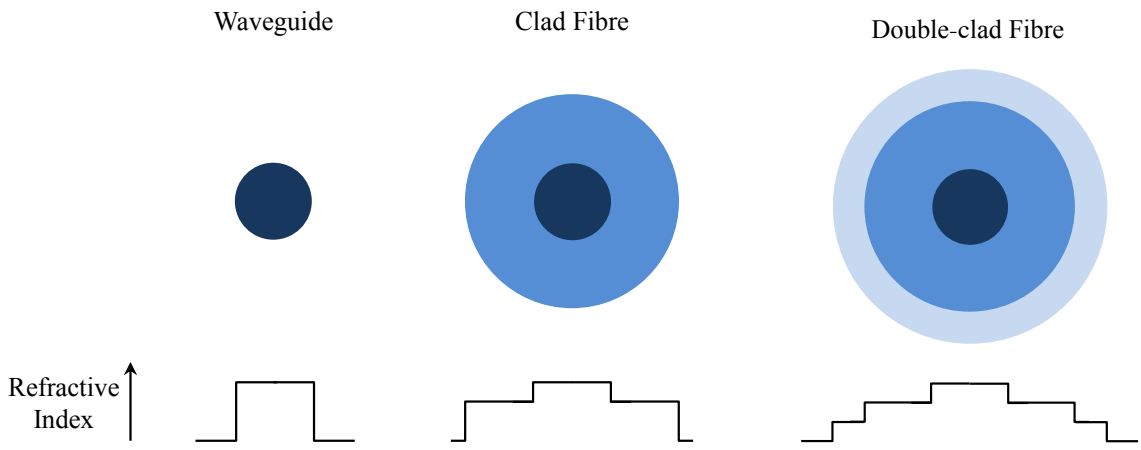

(a) Waveguide (b) Clad Fibre (c) Double-clad Fibre

Figure 4.2: Different types of fibre including (a) a basic waveguide, (b) a clad fibre and (c) a double-clad fibre.

laser that typically produces an asymmetrical laser beam. Often, many diode lasers are stacked on top of each other to increase the power. However, this produces incoherent pump sources of reduced spatial quality. Diode lasers are capable of reaching high powers with high electrical to optical efficiency. To make use of high power pump sources and still retain the high spatial quality of a single mode fibre, a geometry shown in Figure 4.2c is used with yet another cladding layer with a lower refractive index than the first cladding layer.

The layers are referred to as the core, the inner cladding and the outer cladding from the centre to edge respectively. The seed is coupled into the core which is doped with lasing ions and the pump is coupled into the inner cladding. Because the outer cladding has a lower refractive index than the inner cladding, and the core has a higher refractive index than the inner cladding, the pump light is guided within the inner cladding and repeatedly passes through the core pumping the lasing ions.

This geometry allows much higher power pump sources with poorer spatial quality to be efficiently coupled into the considerably larger inner cladding whilst the core is still single mode and therefore provides excellent spatial quality. Given the guiding nature of the fibre, the pump light is confined and interacts with the lasing ions along the length of the fibre until either it is entirely absorbed or the end of the fibre is reached. In a comparable bulk laser system with a longitudinally pumped macroscopic crystal, the interaction length between

the pump and the lasing ions is limited to a few millimetres before the pump light diverges and its intensity decreases [34].

4.3 Polarisation

Another property of the guided light to consider is its polarisation state. If a single mode fibre is perfectly isotropic throughout its length, the polarisation state will remain unchanged. In reality however, a fibre does not have an entirely homogeneous structure and may also experience variable stresses throughout its length from bending and temperature differences. These introduce variable degrees of birefringence that unpredictably alter the polarisation state throughout the fibre [35]. Therefore, a well-defined polarisation state entering a fibre will not be the same upon exiting it.

To overcome this, the structure shown in Figure 4.3 is used wherein two additional pieces of doped glass are used. These are doped to have different degree of thermal expansion and so when the fibre is made and cooled a mechanical stress is induced across the core and it is for this they are named stress rods. The mechanical stress introduces a relatively strong birefringence ($\Delta n \sim 1 \times 10^{-4}$). This will maintain a linear polarisation state along the fibre length provided the linear polarisation was aligned to the axis of the birefringence at the start of the fibre [36]. This is true even if the fibre is bent or if stress is applied to it as the birefringence introduced by these is small compared to that of the stress rods.

To measure the polarisation state of a beam, a polarising beam splitter (PBS) can be used to measure the transmission function of the incident laser beam. A polarising beam splitter splits a laser beam into two separate beams based on the orientation of the polarisation of the incoming beam. One linear polarisation is transmitted while the orthogonal linear polarisation is reflected. A linearly polarised beam entering it will be fully transmitted or fully reflected if it is aligned either parallel or orthogonally to the transmission axis respectively.

If the polarisation of the input beam is at any other orientation, a component along

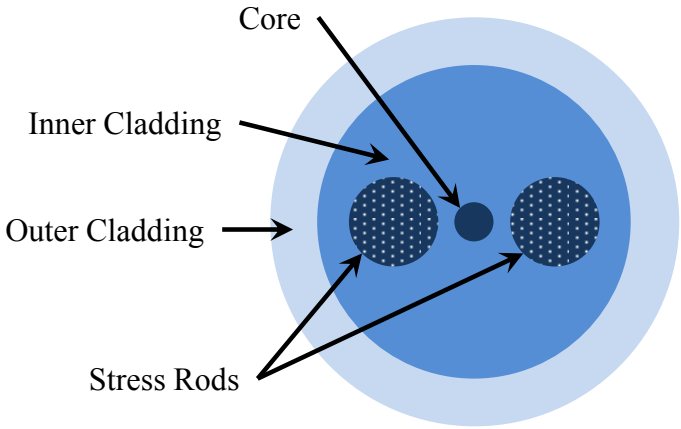

Figure 4.3: Cross-section of a polarisation maintaining fibre that is similar to double-clad fibre but with the addition of stress rods.

each axis of the PBS will be transmitted and another reflected. The transmitted portion is described by Malus' Law in Equation 4.6 where the transmitted intensity I_t of a linearly polarised beam of intensity I_i incident on a PBS is a function of the input polarisation angle θ_i relative to the transmission axis of the PBS.

$$I_t = I_i cos^2(\theta_i) \tag{4.6}$$

By rotating the polarising beam splitter and measuring the transmitted power, the polarisation state can be measured. A perfectly linearly polarised input beam will correspond to Malus' Law directly with full transmission and complete extinction observed when rotating the PBS about the optical axis. Conversely, an input beam with perfectly circular polarisation would have a constant transmission function. A randomly polarised source would also have a constant transmission function. In reality, it's likely that there may be a combination of these cases as shown in Figure 4.4 where the beam exhibits a degree of linear polarisation.

The method described of rotating a PBS is not however, the most common method of analysing the polarisation state of a laser beam. When the PBS is rotated, the reflected beam that usually exits the PBS near perpendicularly to the incident beam is also rotated, which presents a safety hazard. Therefore the PBS is usually placed in a fixed orientation with the two possible output beams orientated parallel to an optical table. Instead of rotating the

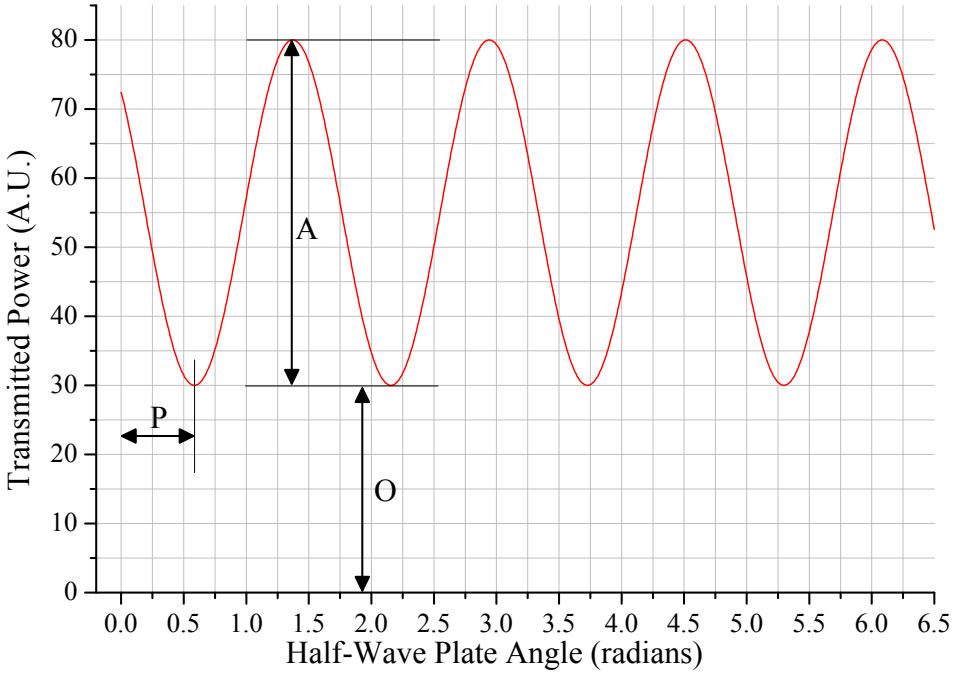

Figure 4.4: Transmission function of a partially linearly polarised source through a half-wave plate and linearly polarising beam splitter with A, O and P describing the amplitude of the modulation; the offset and the phase respectively.

PBS, the input polarisation is rotated instead using a half-wave plate.

A wave plate is a thin piece of a transparent birefringent crystal that has two different refractive indices in two orthogonal axes orthogonal to the direction of the laser beam. This causes a phase delay between two orthogonal linear polarisation components of light travelling parallel to the two axes of the crystal resulting in the polarisation state being changed upon exiting the crystal. Depending on the phase delay between the two components, various polarisation states can be achieved [26]. By using a specific thickness of birefringent crystal, a specific phase delay between each component and hence change in polarisation state can be achieved.

Wave plates are typically designed to introduce either a π or $\frac{\pi}{2}$ phase delay between the two orthogonal axes in the crystal and these are called a half-wave plate and quarter-wave plate respectively.

A half-wave plate will simply rotate the linear polarisation of the incident beam. Rotating a half-wave plate by an angle θ will cause the output polarisation to be rotated by 2θ. A

quarter-wave plate however, will change linear polarisation into circular polarisation. By varying the angle of the quarter-wave plate, this can be varied resulting in an elliptically polarised beam. The refractive indices of the crystal are wavelength-dependent, so a wave-plate is designed by necessity specifically for a given wavelength.

Malus' Law can be modified to describe the transmission function of a general source that is not entirely linearly polarised passing through a half-wave plate and PBS in series, which is described by Equation 4.7 where A is the amplitude of the modulation; θ is the angled of the half-wave plate; ϕ is a phase offset as the input polarisation and the markings on the half-wave plate will not be aligned exactly and O is the offset from 0.

$$I_t = Acos^2(2\theta + \phi) + O \tag{4.7}$$

The degree of linear polarisation (DOLP) as a percentage is then calculated using Equation 4.8.

$$DOLP(\%) = 100\left(\frac{A}{A + 2O}\right) \tag{4.8}$$

4.4 Dopants

Considering amplification in a doped double-clad fibre, a high power continuous wave (CW) pump laser beam is carried in the inner cladding, overlapping the doped core many times as it transits through the fibre. When a pump photon interacts with a laser ion, an electron is excited from the ground state to a higher energy level. Generally, the electron then non-radiatively decays to a metastable upper state energy level. Stimulated emission from an input seed photon causes the electron to fall to the lower state energy level. Further fast non-radiative decay causes the electron to return to the ground state upon reaching which, it is free to begin the same process again. This is the basic stimulated emission process of a four-level laser ion that is the most common [20]. The pump photon has a shorter wavelength

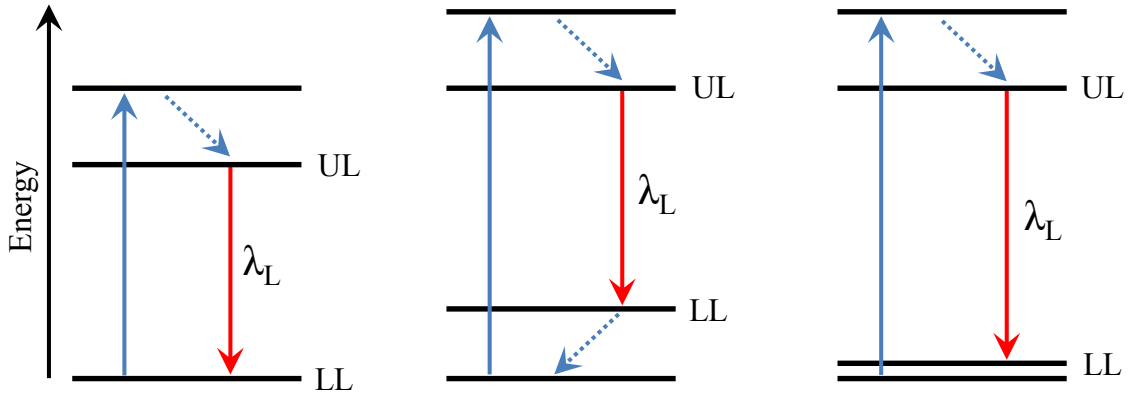

(a) Three-Level Ion (b) Four-Level Ion (c) Quasi-Three Level Ion

Figure 4.5: The three main categories of lasing ions are (a) a three-level ion, (b) a four-level ion and (c) a quasi-three level ion. The upper and lower energy levels are labelled UL and LL respectively and lasing transition between them is labelled λ_L. Non-radiative transitions are depicted by dotted lines and radiative ones by solid lines.

and hence higher energy than the stimulated emission photon.

Three-level laser ions exist but are not commonly used. Here, the lower state is in fact the ground state as shown in Figure 4.5a where there is a high probability of a seed photon being absorbed by an electron in the ground state. A high pumping rate will ensure that few electrons exist in the ground state and that most of the electron population is in the upper state. This does however, require a high power pump source.

Four-level laser ions have little or no population in the lower state as the electrons decay quickly and non-radiatively from this state to the ground state as shown in Figure 4.5b. Because of this, absorption of the seed photon is unlikely giving a four-level ion a lower pumping threshold than a three-level laser ion [20].

Quasi-three-level laser ions are similar to four-level laser ions but can exhibit the behaviour of a three-level laser ion. Here, the lower state is close enough to the ground state that a significant portion of the electron population exists in thermal equilibrium between the ground state and the lower state. These ions require a higher pumping level than four-level systems to overcome some partial absorption of the seed photons, but not as high as three-level. The energy levels of a quasi-three-level laser ion are shown in Figure 4.5c.

The difference between the energy of the pump photon and the laser photon is defined in Equation 4.9 and is referred to as the quantum defect. In a quasi-three-level laser ion, the energy of the photon from stimulated emission is often very similar to that of the pump photon and so quasi-three-level laser ions can exhibit a very high quantum efficiency [37].

$$q = h\nu_{pump} - h\nu_{laser} \tag{4.9}$$

This is important as the difference in energy is often deposited as heat in the gain medium which must be removed by cooling and can lead to various thermal effects that if strong can degrade the spatial quality of the laser beam.

As mentioned in Section 4.2 the core of the fibre can be doped with a lasing ion that would be used conventionally in a macroscopic crystal. Although Neodymium-doped Yttrium-Aluminium-garnet (Nd:YAG) and Titanium-doped sapphire (Ti:Sapp) are common choices for high power bulk laser systems, Ytterbium^{3+} (Yb^{3+}) has proved to be the most popular dopant for high power fibre lasers with many attractive features [34].

Ytterbium is a quasi-three-level laser ion with a gain bandwidth of $\sim$ 40 nm at 1037 nm that theoretically supports pulses as short as $\sim$ 30 fs. The absorption and emission cross-sections are shown in Figure 4.6 [37]. The absorption spectrum covers a large range of wavelengths where high power laser diodes are readily commercially available making Ytterbium suitable for high power applications. A typical diode laser stack will have a spectral bandwidth between 5 nm and 10 nm, which can be engineered to overlap with an absorption peak leading to very efficient pump absorption [38]. The diode lasers themselves also commonly have high electrical to optical efficiencies of up to 60 % [39], again making overall wall plug efficiency very high compared to typical bulk lasers that commonly use much less efficient pump sources. Ytterbium can have a very small quantum defect of around 10 % [40] leading to optical-to-optical efficiencies as high as 88 % [41].

As Ytterbium is a quasi-three-level laser ion, absorption of the lasing wavelength will occur when it is unpumped and therefore a high pump intensity must be used to maintain

Figure 4.6 was removed due to Copyright restrictions

Figure 4.6: Absorption (solid line) and emission (dashed line) cross-sections of Ytterbium^{3+} in germanosilicate glass [37].

at least transparency throughout the fibre.

An attractive quality of Ytterbium is the comparatively long upper-state lifetime of ~ 0.85 ms [30]. This allows energy to be stored in the fibre for a relatively long time that would not be possible with a much shorter upper-state lifetime typical of other dopants. Ytterbium is commonly pumped at the peak of the absorption spectrum at 976 nm which is then emitted at the next lower energy emission peak at 1037 nm.

4.5 Architecture

Although fibre lasers can be used both as oscillators and single pass amplifiers, a master-oscillator power-amplifier (MOPA) architecture is the most practical to achieve the high pulse energies required. This regime consists of a master oscillator (seed) that produces low energy pulses, which are then amplified in either a single or series of amplifiers to the required intensity. In the case of the amplifier(s) being fibre based, this is commonly referred to as a master-oscillator fibre-amplifier (MOFA) architecture.

The seed output is typically low power but very stable and controllable. Subsequent amplifiers can provide a very large gain in many stages with a high degree of scalability.

Because the gain of the amplifier(s) may be very high, parameters such as the spectrum or spatial quality of the beam may be affected. The tolerance of each of these parameters depends on the purpose of the laser.

Amplifiers may also be single or multi-pass where the pulse is either amplified on a single transit or repeatedly passed through it before moving on through the laser system respectively. The later option often involves reducing the pulse repetition rate with a modulator.

In developing a fibre based amplifier system it is useful to consider the achievable gain from such an amplifier and any potential limits. As mentioned in Section 4.1, an energy of 100 μJ per pulse at a repetition rate of 6.49 MHz is required. A double-clad fibre as shown in Figure 4.2c where the pump is coupled into the inner cladding and the seed into the core is the most suitable type of fibre.

To couple both the pump and the seed laser beams into the fibre they must be overlapped and separated afterwards. This is achieved with dichroic mirrors that are engineered to have a very high reflectivity at one wavelength and simultaneously a very high transmission at another. With a single pump source and a seed it is possible to either have the pump and seed co-propagating or counter-propagating. If a second pump source is available, the fibre can be pumped from either end (bidirectional pumping). Often, the counter-propagating geometry is the most favourable as it allows independent alignment of both the seed and the pump as well as providing a marginally higher output levels [42, 43].

In a general fibre amplifier, the input seed will stimulate emission and then this stimulated emission will then stimulate further emission and so on experiencing exponential gain until the end of the fibre is reached. However, both the number of lasing ions and the pump power is finite, so this cannot continue indefinitely and will eventually saturate. Before saturation is reached, the amplification regime is called the small-signal regime and can be easily theoretically modelled and can be shown to demonstrate very high gain of tens of decibels per meter [37]. However, this is not an accurate model of the amplification process and effects such as gain saturation and spontaneous emission must be considered.

Under exponential amplification, the seed initially uses a very small proportion of the excited upper state lasing ions and these unused excited laser ions eventually spontaneously emit and return to the ground state. This spontaneous emission is omnidirectional but a small fraction is guided by the fibre in both directions. This guided fraction then undergoes exponential amplification in a similar manner to the seed and eventually competes with the amplified seed in intensity. This is called amplified spontaneous emission (ASE) and proves to be a practical limit of the achievable gain in any one fibre amplifier [37, 44].

The ASE has a continuous output whereas the seed consists of a series of pulses. The ASE can occur at any wavelength supported by the gain bandwidth and consequently has a spectrum similar in shape to the gain bandwidth in that spectral region of that transition (shown in Figure 4.6) [45].

If the input seed power is high however, a large portion of the excited upper state lasing ions are used leading to efficient extraction of the energy stored in the fibre. Because most of the excited upper state laser ions are used, the gain is saturated and considerably lower than in the small-signal regime. Relatively few excited ions are left unused and therefore less ASE is present.

In summary, two regimes exist; firstly the small-signal regime where the input seed is small and it experiences large gain. The total energy extracted from the fibre is low and ASE can limit the gain. Secondly, in the saturated regime, where the gain is considerably lower but the energy extraction is much greater and there is little ASE present. To reach higher pulse energies, higher gain is needed but this leads to more ASE which in turn limits the achievable gain in a single amplifier. Published theoretical work and experimental results have shown that a gain of approximately 30 dBm^{-1} is the most that can be achieved in a single amplifier stage without significant ASE [30].

To determine which regime an amplifier is operating in it is useful to consider the saturation power of the fibre which can be calculated using Equation 4.10 [20], where h is Planck's constant; ν is the central frequency of the light to be amplified; A_{eff} is the effective area of the mode; Γ_{Seed} is the overlap between the core and the inner cladding where the pump is

carried. σ_{as} and σ_{es} are the absorption and emission cross-sections at the seed wavelength respectively and τ is the upper-state lifetime.

$$P_{Sat} = \frac{h\nu_{Laser}A_{eff}}{\Gamma_{Seed}(\sigma_{as} + \sigma_{es})\tau} \tag{4.10}$$

The saturation power is the power required to reduce the gain to half of the small-signal gain in the steady-state. If the input power to the amplifier is much less than the saturation power, the input will experience the small-signal gain whereas if the power is above the saturation power, the gain will be reduced significantly. Although the gain will be reduced, the maximum amount of power possible will be extracted from the amplifier for that level of pumping.

A full model for the achievable gain in a strongly pumped fibre amplifier with full consideration for ASE over the full gain bandwidth is non-trivial and cannot be solved analytically. Sintov et al. [30] have shown this and have found numerical solutions to their model with multiple iterations. Due to time constraints and practicalities, accurate modelling of the amplification has not been undertaken in this research.

Typically, several fibre amplifiers will be used in series separated by isolators which prevent feedback and possible damage. A high gain amplifier is often followed by a low gain 'power' amplifier. Using amplifiers in series allows overall high gain or energy to be achieved whilst minimising ASE.

Also to note is the size of the core. A larger core will provide a greater number of lasing ions and therefore a greater potential gain per unit length allowing higher pulse energies to be achieved. However, a larger core will also support a greater number of modes which will degrade the spatial quality of the output beam. Fibre manufacturers endeavour to make the core bigger whilst still retaining the same V-number and hence number of modes by decreasing the numerical aperture of fibre (see Equation 4.5). To do this, the difference in refractive index between the core and the cladding layer must be as small as possible.

4.6 Nonlinearities

In Section 4.5, the modelling of CW amplification was considered, however when using optical fibres with laser pulses that have a peak powers much greater than the average power, optical nonlinearities must be considered. Under sufficiently high optical intensities the response of any dielectric medium becomes nonlinear, where the polarisation **P** induced by the electric dipoles is not linearly proportional to the electric field **E** but can instead be described by Equation 4.11 [31]. ϵ_0 is the vacuum permittivity and χ^n is the nth order susceptibility.

$$\mathbf{P} = \epsilon_0 \left(\chi^{(1)}\mathbf{E} + \chi^{(2)}\mathbf{EE} + \chi^{(3)}\mathbf{EEE} + \ldots \right) \tag{4.11}$$

These nonlinearities tend to broaden the spectrum the light and are cumulative. Because of the 2nm bandwidth limit of the laser-wire lens, these must be avoided. If not, a broad spectrum will produce a large focussed spot size due to the chromatic aberrations of the lens.

The first order susceptibility (χ^1) is dominant and responsible for normal refraction and absorption. The second order susceptibility (χ^2) is dependent on the symmetry of the molecular structure and is 0 for silica. The most common nonlinear effects originate from the third order susceptibility (χ^3) which is the next non-zero susceptibility in silica [31]. This is responsible for elastic processes of nonlinear refraction, four-wave mixing and third harmonic generation, all of which generate new frequencies and lead to spectral broadening. These are described as elastic, as no energy is transferred to the medium [31]. Inelastic nonlinear processes such as stimulated Raman scattering and stimulated Brillouin scattering are also caused by the (χ^3) susceptibility but have a much higher threshold than the elastic processes mentioned.

Without special efforts to ensure that newly generated frequencies remain in phase with the original frequencies, four-wave mixing and third harmonic generation are not intrinsically efficient in optical fibres [31]. Nonlinear refraction however, leads to the most relevant and

observable consequences in fibres. With nonlinear refraction, the refractive index of a media can be described by Equation 4.12 where the refractive index is the sum of the the normal frequency dependent refractive index $n(\omega)$ and an intensity dependent part $n_2|\mathbf{E}|^2$. The degree of this is specific to the media as described by n_2, the nonlinear index coefficient.

$$n(\omega, I) = n(\omega) + n_2 I \tag{4.12}$$

n_2 is related to the χ^3 susceptibility as shown in Equation 4.13.

$$n_2 = \frac{3}{8n}\mathrm{Re}\left(\chi^3\right) \tag{4.13}$$

The intensity dependence of the refractive index leads to a large number of nonlinear effects with the two most widely studied being self-phase modulation (SPM) and cross-phase modulation (XPM). In both cases, a phase shift is induced by the change in refractive index due to either the pulse itself in the case of SPM or by the interaction of two pulses in the case of XPM. As the phase shift is a function of intensity, it varies across the length of the pulse leading to the generation of new frequencies, in turn leading to spectral broadening. New frequencies then undergo the same process themselves and the spectrum is broadened further. This effect as well as being intensity dependent is therefore also cumulative and dependent on the interaction length in the media, which in this case is the fibre.

SPM can be easily identified by the changes in the spectrum of the output light. An initially Gaussian spectrum will broaden and develop a flatter top eventually with small peaks at the edge as shown in Figure 4.7.

Stimulated Raman scattering and stimulated Broullouin scattering have thresholds many orders of magnitude higher than either SPM or XPM and require a long interaction length to become evident. Given that the SPM present before either of these effects would result in unacceptable spectral broadening for the purposes of laser-wire, these are not considered in great detail here. Furthermore, fibre amplifiers have limited lengths to mitigate ASE and

Figure 4.7 was removed due to Copyright restrictions

Figure 4.7: The narrow peak in the centre is the spectra of a pulse before entering a fibre while the much broader peak around it is the spectrum of the pulse after passing through the fibre and experiencing self-phase modulation [31].

are often too short for these effects to become evident.

The intensity of a given laser pulse with a given fixed energy in a fibre is proportional to both the area of the mode supported in the core and its temporal duration. Increasing either of these will reduce the intensity and hence the effect of nonlinearities.

The dispersion length scale L_D and the nonlinear length scale L_{NL} are derived in detail in [31] and can be used to determine when either dispersion effects or nonlinear effects will become relevant respectively. The dispersion length scale is defined in Equation 4.14 where T_0 is the initial pulse length (FWHM) and β_2 is the group velocity dispersion (GVD) parameter.

$$L_D = \frac{T_0^2}{\beta_2} \tag{4.14}$$

The nonlinear length scale is defined in Equation 4.15 where P_0 is the peak power of the pulse and γ is the nonlinear parameter.

$$L_{NL} = \frac{1}{\gamma P_0} \tag{4.15}$$

γ is defined in Equation 4.16 where n_2 is the nonlinear-index coefficient of the media, λ is the wavelength of the light and w is the mode field radius.

$$\gamma = \frac{2n_2}{\lambda w^2} \tag{4.16}$$

The mode field radius is the distance from the centre of the intensity distribution to the point where it is $1/e^2$ of its maximum. This can be calculated using the Marcuse formula shown in Equation 4.17 [46].

$$\frac{w}{a} = 0.65 + \frac{1.619}{V^{\frac{3}{2}}} + \frac{2.879}{V^6} \tag{4.17}$$

This requires the V number which can be calculated using Equation 4.5 and the physical core radius a. The mode field radius is not always specified by the fibre manufacturer but can be easily calculated using this method.

Typical undoped optical fibres have a β_2 value of 20 $\text{ps}^2\text{km}^{-1}$ [31] and therefore the dispersion length scale of a 1 ps pulse (which is comparable to the electron bunch lengths in Table 4.1) is approximately 50 m. This is considerably longer than the typical length of normal fibre amplifiers which range from 1 m to at most, a few 10's of metres. Therefore, dispersion will not be a dominant effect for the typical pulses used.

Assuming single mode operation, Equation 4.15 can be used to calculate the maximum peak power within the length of a specific fibre at which nonlinearities will become evident. A typical value of n_2 which is required to calculate the nonlinear γ for undoped silica is 3.2×10^{-20} m^2W^{-1} [31]. One of the fibres used as a fibre amplifier in this research is a Nufern PLMA-YDF-15/130 double-clad Ytterbium-doped fibre which is typical for a fibre amplifier. The lowest order single mode has a mode field radius of 6.64 μm for a wavelength of 1037 nm. A typical length of a fibre amplifier is 3 m and therefore, using Equation 4.16, γ is 1.4×10^{-3} $\text{m}^{-1}\text{W}^{-1}$ and the peak power at which nonlinearities become evident in 3 m of this fibre is 238 W. This is considerably lower than the required 50 MW described in

Figure 4.8 was removed due to Copyright restrictions

Figure 4.8: Simulation of pulse intensity through a fibre amplifier for (1) co-propagating, (2) bidirectional and (3) counter-propagating pumping regimes [42].

Section 4.1 and so any pulses with peak powers greater than 238 W are likely to experience nonlinearities that will broaden their spectrum.

A simple view would say that to reach the desired energy and hence peak power, several fibre amplifiers could be used sequentially with different pump sources. These calculations however, show that before the required pulse energies can be reached nonlinearities will become evident over the length of the fibre. These will lead to significant spectral broadening as the pulse energy and hence the intensity increases. A wide spectrum will lead to chromatic aberrations in the focussed laser beam and which will negate the potentially better resolution of the higher spatial quality beam from a fibre laser.

Furthermore, the pumping geometry can significantly affect the the evolution of the seed pulse energy throughout the fibre. This is shown in Figure 4.8 where Parvin et al. [42] simulate co-propagating, bi-directional pumping and counter-propagating pump regimes. In the bidirectional case, two pump sources of exactly half the power used in the co-propagating and counter-propagating cases are used.

This simulation shows that although the output pulse energies may be similar in all three pumping geometries, the pulse energy remains lower throughout most of the fibre the counter-propagating geometry. Using this regime will prevent the onset of and lower the

effect of nonlinearities in the fibre.

Although the peak power is limited by nonlinearities, the interplay between peak power, energy and pulse length can be used to some advantage. By stretching a fixed energy pulse in time, the peak power is lowered and the nonlinearities can be avoided. It should also be noted that the length scales measured are derived with a pulse of constant intensity being transmitted in a single mode fibre. Since this research is concerned with amplification in fibres, the pulse energy will increase throughout the fibre and if using the counter-propagating geometry, will only have a comparable energy to the final output energy at the very end of the fibre.

From this discussion of nonlinearities, it is clear that the counter-propagating approach is the most desirable as it not only achieves the greatest output energy through the most efficient extraction of gain in the fibre but maintains a low pulse energy throughout the fibre mitigating the onset of nonlinearities.

It is also clear that to avoid nonlinearities whilst achieving the peak power necessary for laser-wire, the diameter of the core of the fibre will have to be large. As previously mentioned in Section 4.2, a larger fibre supports a greater number of modes and a fibre can only be made single mode in this case with a very small difference in refractive index between the core and the cladding. With a greater number of modes the spatial quality of the output may be degraded.

4.7 Spatial Quality

As discussed in Section 4.2, one the main advantages of a fibre is its waveguiding nature which allows a high spatial quality to be achieved by design that is maintained purely by the shape of the fibre. Quantifying the spatial quality of a laser beam will allow its propagation either unguided or through known optics to be predicted.

As mentioned in Chapter 2, a transverse Gaussian intensity profile will produce the

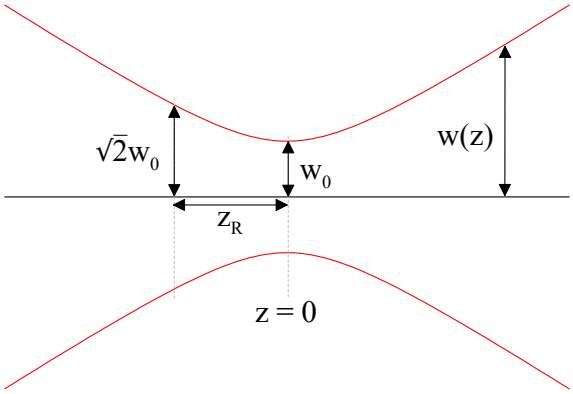

Figure 4.9: The propagation of a focussed beam with a Gaussian transverse intensity profile. The beam radius $w(z)$ reaches a minimum w_0 at $z = 0$. z_R is the Rayleigh range.

smallest possible focussed spot size [20]. The focus of a Gaussian beam is shown in Figure 4.9. A Gaussian beam will propagate as a Gaussian and since its Fourier transform is also a Gaussian, the focussed spot also has a Gaussian intensity profile [26]. Here the beam radius $w(z)$ reaches a minimum w_0 at $z = 0$ where z is the optical axis. $w(z)$ is defined as the distance from the centre of the intensity distribution to where the intensity drops to $1/e^2$ of its maximum value (~ 13.5 %).

The beam radius is described more generally as a function of the distance along the optical axis z by Equation 4.18 where the beam waist is located at an arbitrary location z_0.

$$w(z) = w_0 \sqrt{\left(1 + \left[\frac{z - z_0}{z_R}\right]^2\right)} \tag{4.18}$$

where z_R is the Rayleigh range which is the distance from the beam waist for the beam area to double or alternatively, for the beam waist to reach $\sqrt{2}$ of its minimum value w_0. The Rayleigh range is defined Equation 4.19.

$$z_R = \frac{\pi w_0^2}{\lambda} \tag{4.19}$$

This is illustrated in Figure 4.9. The confocal parameter b, which is twice the Rayleigh range, is a commonly used parameter as it is the range over which the laser beam remains

for practical purposes at approximately the same size and is used as an interaction length.

In practice various aberrations and imperfections in optics cause the beam not to be a perfect Gaussian. Whilst a beam may not be a perfect Gaussian, it will propagate in a similar fashion. It is therefore useful to model how such real-life beams will propagate.

This can be achieved by modelling the beam as a superposition of higher order Hermite-Gaussian modes and scaling the perfect Gaussian model by a factor called M^2 [25]. This describes the beam as the beam radius, W, being M times larger than the embedded perfect Gaussian at any given place along the optical axis, z. Here, the capital letter W is used to denote the multimode beam as opposed to the single mode beam denoted by w. Since the size of the laser beam scales with M, the Rayleigh range can therefore be modified as shown in Equation 4.20

$$z_R = \frac{\pi W_0^2}{M^2 \lambda} \tag{4.20}$$

This can then be substituted into Equation 4.18 to give Equation 4.21 [47, 20].

$$2W(z) = 2W_0 \sqrt{\left(1 + \left[\frac{(z - z_0)M^2\lambda}{\pi W_0^2}\right]^2\right)} \tag{4.21}$$

Although w in Equation 4.18 is specified as the beam radius, it is more common to measure the full width of the beam which is why Equation 4.21 refers to $2W(z)$. The focussed spot size of a laser beam can be calculated using Equation 1.25. For a laser beam with a measured M^2 value, both the input beam size and focussed spot size are M times larger. However, if the input beam size is fixed, the spot size of the focussed beam scales with M^2.

Equation 4.21 can therefore be used to fit measured beam widths as a beam is focussed to find its M^2, quantifying its spatial quality. Since the M^2 is a scaling of a perfect Gaussian, its value can only be 1 or greater. An $M^2 < 1$ is non-physical and most likely due to measurement uncertainties and the the uncertainty in fitting to a model with three free

parameters.

To measure the M^2 of a laser beam, a lens is used to generate a focus and transverse beam width measurements made along the optical axis. These are typically measured using either a knife edge that is translated across the beam whilst measuring the transmitted power or using a CCD camera. Commonly, a CCD camera is mounted on a translation stage which is then moved along the optical axis to measure the beam width at various points throughout the focal region. The data must encompass the beam waist as well as the beam in the far field, several Rayleigh ranges from the waist for best results [47].

An ambiguity in the already mentioned definitions of how to measure the beam width exists. For a perfect Gaussian beam the radius w is defined as $1/e^2$, however for a more realistic beam this may lead to an unrealistic M^2. In the ISO standard 11146 [48] that describes this measurement, the beam width measurement is defined as 4σ using the second-moment of the intensity profile as defined by (for example along the x axis) Equation 4.22 where x_0 is the centre of gravity of the beam and $I(x, y)$ is the intensity of the beam in the x, y plane[25]. This is applicable for any intensity distribution. For a perfect Gaussian, 4σ via the second-moment and $1/e^2$ are equivalent.

$$\sigma_x^2 = \frac{\int\int_{-\infty}^{\infty}(x - x_0)^2 I(x, y)\ dx\ dy}{\int\int_{-\infty}^{\infty} I(x, y)\ dx\ dy} \tag{4.22}$$

The beam waist measurements are very sensitive to noise at the edge of the profile because of the square dependence with distance from the centroid which can affect the 4σ diameter measured.

The lens chosen must have a sufficiently long focal length so as not to introduce aberrations. If a short focal length with even small aberrations due to manufacturing tolerances was used, the M^2 would more be a measure of the effect of the lens on the beam rather than the beam itself. A typical setup for an M^2 measurement is shown in Figure 4.10.

In addition to the transverse spatial quality, the pointing jitter of a laser is important for a laser-wire as the laser may have to travel as much as 100 m from the laser to the interaction

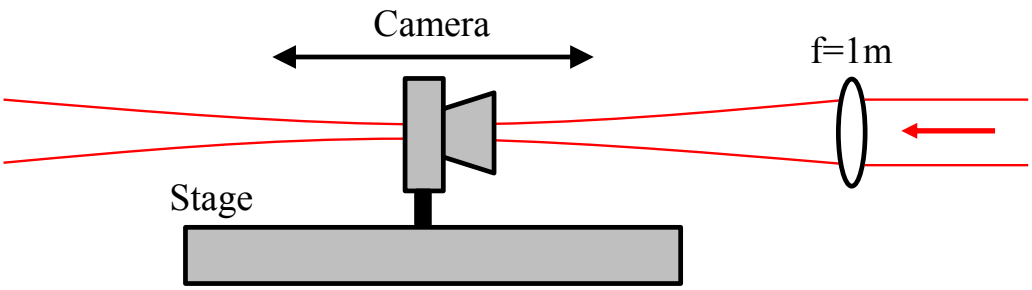

Figure 4.10: A typical M^2 setup with a long focal length lens used to focus the beam. A camera on a moveable stage is translated along the optical axis through the focus of the laser beam.

point. If the pointing stability is low and there is a relatively large jitter in the position of the laser beam on the laser-wire lens this will corresponds to jitter at the interaction point. This scales linearly with the size of the beam and so the absolute position jitter will be substantially reduced by the focusing. However, if this is still comparable to the size of the laser focus or the electron beam, this may limit the resolution of the laser-wire.

Because of their waveguiding nature, fibre lasers typically have a lower pointing jitter than a bulk laser. A bulk laser system with a macroscopic gain medium will experience greater thermal gradients than a fibre which has a higher surface to volume ratio. Thermal distortions of the gain medium will lead to increased pointing jitter. Pointing jitter can be measured by measuring the standard deviation σ of the laser beam centroid at a known distance d as shown in Equation 4.23.

$$\theta = tan^{-1}\left(\frac{\sigma}{d}\right) \tag{4.23}$$

In the small angle approximation this can be further simplified to

$$\text{for}\,\sigma \ll d \qquad \theta \approx \frac{\sigma}{d} \tag{4.24}$$

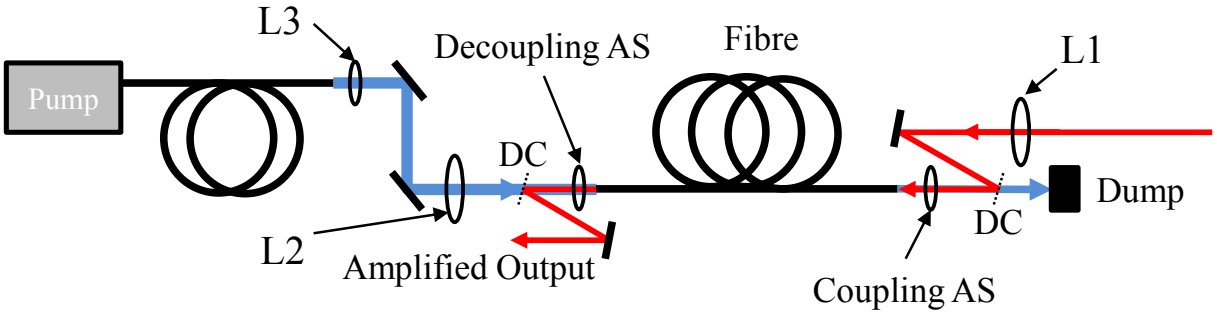

Figure 4.11: General layout for a fibre amplifier. Black lines represent silver coated mirrors and dashed lines are dichroic mirrors(DC). Red represents the path of the seed laser and blue the path of the pump laser. L1, 2 and 3 are long focal length plano-convex lenses. Coupling and decoupling aspherics are labelled AS.

4.8 Fibre Amplifiers

The setup shown in Figure 4.11 is the layout of a typical fibre amplifier. Both the pump and the seed must be coupled into the fibre and decoupled out of this. A counter-propagating geometry is shown where the pump and seed enter from opposite ends of the fibre for both ease of alignment and increased efficiency [49, 43].

As the pump traverses the fibre it is absorbed and its intensity decreases. This leads to high gain at the end of the fibre the pump starts at and lower gain at the other end. Any transmitted pump light is safely contained by a beam dump. The seed intensity grows as it traverses the fibre in the opposite direction. The optics at each end are primarily chosen and positioned to achieve the best coupling of each beam entering the fibre at that end.

Two lenses or more are usually required to efficiently couple light into the fibre as the input beams often start with macroscopic diameters of several millimetres and must be reduced to the size of the fibre core or cladding that they are to be coupled into which range from approximately 5 to 150 μm. A long focal length lens (L1 in Figure 4.11) is first used to generally reduce the size of the beam, followed by a short focal length aspheric lens to create the small focus necessary to couple into the fibre core. Lenses used are for the most part plano-convex lenses orientated with the flat side towards the focus to minimise any spherical aberrations [26]. A lens with an aspherical surface ('aspheric') is used as the final optic to couple light into the fibre as these are specially designed to minimise spherical aberrations

and achieve the small spot sizes necessary for efficient coupling into the microscopic fibre core. These are only necessary when a very small focus is desired and are not necessary for the long focal length lenses. These are labelled AS in Figure 4.11.

Although the small spot size required could be achieved with one lens and a large input beam, the divergence of the input beam must be within the numerical aperture of the fibre for optimal coupling. Irrespective of the spot size of the laser on the fibre, if the divergence of the beam is greater than the the numerical aperture it will not be guided by the fibre resulting in a low coupling efficiency. The coupling efficiency is defined as the fraction of light entering the fibre that is successfully coupled into it and guided along the fibre. Typically, this is approximately 70 - 80 % [50]. The coupling efficiency is difficult to measure accurately as the light in the core is absorbed by the laser ion.

To separate the overlapped seed and pump beams, dichroic mirrors are used which have a very narrow range of angles over which they can be used to provide their specified properties. This often constrains the placement of other optics and therefore which ones can be used.

Diode lasers used for pumping are commonly supplied fibre coupled and the beam from the fibre end must be collimated. L3 in Figure 4.11 is an aspheric lens that is used to collimate the pump light from the fibre. L2 is a long focal length lens used to focus the transported pump laser beam before passing through the dichroic mirror and the aspheric before the fibre.

Commonly fibres can be manufactured with connectors allowing simple connection without complicated alignment. Additionally, various fibre splitters and combiners are commercially available that have similar connectors for simplicity of alignment. These technologies however, were not considered as they currently do not support the high peak and average powers that are required by this research. Because of this, only free-space coupling where the laser beams are directed towards the fibre and a series of lenses used to couple the light in was considered here. Where multiple fibres are used, optics are used in between fibres to manipulate the size, divergence and direction of the beam. This approach allows much higher powers to be used without incurring damage.

Although each aspheric lens at either end of the fibre is both coupling and decoupling a beam, the lens at the seed input end will be referred to as the coupling lens and the one at the other end as the decoupling lens for the purposes of this thesis.

Chapter 5

Fibre Laser Results

This chapter presents the experimental results of a test bed system and a discussion of the results achieved. Firstly, the gain achievable in a double-clad multimode fibre is investigated using a commerically available seed with a wavelength of 1053 nm. In Section 5.2, the presence of ASE is recognised and quantified by analysing the spectrum of the output light. After this, the amplification of a seed with a more suitable wavelength of 1037 nm is investigated in Section 5.4. A novel method for measuring the proportion of ASE by analysing the output polarisation is then developed. Finally, the spatial quality of different types of fibres is characterised. In conclusion, a possible architecture for a laser for laser-wire is proposed as well as some of the potential issues with fibre lasers.

5.1 Amplification

To investigate the suitability of fibre lasers for a new laser-wire laser system, experiments were conducted on various fibres on a small test bed system using a small commercial fibre oscillator as the seed and a 20 W diode laser as the pump. These were used to assess if the high power, pulse energies and spatial quality were achievable in fibre lasers.

The commercial fibre oscillator was a Fianium 120 mW laser with 5 ps pulses at 32.5 MHz and with a wavelength of 1053 nm and will be referred to as the Fianium laser. A continuous wave Jenoptik 20 W air-cooled fibre-coupled diode laser with a wavelength of 976 nm was used as the pump.

As mentioned in Section 4.6, single mode fibres have the best spatial quality but the core is very small, which leads to a lower gain per unit length, a higher core intensity and therefore a greater likelihood of nonlinearities. Slightly multimode fibres however, can with careful alignment be made to operate in the lowest order mode. In a multimode fibre, the area of the core and therefore the lowest order mode are larger, reducing the core intensity. This decreases the risk of incurring nonlinearities and increases the achievable gain per unit length. It was for these reasons that slightly multimode fibres were considered first.

For initial experiments, a 2.2 m Nufern PLMA-YDF-15/130 double-clad Ytterbium-doped fibre was used. The diameter of the core and the inner cladding were 15 μm and 130 μm respectively. The cladding absorption at 976 nm was specified to be 6.0 dBm^{-1}. This is quoted for the cladding, which has no dopant but therefore includes the overlap ratio of the core to the cladding. The numerical aperture of the core was also specified as 0.08. Using this information and Equation 4.5, the V number for this fibre is 3.58 at 1053 nm, the wavelength of the Fianium laser. This is greater than the single mode cut-off of 2.405 meaning that it will support higher order modes. However, the cut-off for the next highest mode is 3.830, meaning that the fibre is only slightly multimode.

With careful alignment and coupling it was possible to couple light into the lowest order single mode. The increased mode field radius of the single mode in the larger diameter fibre increases the level of achievable amplification for the same maximum intensity limit of nonlinearities.

The amplifier was set up as shown Figure 4.11 on Page 110 with an f = 300 mm plano-convex lens used for both L1 and L2. Aspherics with focal lengths of f = 11 mm and f = 6 mm were used for the coupling and decoupling lenses respectively. Additionally, L3 was an f = 6 mm aspheric. A WinCamD camera was initially placed in the unamplified output seed beam and the position of the decoupling aspheric adjusted along the optical axis to form an image on the camera. This image was then used to couple light into the core of the multimode fibre as shown in Figure 5.1. Care was taken to ensure that the laser beam was level before lenses were placed in it by observing its height over a distance of several

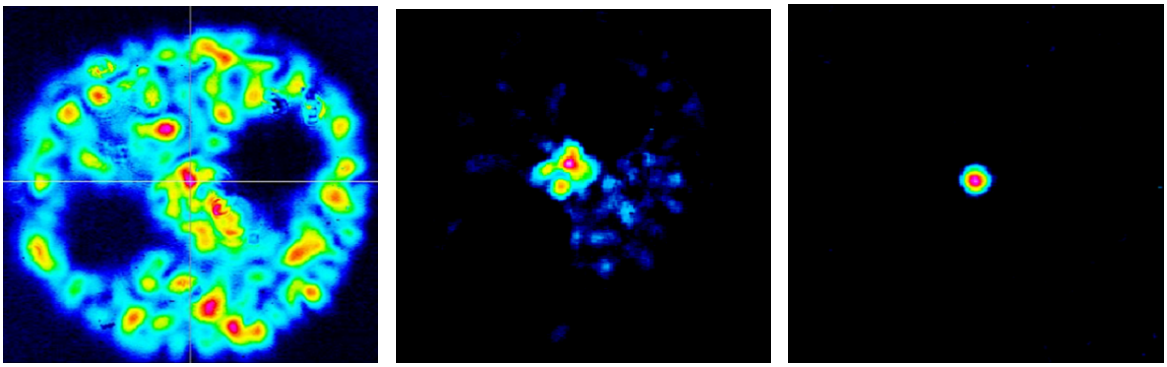

(a) Bad coupling (b) Multimode coupling (c) Good coupling

Figure 5.1: Alignment of seed into core by imaging decoupling end of the fibre. (a) shows coupling into the inner cladding but not the core with the polarisation maintaining stress rods visible, whereas (b) shows coupling into the core. However, a higher order mode is present and with careful alignment single mode operation was achieved as shown in (c).

metres.

After this, lenses were placed sequentially in the beam ensuring that the position of the beam far from the lens did not change, which ensured that the beam was passing through the centre of each lens. The fibre was then mounted on top of a ThorLabs Nanomax 3 axis (x,y,z) stage with micrometre resolution and moved to find the optimum coupling. This was achieved by starting with the fibre beyond the focus of the beam and moving it horizontally and vertically to give the brightest image on the camera (with a fixed exposure time). The fibre was then stepped closer to the aspheric lens before repeating the transverse alignment again. This processes was iterated until the optimum coupling was found. Coupling light into the inner cladding as shown in Figure 5.1a is fairly trivial due to its large size, but coupling into the core is more difficult.

The light coupled into the inner cladding is very highly multimode and there is no clear indication of an input spot that moves as the fibre is translated. As the fibre is moved along the optical axis closer to the focus of the laser, the transverse range over which it is coupled into the fibre becomes very small and this small range can be measured on the stage micrometers and approximately halved to get close to the centre of the fibre where the core is. When any light is coupled into the core, it is immediately clear and easy to optimise as shown in Figure 5.1b.

As discussed, the fibre used is slightly multimode and the initial alignment shows this. It was not possible to achieve single mode coupling by moving the fibre alone. The fibre was aligned to achieve the highest contrast between the core and the cladding and then the angle of the beam on the coupling aspheric and hence the fibre was changed by tweaking both the horizontal and vertical alignment of the dichroic mirror immediately before the aspheric. This very small adjustment in angle along with a final tweak of the fibre position made single mode coupling possible as shown in Figure 5.1c. This alignment procedure, once developed, was the standard procedure used for all fibres for various experiments.

With good coupling achieved, the camera was replaced by a Gentec-EO UP19K-15S-H5-D0 power meter to measure the output from the fibre. This meter has a monitor unit that can be connected to many different detectors that can measure power or energy over different ranges and different wavelengths. The power meter detector used is a thermopile that can measure up to 15 W of CW power with a wavelength ranging from 0.19 to 20 μm and was used for all subsequent power measurements in this chapter.

With the seed switched on, the pump laser, which had been roughly aligned in the same manner as the seed, was used at a very low power to give a small amount of amplification. The decoupling aspheric was then adjusted to maximise the output power. The optimum pump coupling can be found in this way as when the coupling is maximised, there will be the maximum pumping, level of amplification and hence output power. The pump power was then slowly increased and the decoupling aspheric tweaked to optimise the pump coupling because as the output power increased the sensitivity to pump coupling did too. Particular care had to be taken in alignment of the pump laser as any misalignment at powers greater than several hundred milliwatts would cause the low index polymer outer cladding coating to catch fire. The fibre would then have to be cleaned and cleaved again.

The seed input power was measured just before the coupling aspheric to be 117.0 ± 0.2 mW as it was not possible to place the power meter between the aspheric and the fibre without moving the fibre and losing the alignment. The aspherics as well as the other lenses used are anti-reflection coated for this wavelength and are specified to have less than 0.6 %

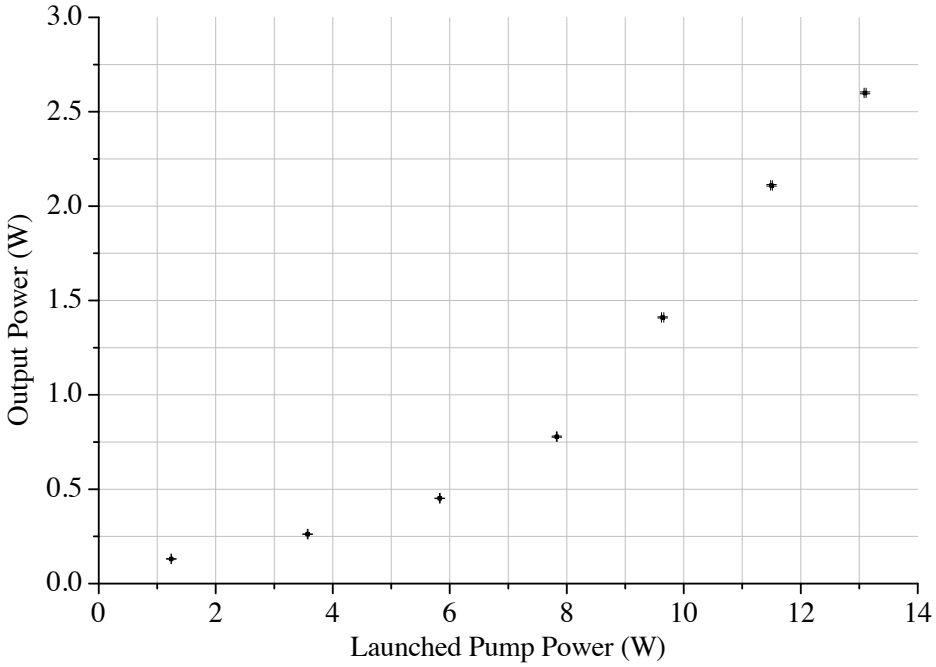

Figure 5.2: Output power from a 2.2 m Ytterbium-doped double-clad fibre amplifier seeded with the Fianium 1053 nm laser.

reflectance.

The pump laser power was increased by setting its power supply to successively higher drive currents. At each setting, the system was allowed to settle as the the output power and wavelength of the pump vary with its temperature which must be allowed to settle after being changed. Once the output power of the amplifier was found to have settled to a constant value, the output power was measured using the power meter placed in the beam reflected from the dichroic at the decoupling end. Putting the power meter directly at the output of the fibre would block in the incoming pump beam and there would be no amplification. The power meter was set to take 10 samples per second for 60 seconds, after which a statistical summary of the measurement is displayed. As well as the amplified output power, the input pump power was measured by placing the power meter before the decoupling aspheric and repeating the same measurement procedure with the power meter. These measurements are plotted in Figure 5.2.

This shows an initially gradual and almost linear increase with a sharp increase around 7 W of launched pump power, which proceeds to increase linearly again but with a greater

slope. This shape of little increase followed by a linearly increasing section is to be expected as the amplifier overcomes threshold. Below threshold, the fibre is not transparent throughout its length because of the quasi-three-level nature of Ytterbium. The initial data point with 1.24 W of launched pump power has only 131 ± 0.5 mW of output power which is only marginally greater than the 117.0 ± 0.2 mW entering the fibre. However, as the pump power increases, the fibre becomes transparent and the gain increases. No roll-off and hence saturation was observed. Although specified at 20 W, the pump laser produced a maximum output power of 14.5 W at its maximum rated drive current of 40 A.

The portion of the data that appeared to be linear was fitted to a linear model as shown in Figure 5.3. The slope efficiency from this fit is shown to be 35 ± 1 % which is lower than the published literature. The maximum gain expressed in decibels is 13.46 ± 0.01 dB which given the 2.2 m length of the fibre is 5.95 ± 0.01 dBm^{-1}. This is lower than published results at this wavelength which has shown that up to 14 dBm^{-1} is theoretically possible [37]. This is most likely due to the to poor coupling of either the seed or the pump as well as the pump wavelength shown in spectra recorded in the same experiment and discussed later in Section 5.3.

The seed input power of ∼ 117 mW is below the saturation power of this fibre of 0.454 W which was calculated using the cross sections in Figure 4.6, the fibre specifications and Equation 4.10. It is however, close to the saturation level so the gain will be lower than the small-signal gain which explains the discrepancy between the measured result and that of published literature.

5.2 Spectra

To fully characterise the output of the amplifier the spectra of the output was recorded at the same time as the power measurements using an Ocean Optics fibre coupled spectrometer. The spectrometer has a fibre as the input and this is usually directed towards the source to be measured. A piece of white card was used to scatter the light to avoid any coupling

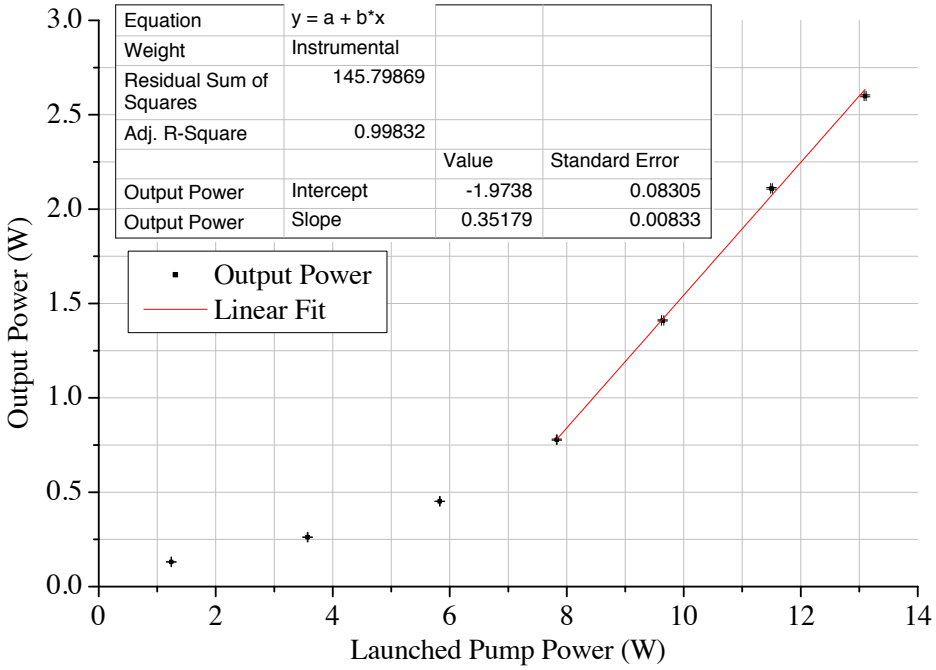

Figure 5.3: Partial fit of the data in Figure 5.2.

dependence of the fibre.

Figure 5.4 shows the spectra for each of the measurements in Figure 5.2. These are labelled by the current of the pump laser. As the current increases the output power increases as well. Each spectrum was recorded under the same conditions with the same integration time so each of the spectra are comparable.

As the pump laser current increases, and therefore the gain, the seed centred at 1053 nm can be seen to increase accordingly. However, at high levels of gain, a second broader peak emerges centred around 1037 nm appears and eventually becomes comparable to the amplified seed. This is the broad emission of ASE and is understandable as the emission cross section at 1037 nm is almost double that than at 1053 nm as shown in Figure 4.6 on Page 96.

Figure 5.5 shows the spectra at the highest level of amplification with the sharp peak of the amplified peak to the right and the broad peak of the ASE to the left. To compare the fraction of the power in each part of the spectrum, each part was background subtracted and integrated in Origin graph plotting software. The cut-off between each part was chosen

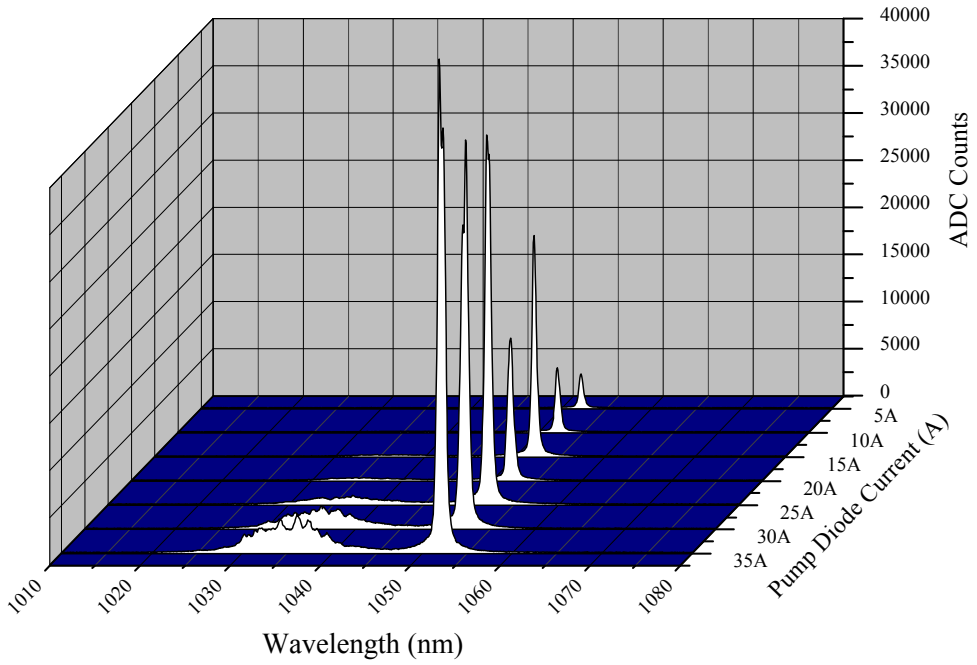

Figure 5.4: Spectra of the output beam showing significant ASE at high levels of amplification.

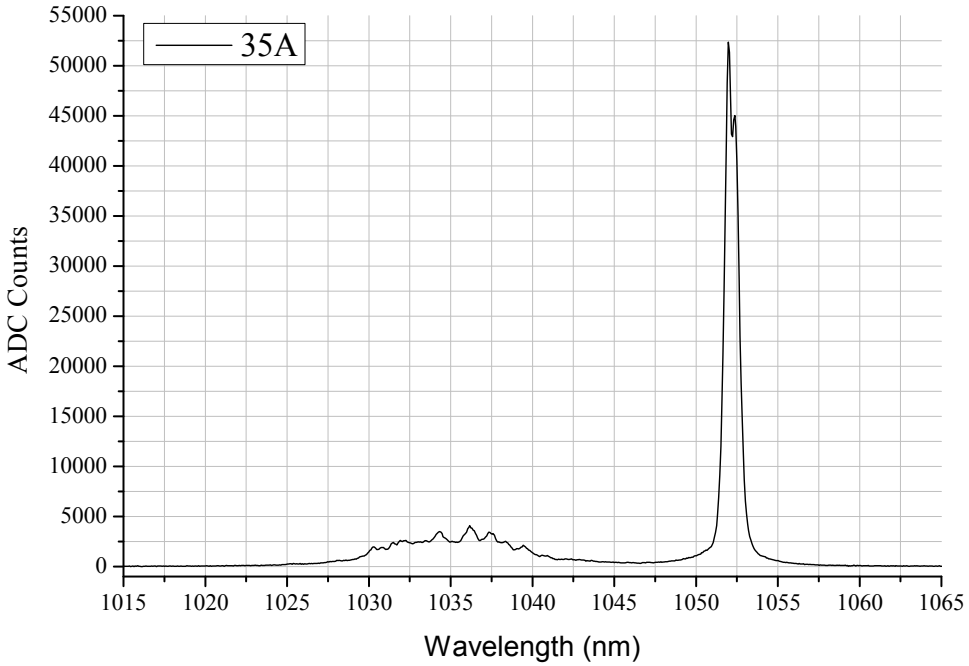

Figure 5.5: Single spectra of the output beam at the maximum pump level showing both ASE and the amplified seed.

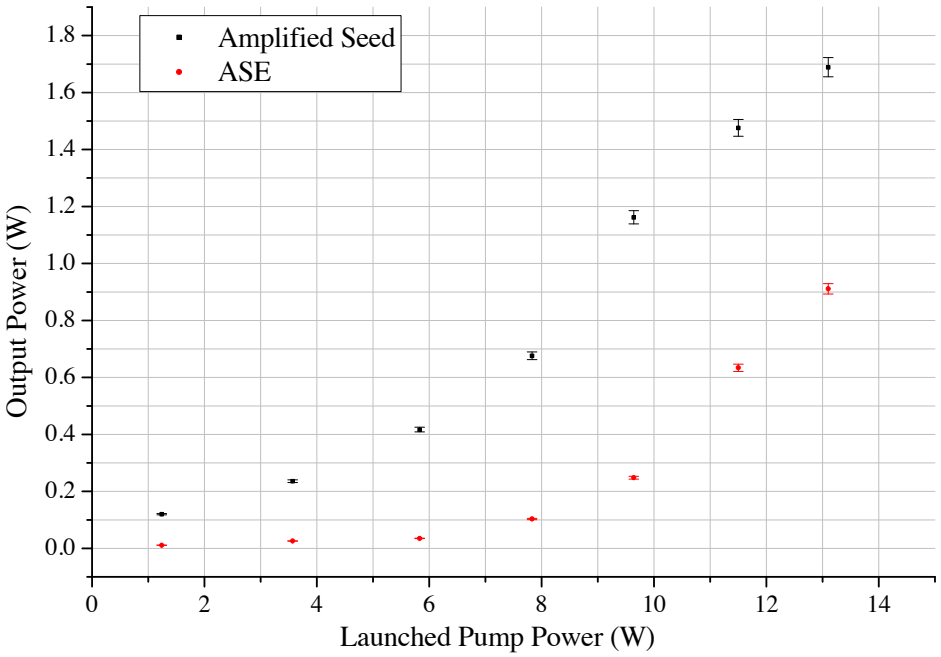

Figure 5.6: Power of the ASE and the amplified seed found by subdividing the output power by the area of the corresponding spectral areas.

to be 1047 nm as the spectra seemed flattest at this point.

This was repeated for all of the spectra where ASE was visible. Equation 5.1 and Equation 5.2 were used to proportion the output power between the amplified seed and the ASE which is shown in Figure 5.6.

$$P_{ASE} = P_{Output}\left(\frac{Area_{ASE}}{Area_{ASE} + Area_{Seed}}\right) \tag{5.1}$$

$$P_{Seed} = P_{Output}\left(\frac{Area_{Seed}}{Area_{ASE} + Area_{Seed}}\right) \tag{5.2}$$

The proportions of each power measurement of the total are shown in Figure 5.7 for the gain of amplifier in decibels calculated in reference to the input seed power of 117.0 ± 0.2 mW. This shows that at low gain, there is little ASE but as the pump power increases, the proportion of ASE also gradually increases.

The spectra shown in Figure 5.5 is at the highest gain with the pump laser at a current

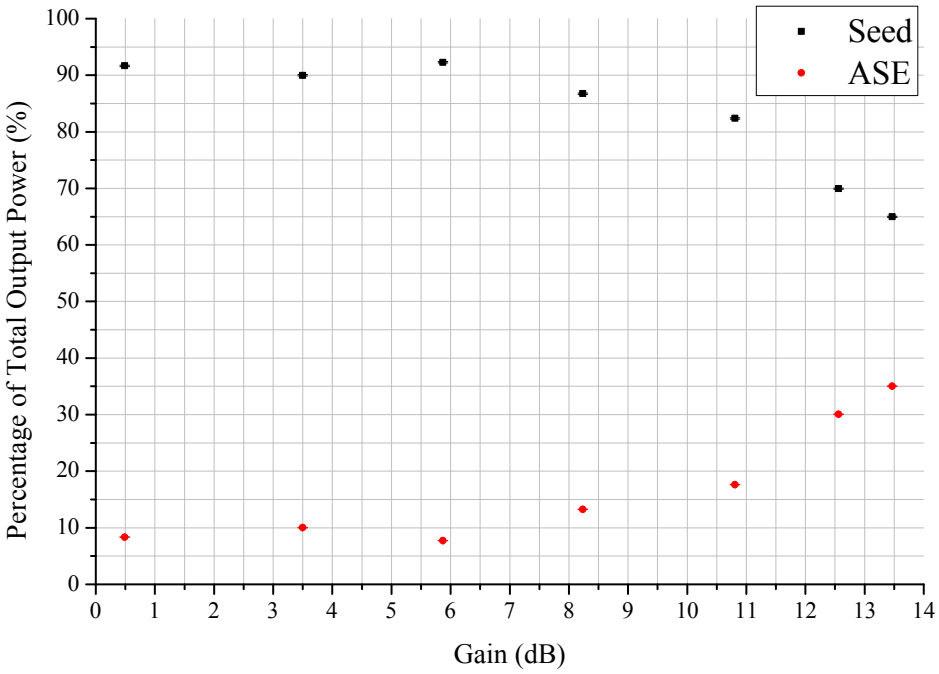

Figure 5.7: Proportions of both ASE and amplified seed in the total output power.

of 35.0 A. In this instance, the ASE accounts for 35 $\pm$ 1 % of the total output power from the amplifier as scaled by the spectral area. As mentioned in Section 4.5, this is CW light and will not contribute significantly to the pulse energy and hence the purpose of the laser. It is therefore undesirable and should be avoided. It also indicates that there is a significant proportion of the pump energy not being used to amplify the seed pulses and therefore lowering the overall efficiency.

The spectra recorded have shown that this amplifier is even less efficient than thought with only the output power measurements alone as this did not highlight the difference between the QCW amplified pulses and the CW ASE that is useless for the purposes of laser-wire. Taking into account both the power and the spectral measurements the amplifier demonstrated a lower optical to optical efficiency than expected for a Ytterbium-doped fibre amplifier.

However, this is not unexpected as the Fianium laser used as a seed for these experiments has a wavelength of 1053 nm which is relatively far from the emission peak of Ytterbium at 1037 nm and hence the maximum gain. The Fianium laser was one of the highest power

QCW fibre based lasers commercially available at the time of purchase and although it contains a Ytterbium-based fibre amplifier inside, the initial oscillator is a bulk laser with a wavelength of 1053 nm. Although less efficient, using a seed at a wavelength not at the emission peak of Ytterbium at 1037 nm was useful as it highlighted the likely possibility of ASE in a high gain amplifier.

Using a seed at the peak of the Ytterbium emission should result in a higher gain, more energy extracted from the fibre amplifier and therefore less ASE. Although the 35 % slope efficiency is lower than expected, it is high for a single pass amplifier of comparable bulk laser technology [51].

5.3 Pump Laser Spectra

To fully characterise the amplifier, spectra of the pump laser were recorded using the same spectrometer. The peak of the absorption cross section at 976 nm has a full width at half of the maximum (FWHM) of 8 nm [52]. The spectrum from the pump laser is expected to be of a similar width as is typical of a diode laser [53]. If the central wavelength of the pump laser spectrum shifts or is not overlapped with the absorption peak of Ytterbium at 976 nm, the pump absorption will decrease strongly and the efficiency of the fibre amplifier will decrease significantly.

Figure 5.8 shows the centroid wavelength of the spectra for various drive currents of the pump laser. This was found by integrating the peak using Origin software which provided the centroid. This shows that as the current increases, the centroid wavelength shifts over 10 nm across the range of pump currents. The centroid was used instead of simply the peak of the spectrum because the spectrum was not smooth.

Figure 5.9 shows spectra at the highest and lowest operating currents of 40 A and 5 A, respectively. The two spectra are clearly separated, demonstrating the considerable shift over operating currents. Furthermore, the spectrum recorded at 40 A is broader than the spectrum recorded at 5 A, however the 5 A spectra is just above the operating threshold of

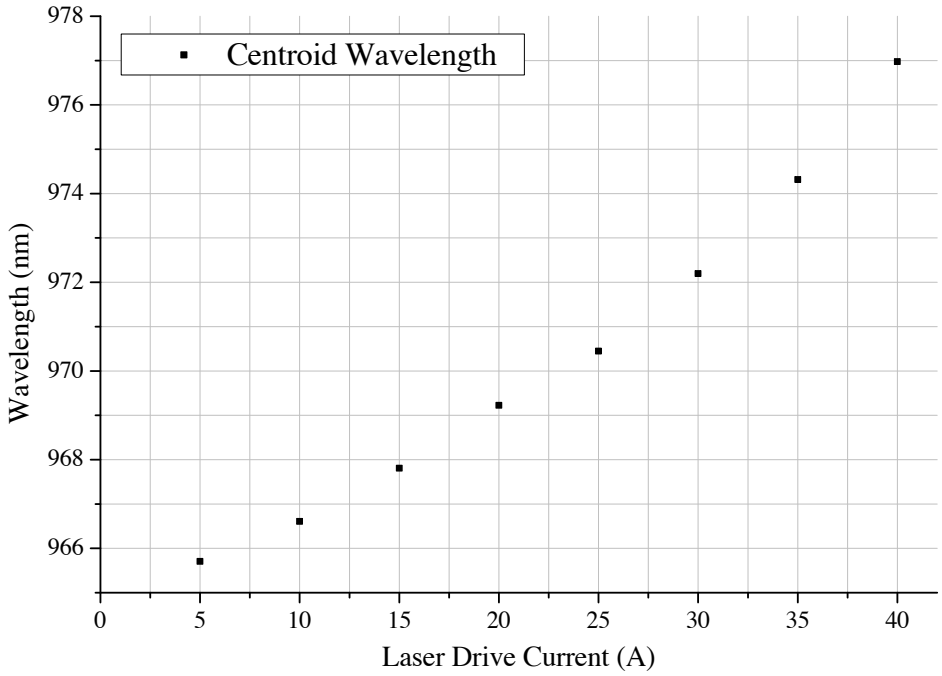

Figure 5.8: Central wavelength of pump laser plotted against drive current.

the laser.

The diode laser was specified to operate at 976 nm and does so at its maximum current. It is expected that the diode laser wavelength will shift to longer wavelengths as the bandgap in the semiconductor is temperature dependent and despite active cooling of the diode laser, the temperature of the diode laser does increase at higher operation currents, which causes the centre wavelength to shift [54]. Typically, the temperature-dependent wavelength shift of a diode laser is 0.3 nmK^{-1} [54]. Whist wavelength stabilisation is possible, it often results in a considerably lower output power [55, 54].

5.4 Amplification with 1037 nm Seed

To investigate the full potential of fibre amplifiers, another laser source detailed in greater detail in Section 6.2 was used that had a wavelength at the peak of Ytterbium emission at 1037 nm. It was built by a company called Amplitude Systemes and will be referred to as the AS laser for the remainder of this thesis. It is specified to produce pulses with an energy

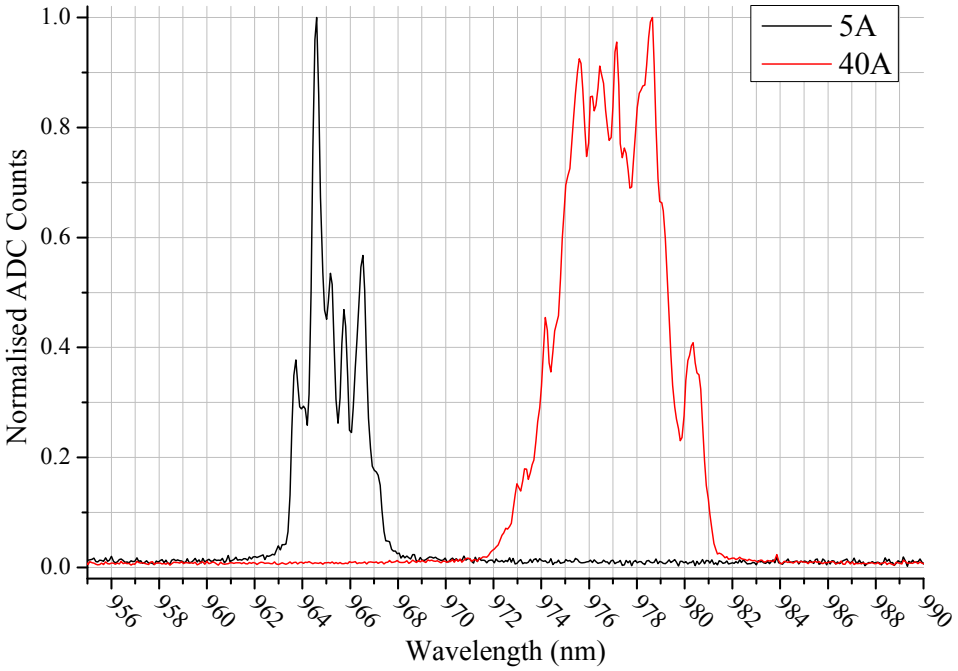

Figure 5.9: Spectra of Jenoptik diode laser at 5 A and 40 A demonstrating the spectral shift from its lowest and highest operating currents.

of up to 1 μJ at 6.49 MHz.

Using a seed with a wavelength at the emission peak it was expected that the greater levels of amplification and efficiency could be achieved with the same fibre and pump laser.

The fibre amplifier was set up as before in Figure 4.11 using the same 2.2 m Nufern PLMA-YDF-15/130 double-clad Ytterbium-doped fibre but with the AS laser as the seed. Additionally, an f = 500 mm plano-convex lens was used for L1 for optimal coupling which was repeated as before. The power of the seed measured before the coupling aspheric was 1.01 $\pm$ 0.01 W. The output power was measured as before by placing the power meter in the reflected beam from the dichroic at the decoupling end. The input pump power was measured in front of the decoupling aspheric. The drive current of the pump diode was recorded and the measurements are shown in Figure 5.10.

The most linear part of the data, representing when the amplifier had overcome threshold, was fitted as shown in Figure 5.10. A significantly higher slope efficiency of 82.0 $\pm$ 0.1 % was achieved. This is much closer to other published results from Ytterbium-doped fibre amplifiers [41].

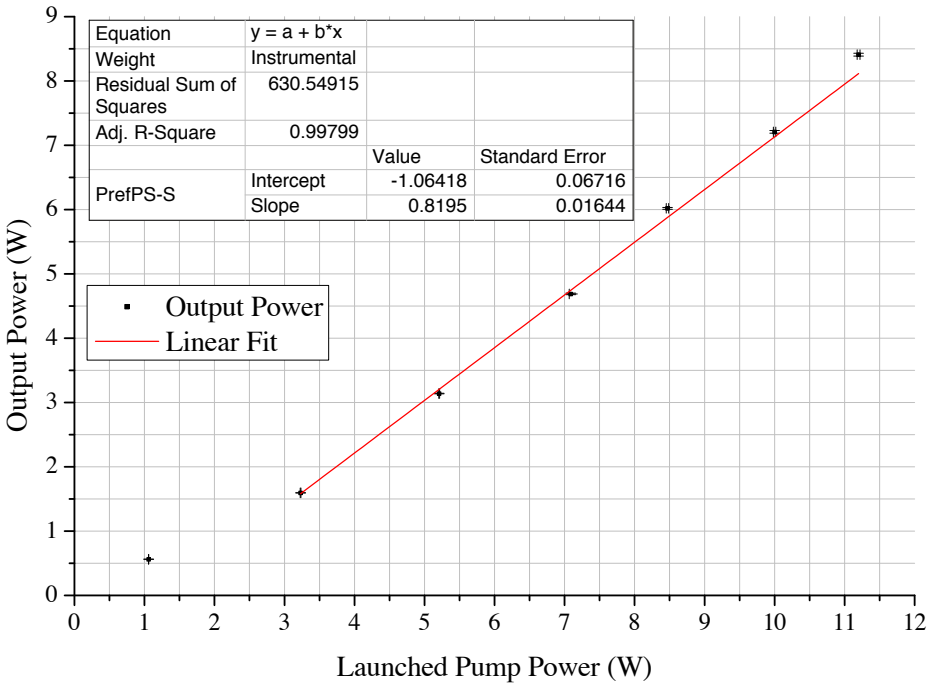

Figure 5.10: Output power from a 3 m Ytterbium-doped double-clad fibre amplifier with a 1037 nm seed.

The maximum amplified output was measured to be 8.41 ± 0.01 W, which corresponds to an overall gain of 9.21 ± 0.01 dB. This in turn corresponds to a gain of 4.19 ± 0.01 dBm^{-1}. Although the wavelength of the seed is at the peak of the Ytterbium emission at 1037 nm, the approximately 1 W input power is above the saturation power of the fibre of 0.454 W, and so the gain will not be as high as the small-signal gain experienced by the Fianium seed with ∼ 117 mW input power [42].

This is however a useful investigation of the amplification achievable in a final power amplifier stage as discussed in Section 4.5 where the gain is lower, but more energy is extracted from the fibre.

As discovered in previous amplification experiments, ASE may be present as part of the measured output power which is detrimental to the amplification of the seed and not useful for the purpose of laser-wire. Spectra were recorded in a similar manner as mentioned in Section 5.2 to ascertain if ASE was present in the output of the amplifier.

The spectrum of the seed as well as the amplified output are shown in Figure 5.11. The spectrum of the output was recorded at the highest level of gain with the pump laser at

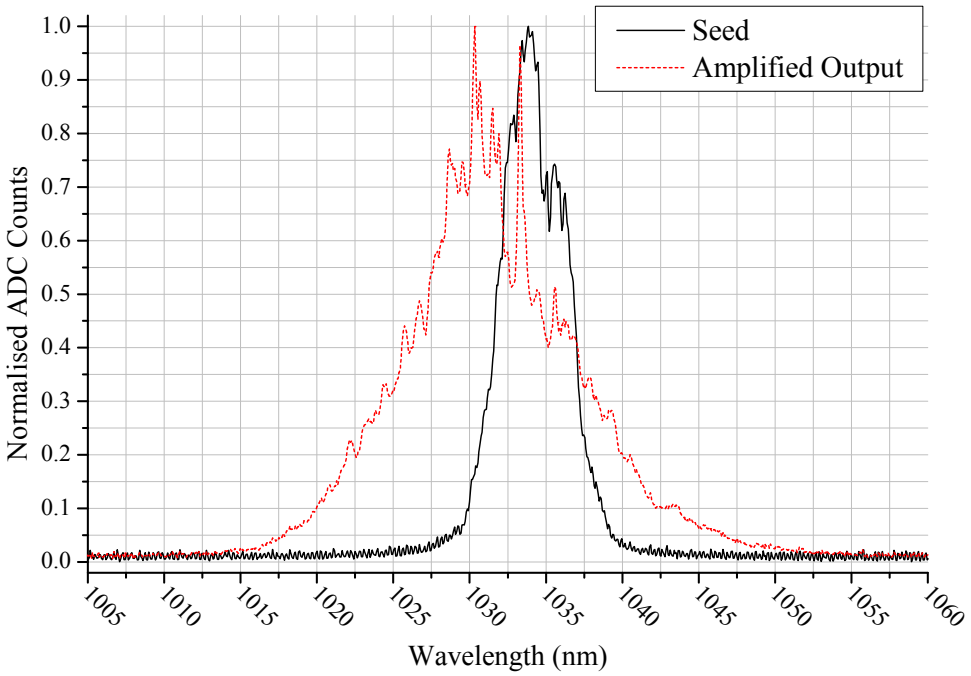

Figure 5.11: Spectra of both the AS laser before and after amplification in a 2.2 m Ytterbium-doped double-clad fibre.

35 A. It is not possible to tell directly whether there is any ASE present as there was in Figure 5.5, as any ASE that is present would be at the same wavelength as the amplified seed.

However, it can be clearly seen that the output spectra is considerably wider than that of the input seed. Using Equation 4.15 and the nonlinear γ calculated in Section 4.6 of 1.4 $\times 10^{-3}$ $\mathrm{m^{-1}W^{-1}}$, the peak power at which nonlinearities are expected to become evident in this fibre is 325 W. At 8.41 $\pm$ 0.01 W, the average pulse energy is $\sim$ 1.3 μJ. The pulses from the AS laser in these experiments are approximately 250 ps long and therefore the peak power of the 1.3 μJ pulses is 5.3 kW, which is higher than the predicted peak power at which nonlinearities will become evident.

However, the spectrum does not have a similar shape to Figure 4.7 with the flat top indicative of self-phase modulation. As the pulses are being amplified, the peak power will be lower at the coupling end of the fibre and as it increases along the fibre length, so will the degree of nonlinearities introduced. Therefore, it is likely that the spectrum in Figure 5.11 is a combination of both nonlinear effects and some ASE. Because the ASE and the amplified

seed have the same wavelength, it was not possible to ascertain if any ASE is present or what fraction it is of the output power.

It should also be noted that there is a shift in the centroid wavelength during amplification. The spectra of the AS laser ('seed') in Figure 5.11 has a centroid at 1034.2nm ± 0.5 nm where as the spectrum of the amplified output has a centroid at 1031.5 ± 0.5 nm. The centroid will shift towards the local maximum of the emission spectrum of the Ytterbium. The emission peak at this wavelength is broad with a smooth peak and the exact peak may be different depending on the host that the Ytterbium has been doped into.

The AS laser has a bulk laser oscillator consisting of a Ytterbium doped gain media. The wavelength of the oscillator is slightly different from the emission peak of Ytterbium doped fibres because of the different host structure. For the purposes of laser-wire, a shift of a few nanometres in the centroid wavelength is acceptable as peak will still be suitable for the design and coatings of the final focus lens. The spectral width is more important though as a spectrum wider than the 2 nm bandwidth of the lens will cause chromatic aberrations to increase the focus spot size and hence lower the laser-wire resolution.

To ascertain the proportion of ASE present in the amplified output, another method was devised based on a different parameter: polarisation. Given the ASE originates from spontaneous emission, it should be randomly polarised. In contrast, the seed has a high degree of linear polarisation and it should therefore be possible to separate the two based on polarisation.

To verify this hypothesis, the polarisation of the seed, ASE from an unseeded amplifier and the amplified output were measured.

5.5 Input Polarisation

Before the polarisation of the output could be characterised, the degree of linear polarisation of both seed lasers had to be measured. Both were measured, as the Fianium laser could

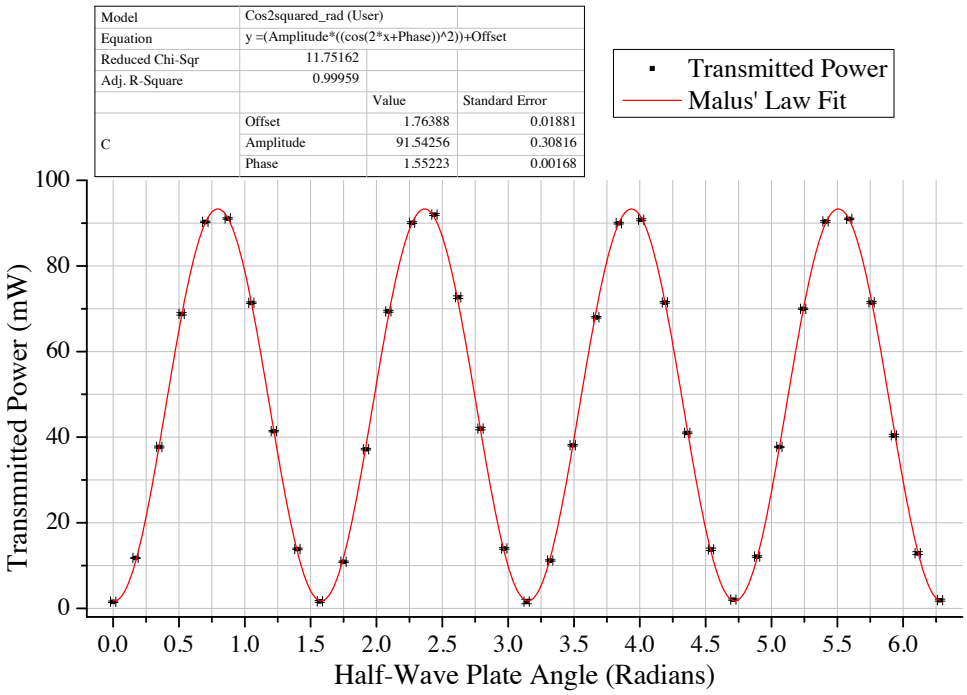

Figure 5.12: Transmitted power of Fianium laser through a rotated half-wave plate and a polarising beam splitter.

be used to ascertain the correlation between the output polarisation and the proportion of ASE by using the established method of spectral integration used in Section 5.2.

The degree of linear polarisation of both the Fianium laser and the AS laser were measured by measuring the transmitted power through a half-wave plate and a polarising beam splitter. The data was fitted to Equation 4.7 using Origin software and in the case of the Fianium laser is shown in Figure 5.12. A and O were found to be 91.54 $\pm$ 0.08 mW and 1.76 $\pm$ 0.02 mW respectively for the Fianium laser. Using Equation 4.8, this corresponds to a degree of linear polarisation of 96.6 $\pm$ 1.1 %.

The degree of linear polarisation of the AS laser was measured in a similar fashion with A and O found to be 591.23 $\pm$ 0.35 mW and 1.23 $\pm$ 0.02 mW respectively. Again, using Equation 4.8 this corresponds to a degree of linear polarisation of $99.59^{+0.41}_{-3.19}$ %.

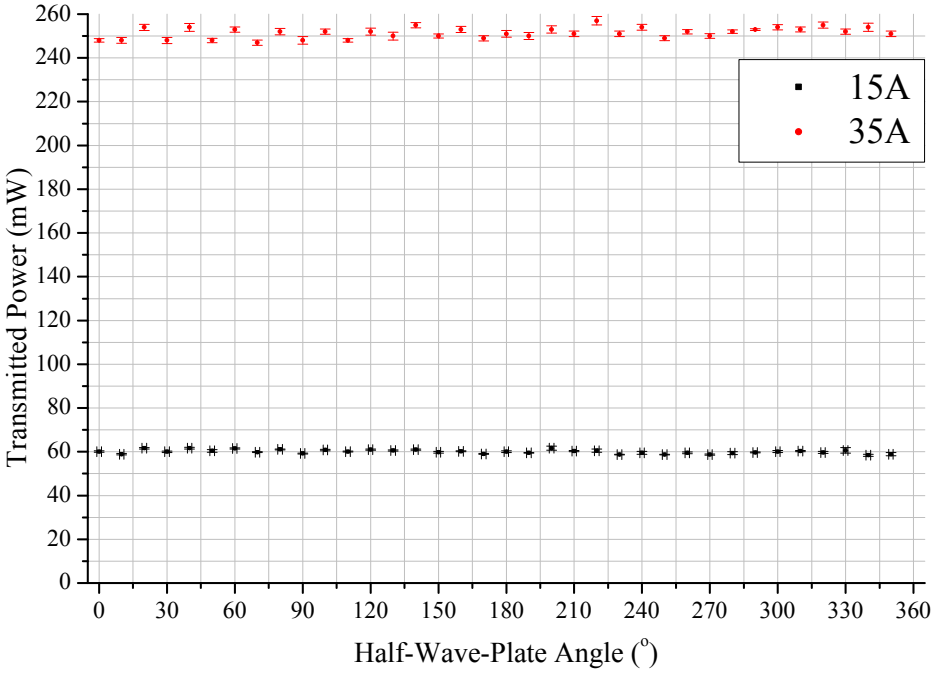

Figure 5.13: Transmitted ASE power through rotated polarising beam splitter.

5.6 ASE Characterisation by Polarisation

To measure the polarisation of ASE, ASE alone was generated in the double-clad polarisation-maintaining fibre used in Section 5.1 by pumping it without a seed. Figure 5.13 shows the measured transmitted power of ASE through a half-wave plate and PBS for two settings of the pump laser current producing different output powers of ASE.

There is no discernible variation in the transmitted power in either case that would correspond to a $cos^2 2\theta$ function indicative of any degree of linear polarisation. The measured output power of the ASE before the half-wave plate and the polarising beam splitter was 128.0 ± 0.4 mW and 535 ± 1 mW for the 15 A and 35 A settings of the pump laser, respectively. The transmitted power on average is approximately half of the incident power, again confirming a randomly polarised source.

To ensure the absence of circular polarisation, a quarter-wave plate was added before the half-wave plate and rotated to various angles without any change to the observed transmission function. This experiment shows that the ASE indeed has a random polarisation and that in principle the method of using the polarisation of the output from an amplifier to

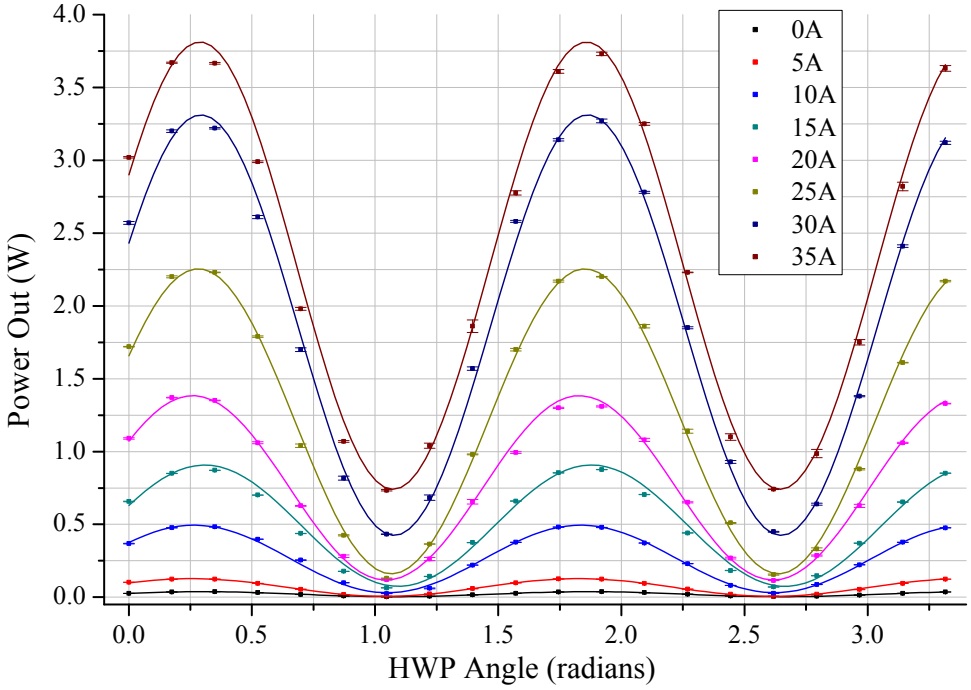

Figure 5.14: Polarisation measurements of Fianium laser amplified in 3 m Ytterbium-doped double-clad fibre for various pump laser currents and hence levels of amplification.

identify the proportion of ASE is feasible.

As mentioned in Section 5.5, the Fianium can be used for comparison because the amount of ASE can be measured using spectral integration. For this reason, the Fianium laser was used as a seed and amplified as before in Section 5.1 for various settings of the pump laser and hence levels of amplification.

At each pump laser current setting, the degree of linear polarisation of the output was measured and the spectra recorded. Power measurements of the input pump power and the total output power were also made. Figure 5.14 shows the data recorded for the degree of linear polarisation at each setting. As the pump laser current increases so does the pump power and hence the amplified output power which is shown by the amplitude of the modulation increasing. Additionally, it can also be seen that the offset of the modulation also increases at higher currents.

Each of the polarisation data sets was fitted to Equation 4.7 using Origin software and the parameters used to calculate the degree of linear polarisation using Equation 4.8 .

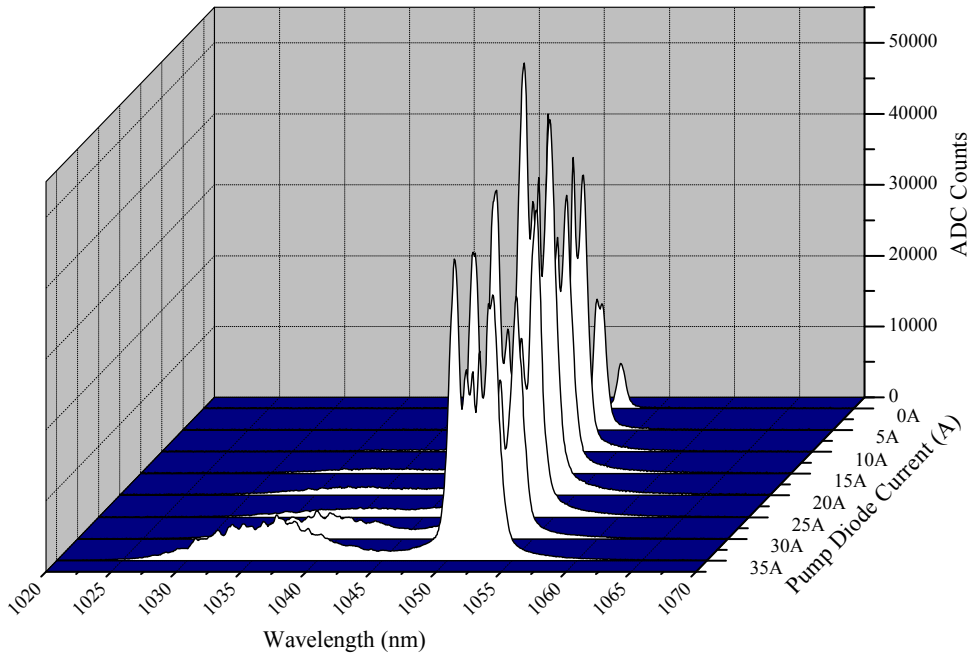

Figure 5.15: Spectra of Fianium laser amplified in 3 m Ytterbium-doped double-clad fibre for various pump laser currents and hence levels of amplification.

The spectra that were simultaneously recorded are shown in Figure 5.15 for the corresponding pump laser currents. As before, the spectra recorded were integrated from 1020 nm to 1047 nm and 1047 nm to 1060 nm for the ASE and the amplified seed respectively. The proportion of ASE was calculated from the spectra using Equation 5.1.

The proportion of ASE from both spectral integration and degree of linear polarisation are shown in Figure 5.16. These do not overlap within their uncertainties but do show a strong correlation and are closer at higher pumping levels where there is a higher level of ASE. The apparent proportion of ASE at 0 W of launched pump power from the polarisation method is anomalously high as with no pump present and only the transmitted seed there can be no ASE. However, the degree of linear polarisation was not the same as the measurement of the Fianium laser alone (96.6 $\pm$ 0.6 %). This is because not all of the seed light is coupled into the fibre core and the light that isn't coupled into the core is carried in the inner cladding. The inner cladding does not maintain the polarisation of the light in it and therefore any light not coupled into the core will have a scrambled polarisation upon exiting the fibre. Figure 5.16 assumes that all of the unpolarised light is due to ASE, which is not true in the

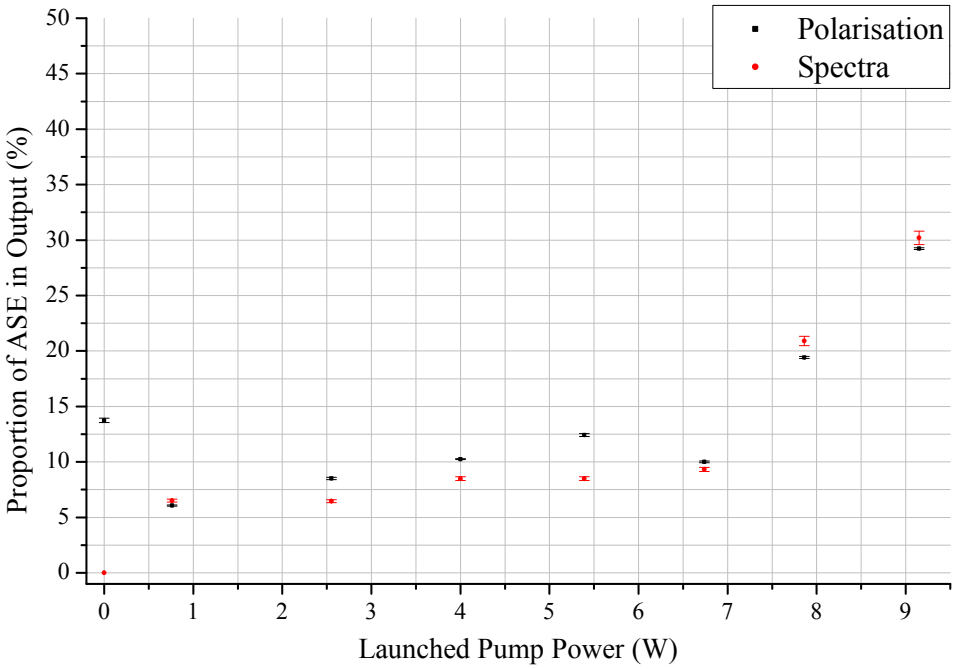

Figure 5.16: Proportion of ASE in the output of a 3 m Ytterbium-doped double-clad fibre amplifier.

absence of pump hence the difference between the two methods.

This light in the inner cladding experiences no significant amplification, as the inner cladding is undoped and is therefore a very small fraction of the total output under normal amplification. Indeed, at low levels of amplification, the fraction of the output that is unpolarised is considerably less. The same uncoupled light is still present in the inner cladding, but is small in comparison to the amplified output.

Additionally, the proportion of amplified seed and ASE may not be accurate from the integration of the spectra as there is not a clear separation between the amplified seed and the ASE where the spectrum returns to 0. Furthermore, it is assumed that the unpolarised component of the output power is entirely due to ASE and that the degree of linear polarisation in the amplified output has remained the same as the seed.

It is clear that whilst neither method may provide a highly accurate measurement of the ASE both are able to show when ASE is present and to what degree. The polarisation method is comparable to the spectral integration method and therefore can be used to ascertain if ASE is present when the wavelength of the seed is similar to that of the ASE.

This method was therefore used to measure the amount of ASE present with the AS laser (1037 nm) amplified in the same fibre. It was noted from Figure 5.11 that the spectrum of the output was wider than before and would perhaps indicate ASE but that it could not be identified directly from the spectra. Repeating this experiment, ASE was found to be 11.3 ± 0.5 % of the total output power at the highest gain with the pump set to 35 A.

This proportion of ASE is significantly lower than the approximately 30 % of ASE in the amplified output of the Fianium laser under the same pump conditions in the same fibre as to be expected with the higher emission cross-section at 1037 nm and higher input power. At ∼ 11 %, it is however a significant fraction of the output power and demonstrates that ASE must be considered when designing a high power fibre laser system.

An amplifier longer than this one would provide a greater output power but also a greater proportion of ASE as well. Therefore, an amplifier of this length or shorter would better minimise ASE.

5.7 Evidence of Nonlinearites

When recording the spectra in Section 5.6, it was noticed that the spectra showed clear signs of self-phase modulation in the amplified seed. The spectrum recorded at the highest gain is shown in Figure 5.17.

Here, the broad emission peak of ASE can be seen to the left and the amplified seed to the right. The spectrum of the seed is wider than that of any of the amplified seed spectra in previous spectra (Figure 5.4 for example) and has a flat top with pointed edges. This is indicative of self-phase modulation (SPM) as described Section 4.6.

This is understandable when considering the nonlinear length scale as defined in Equation 4.15. For this fibre γ is 1.4×10^{-3} $\mathrm{m^{-1}W^{-1}}$. The output power from the spectra in Figure 5.17 is 4.85 ± 0.02 W. Looking at Figure 5.16, ∼ 30 % of this output power is ASE meaning that the power of the amplified seed is 3.40 ± 0.02 W. Given the 32.5 MHz

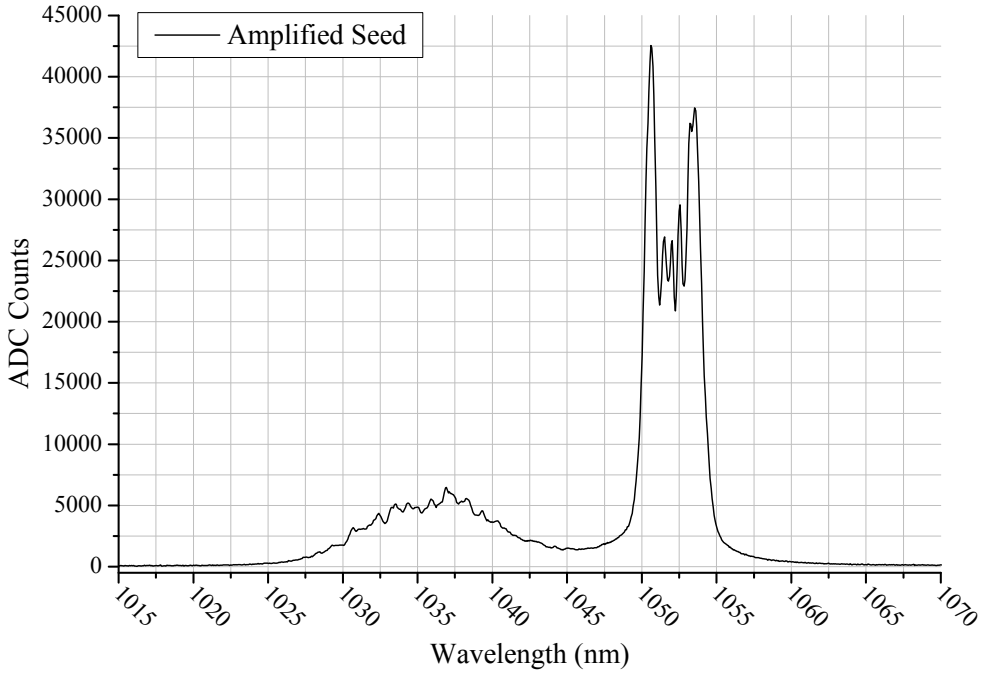

Figure 5.17: Spectra of amplified Fianium laser showing a broad ASE peak to the left and the amplified seed to the right. The amplified seed has a flat top with pointed edges indicitave of self-phase modulation.

frequency of the Fianium laser, the average pulse energy is 104.6 ± 0.1 nJ. The Fianium laser is specified to have a pulse length of 5 ps which means the peak power of the output pulses is 20.9 kW. Similar to the amplification of the AS laser, the peak power is above the 325 W peak power calculated in Section 5.4 above which nonlinearites are expected.

It should be noted that the total output power of 4.85 ± 0.02 W is greater than the previously achieved maximum output of 2.38 ± 0.02 W, which is due to improved coupling of both the seed and the pump laser. Using the spectral integration method in both cases to subtract the power of the ASE, the amplified seed power was previously 1.37 ± 0.02 W and is now 3.40 ± 0.02 W.

5.8 Characterisation of Spatial Quality

To investigate the spatial quality of the output from a fibre amplifier, several spatial quality measurements were made using various types of fibre. These consisted of measuring the M^2

of the beam using a long focal length lens, a camera to measure the size of the beam and a computer controlled stage to move the camera.

For all of the following experiments, a WinCamD camera was used to measure the transverse intensity profile of the laser beam. The software supplied provides 4σ diameters compliant with the ISO 11146 standard mentioned in Section 4.7 in Chapter 4.

The camera was mounted on a Phisik Instrument M500 stage with micrometre position resolution. The stage and camera were controlled using a LabView VI (program) that would determine, given the approximate focus point and sample number required, the positions the stage should move to and the number of camera images to record. The DataRay software supplied with the camera allowed for a maximum of 64 images to be saved in one file.

The LabView VI made to record the data was developed over some time with extra methods written to account for inconsistencies in the supplied DataRay software as well as various verification routines ensuring that area of the CCD being recorded and the exposure were correct. A further LabView VI was also written to analyse the files recorded by the camera in its proprietary file format to provide the ISO 11146 compliant 4σ diameters for each of the 64 recorded images of the laser beam.

Before the lens was placed in the experiment, the camera was translated along the full length of the stage whilst observing the laser beam on the computer. Using the two mirrors before the beam path to the camera, the direction of the laser beam was corrected so that it didn't detectably move on the camera image across the full length of the stage. This ensured the laser beam was parallel to the stage and the table.

With the camera on the stage as far away as it could go from the lens (~ 3 m), the lens was then inserted into the laser beam and positioned so that the beam was at the same place on the camera. The orientation of the lens was aligned to be perpendicular to the incident laser beam. This care in alignment ensured that the laser beam passed perpendicularly through the lens as well as through the centre. If this were not the case, aberrations would be introduced and increase the M^2 measurement. Furthermore, the lens used for the following

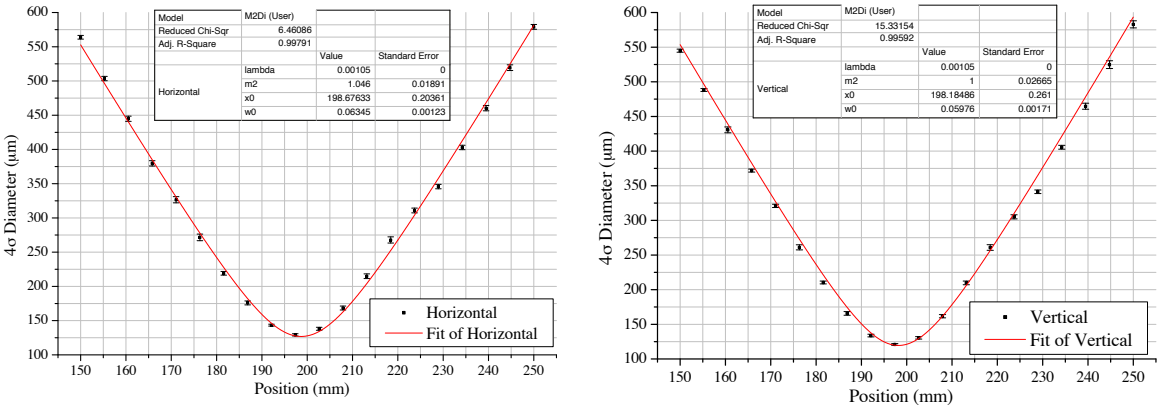

(a) Horizontal M^2 (b) Vertical M^2

Figure 5.18: M^2 measurement of the Fianium laser in free space in both horizontal and vertical dimensions.

experiments was a plano-convex lens of diameter 50.8 mm with a focal length of f = 1 m. To minimise any spherical aberration the flat side was placed facing towards the focus [26].

A further consideration when building the experiment was to ensure that the focus of the laser beam covered a minimum of 10 camera pixels to ensure a sufficient resolution. The pixels are specified at 6.7 μm square and therefore the beam must be at least 67 μm in diameter at the focus.

Before measuring the output spatial quality of the fibre amplifiers, M^2 measurements of both the Fianium laser and the AS laser were made for reference. These were made using a series of mirrors to direct the beam directly from the source to the setup shown in Figure 4.10. Neutral density filters were used to adjust the intensity of the laser beam to within the dynamic range of the camera at each position.

Figure 5.18 shows the free space M^2 measurement of the Fianium laser in both the horizontal (a) and vertical (b) dimensions. From the fits to the model the M^2 was measured to be 1.05 $\pm$ 0.2 and 1.00 $\pm$ 0.03 in the horizontal and vertical respectively. This excellent spatial quality is to be expected as the laser was purchased with the specification of $M^2 < 1.1$.

A similar measurement of the AS laser was made and is shown in Figure 5.19. The M^2 was measured to be 1.09 $\pm$ 0.02 and 1.39 $\pm$ 0.02 in the horizontal and vertical respectively.

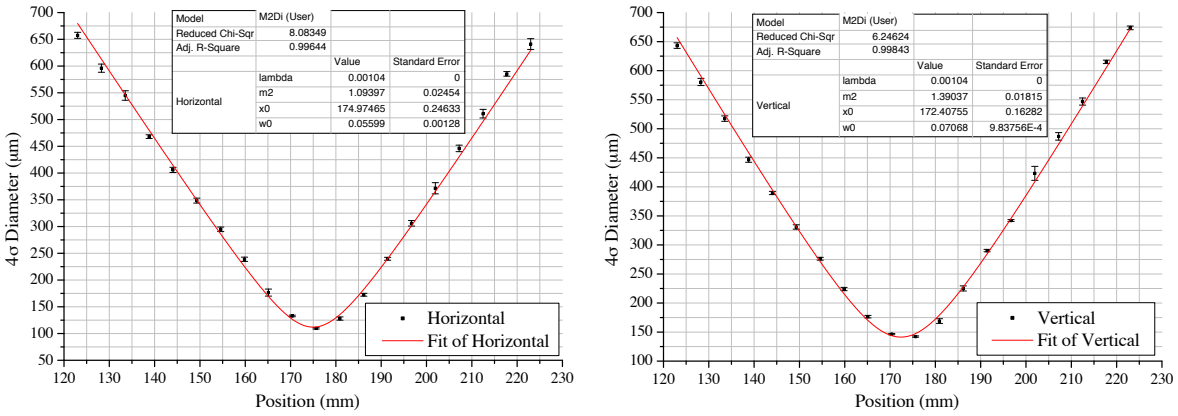

(a) Horizontal M^2 (b) Vertical M^2

Figure 5.19: M^2 measurement of the AS laser in free space in both horizontal and vertical dimensions.

This laser was specified to have an $M^2 < 1.1$ so whilst the horizontal is within specification, the vertical is outside it. Although this system is mentioned in greater detail Chapter 6, it has been realigned and modified since its purchase for maintenance. These changes may have caused the M^2 to increase in the vertical dimension.

To begin the investigation of the spatial quality from fibre amplifiers, the Fianium laser was amplified in a 2 m long Thorlabs SM-YDF-7/210 Ytterbium-doped double-clad single mode fibre that was not polarisation maintaining. This fibre is single mode for both the 1037 nm and 1053 nm wavelengths of each source. The core was 7 μm and the inner cladding was 210 μm.

The fibre was replaced in the experimental setup used for previous amplification measurements in Section 5.1. Despite the previously successful alignment procedure for slightly multimode fibres, only poor coupling of the seed into the core was achieved in the single mode fibre. This was due to the very small size of the core. The coupling aspheric was then replaced by a microscope objective consisting of a series of chromatically corrected lenses mounted in a metal cylinder. Such a microscope objective was used as they are specifically designed to image small objects. In reverse, this could be used to focus a laser to a small spot.

Using the microscope objective, acceptable coupling of a similar level to the large slightly

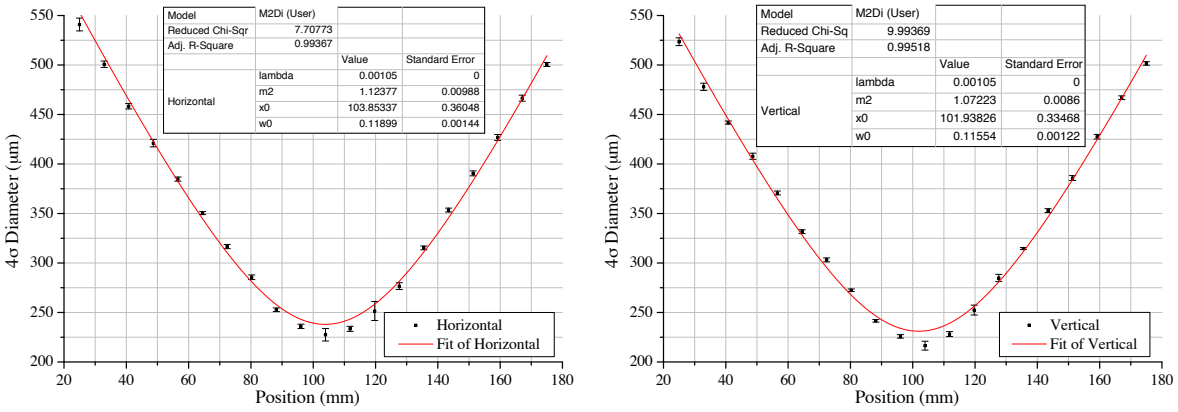

(a) Horizontal M^2 (b) Vertical M^2

Figure 5.20: M^2 measurement of the Fianium laser amplified in a single-mode fibre for both the horizontal and vertical dimensions.

multimode fibres was achieved used for previous amplification experiments.

The Fianium was measured at the coupling aspheric to be 108.1 ± 0.1 mW. The Jenoptik pump laser was set to 5.0 A and measured to be 1.35 ± 0.0 1 W at the decoupling aspheric. The output power was measured to be 45.2 ± 0.1 mW. The M^2 of the output beam was measured as before and the results are shown in Figure 5.20.

The M^2 was measured to be 1.12 ± 0.01 and 1.07 ± 0.01 in the horizontal and vertical dimensions respectively. This is marginally worse than the free space measurement, but is still an acceptably good spatial quality beam. It should also be noted that the amplification was poor in the single mode fibre and also more so at the wavelength of the Fianium as opposed to the AS laser. Because of this, there wasn't a great a contrast between the amplified core and the uncoupled light in the inner cladding, which may have increased the value of M^2 measurement.

The AS laser was then coupled into the the single mode fibre with the same setup as before. The long focal length lens before the coupling aspheric, L1, was changed to a f = 1 m plano convex lens. The microscope objective was again found to the be only way to achieve acceptable coupling into the fibre. The power of the AS laser was then reduced for comparability using a half-wave plate and a polarising beam splitter. It was measured to be 127.0 ± 0.1 mW before the coupling aspheric. The Jenoptik pump laser was again set to

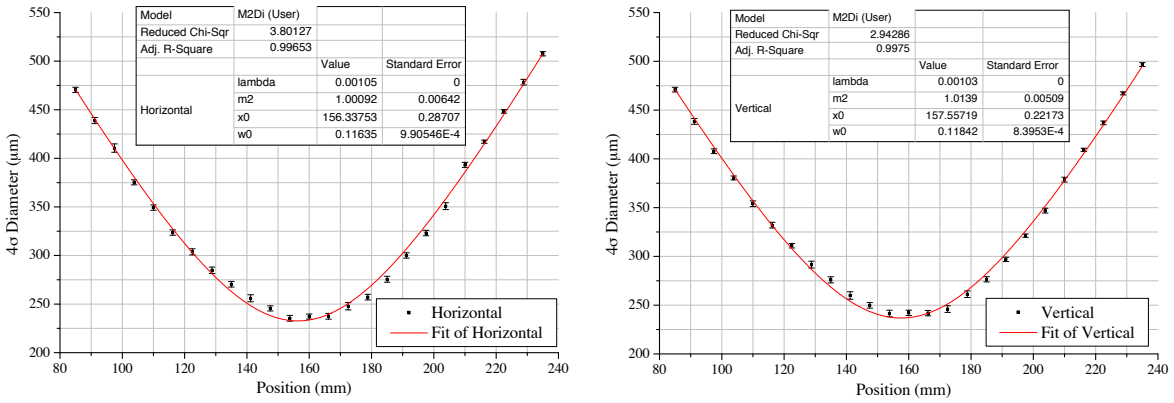

(a) Horizontal M^2 (b) Vertical M^2

Figure 5.21: M^2 measurement of the AS laser amplified in a single-mode fibre for both the horizontal and vertical dimensions.

5 A and measured to be 1.34 ± 0.01 W at the decoupling aspheric and the amplified output was measured to be 89.6 ± 0.1 mW.

The results of the M^2 measurement are shown in Figure 5.21 where the horizontal and vertical M^2 was measured to be 1.00 ± 0.01 and 1.01 ± 0.01 respectively.

This clearly shows that despite the poor M^2 of the AS laser in the vertical dimension, the fibre only supports the lowest order mode which as expected has an M^2 value close to 1. The fibre amplifier effectively acts as a spatial filter and the only consequence of the higher input M^2 is poorer coupling efficiency.

It can also be seen that the gain is poor compared to results detailed in Section 5.1. Due to the small core size of 7 μm, there is over 4 times less dopant per unit length than the multimode fibres used in that section and hence less pump absorption and lower gain. Due to the lower pump absorption, a high proportion of the pump light was transmitted through the fibre and the pump could not be operated at high power without risking damage to the microscope objective by the transmitted pump light. It was for these reasons that single mode fibre was not used during the amplification experiments in Section 5.1.

Furthermore, the output power would drop over a period of about an hour. This was found to increase with the level of amplification and is assumed to be due to thermal expansion of the fibre coating affecting the coupling into the small diameter core. Even a small

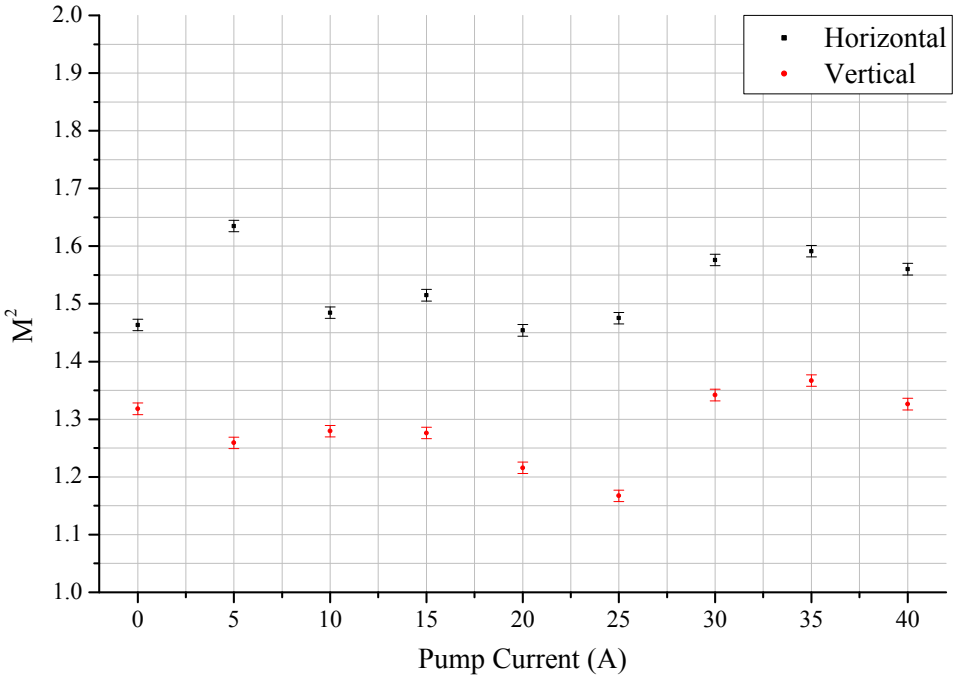

Figure 5.22: M^2 measurements of the AS laser in a multimode fibre for various levels of amplification.

movement of the coupling optics caused a lower coupling efficiency and hence a lower output, whereas the multimode fibres with a larger core were less susceptible to this.

Given the more desirable amplification in a multi-mode fibre and the fact that given careful coupling they can be made to operate in the lowest order mode, M^2 measurements of the AS laser in the 3 m Nufern PLMA-YDF-15/130 double-clad Ytterbium-doped fibre mentioned in Section 5.1. This fibre is slightly multimode and the coupling was adjusted until an image of a single mode was achieved when imaging the end of the fibre.

M^2 measurements were made at various pump laser currents and hence levels of amplification to ascertain if the spatial quality is dependent on the level of amplification. Figure 5.22 shows the M^2 measurements made for both horiztonal and vertical dimensions.

The M^2 is on average, 1.53 ± 0.6 and 1.29 ± 0.6 in the horizontal and vertical respectively. These values are higher than are desirable but are comparable to the free space measurement of the AS laser as shown in Figure 5.19 however, it was noticed that with the high pump powers required to provide a range of different gains, the coupling alignment of the fibre would change over time again, due to thermal effects.

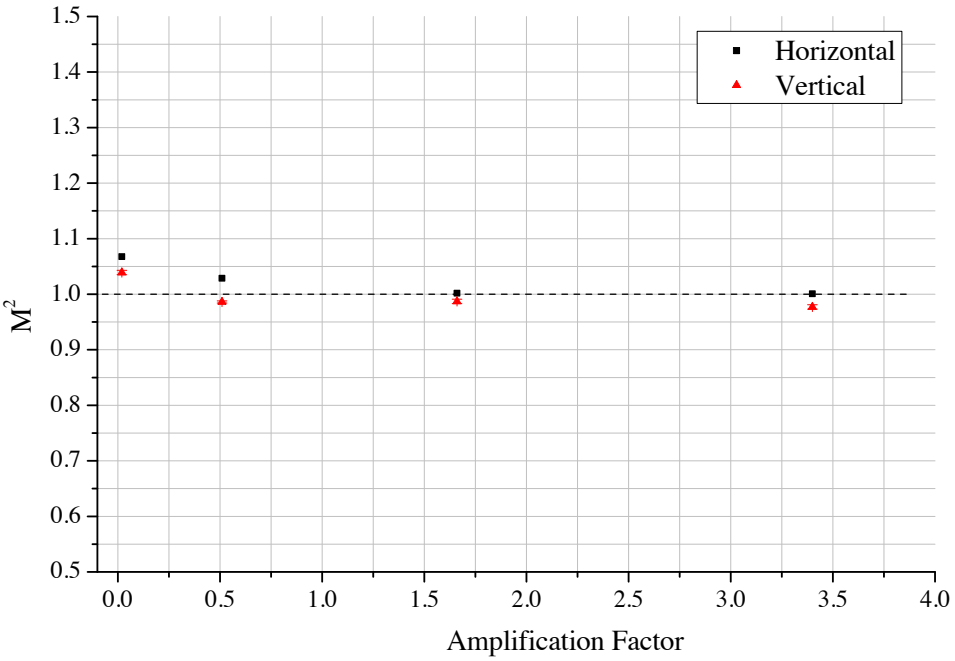

Figure 5.23: M^2 measurements of the AS laser in a single-mode fibre for various levels of amplification.

Because the measurements for this experiment took 8 hours, slight adjustments had to be made to the coupling to achieve the best M^2 measurement at each level of amplification. This is shown in Figure 5.19 by the variation in M^2 between different measurements.

In these measurements, the vertical M^2 is lower than the horizontal which contradicts the free-space measurement of the AS laser in Figure 5.19. This is because the fibre rotates throughout its length and so the output is rotated with respect to the input.

The same experiment was repeated using the single mode fibre that was used for the M^2 measurement shown in Figure 5.21 and the results are shown in Figure 5.23.

Here, an M^2 measurement of the unamplified transmitted beam was made which as expected has an amplification factor close to 0 due to the absorption by the Ytterbium dopant. As the amplification factor increases, the M^2 remains close to 1 in both dimensions. The M^2 measurement made of the unamplified transmitted beam is slightly higher due to the uncoupled light carried in the inner cladding affecting the measurement.

From these experiments it is clear that the spatial quality of the output from a fibre

amplifier does not depend on the level of amplification. This is a significant advantage over bulk laser systems which often produce lower spatial quality output with high pumping levels and therefore higher levels of amplification.

5.9 Summary

Experiments in this chapter have shown that Ytterbium-doped fibre amplifiers can achieve high efficiencies and high power with a high degree of linear polarisation. Care must be taken however, to design the amplifier to avoid ASE that can be detrimental to the amplification of the seed. A system consisting of several amplifiers with a modest gain would appear to be the best method to achieve a high output power.

The relatively high slope efficiencies demonstrated indicate that at high powers less thermal management will be necessary as less of the pump power is wasted as heat. Indeed, despite dealing with tens of Watts of power, not active cooling of the fibre was required. The pump laser was also air cooled which considerably simplified the system. A comparable solid-state laser system would require water cooling for the gain medium and generally require greater thermal management due to a lower efficiency.

Single and multimode fibres would appear to show two different dependencies. Single mode fibres demonstrate a strong dependency of output power on coupling alignment due to the small core size with no difference in output spatial quality as only the lowest order mode is supported. On the other hand, multimode fibres with a larger core diameter do not show such a strong dependency of output power on alignment. However, they do have a lower spatial quality output as compared to the single mode fibres and this was found to be sensitive to the alignment and coupling of the beam into and out of the fibre.

Nonlinearities were found in amplification experiments in multimode fibre with a peak power of approximately 20 kW which is substantially lower than the required 50 MW of laser-wire. However, it should be noted that the pulses in this case were 5 ps long, which for a given energy increases the peak power of the pulse. Whilst techniques exist to stretch and

compress pulses before and after amplification respectively, a peak power of 50 MW would not be achievable without the presence of nonlinearities in a fibre of a similar diameter to the multimode fibres in this chapter.

Ideally, a fibre with a larger core would allow a higher peak power pulse to be achieved without a significant introduction of nonlinearities. Such a fibre exists and is called a photonic crystal fibre. This type of fibre and its suitability for a laser for laser-wire are discussed in Chapter 6.

Chapter 6

A Fibre Laser for Laser-wire

In Chapter 5 it was found that nonlinearites limit the scalability of fibre lasers. Here, a laser system for a laser-wire is developed using a photonic crystal fibre (PCF), which has the much larger core needed to simultaneously reach higher pulse energies and avoid nonlinearities. The choice of architecture is discussed in Section 6.2 and a burst amplification regime that takes advantage of the required low duty cycle of the laser system is described in Section 6.3. A technique used to make the necessary high repetition rate pulse energy measurements is described in Section 6.4 and the full characterisation of the laser output is described in the remaining sections.

6.1 Photonic Crystal Fibre

As mentioned in Chapter 5, a fibre with a larger core that is ideally single mode would be required to reach the high pulse energies as well as have the excellent spatial quality necessary for a laser-wire. The number of modes a fibre can support depends on its V number. To remain single mode as the core diameter increases, the difference in refractive index between the core and the inner-cladding must reduce. Differences in refractive index smaller than 1 in 10^{-3} are required to reach higher pulse energies than normally possible, which exceeds current manufacturing capabilities. This in turn limits the size of fibre core that will only support a single mode.

Larger mode areas can be achieved using a multimode fibre by coiling it. The higher order modes experience greater bending losses than the lowest order mode, filtering them

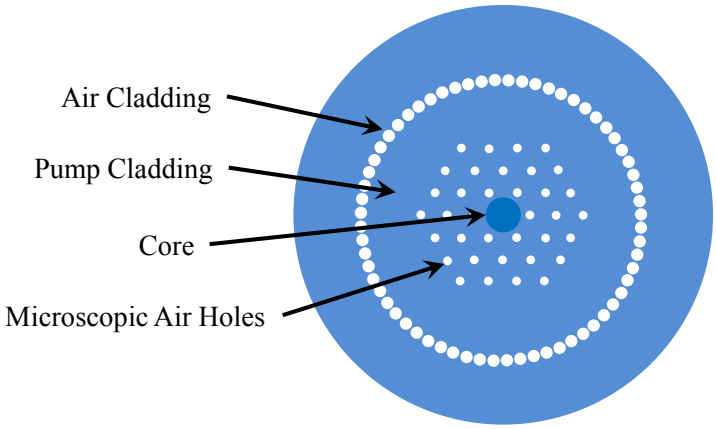

Figure 6.1: Schematic of a typical PCF with microscopic air holes to guide light in the doped core. A further series of air holes around the pump cladding provide a high numerical aperture to guide the pump light.

out. This results in higher spatial quality as well as higher output pulse energies due to the larger mode area [56].

However, a new type of fibre called photonic crystal fibre has recently become available [57] that offer a considerably larger fibre core and thus mode area whilst being single mode. These fibres differ from ordinary step-index fibres by guiding the light using a single piece of glass containing microscopic closely packed air holes as shown in Figure 6.1. The guiding mechanism is understood through an average refractive index model where the air holes lower the average refractive index over the area they are present [58].

This effect can be engineered to produce a very small difference in refractive index between the solid glass core and the micro-structured part of the fibre allowing the fibre to have a core up to 100 μm in diameter whilst being solely single mode. For the same intensity limits imposed by nonlinearities, this greatly increases the achievable pulse energy as well as providing excellent spatial quality.

The guiding of the light in the core is very weak due to the very small difference in refractive index between the core and the cladding in a PCF and so considerably greater bending losses are experienced [59]. To avoid this, PCFs with large core diameters are encased in a glass rod several millimetres in diameter to keep the fibre straight.

Although the structure is different from a normal step-index fibre, PCFs can be polarisation-

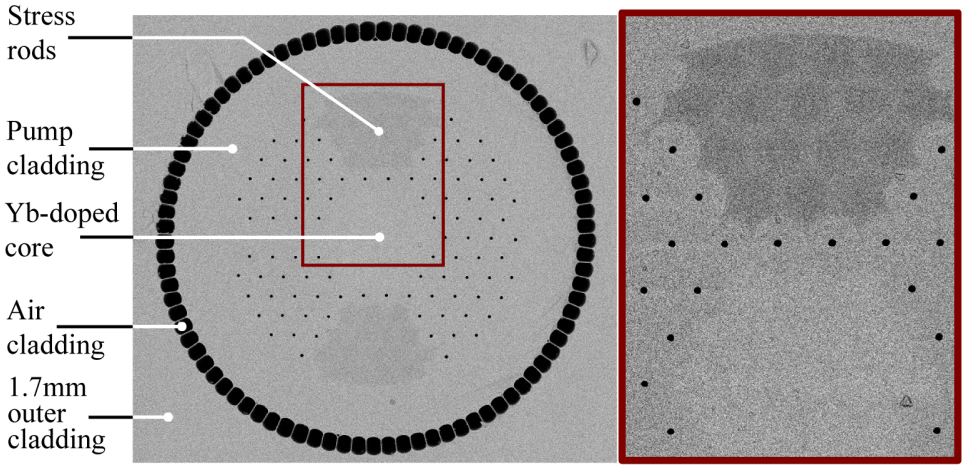

Figure 6.2: Cross-section of a photonic crystal fibre showing the core, pump cladding, guiding micro-structure and birefringence inducing stress-rods [61].

maintaining in a similar manner to step-index fibres. Like step-index fibres, they are constructed by heating and extruding a macroscopic 'preform'. In the case of a PCF, glass straws are packed in a hexagonal array before being extruded. To make a polarisation maintaining PCF, some of these straws are replaced with boron-doped silica straws which create the same mechanical stress-induced birefringence across the core when cooled after extrusion [60]. The air holes in the PCF are sealed at each end of the PCF to avoid contamination, which would affect their refractive index and hence the guiding properties of the fibre.

Figure 6.2 shows a photograph of a PCF with a doped core surrounded by air holes. The boron-doped stress rods are visible above and below the core. The dark ring around the air holes is the air cladding which gives the pump cladding (similar to the inner cladding in a step-index fibre) a high NA. This allows high power pump sources which often have poorer spatial quality to be used. The surrounding material outside of the air cladding is the macroscopic rod that supports the fibre and maintains its straightness.

Additionally, since such fibres are also designed for very high powers and pulsed operation, an end cap consisting of an unstructured cylinder of fused-silica can be fusion spliced to the end of the fibre, which allows the light exiting the fibre to expand. The intensity of the light at the end surface of fibre where damage is most likely to occur, is lower. This is done as the surface damage threshold of silica is typically 2 to 10 times lower than the damage threshold

of bulk silica [40, 62].

In a typical counter propagating geometry of pump and seed, one end experiences the high intensity of both the amplified seed output and the pump input and therefore it is common for only this end to be fitted with an end cap.

6.2 Chosen Laser Architecture

To build a fibre based laser for laser-wire it was decided to purchase a laser system with the highest commercially available pulse energy and then supplement it with a further amplifier using a PCF. Additionally, a frequency doubling stage would be added to increase the resolution of the laser-wire.

The laser purchased was the AS laser mentioned in Chapter 5, which is specified to produce 1 μJ pulses at 6.49 MHz with an $M^2 <$ 1.1. A master-oscillator-fibre-amplifier (MOFA) architecture using a bulk seed laser was used. In fibre oscillators the cavity length is typically tuned by thermally expanding the fibre or by stretching it mechanically, which can take a relatively long time [25]. Therefore, a bulk seed laser was chosen over a fibre based oscillator as it has a greater tuning range of $\pm$ 20 kHz and quicker tuning response.

To reach higher pulse energies in a series of fibre amplifiers without incurring nonlinearities and also maintaining a high spatial quality, a chirped pulse amplification (CPA) architecture was used. In CPA, the pulses are stretched temporally to lower the peak power in the fibre during amplification and then compressed to their original pulse length afterwards. The pulses are stretched and compressed using gratings that diffract the beam geometrically and the different spectral components therefore travel different geometrical paths before being recombined together again [63]. The stretching process introduces a linear frequency increase across the pulse or chirp, hence the name chirped pulse amplification.

In the case of the AS laser, the initially $<$ 1 ps long pulses are stretched to approximately 250 ps long, which lowers the peak power by a factor of 250. Consequently, for the same

intensity limit imposed by nonlinearities in a given fibre, the achievable pulse energy is 250 times greater. Given nonlinearities were observed with a peak power of approximately 20 kW in Chapter 5, this method would allow peak powers potentially over 1 MW after compression without incurring nonlinearities. Indeed, 1 μJ in a 1 ps pulse corresponds to 1 MW of peak power.

It should be noted that this laser system was the highest energy available at the time and involved considerable research in itself [64]. Whilst there were other fibre laser systems with comparably high pulse energies demonstrated at the time, they had a lower repetition rate of kilohertz.

The AS laser system also contains two modulators. Firstly, an acousto-optic modulator (AOM) reduces the 51.92 MHz pulse frequency of the seed oscillator to the specified 6.49 MHz by selecting every eighth pulse. This is the only practical option as an oscillator would need to have a 23.1 m long cavity to produce this relatively low repetition rate. Whilst this length could be folded many times within the laser enclosure, a shorter cavity would be less sensitive to misalignment and therefore be more stable over a long period of time. Additionally, the pulse repetition rate can be reduced with a modulator but not increased so using the modulator makes the laser system more flexible should the desired frequency change.

Secondly, an electro-optic modulator (EOM) after the amplifiers is able to modulate the output of the laser system to provide a burst of a desired number of pulses, again to match the bunch pattern of the accelerator. This can be used to make bursts of as few as 5 pulses up to a QCW beam.

There are two amplifiers in the AS laser system. The first increases the nanojoule pulses from the oscillator that are attenuated by the stretcher and the AOM cumulatively (by $\sim$ 50 % [64]), to $\sim$ 150 nJ. After this a second amplifier, which is separated from the first by an optical isolator, increases the pulse energy from 150 nJ to approximately 2 μJ. The EOM and compressor are placed after the amplifiers which each have $\sim$ 70 % transmission [64]. The AS laser is shown schematically in Figure 6.3.

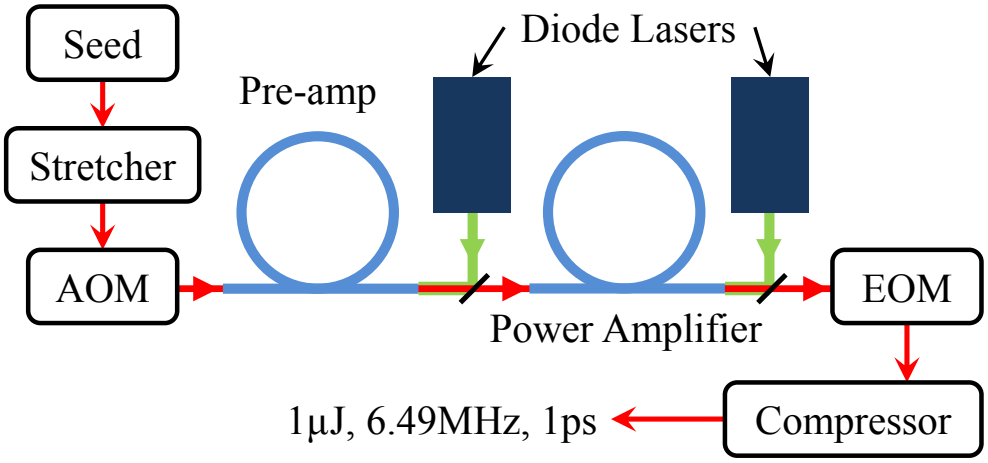

Figure 6.3: Schematic of the AS laser showning the order of the major components with two amplifiers (pre-amp and power amplifier) in series.

The AOM is locked to the seed oscillator using the signal from a photodiode in the stretcher that detects leakage from the diffraction grating. The EOM however, can be externally controlled with an appropriate digital voltage signal. Althought this system came with a compressor already installed, this was removed to leave the output pulses uncompressed for further amplification. The same compressor was then used after further amplification to recompress the pulses.

6.3 Burst Amplification

The laser pulse pattern required for laser-wire with short ($\sim$ 1ms) bursts of picosecond pulses at a high frequency, (6.49 MHz) is an unusual pattern to produce with a laser. Pulsed laser systems are most commonly designed to produce pulses at a constant frequency, be it megahertz or hertz depending on the architecture and pulse energy requirements.

Generally speaking, a lower frequency redistributes the available power amongst fewer pulses giving a higher energy per pulse. Building a laser system capable of the high energy pulses required for laser-wire that would work continuously would be unnecessary, inefficient and lead to a greater requirement for thermal management. Therefore, the amplification in the PCF after the AS laser was designed to match this pattern.

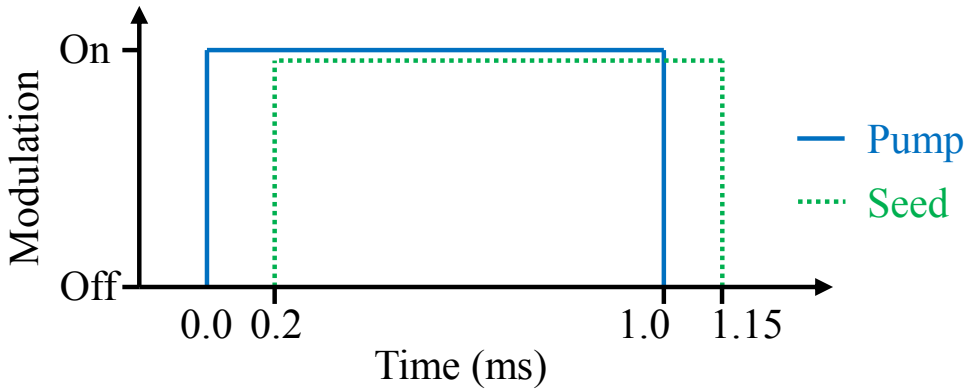

Figure 6.4: Timing diagram of the pump and seed lasers for optimal amplification.

6.3.1 Burst Seed Operation

Given the low duty cycle of 0.2 %, there was the potential to store energy in the fibre before the seed entered it and achieve a greater gain than the amplifier would in a steady-state. Energy could be stored in the fibre by turning on the pump laser before the seed as shown in Figure 6.4. The later arriving seed would experience a greater gain than the system could normally provide in steady state operation due to the build of excited lasing ions.

In this regime, there would be a large amount of stored energy initially which would be depleted as more seed pulses are amplified. The large amount of stored energy would present itself as a large gain which would then decrease as the high repetition rate seed pulses would extract gain at a greater rate than it would be replenished. This would lead to a train of pulses that decay in energy eventually reaching a steady-state regime where the energy extracted by each seed pulse is able to be replaced by the pump in the intervening time between pulses. Whilst this pulse train shape may not be suitable for a full train of pulses in a future accelerator, the initial pulses would be suitable. Ideally these would also be considerably higher than the steady-state level of amplification. This regime was envisioned as a stepping-stone to sustainable higher pulse energies. Additionally, it was expected that the seed could not be delayed more than the upper-state lifetime of Ytterbium which is 0.85 ms, as on this time scale electrons in the upper-state will spontaneously emit, which would lead to ASE.

A Stanford Research Systems DG645 Digital Delay Generator (DDG) was used to create

trigger signals to control both the pump and seed lasers. The DDG subdivided a photodiode signal from inside the AS laser by 3245000 to create a 2 Hz trigger with a stable phase relationship to the master oscillator. From this master trigger, other trigger pulses of variable voltage, length and delay were created for the pump and seed lasers.

6.3.2 Pump Burst Operation

With the intention of amplifying a 1 ms burst of seed pulses, the temporal nature of the pump source for the PCF must also be considered. In Chapter 5, a CW diode laser was used as diode lasers have a high electrical efficiency and high spectral density that can be centred on the absorption peak of Ytterbium at 976 nm. However, in Chapter 5 the diode laser was operated continuously and allowed to thermally stabilise. Diode lasers can be pulsed but, as experiments have shown in Section 5.3, the wavelength of the diode laser is sensitive to its temperature and therefore changes with operating current.

Pulsing a diode laser will cause its wavelength to sweep as its temperature changes with the large change in current. Because of the relatively narrow absorption peak of Ytterbium at 976 nm this could affect the gain in the amplifier throughout the pulse.

For this reason a special diode laser was developed in collaboration with Newport Spectra Physics who engineered a diode laser that would provide a stable wavelength over 5 ms pulses. The shortest burst length the laser could be safely operated at without incurring damage is 1 ms. The diode laser consists of two diode bars containing many stacked diode lasers with micro-fluidic cooling channels between the layers. The output of the diode laser is fibre coupled and an aspheric lens was used to recollimate the output. Because of the proprietary nature of this product, there is no further information on its design.

Because the diode laser cannot be operated for a burst shorter than 1 ms, the seed must also be present for such a time. If no seed is present, the large amount of energy stored in the fibre may results in self oscillation from the uncoated ends of the PCF leading to permanent damage. With the seed present, the pump energy is safely extracted avoiding this possible

catastrophic damage to the fibre.

A 1 ms burst is also longer than would required should the laser system be demonstrated at the ATF2 where a maximum of 5 pulses could be produced at this repetition rate [21].

6.4 High Repetition Rate Energy Measurements

From the discussion of burst amplification in Section 6.3, it is expected that the pulses from the burst amplification will have different energies and given the short duration of the burst transient effects may be present. It is therefore necessary to be able to measure individual pulse energies at megahertz repetition rates.

The maximum sample rate of any commercially available energy meter was found to be $\sim$ 10 kHz at the outset of this research, which is considerably lower than the 6.49 MHz of the pulses within the burst. Recent energy meters have now reached $\sim$ 100 kHz, but this is still insufficient.

Laser energy and power meters are typically based on three technologies. Firstly, thermopile detectors which are commonly used for power measurement. When the laser strikes the detector it heats one side of the detector and the difference in temperature between the two sides generates a voltage. This is proportional to the temperature difference and hence the laser power.

Secondly, pyroelectric detectors which produce a voltage across a crystal when the whole crystal changes from one temperature to another. Once the temperature of the crystal stops changing the voltage returns to 0 V. This makes pyroelectric detectors much more suited to measuring the energy of discrete pulses as opposed to a continuous beam.

Lastly, there are photodiode detectors that use photodiodes. Light striking the semiconductor junction in the photodiode generates a detectable current proportional to the intensity of the light. These can be used for both power and energy measurements. For energy measurements, $\sim$ 40 kHz was the highest measurement rate of any commercially

available detector found. To measure the pulses at 6.49 MHz within a seed burst, a method was devised that used a combination of both an energy measurement and photodiode traces.

Given that the electrical signal from the photodiode is proportional to the laser intensity, an electrical pulse representative of the laser pulse is generated. The photodiode has a resistance and capacitance that together gives it a maximum frequency response, or bandwidth, which places a limit on the shortest resolvable pulse. For shorter pulses, the photodiode acts as a low-pass filter producing an electrical signal longer than the laser pulse itself. To avoid this, a high speed photodiode was chosen that could resolve the $\sim$ 250 ps laser pulses.

To measure the electrical pulse generated by the photodiode, an oscilloscope was used to sample the voltage produced by the photodiode. However, no oscilloscope was available with a sufficient bandwidth to fully resolve the $\sim$ 250 ps laser pulses. An oscilloscope with a lower input bandwidth therefore acts as a low-pass filter and produces a pulse longer than that of the photodiode pulse. In this regime the peak of the voltage pulse displayed by the oscilloscope is proportional to the integral of the photodiode signal which in turn is proportional to the total energy of the laser pulse.

The peaks of the pulses observed on an oscilloscope can therefore be used to represent the energies of the incident laser pulses. A photodiode trace of all the pulses in the burst can then be used to subdivide the total burst energy amongst the voltage peaks. This is described in Equation 6.1.

$$E_{peak(i)} = \left(\frac{\sum_i V_i}{E_{total}} \right) V_{peak(i)} \tag{6.1}$$

Additionally, the semiconductor in a photodiode does not commonly have a linear response as this method assumes. However, many commercial photodiodes are engineered to have a linear response within a certain range and so the linearity of the photodiode used would need to be measured.

6.5 Preparative Characterisation

In the following sections results pertaining to the characterisation of the pump diode laser as well as the experiences in alignment and use of the high repetition rate pulse energy measurement technique are presented.

6.5.1 Pump Characterisation

The Newport Spectra Physics diode laser used is capable of a maximum output of 400 W. The power supply can be controlled by either manually using the current dial on the front for a CW output or by supplying a voltage signal from an external source. The power supply responds in an analogue fashion to the voltage with 1.6 V corresponding to the maximum output of the laser and 0 V to the laser being off.

A Tektronix AFG 3022B arbitrary function generator (AFG) was used to generate a rectangular voltage pulse 1 ms long of variable peak voltage which was triggered from a 3.5 V output pulse from the DDG. An f = 6 mm aspheric lens was used to collimate the output of the diode laser fibre. The energy meter was placed immediately after this and the burst energy recorded for various voltages as shown in Figure 6.5.

Above 250 mV, the burst energy increases linearly with the voltage of the control pulse. This portion of the data was fitted to a linear model and the gradient was found to be 0.29 ± 0.01 JV^{-1} with an offset of -0.0428 $\pm$ 0.0012 J.

To ascertain how the output power of the laser evolved with time a Thorlabs DET10C-M biased photodiode was used and its signal recorded on an oscilloscope. This data recorded for a 1 ms long pulse for various voltages is shown in Figure 6.6. In each case, 10 photodiode traces were averaged. It can be seen that as the voltage of the rectangular pulse from the AFG increases, the time taken for the laser output to reach its maximum decreases. With a 500 mV pulse the laser takes $\sim$500 μs to reach its maximum output whereas it takes $\sim$ 150 μs for a 1.5 V pulse. It can also be seen that as higher voltages and hence pump powers are

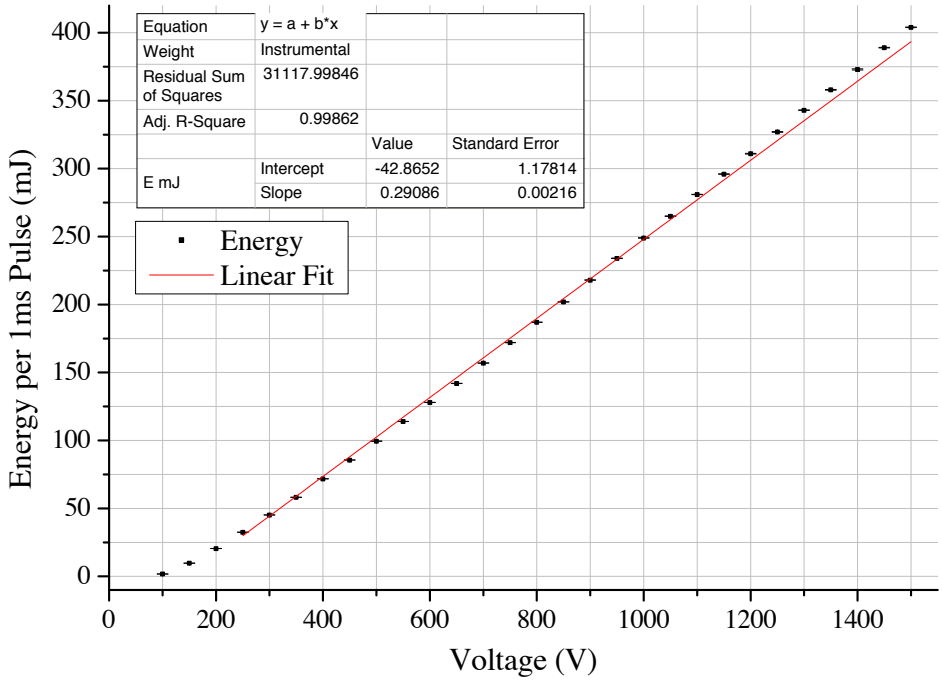

Figure 6.5: Output burst energy for a 1 ms pulse for various input pulse voltages.

used, the decay of the output takes longer to reach zero after the end of the 1 ms control pulse. In the case of the highest voltage of 1.5 V shown in Figure 6.6, it takes $\sim$ 300 μs before the diode laser output stops.

From the discussion of diode lasers in Subsection 6.3.2, the wavelength of the diode laser and its dependency on operating current and temperature are important. With the width of the absorption peak of Ytterbium at 976 nm being $\sim$ 6 nm FWHM, any shift in centre wavelength of a few nanometres will significantly affect the absorption and hence gain in an amplifier.

Firstly, the power dependence of the spectrum was investigated. As before, a piece of white card was set up in the beam path of the laser and the fibre of the spectrometer positioned to collect the scattered light from the card. For each voltage setting on the signal generator, 20 spectra were averaged. This data is shown in Figure 6.7. In all cases the burst was 1 ms long and the spectra were normalised to account for the different intensities. Origin software was used to integrate the spectra from 960 nm to 980 nm which provided their centroid wavelengths.

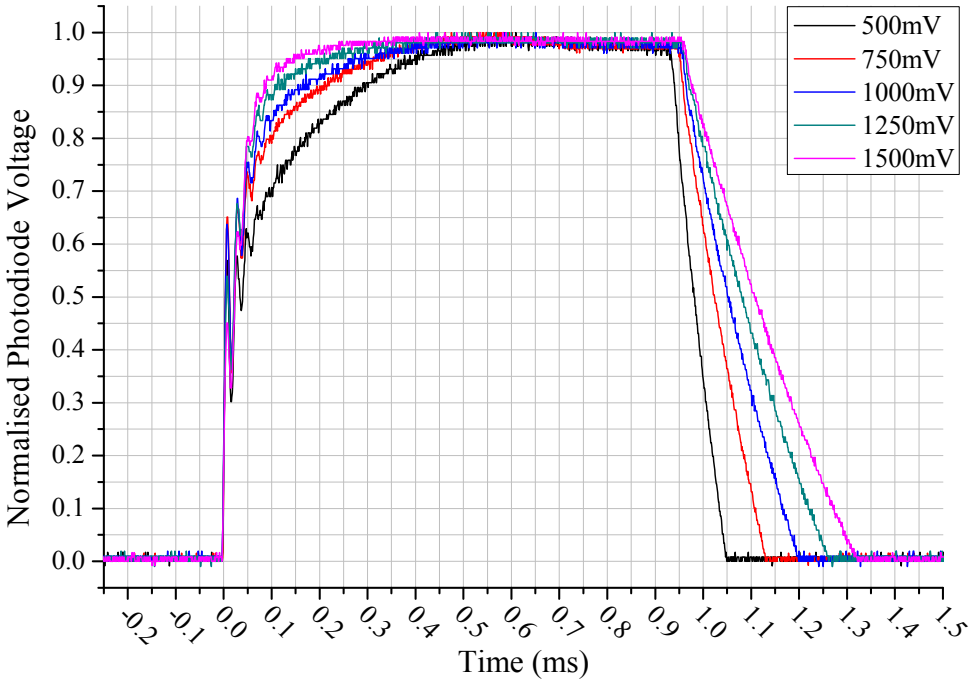

Figure 6.6: Photodiode trace of Newport diode laser showing rise and fall of output power for a 1 ms control voltage pulse.

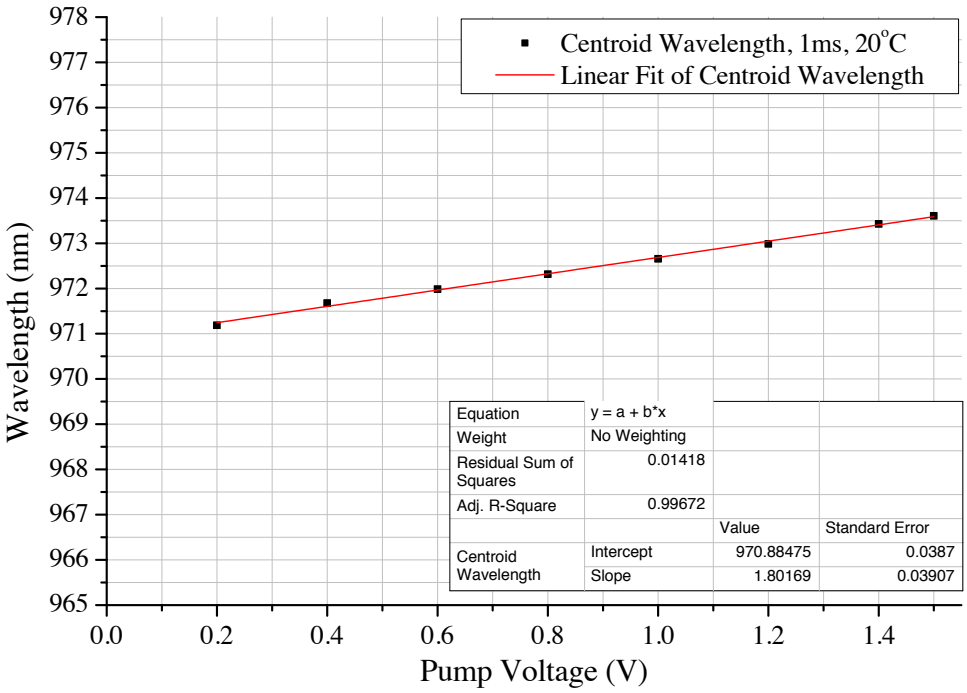

Figure 6.7: Wavelength of the Newport Diode laser with 1ms burst controlled by external voltage pulse.

It can be seen that as the voltage increases and hence the output power of the laser increases, the centroid wavelength increases. The data was fitted to a linear model using Origin software and a gradient of 1.80 ± 0.04 nmV^{-1} wavelength shift was measured. As the voltage increases, the laser output increases and so does the operating temperature which makes the laser wavelength longer as expected. The centroid wavelength of this pump laser changes by ~ 2 nm over its full operating range whereas the pump laser used in Chapter 5 changes by ~ 12 nm.

The centroid wavelength, although increasing with operating voltage, does not reach 976 nm at its full power. This is because the 1 ms pulse length used for Figure 6.7 is shorter than the minimum specified pulse length of 5 ms. The laser was operated at 1 ms pulses after consultation with the manufacturer who could not guarantee the wavelength of 976 nm at this duration but indicated that pulses no shorter that 1 ms would not damage the laser.

The data collected in Figure 6.7 was taken with the cooling water set to 20°C as originally specified by the manufacturer. However, after further consultation with the manufacturer, the laser could be safely operated at a slightly higher temperature without damaging the laser. This allowed the wavelength to be controlled through temperature.

To investigate the temperature sensitivity, spectra of a 1 ms burst from the laser at 1.5 V were recorded and for various temperature settings of the water cooler. The laser was allowed to thermally settle for 10 minutes before the spectra were taken. The data is shown in Figure 6.8.

As the temperature increases, so does the centroid of the spectra. Although the centroid of the spectrum at 25°C is 975 nm, its peak is greater than 976 nm. Therefore, a temperature of 24°C was chosen as the peak overlapped with the Ytterbium absorption spectrum provided by Amplitude Systemes [65]. Both the spectrum of a 1 ms burst from the pump laser at 24°C and the Ytterbium absorption data are shown in Figure 6.9.

This temperature was chosen as it provided good overlap with the absorption peak of Ytterbium at 976 nm. For all further experiments, the pump laser chiller was set to a

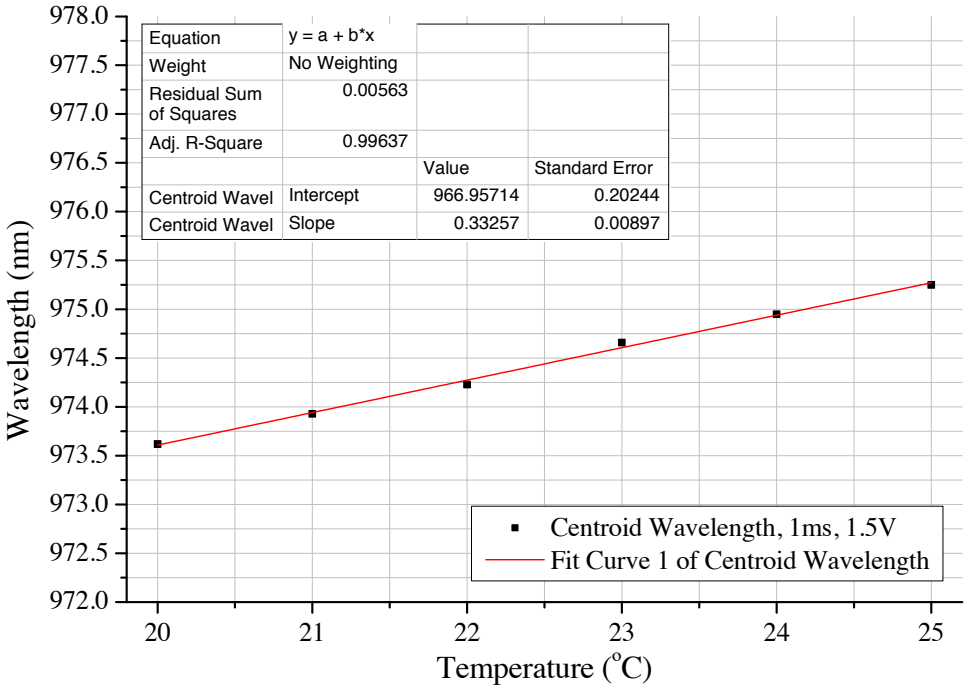

Figure 6.8: Temperature dependence of wavelength for Newport Diode laser with 1 ms burst at 1.5 V.

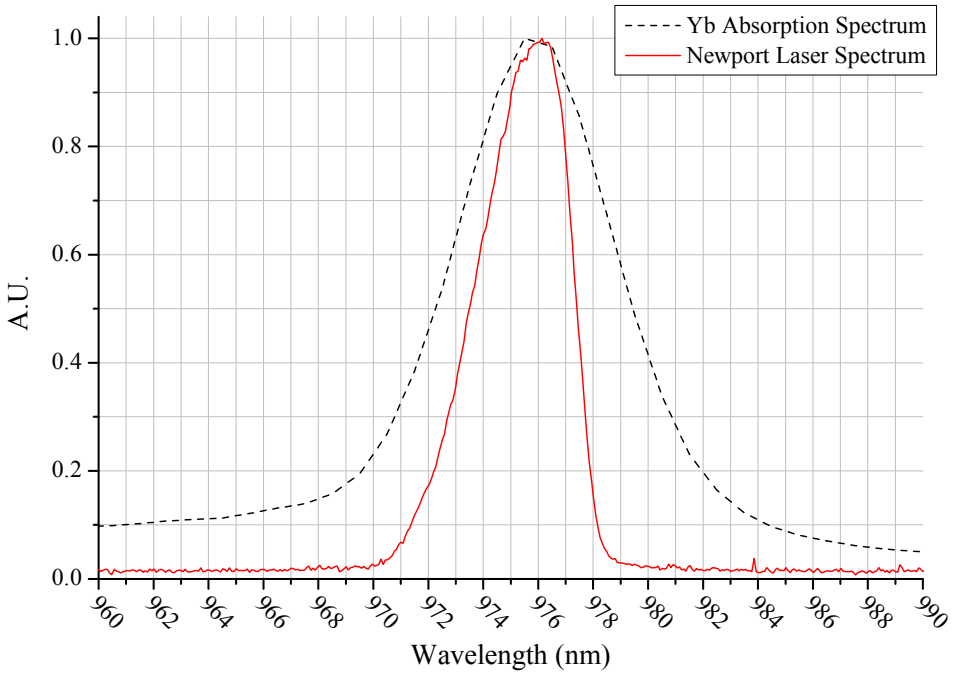

Figure 6.9: Overlay of both the spectrum of the Newport diode laser (1 ms, 1.5 V, 24°C) and the absorption spectrum of Ytterbium.

Table 6.1: Key parameters of the Crystal Fibre DC-200/70-PM-Yb-ROD PCF used.

Parameter	Value
Mode Field Diameter	55 μm
Core NA	0.02
Cladding Diameter	200 μm
Cladding NA	0.6
Pump Absorption @ 976 nm	30 dBm^{-1}
Length	0.70 m
End Cap	8 mm Silica

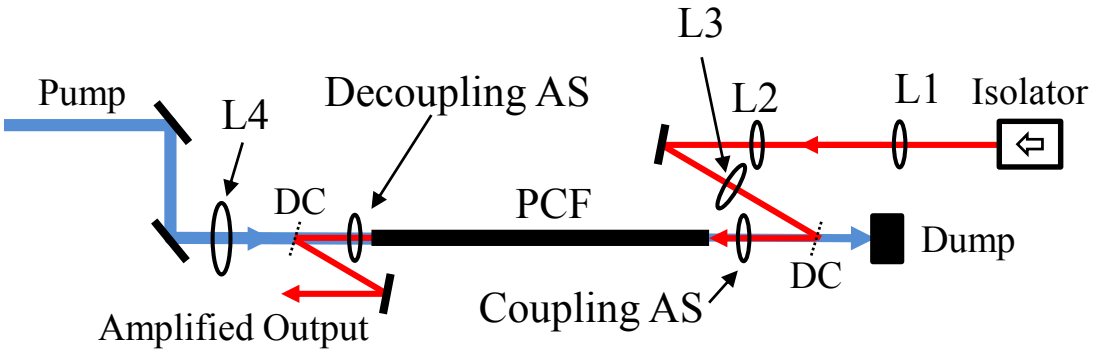

Figure 6.10: Experimental layout used to investigate amplification in the PCF.

temperature of 24°C.

6.5.2 Alignment

For the following experiments the PCF used was a Crystal Fibre DC-200/70-PM-Yb-ROD whose properties are outlined in Table 6.1.

The output of the AS laser was used as a seed to the PCF which was set up as shown in Figure 6.10. An optical isolator was used to separate the PCF amplification stage from the AS laser to prevent any backward reflections or ASE providing a feedback that may lead to a catastrophic failure. The isolator requires a linearly polarised input aligned to its transmission axis and the output is also linearly polarised.

L1 and L2 in Figure 6.10 are plano-convex lenses with focal lengths of 200 mm and 50 mm respectively. The flat sides of each lens face each other and together with a spacing of approximately 250 mm they form a confocal Keplarian telescope that reduces the beam

size by the ratio of the focal lengths, which in this case is 4. The dichroics, labelled DC in Figure 6.10, must be used at 22.5 ± 1° from the axis of the transmitted beam in order to achieve the >99 % transmission and reflectivity specified for the pump and seed wavelengths respectively.

L3 is a plano-convex lens with a focal length of 300 mm used to further focus the beam before the final f = 15 mm coupling aspheric. This arrangement was found to provide the best coupling. L4 is an f = 75 mm plano convex lens that was used to focus the pump beam before it was coupled into the PCF by the f = 11 mm decoupling aspheric.

Considerable time was spent improving the coupling efficiency of both the input laser beam to be amplified and the pump laser beam. Unlike the conventional step-index fibres described in Chapter 5, the PCF cannot be bent and is supported by a macroscopic glass rod to avoid this. The flexibility of the conventional fibres was utilised previously as with the laser beam and coupling optics carefully aligned to an optical axis, the fibre itself could be moved on a translation stage to achieve the best coupling.

With the PCF however, one end could not be moved like this without affecting the other considerably. Therefore, considerable care had to be taken to have the input laser beams aligned to the axis of the PCF before they were coupled in. As was done in Section 5.1, one lens at a time was inserted into the beam paths sequentially whilst verifying that the position of the laser beam had not changed after passing through the lens.

The PCF was mounted in an anodized aluminium mount which was a bar the same length as the PCF with a 2 mm V-groove cut into the top surface. The position of the laser beam at either end of the support was used to align the laser beam before placing the PCF in the groove.

The input laser beam to the fibre must match its core diameter and its numerical aperture in order to achieve good coupling. Any light outside these constraints will not be guided by the fibre and is therefore wasted. In a standard step index fibre with a typical numerical aperture of 0.1, coupling efficiencies of 80 % are readily achievable, although experiments

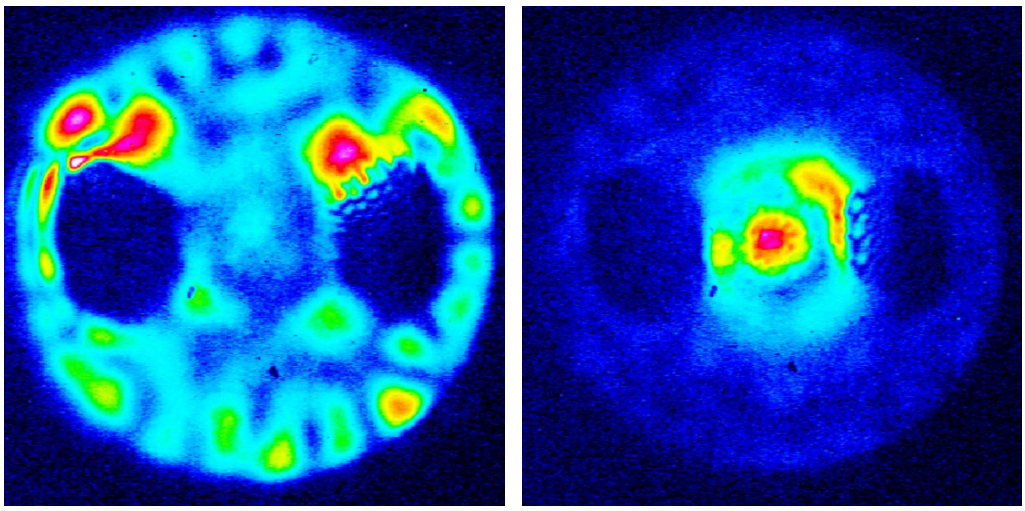

(a) Incorrect polarisation alignment (b) Correct polarisation alignment

Figure 6.11: Effect of polarisation orientation on coupling efficiency in the PCF recorded with the same optical layout but with orthogonal polarisation orientations.

in Chapter 5 showed a lower coupling efficiency was achieved with single mode fibre due to the small core size. Whilst the core of the PCF used was considerably larger than that of a single mode fibre, its numerical aperture was much lower.

Step index fibres that are single mode support two orthogonally polarised modes and therefore a linearly polarised input can always be coupled successfully into the fibre. The PCF used was experimentally demonstrated to only support one polarisation mode with the other unguided which although not specified in by the manufacturers [66] is a known feature [67]. Therefore, care had to be taken to align the polarisation axis of the linearly polarised input beam to the fibre to achieve any coupling at all. The effect of this can be seen in Figure 6.11 where alignment of the coupling optics remains the same but the half-wave plate used to rotate the linear polarisation of the input changes.

At the decoupling end of the PCF, two silver mirrors were used to align the pump beam to the axis of the PCF. The decoupling aspheric was aligned to best collimate the output from the core of the fibre and ensure that the output remained parallel to the axis of the PCF. This was achieved by observing the collimated output from the core several metres away from the PCF. This ensured that the output was passing through the centre of the decoupling aspheric and that no aberrations were introduced. To achieve best pump coupling, the L4

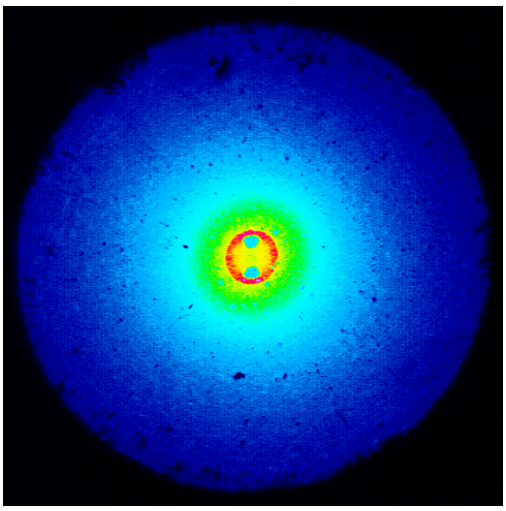

Figure 6.12: Image of the end face of the PCF at the seed decoupling end showing the core, inner cladding and supportive rod.

lens was aligned to move the pump laser beam. This enabled alignment of the pump beam without affecting the decoupling of the seed from the core.

Initially, an f = 100 mm plano-convex lens was used as L4 to focus the pump beam. It was found that a shorter focal length lens resulted in better pump coupling but because of the fixed angle of the dichroic there needed to be a approximately 100 mm between L4 and the decoupling aspheric. If the dichroic mirror was moved closer to the decoupling aspheric, the reflected beam of the amplified output would hit the mount of the aspheric. This spacing proved to be a practical limit.

However, a mount for the decoupling aspheric was eventually devised that was more compact allowing the dichroic to be closer to the decoupling aspheric and in turn, a shorter focal length lens used for L4. By using an f = 75 mm lens in place of an f = 100 mm lens, significantly better pump coupling was achieved.

The degree of pump coupling was observed by placing a camera before the coupling aspheric and repositioning it to create an image of the fibre on the camera. Figure 6.12 shows the image recorded.

This shows a small amount of light in the macroscopic support rod with most of the light carried in the inner cladding. The core of the fibre appears to be less bright than the air

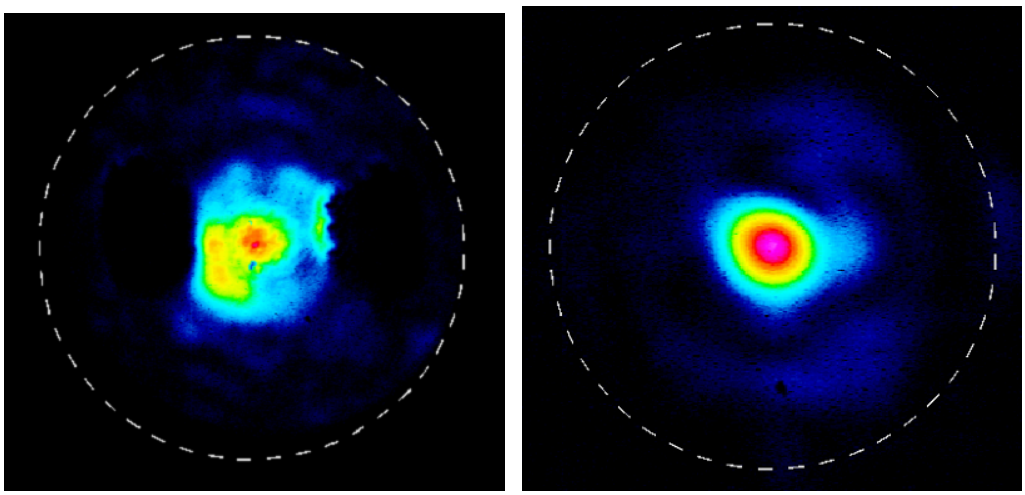

(a) PCF near-field coupling (b) PCF far-field coupling

Figure 6.13: Image of fibre end face at output end showing the best achieved seed coupling into the core. The dotted line represents the edge of the inner cladding.

cladding around the inner cladding because the pump light is absorbed by the Ytterbium dopant.

It should also be noted that the images of either facet of the PCF in Figure 6.11 and Figure 6.12 were recorded with the fibre fixed in the same orientation. These show that the bow-tie-like stress rod structure has rotated by 90°. When observing the output of the PCF, the opposite dimension than is required by the image should be adjusted, i.e. if the beam appears to be horizontally misaligned to the core, the vertical dimension should be adjusted at the coupling end of the PCF.

Figure 6.13 shows the final achieved level of coupling into the core. This is considerably better than the coupling demonstrated in Figure 6.11 due to improved coupling procedure and alignment of the coupling optics.

The two images in Figure 6.13 are the images of the output from the core of the fibre with the decoupling aspheric in two different positions. Figure 6.13a shows the aspheric at a position set to create an image of the fibre structure. This was useful for alignment but did not produce the most collimated output beam. With the aspheric closer to the PCF, a point further into the core was imaged which produced the image shown in Figure 6.13b. This produced a beam that remained circular with a better degree of collimation. This profile

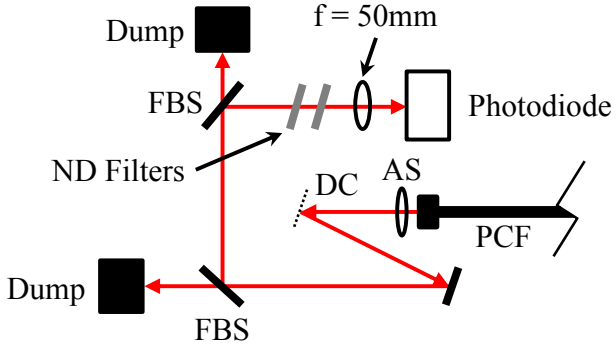

Figure 6.14: Beam path built to reduce intensity of amplified output to within the dynamic range of the photodiode using a two Fresnel beam splitter (FBS)and neutral density filters (ND filters).

increased in size but didn't change shape with distance from the fibre.

Final small adjustments were made to both of the aspherics when the pump was used to amplify the seed. The adjustments were made to achieve the highest output burst energy from the amplifier. In this case the alignment must be the best for both the seed and the pump.

With good alignment achieved, amplification in a burst regime was investigated in the PCF.

6.5.3 Pulse Energy Measurements

As described in Section 6.4, a method using both a photodiode trace and an energy measurement of the entire burst was devised to measure the individual pulse energies. The beam path of the output from the PCF was set up as shown in Figure 6.14.

Two Fresnel beam splitter (FBS) and various reflective neutral density filters were used to significantly reduce the intensity of the amplified output to within the dynamic range of the photodiode. The transmitted beam from each Fresnel beam splitter was dumped safely in a high power beam dump. The final intensity was $\sim 10^{-6}$ times lower than the amplified output of the PCF. A plano-convex lens with a focal length of 50 mm was then use to focus the beam onto a photodiode. The position of the plano-convex lens before the photodiode was adjusted to give the maximum response from the photodiode. The photodiode used

Table 6.2: Newport 818-BB-25 InGaAs high speed biased photodetector specifications

Material	InGaAs
Rise Time	<35 ps
Fall Time	<35 ps
Cut Off Frequency	12.5 GHz
Saturation Current	10 mA
Active Diameter	32 μm

was a Newport 818-BB-35 InGaAs high speed biased photodetector whose specifications are listed in Table 6.2.

The signal from the photodiode was recorded on a LeCroy WaveRunner MXi-A digital oscilloscope which had a bandwidth of 3 GHz and a maximum sampling rate of 10 GSs^{-1}. Additionally, it has a 20 million sample memory that at its maximum sampling rate allows 2 ms of data to be recorded which was sufficient to cover the 1 ms amplified bursts.

The photodiode traces were recorded into binary data files on the oscilloscope and a program written in Python was used to analyse them. Ten photodiode traces of subsequent amplified bursts were recorded under the same conditions to provide a reasonable level of statistics within an acceptable amount of memory (200 Mb).

Software was written in Python to analyse the binary oscilloscope data files. The software detected the peaks of each laser pulse and averaged other samples of the same pulse from different data files ensuring that the same pulses were being averaged. The average peak voltages and their standard deviation were returned.

Immediately after the photodiode traces were recorded, the total burst energy was recorded using a Gentec-EO QE25-ELP-MB-DO pyroelectric energy meter which was specially designed and calibrated to measure bursts as long as 4 ms at a maximum rate of 2 Hz. The energy meter was placed immediately after the dichroic at the output of the PCF. This reported the average and standard deviation of 60 bursts .

A further piece of software written in Python used the total measured burst energy in conjunction with the average peak voltages to calculate the voltage to energy normalisation. The average peak voltages were then multiplied by this normalisation to give the individual

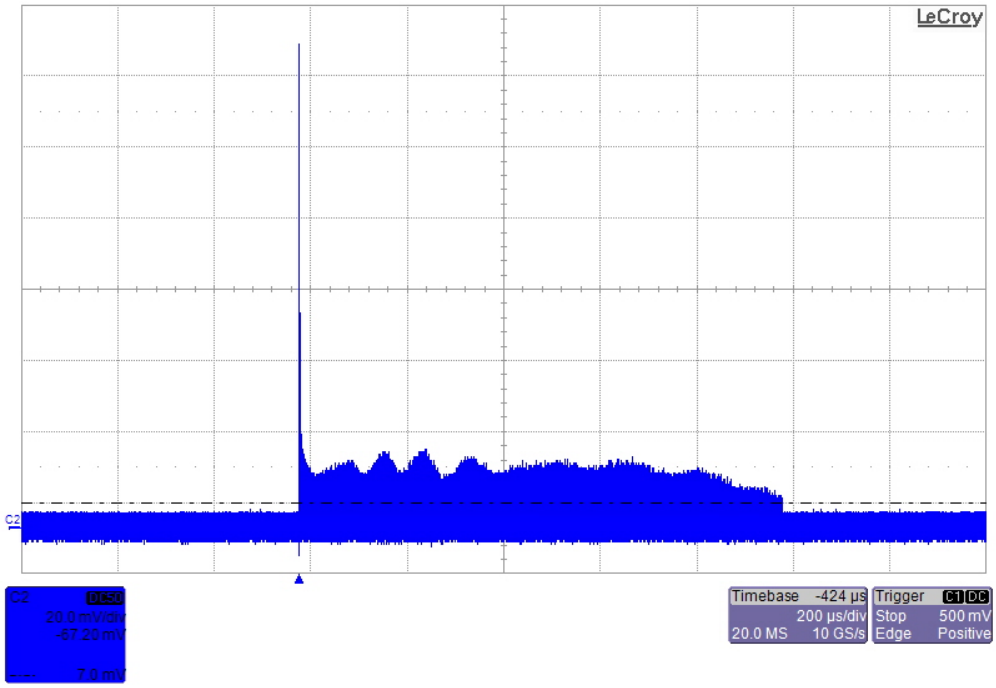

Figure 6.15: A typical photodiode trace with 20 million samples over a period of 2 ms. Due to the very high number of points the 6000+ individual pulses are displayed as a solid blue area.

pulse energies.

Figure 6.15 shows a typical trace of a 0.95 ms amplified burst with 20 million samples over 2 ms. Despite the display representing the thousands of pulses as a single coloured area, the pulses are considerably shorter than the separation between successive pulses and are merely rendered this way on the oscilloscope screen when a very large number of points are displayed.

The shape of the photodiode trace is explained in greater detail in Section 6.6, however, the approximately first fifty pulses were over an order of magnitude greater than the several thousand remaining pulses.

The data from the oscilloscope of a single pulse is shown in Figure 6.16. Here the individual digital samples of the signal from the photodiode can be seen. Initially, fitting the peak to a Gaussian distribution was attempted but this produced a peak height lower than maximum data point for the pulse. The signal shape is also not expected to be Gaussian although the data is close. For these reasons, the maximum data point within a pulse

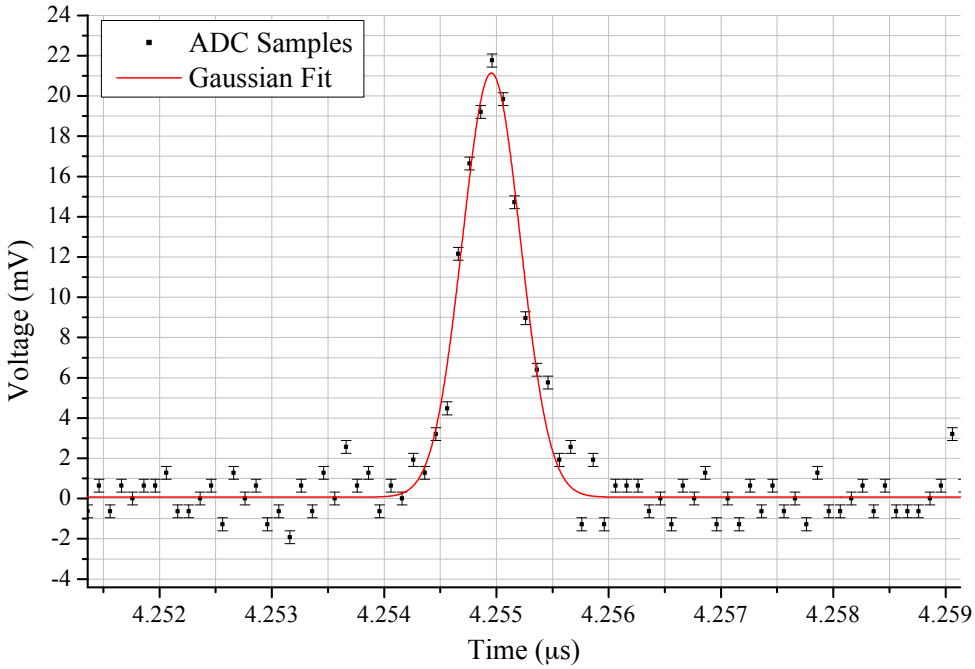

Figure 6.16: Data from the oscilloscope of a single laser pulse with a Gaussian fit.

was used as the peak voltage which was considerably simpler to implement. Given the approximately 6000 pulses in a burst, it would be impossible to manually check each Gaussian fit which may provide unpredictable fitting results with the variation of the data.

This method of combining a photodiode trace and the total burst energy measurement was able to provide individual pulse energies. However, the fractional uncertainty in each pulse energy was as large as 50% for some pulses, particularly near the end of the burst. This was because the limited 8-bit resolution of the ADC in the oscilloscope was required to cover a large voltage range. With the voltage scale and offset set on the oscilloscope, the ADC converts the analogue photodiode voltage to one of 256 ($2^8 = 256$) values.

To accommodate the large initial pulses in the burst the range chosen made the resolution of the remaining pulses in the burst low. Figure 6.17 shows a photodiode trace of the end of an amplified burst. Here the limit of ADC resolution in the vertical dimension is clear with only discrete voltage values. In this data file, the ADC resolution was 0.6 mV and the voltage peaks are approximately 6 mV. This corresponds to a fractional uncertainty of approximately 10 % for several thousand pulses at the end of the burst.

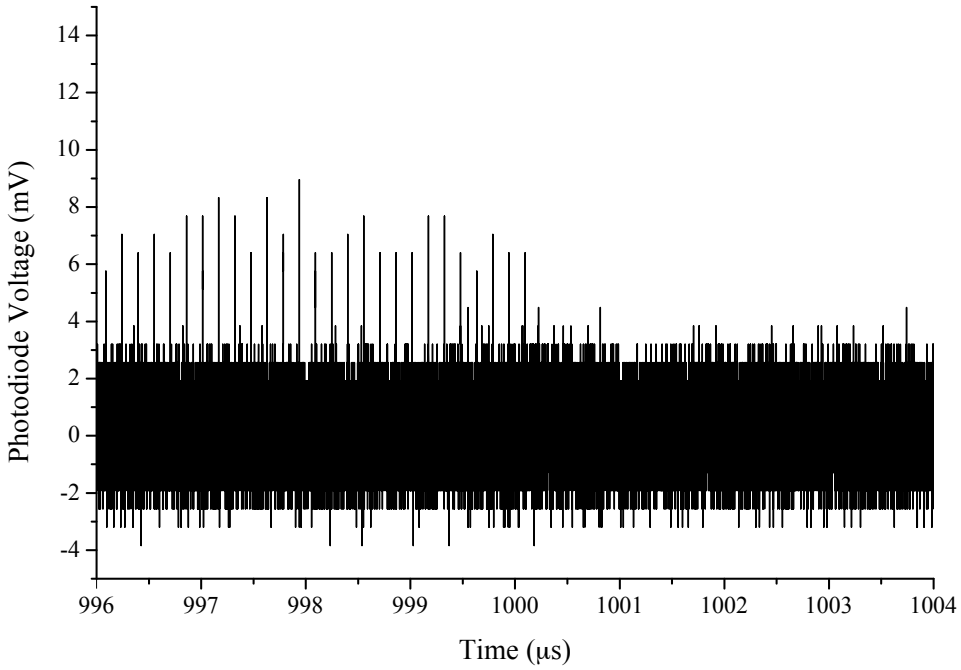

Figure 6.17: Part of a photodiode trace showing the end of the amplified burst. The limited ADC resolution of the oscilloscope can clearly be seen by the discrete voltage values in the trace.

Since these peaks are added together as described by Equation 6.1 this results in a large fractional uncertainty in the individual pulse energies.

To overcome this, two photodiode traces were recorded with the voltage range on the oscilloscope adjusted to accommodate in one case the initial high voltage pulses and for the other the remaining low voltage pulses. With the voltage range set to suitably accommodate the majority of the low voltage pulses, the initial high voltage pulses were clipped.

A further piece of software written in Python was used to combine to the two data sets at a point where they overlapped. Figure 6.18 shows two sets of average peak voltages for two different vertical voltage scalings on the oscilloscope. For each, 10 photodiode traces were analysed and averaged to give the average peak voltages. The manually chosen point to concatenate the two data sets is shown by the vertical line at 3.25 μs in Figure 6.18.

This method decreased the fractional uncertainty in the measurement of the peak voltages as well as increasing the signal to noise ratio. This substantially decreased the final calculated fractional uncertainties of the pulse energies.

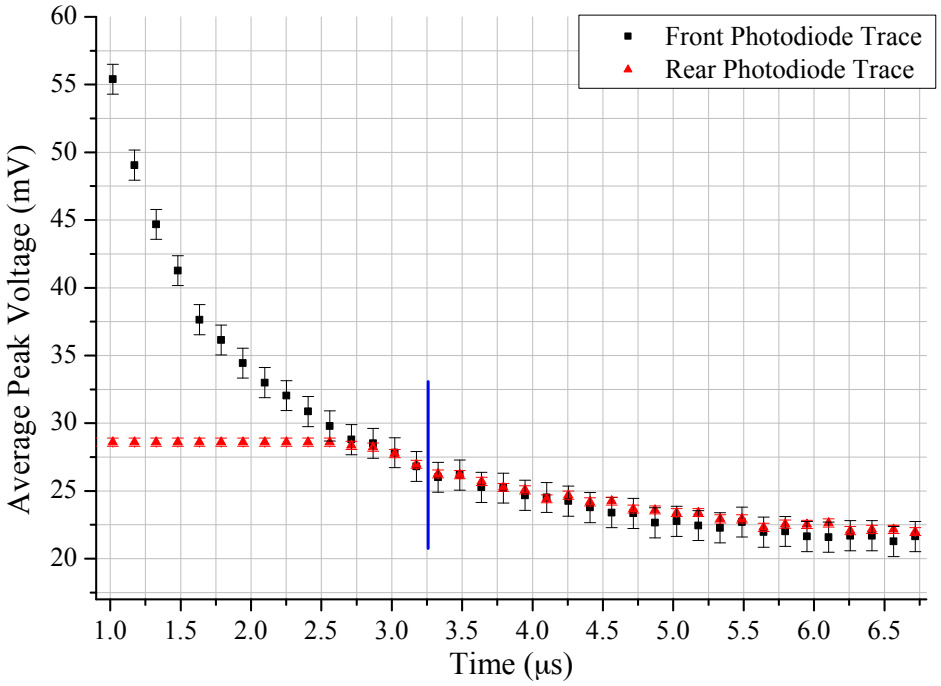

Figure 6.18: The voltage peaks from two data sets each with different vertical voltage scalings on the oscilloscope to look at the initial high voltage pulses (front) and the remaining low voltage pulses (back). The chosen point to join the two datasets is shown by the vertical line at 3.25 μs.

This method has successfully and accurately measured individual laser pulse energies at the megahertz repetition rates necessary for amplification experiments in the following sections. Without this method it would not have been possible to characterise the performance of the amplifier.

6.6 Burst Amplification

Initial burst amplification experiments use a concurrent seed and pump 1 ms burst that started and stopped at the same time. A photodiode trace of the amplified output is shown in Figure 6.19.

Figure 6.19 shows that after both the seed and the pump are turned on by the control pulse, the amplified output rises to its maximum after $\sim$ 150 μs. After 1 ms, both the pump and seed are turned off. However, after this point there is a further burst of output.

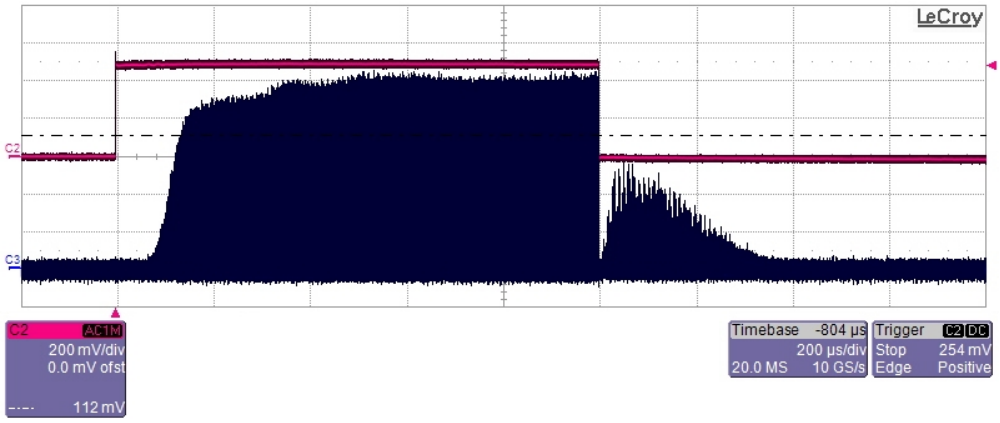

Figure 6.19: Photodiode trace of the amplified output (black line) of the PCF amplifier with the seed and the pump starting and finishing at the same time. The rectangular control pulse to both the seed and pump is shown above the photodiode trace (red).

The electro-optic modulator (EOM) used to modulate the seed beam has a finite extinction ratio and so even when the output of the seed is switched off, some leakage still remains. The contrast ratio of the EOM was measured to be $> 500{:}1$. Also, from Figure 6.6 the pump once switched off can take up to 300 μs to turn off completely. During this time the Ytterbium in the PCF is still being pumped and gain builds up in the amplifier. The very low intensity seed leakage from the EOM is then amplified. This cannot be directly verified from Figure 6.19 alone, but upon examination of the photodiode trace on a shorter timescale, the spurious output consists of pulses at same repetition rate of the seed.

Because the laser pulses in this spurious output decay to small energies, it is not possible to accurately determine their peak voltage in the photodiode trace. This leads to an uncertainty about the number of pulses present and exactly which pulses contribute to the total burst energy measurement. In turn, this reduces the accuracy of the pulse energy measurement technique outlined in Subsection 6.5.3.

Therefore, to avoid this, the seed burst was extended beyond the 1 ms of the pump burst. The time at which the seed was stopped was chosen to give a clear end to the amplified burst without the presence of any amplified leakage afterwards. This was found experimentally to be 200 μs and for all further experiments the seed burst was set to end 200 μs after the pump stopped.

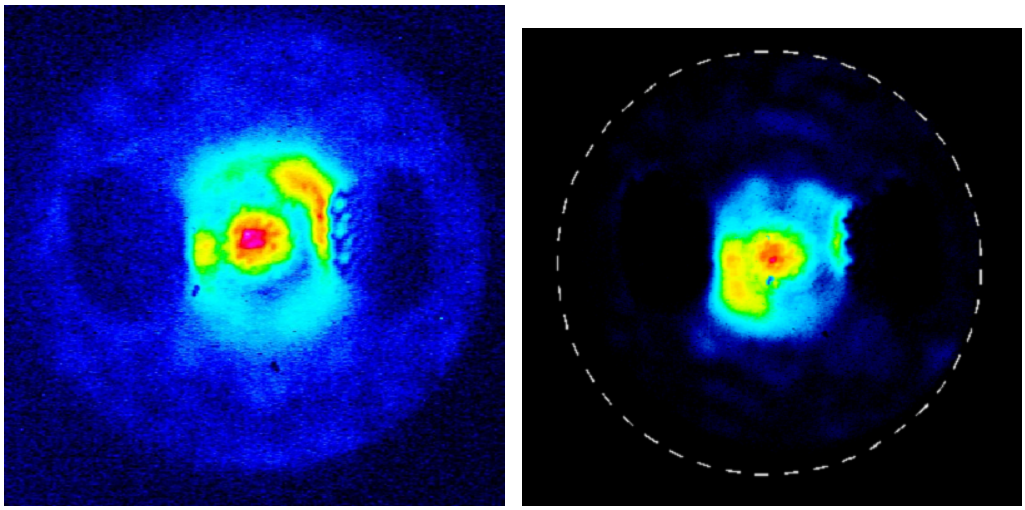

(a) Original PCF coupling (b) Improved PCF coupling

Figure 6.20: Images of the decoupling end of the fibre showing the original coupling ((a)) and the improved coupling ((b)) with a greater contrast between the core and the pump cladding.

For all further experiments, the AS laser which was the seed to the PCF amplifier was set to its maximum output by setting the current of the main amplifier pump laser within the AS laser to 21.0 A. This provided approximately 1.5 μJ per pulse at the coupling aspheric.

During initial experiments the amplified burst energy was measured after the dichroic at the decoupling end to be approximately 50 mJ. The improvements in alignment and coupling of the seed described in Subsection 6.5.2 made a significant improvement with the output reaching $\sim$ 80 mJ. The difference in coupling can be seen in Figure 6.20.

After this a substantial increase to the amplified output burst energy was made by changing the plano-convex pump lens (L4 in Figure 6.10) before the decoupling aspheric from an f = 100 mm lens to an f = 75 mm lens. This was only possible by finding an alternative mounting solution for the decoupling aspheric. As mentioned in Subsection 6.5.2, the dichroics must be used at a specific angle, which causes the reflected amplified output to return very close to the mount of the decoupling aspheric. This places a constraint on the distance of the dichroic from the decoupling aspheric and in turn the plano-convex pump lens behind it.

After making this change the amplified burst energy was measured to be $\sim$ 180 mJ.

Given this was found with the same input seed and pump levels and burst lengths, this significantly improved the pump coupling and hence the gain of the amplifier.

As the the seed and the pump are turned on at the same time, the initial pulses are not amplified, but instead absorbed by the Ytterbium ions. From Figure 6.6, it takes ~ 150 μs for the pump output to reach over 95 % of its maximum output. As discussed in Section 6.3, if the pump is delayed, energy will be stored in the Ytterbium ions in the upper-state energy level increasing the gain.

To investigate this, the timing of the start of the seed burst with respect to the pump was varied and pulse energy measurements made.

The main amplifier in the AS laser was again set to its maximum output by setting the current of its pump laser to 21.0 A. A 1 ms burst, consisting of the 6490 seed pulses, was measured immediately before the coupling aspheric to have a total energy of 10.30 ± 0.02 mJ. The pump laser was set to 1.2 V with a 1 ms burst also. The pump burst energy was measured to be 306.0 ± 0.4 mJ at the decoupling aspheric. The seed was set to end 200 μs after the 1 ms pump burst. The starting point of the seed burst was then varied with respect to the pump burst, initially starting concurrently with no delay and then increasing the delay of the seed burst to a maximum of 240 μs.

For each seed delay, the seed burst energy was measured before the coupling aspheric as well as the amplified output, which was measured after the dichroic and the decoupling end. ND filters were used as part of the layout shown in Figure 6.14 to adjust the intensity of the beam to take photodiode traces of the amplified output. Initially, when the amplified output resembled Figure 6.19, one photodiode trace was sufficient whereas when the output resembled Figure 6.15 with much greater peaks at the beginning of the burst, two photodiode traces were recorded with different vertical scalings on the oscilloscope. In each case, 10 photodiode traces were recorded

The photodiode traces were then used with the total burst energy measurements to determine the individual average pulse energies from the 10 photodiode traces. From each

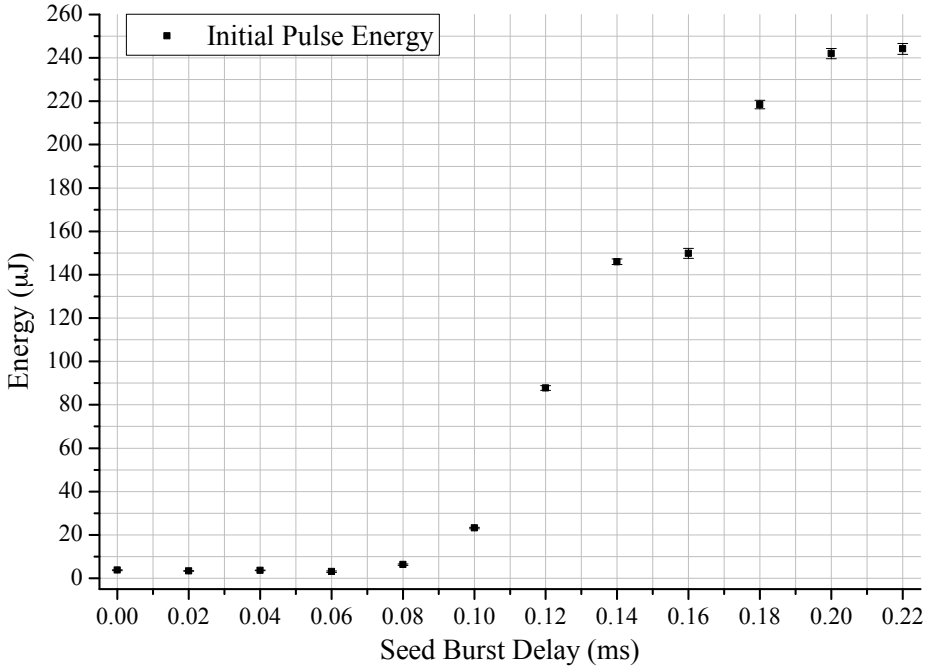

Figure 6.21: Dependence of the energy of the first pulse in the burst against the delay of seed burst with respect to the pump.

of these lists of burst energies, the energy of the first pulse is plotted in Figure 6.21 as a function of the seed delay time with respect to the 1 ms pump burst.

No change in the initial pulse energy was observed between 0 μs and 60 μs delay of the seed burst. Here, the pump hasn't reached a high enough level to make the fibre transparent and the pulses have a lower energy than the 1.6 μJ input pulses.

At increasingly longer seed burst delays, the first seed pulse experiences increased gain and its the initial pulse energy was observed to rise sharply. Eventually, this was seen to saturate at $\sim$ 200 μs seed burst delay. At this point, increasing the delay further did not increase the energy of the initial pulse.

The data point at 160 μs delay is noticeably different from the general trend of the data. At the time of recording the data, the photodiode trace looked very similar to the others being recorded and nothing unusual was suspected. However, upon analysing the photodiode traces it was noted that this data point was lower than expected to fit in the general trend. This was investigated and it was found that the exact delay programmed in the digital delay generator caused the switching period of the EOM to occur during the initial pulse.

Whilst the digital delay generator generates its own trigger by subdividing a photodiode signal from the AS laser, this only ensures that the master trigger on the digital delay generator has a stable phase relationship to the seed frequency. As the delay before triggering the EOM is by necessity variable this may cause the switch on or off to occur during a pulse. The rise and fall time of the EOM is short enough to be able to turn on and off between pulses at 6.49 MHz, but not as short as the laser pulses themselves.

It was found that by adjusting the timing slightly away from 160 μs delay this clipping of the seed pulse was overcome. With the full energy of the seed pulse, the initial amplified pulse increased in energy. This data from this repeated experiment is not included in Figure 6.21 as it was recorded under different conditions.

From the data gathered in this experiment, 200 μs was chosen as the delay time for further experiments as the first pulse energy was very similar to that of a delay of 240 μs. However, with a shorter delay there will be less spontaneous emission and therefore less ASE. This was investigated by looking at the spectra and is discussed in Section 6.7.

As before, the output of the PCF amplifier was measured as a function of input pump power which given the burst temporal structure being employed is more usefully expressed by the total burst energy. For this experiment the seed burst was 1 ms long and started 200 μs later than the 1 ms pump burst. The output energy was measured after the dichroic at the decoupling end of the PCF and the pump input before the decoupling aspheric. Given the temporal structure was fixed and only the power of the pump laser was changed as well as the common relationship between power and energy (Equation 4.1), the definition of the slope efficiency used in Chapter 5 for QCW powers will still be true. The amplified burst energy as a function of input pump burst energy is shown in Figure 6.22. The pump control voltage was varied from 0.5 V to 1.2 V.

This shows a clearly linear relationship between input and output. The data was fitted to a linear model and the slope efficiency was found to be 53.6 $\pm$ 0.1 %. Whilst not as high as the double-clad fibres demonstrated in Chapter 5, this is close to the slope efficiency of 60 % specified by the manufacturer of the PCF.

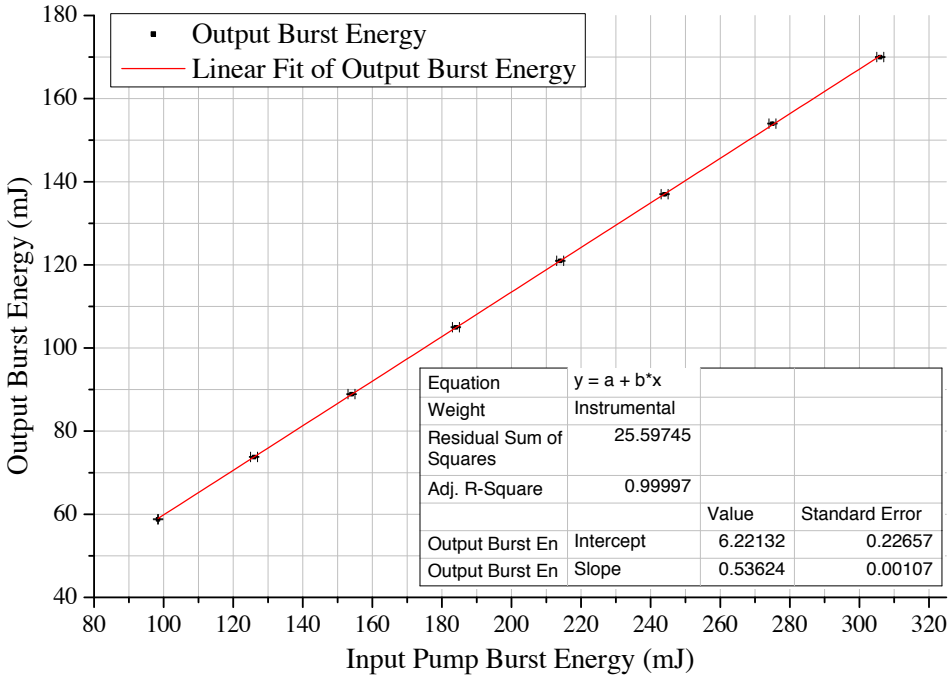

Figure 6.22: The total output burst energy for different pump burst energies. The 1 ms seed burst both started and finished 200 μs after the 1ms pump burst.

Although the timing of the bursts, the burst energy, the spectrum and the spatial quality are discussed in different sections in this chapter, these were observed or measured simultaneously because of their interconnectivity. It was for this reason that pump control voltages of only up to 1.2 V were used as beyond this spectral broadening was observed which is indicative of ASE or nonlinearities.

A pulse energy measurement was made with the pump control voltage at 1.2 V and hence the highest level of amplification. The input seed burst energy was measured to be 9.34 $\pm$ 0.02 mJ before the coupling aspheric and the amplified seed burst out was measured after the dichroic at the decoupling end to be 177.0 $\pm$ 0.2 mJ. The pump burst was measured to be 313 $\pm$ 1 mJ before the decoupling aspheric and the transmitted pump was measured behind the dichroic at the coupling end to be 35.5 $\pm$ 0.1 mJ.

Figure 6.23 shows the pulse energies of the first 50 pulses calculated using the total burst energy measurement and the photodiode trace recorded of the burst. The first pulse has an energy of 267.7 $\pm$ 2.5 μJ.

This not only exceeds the design specification by more than that a factor of two for the

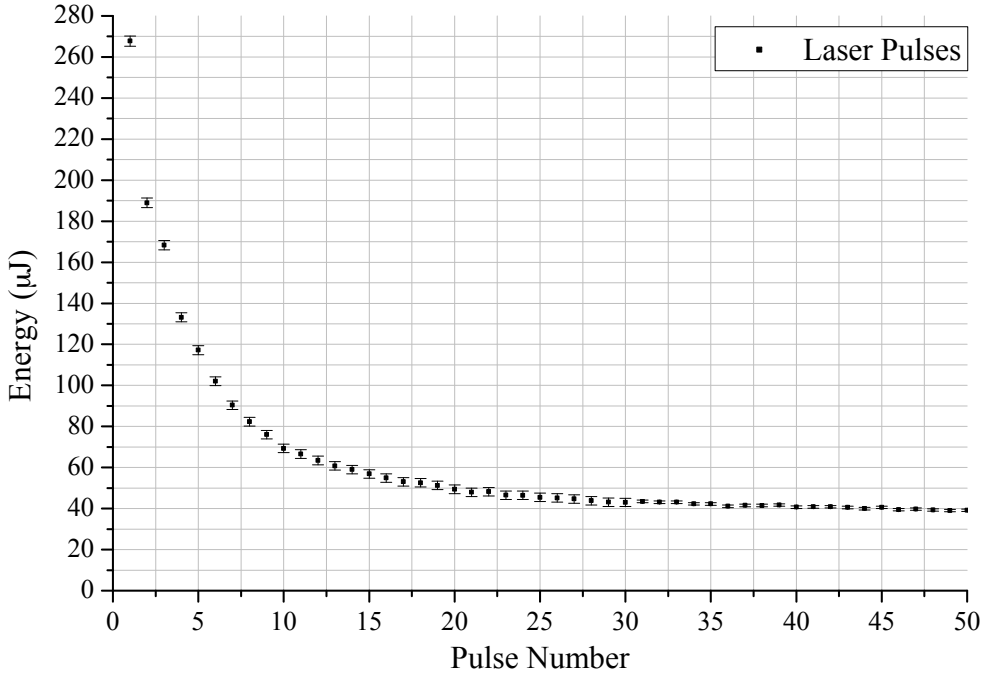

Figure 6.23: Maximum achieved pulse energies from the amplification in the PCF. Only the initial part of the 1ms burst is shown.

initial pulse but the first 6 pulses are over 100 μJ. This would enable this laser system to be used at the ATFII for more than a single electron bunch. The gain in the initial pulse from 1.52 μJ to 267.7 μJ is the highest single pass gain of any PCF based fibre amplifier compared to published literature. This corresponds to a gain of 32 dBm^{-1}. The increased laser energy will not only aid in any greater losses than expected with compression and frequency conversion to the second harmonic but also provide an increased laserwire signal.

6.7 Amplified Spectra

To verify the absence of any nonlinearities in the PCF, spectra of the amplified output were recorded. Before this however, the spectrum of the AS laser which was the seed to the PCF was recorded for comparison. For the purposes of laser-wire a spectral bandwidth greater than the specified acceptance of 2 nm of the final focus lens will cause chromatic aberration to increase the final focus spot size and limit the resolution of the laser-wire.

The spectrum of the AS laser was recorded by placing a piece of white card in the

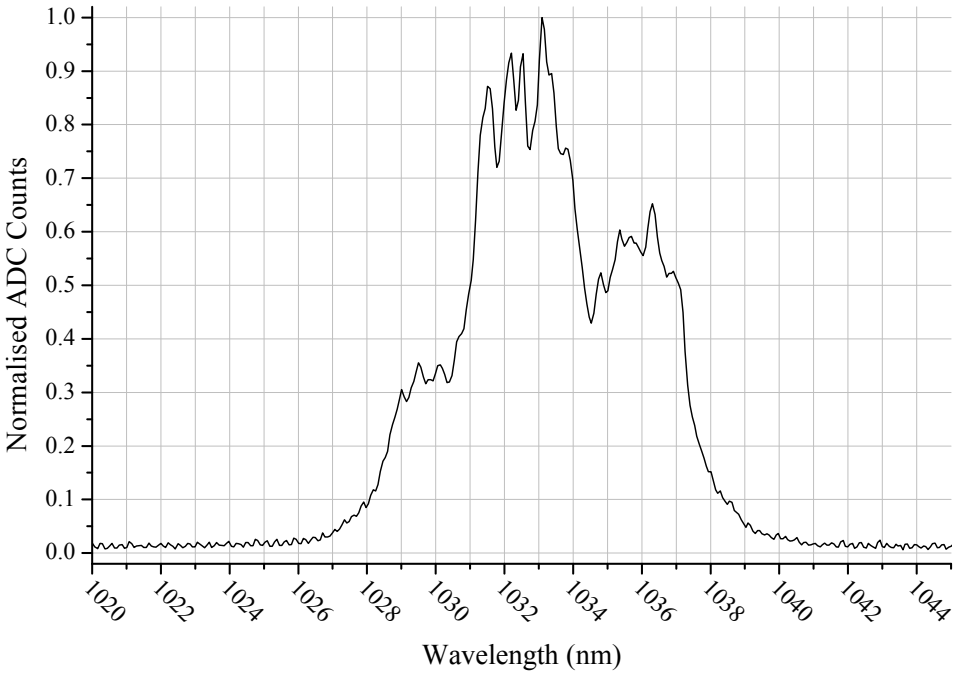

Figure 6.24: Spectrum of the AS laser recorded before the PCF with the AS laser main amplifier set to its maximum of 21.0 A.

beam before it entered the PCF. The Ocean Optics fibre coupled spectrometer described in Section 5.2 was used to record the spectra. 20 spectra of 3 ms bursts were averaged to produce the spectrum shown in Figure 6.24.

This is not ideally a smooth Gaussian distribution. It has a FWHM of 6 nm which is wider than the desired 2 nm. However, it was expected that this would narrow with the final frequency conversion stage to the second harmonic of the laser-system which will half the spectral bandwidth.

Spectra were recorded for various levels of amplification in the PCF that were achieved by varying the control voltage to the pump laser from 0.5 V to 1.5 V to explore the full amplification range although 1.2 V had been the common control voltage used for previous experiments. A white piece of card was placed in the output beam of the PCF and the fibre coupled spectrometer was positioned to detect the scattered light. 20 spectra were averaged for each voltage setting. The spectra recorded at different control voltages were all relatively similar with no macroscopic change to the shape of the spectrum. Two sample spectra are shown in Figure 6.25 for the pump control voltages of 1.2 V and 1.5 V.

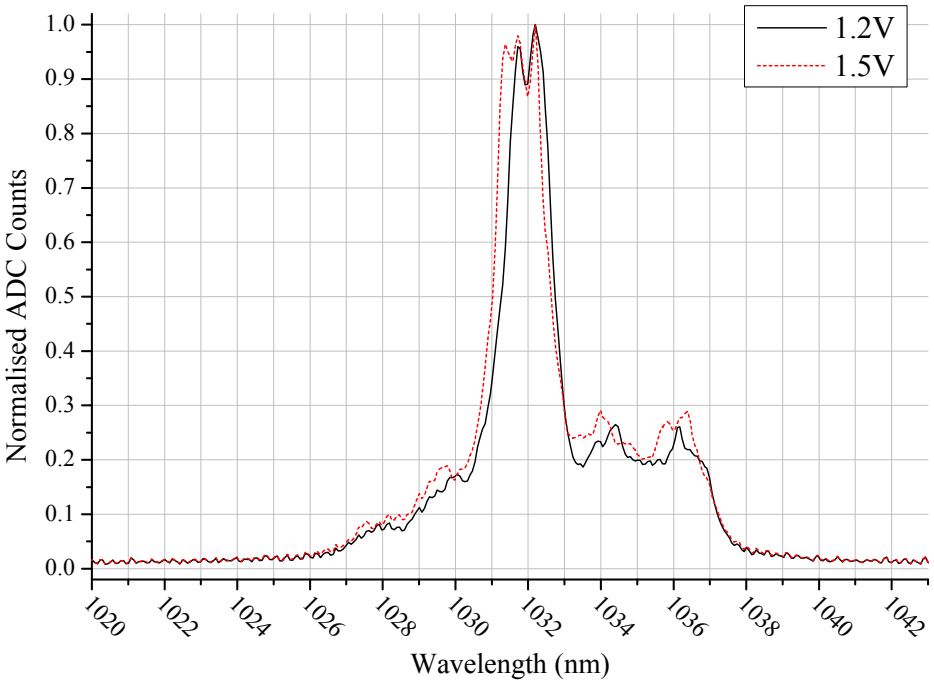

Figure 6.25: Spectra of the amplified output of the PCF amplifier with the pump laser control voltage at 1.2 V and 1.5 V.

1.2 V was chosen as the control voltage and hence pump power and gain. This setting was chosen as the spectra was slightly narrower and more stable. From the pulse energy measurements in Section 6.6, the initial pulse energy with a pump control voltage of 1.2 V was also sufficient for the purposes of this laser system and with the peak power of ~ 1 MW close the manufacturers specified limit, higher pumping levels were not used to avoid damaging the PCF.

During initial amplification experiments, a much broader spectrum indicative of ASE was observed with the same pump control voltage of 1.2 V. At this point, the coupling of the seed into the PCF was poorer and therefore for the same pumping level but lower input, more ASE would be expected. With the improved seed coupling, the spectrum of the PCF output with a pump control voltage of 1.2 V was narrower.

It should also be noted that the discussion of Ytterbium in previous chapters has described the peak of the emission at a wavelength of 1037 nm. However, it is clear from Figure 6.25 and Figure 6.24 that this is not the case. In both cases the centre of the spectrum is closer to 1032 nm. The spectrum of the AS laser recorded in Figure 5.11 is noticeably

narrower than in Figure 6.24. This may have been caused by the tuning of the AS laser to increase the output power.

However, the spectrum of the amplified output from the PCF at 1.2 V, which has a FWHM of $\sim$ 1.8 nm, will halve when it is frequency converted to the second harmonic, reducing it to $<$ 1 nm. This is well within the bandwidth acceptance of 2 nm of the final focus lens for laser-wire. Although the FWHM is relatively narrow, a significant amount of energy is contained within the wings of the spectrum so the spectrum of the second harmonic output will need to be measured to ascertain its width.

The spectra recorded so far are of the entire burst. It is already known that the energies throughout the amplified burst vary by over an order of magnitude. With the equipment available it was not possible to measure the spectrum of only the initial pulse. The spectrometer has a minimum integration time of 3 ms and this cannot be externally triggered. It was also not possible to deflect or isolate the first pulse from the remainder of the burst.

To overcome this, spectra were recorded whilst varying the delay of the seed burst with respect to the pump. With no delay and both the pump and seed starting concurrently, there would be a larger number of pulses but the pulse train would resemble the photodiode trace shown in Figure 6.19 where the majority of the pulses were the same energy.

By increasing the delay of the seed burst with respect to the start of the pump burst, the energy of the initial pulses in the burst rose until the photodiode trace of the amplified burst resembled Figure 6.15 with the first pulse of considerably higher energy than that of the remain pulses in the burst. Two of the spectra recorded are shown in Figure 6.26.

The pump control voltage was fixed at 1.2 V. The spectra in Figure 6.26 show both the spectrum recorded when there was no delay of the seed burst and when there was 0.22 ms delay. The difference between the two is negligible. This is to be expected as although it would likely be the first few pulses in the burst that would show evidence of nonlinearities, these represent $<$ 1 % of the total burst energy and therefore if their spectrum was only slightly different, it would be difficult to resolve in the spectrum integrated over the whole

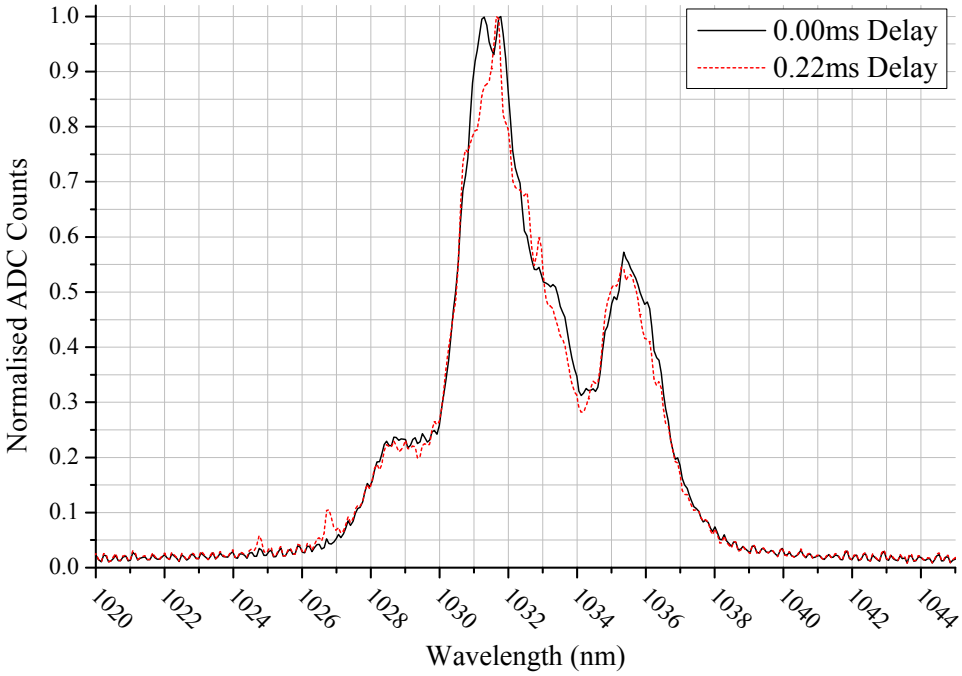

Figure 6.26: Spectra of the amplified output from the PCF for 0.00 ms and 0.22 ms delay of the seed burst with respect to the pump.

burst.

The PCF used is specified to have very low nonlinearites and capable of handling up to megawatt peak powers [66]. The mode field area is almost a factor of 20 greater than that of the lowest order mode in the step-index fibre used in Chapter 5. Using Equation 4.16, the specified mode field radius of 27.5 μm and a nonlinear-index coefficient of $n_2 = 3.2 \times 10^{-20}$ m^{2}W^{-1} for undoped silica, the nonlinear parameter γ of the PCF is 8.200×10^{-5} m^{-1}W^{-1} for a wavelength of 1032 nm. The maximum achieved pulse energy was 267.7 ± 2.5 μJ which using the specified pulse length of 250 ps equates to a peak power of $\sim$ 1.1 MW. Using this peak power and the calculated value of γ in Equation 4.15, the nonlinear length scale is 11 mm.

Since the calculated nonlinear length scale is considerably shorter than the length of the PCF it would therefore be expected that nonlinearities are incurred. However, due to the exponential amplification of the pulse within the PCF it is likely that it the pulse energy is much lower than its final value throughout the majority of the PCF and only reaches a comparable energy near the output end. Additionally, the PCF is specified to have very low

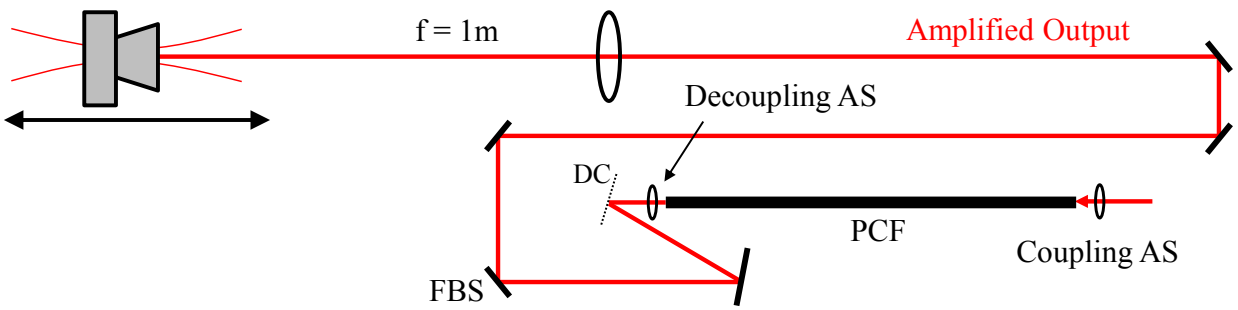

Figure 6.27: Experimental setup to measure the M^2 of the amplified output.

nonlinearities so the use of the nonlinear-index coefficient of silica may not be accurate here.

Without recording a spectra of the first pulse in the burst it is not possible to ascertain if nonlinearities are present. The first few pulses are a small fraction of the total burst energy and therefore as expected, the spectrum of the full burst shows no clear signs of SPM or other nonlinearities that may be present in the initial pulses.

6.8 Spatial Quality

Of particular interest with the PCF is the spatial quality of the amplified output. Despite the large core size of the PCF, which would support many transverse modes in a conventional step-index fibre, it is solely single mode. Being single mode, the output beam should have an M^2 very close to 1.

To measure the transverse spatial quality of the beam an M^2 measurement was made with the setup shown in Figure 6.27. Here, AS is the collimating aspheric and DC is the dichroic mirror used to separate the amplified output and the pump beams. To reduce the intensity to avoid damage to the camera, a Fresnel beam splitter (FBS) was used in place of one of the normal mirrors.

An f = 1 m plano-convex 2" lens was used with the flat side towards the focus to minimise the spherical aberration of the lens. The PCF was operated at its maximum output demonstrated in Section 6.6 and several Fresnel beam splitters and neutral density filters were used to attenuate the intensity of the laser to within the camera's dynamic range.

This ensured the spatial quality measurements made were an accurate representation of the output of the PCF under what would be normal operating conditions if it were used as a laser source for a laser-wire. It has been demonstrated in Section 5.8 that the spatial quality of the fibre output should not vary with the level of amplification however, this was not verified at such high intensities. The neutral density filters were placed immediately before the camera sensor to avoid introducing any aberrations.

As mentioned in Section 4.7, the M^2 measurement is made by measuring the 4σ diameter of the laser beam as it is focussed by a long focal length lens. The input beam size was measured immediately before the lens to have a 4σ diameter of 6.1 $\pm$ 0.1 mm in both the horizontal and vertical dimensions.

The M^2 was initially measured to be 1.48 $\pm$ 0.02 and 1.50 $\pm$ 0.03 for the horizontal and vertical dimensions respectively. This was higher than expected from a single mode fibre as measured in Section 5.8 and it was also known that the spatial quality of the laser beam can be degraded by improper alignment or placement of optics. Therefore, the M^2 measurement was repeated whilst iteratively adjusting various optics. Firstly, the position of the decoupling aspheric along the optical axis was adjusted. This altered the imaging point within the end of the PCF and the unstructured taper at the decoupling end of the fibre and hence the divergence and spatial quality of the beam.

Initially, the decoupling aspheric had been moved transversely to provide the best pump coupling and hence highest energy output. However, this meant that the decoupling aspheric was off-axis compared to the output beam from the PCF. To rectify this the pump beam optics were removed and the decoupled output beam was observed several metres from the PCF. The decoupling aspheric was then moved to give the most collimated beam that was collinear with the PCF.

The pump beam optics were then replaced and the pump beam carefully aligned to be collinear to the PCF. Instead of adjusting the position of the decoupling aspheric to maximise the pump coupling, the plano-convex lens in the pump beam path (L4 in Figure 6.10) was adjusted to give the best pump coupling. Given the pump beam was already aligned nearly

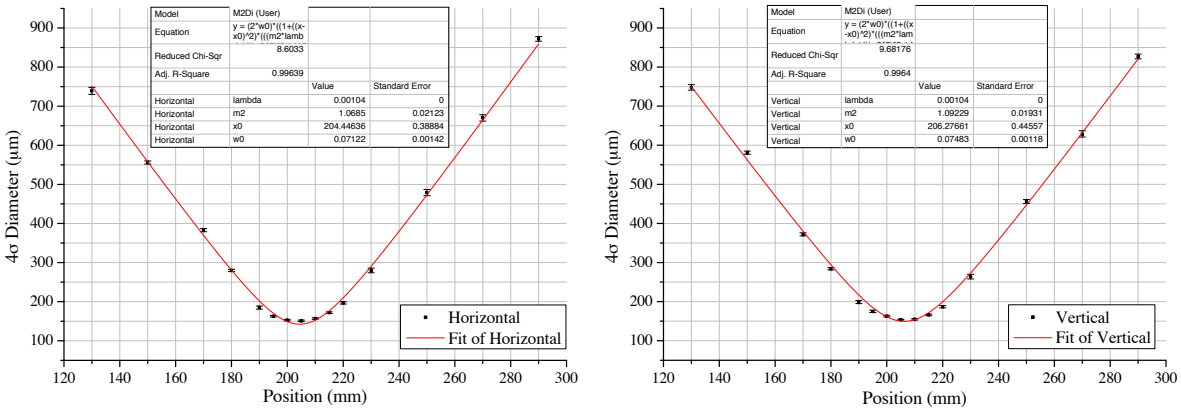

(a) Horizontal M^2 (b) Vertical M^2

Figure 6.28: M^2 measurement of the amplified output of the PCF in both horizontal and vertical dimensions.

collinear with the PCF, only a very small movement of the lens was required.

The M^2 measurement was then iterated, moving the decoupling aspheric along the optical axis each time. The best M^2 measurement of 1.07 ± 0.02 and 1.09 ± 0.02 for the horizontal and vertical dimensions respectively was then made. With an M^2 of 1 being a perfect Gaussian, this is a very good result and demonstrates the excellent spatial quality achievable in a PCF at high levels of amplification. Also, as the achievable focussed spot size depends linearly on the M^2 of the laser beam (for a fixed input beam size) having an M^2 as close to 1 as possible will ensure the best resolution of the laser-wire.

The data is shown in Figure 6.28 along with the fit to the model outlined in Equation 4.21 for this measurement. The measurement was iterated because both the M^2 of the beam and the measurement of the M^2 are sensitive to the alignment of the lenses used in the laser beam. A misaligned lens can introduce aberrations that increase the M^2. By repeating the measurement and adjusting the lenses the optimal alignment was found and the best performance of the system demonstrated.

A profile of the output from the PCF is shown in Figure 6.29. This was recorded approximately 2.5 m from the PCF. Comparing this to Figure 3.4, it can be seen that the spatial quality of the output from a PCF is considerably more Gaussian and symmetric than that from the bulk laser system at the ATF2.

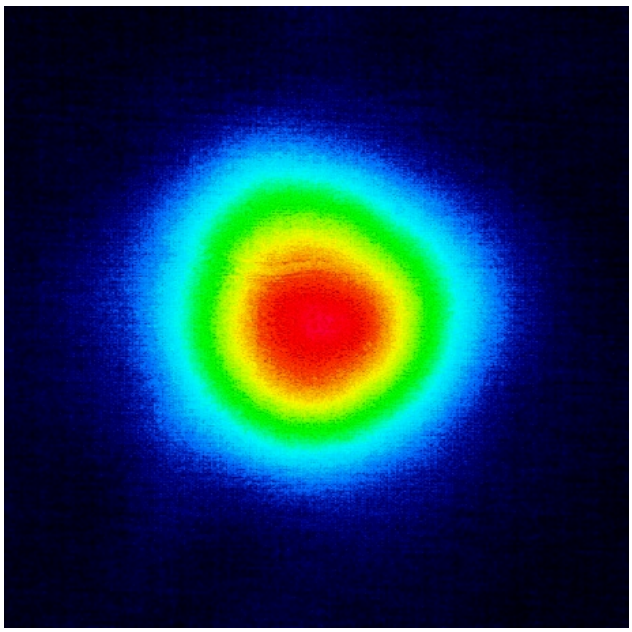

Figure 6.29: Image of output from the PCF amplifier recorded $\sim$ 2.5 m from the fibre.

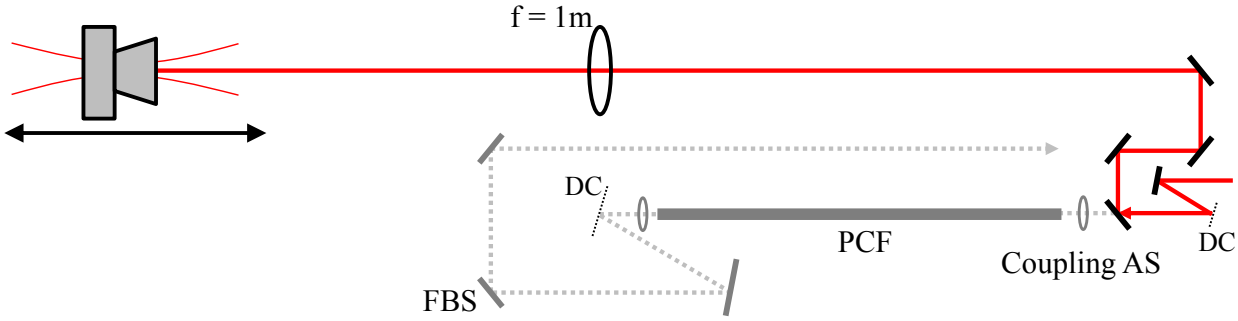

Figure 6.30: Experimental layout showing diversion of seed beam for M^2 measurement. Normal beam path is shown in grey.

For comparison, the M^2 of the seed to the PCF was also measured. Figure 6.30 shows the experimental layout used to make the M^2 measurement of the seed. Because the introduction of lenses and their alignment can affect the spatial quality of the beam, the measurement was made by deflecting the beam immediately before the coupling aspheric. It was not possible to remove the PCF and do this after the aspheric as the beam would be too divergent after it to make the M^2 measurement.

The data from this measurement along with the fit to the M^2 model is shown in Figure 6.31. The horizontal and vertical M^2 were measured to be 1.69 $\pm$ 0.03 and 1.65 $\pm$ 0.02 respectively. This is higher than the specified $M^2 < 1.1$ of the AS laser.

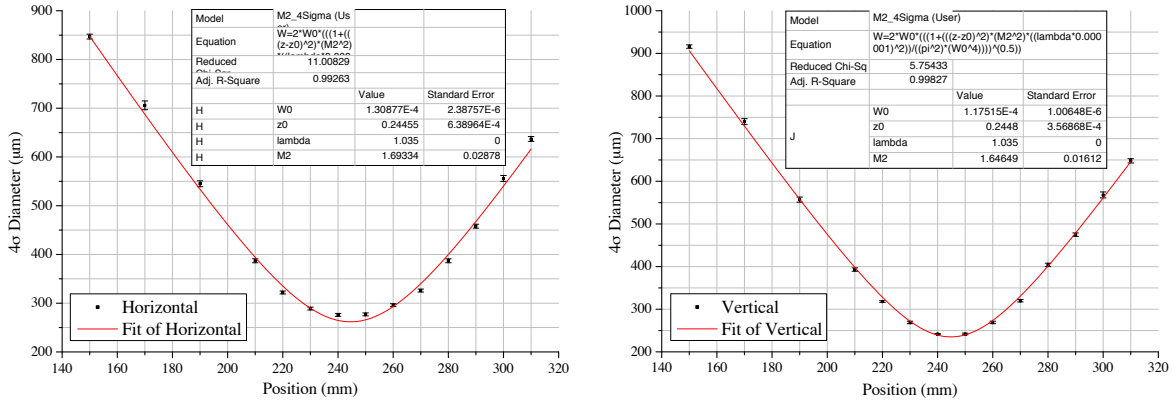

(a) Horizontal M^2 (b) Vertical M^2

Figure 6.31: M^2 measurement of the input seed beam to the PCF.

During the course of the experiments in this chapter, the alignment of the AS laser was often adjusted to maintain the maximum output power. This in turn sacrificed spatial quality due to slightly poorer alignment. Additionally, when the alignment was adjusted the direction of the output beam from the AS laser changed. The subsequent lenses were then realigned but misalignments may still have been present that would have introduced aberrations.

The single mode nature of the PCF however improved the spatial quality of the beam and the higher M^2 of the AS laser did not therefore affect the spatial quality of the output of the full system. The PCF is therefore acting as a spatial filter which provides a greater tolerance on the spatial quality of the laser before the PCF. However, poorer spatial quality before the PCF will results in a lower coupling efficiency and therefore lower output energy. It is therefore advantageous to maintain the spatial quality of the laser before the PCF.

6.9 Polarisation

For efficient frequency conversion, the input laser beam must have a well defined linear polarisation and so the degree of linear polarisation of the amplified output from the PCF amplifier was measured.

The degree of linear polarisation was measured before the PCF for comparison using a

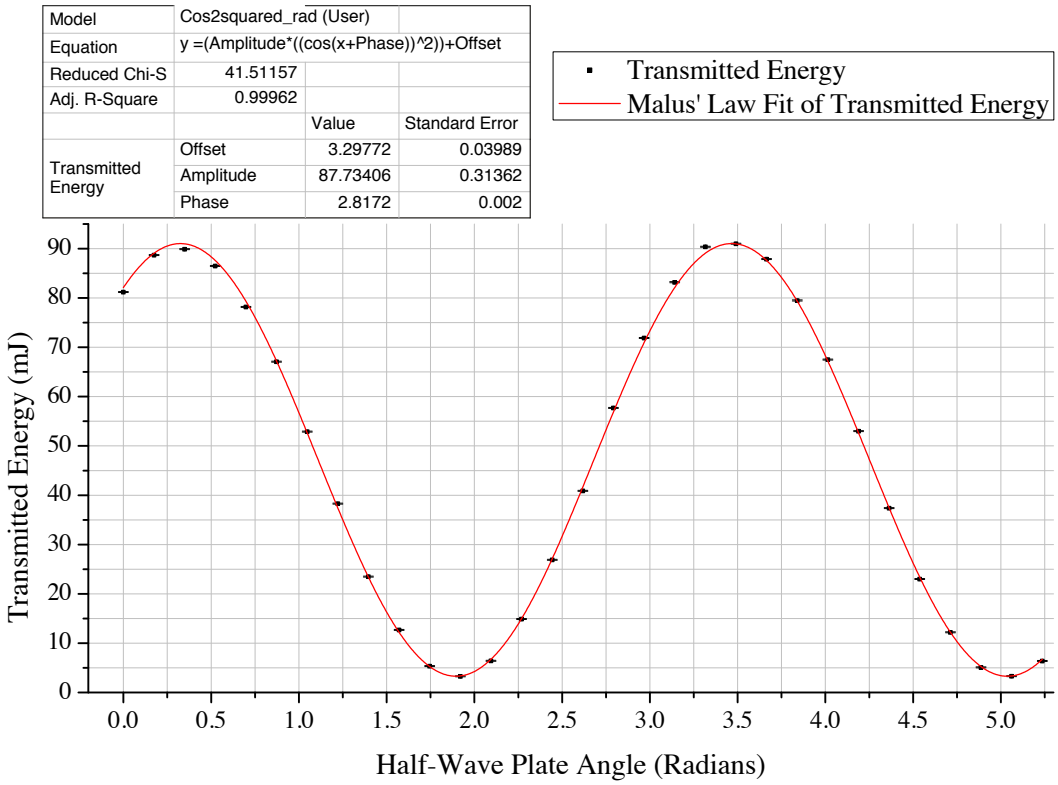

Figure 6.32: Measurement of the degree of linear polarisation of the amplified output from the PCF amplifier.

half-wave plate and PBS as detailed in Section 5.5. The degree of linear polarisation (DOLP) was measured to be ~ 68 % which was much lower than expected. The AS laser is specified to have a DOLP > 99.9 %. This was verified in Section 5.5 to be $99.59^{+0.41}_{-3.19}$ % by making the same DOLP measurement on the output of the laser system. The problem was therefore found to lie with the optical isolator which was found to be tuned for the wrong wavelength. After recalibration by the manufacturer, the DOLP after the isolator and hence input to the PCF was measured to be 95.2 ± 1.8 %.

The DOLP of the output from the PCF was then measured by placing a PBS in the output beam line and the Gentec energy meter placed after it to measure the transmitted burst energy. No half-wave plate was used in this case as the PBS used had a cover that safely contained the reflected beam. The amplification regime was the same as that in Figure 6.23 with the maximum achieved output. The data recorded is shown in Figure 6.32 with a fit to Malus' Law using Equation 4.7 with the factor of 2 removed from the angular frequency as only a PBS was used.

The offset and the amplitude were measured to be 3.3 ± 0.2 mJ and 87.7 ± 0.3 mJ respectively and using Equation 4.8, the degree of linear polarisation is 93.0 ± 1.6 %, which is within the measurement uncertainty of the DOLP of the input to the PCF and therefore it is not degrading the DOLP. The high degree of linear polarisation will allow efficient frequency conversion after the PCF amplifier.

Furthermore, using from the technique derived in Section 5.6, the high degree of linear polarisation of the amplified output places a limit of the maximum amount of ASE that could be present.

6.10 Summary

In this chapter, a laser system with a master-oscillator-fibre-amplifier based on chirped-pulse amplification was demonstrated as a suitable laser system for laser-wire. The specially commissioned Newport diode laser was characterised and demonstrated to have a stable spectral output that was set to overlap with the absorption peak of Ytterbium at 976 nm under burst operation. The stretched pulses from a state-of-the-art commercial laser system were amplified in a burst regime in a photonic crystal fibre amplifier.

A novel method to measure individual pulse energies at megahertz repetition rates was developed and demonstrated. This method was then used to measure the pulse energies from the PCF amplifier demonstrating pulse energies as high as 267.7 ± 2.5 μJ were demonstrated, which are considerably higher than the required 100 μJ.

Furthermore, the single mode nature was highlighted with the excellent spatial quality of the amplified output beam which was measured to have an M^2 of 1.07 ± 0.02 and 1.09 ± 0.02 for the horizontal and vertical dimensions respectively. This M^2 measurement is lower than any published measurements using a PCF demonstrating the excellent and highly efficient alignment.

The spectrum of the output was measured to have a FWHM of ∼ 1.8 nm which is less

than the 2 nm acceptance bandwidth of the custom built laser-wire lens. After frequency conversion to the second harmonic this will in turn halve to < 1 nm. This narrow spectral bandwidth will ensure that chromatic aberration does not increase the focussed spot size of the laser beam and hence decrease the resolution of the laser-wire.

Chapter 7

Conclusions and Outlook

7.1 Conclusions

In this thesis, a laser-wire at the ATF2 was set up, commissioned and used as a diagnostic for the electron beam in the extraction line.

After not observing collisions during laser-wire operation in spring 2010, an alignment laser was used in place of the electron beam to confirm the alignment of the scattered photons from the laser-wire during the summer shutdown of the ATF2. This was accomplished by referencing the alignment laser beam with wire scanners on either side of the LWIP. The detector was also modified and inserted immediately behind the laser-wire signal window in the vacuum pipe to prevent the scattered photons being blocked by the poles of an intermediate quadrupole. This, in conjunction with the new horizontal alignment possible because of damage to the OTR screen, allowed accurate alignment that ultimately led to collisions between the laser and electron beams being detected immediately. This process was repeatable and collisions were reliably found for each operation period thereafter.

The data from operation during December 2010 was presented showing the convoluted beam size of both the electron and laser beams. An initial vertical scan showed a convoluted beam size of $\sigma_y = 18.4 \pm 0.4\ \mu$m, which after correcting the magnet settings in the accelerator

was reduced to $\sigma_y = 11.3 \pm 0.7$ μm. The laser-wire was used as a diagnostic while dispersion and x-y coupling corrections were made and the smallest convoluted beam size measured was $\sigma_y = 8.07 \pm 0.35$ μm. Due to the failure of the OTR camera, it was not possible to deconvolute the laser-wire scans and ascertain the size of the electron beam. Consequently, confirmation of the focussed laser spot size was not made, however, in the future this will be remedied with replacement hardware.

In addition to this, the pulse length, energy and spatial quality of the laser system at the ATF2 were characterised. A calibrated telescope was constructed and used to manipulate the size of the input laser beam to the laser-wire lens from the accessible laser laboratory outside the accelerator enclosure. The size of the input laser beam to the lens was adjusted to match the simulations and measurements that describe the performance of the laser-wire lens.

In conjunction with the development of the laser-wire at the ATF2, the design of a laser source capable of a higher resolution and intra-train scanning for a laser-wire was considered. A test bed system was built to investigate the properties of fibre lasers. Results from this system were presented demonstrating very high spatial quality output irrespective of the level of pumping and amplification and high slope efficiencies. However, evidence of nonlinearities that caused spectral broadening was observed indicating the peak power limit of step-index fibres.

A fibre laser system suitable for demonstration at the ATF2 was constructed using a commercial chirped-pulse amplification laser system, which was extended with the addition of a photonic crystal fibre amplifier. The photonic crystal fibre used allowed much higher pulse energies to be achieved without incurring nonlinearities and as it was single mode, also provided excellent spatial quality. A burst amplification regime taking advantage of the required low duty cycle of the laser to match that of the accelerator was devised. By storing energy in the photonic crystal fibre in this manner, higher pulse energies were achieved that would not be otherwise possible under continuous operation.

A maximum pulse energy of 267.7 $\pm$ 2.5 μJ was demonstrated and the spatial quality of

the output from the fibre was measured to be $M_x^2 = 1.07 \pm 0.02$ and $M_y^2 = 1.09 \pm 0.02$ in the horizontal and vertical dimensions respectively. This excellent spatial quality will provide a smaller focus and thus better laser-wire resolution than the existing laser system at the ATF2 should it be used there. The spectrum of the laser output was measured to be 6 nm, which is greater than 2 nm acceptance bandwidth of the laser-wire lens, however, this spectrum was of the infra-red output of the photonic crystal fibre that has yet to be frequency doubled, where it is expected to halve.

The fibre laser system built has demonstrated several very high energy pulses for a fibre laser system with excellent spatial quality that would allow intra-train scanning with increased resolution if demonstrated at the ATF2.

7.2 Future Work

7.2.1 Laser-wire Experiment

Whilst the laser-wire at the ATF2 was commissioned and demonstrated to be operational, it is far from fully developed and much work remains to improve it further. The 2011 Tohoku earthquake and tsunami prevented further development and data taking in the spring operation of the ATF2 in 2011. The laser-wire installation was not damaged but will have to be realigned. The ATF2 is undergoing complete mechanical realignment of the linac, damping ring and extraction line and after this, beam-based alignment will be required to tune the accelerator performance to its previous level. Before operation of the ATF2 and the laser-wire several key improvements can be made.

Hardware Improvements

During the laser-wire operation reported in Chapter 3, the OTR camera failed and a replacement was not available. In future, a new OTR camera will allow the OTR monitor to be used to calibrate the laser-wire as well as confirming the spatial propagation model of the

laser beam. Additionally, the OTR monitor can be used to initially tune the electron beam to be suitable for laser-wire operation in a much shorter period than performing successive laser-wire scans.

The energy meter used for energy normalisation was also unreliable and was not able to be used during data taking. With operational energy normalisation, the removal of the laser pulse energy jitter will allow more precise laser-wire scans to be made. Similarly, the high resolution cavity BPMs around the LWIP can be used to subtract the spatial jitter of the electron beam at the LWIP during a laser-wire scan. Combined, these two improvements will significantly lower the noise in the laser-wire scan and increase the precision.

The electron beam optics developed provide a small focus at the LWIP, however, the model is not truly accurate after the iterative tuning of the magnet settings in the extraction line to minimise the background signal in the LW detector. The Flight Simulator [68] software now available provides real time electron beam optics based on readouts of the accelerators settings. This software can be queried by the laser-wire software to integrate the electron beam optics into our recorded data. This will allow emittance measurement using quadrupole scans to be easily and quickly made with the precise knowledge of the electron beam.

A major limitation for the operation and development of the laser-wire at the ATF2 is the nominal ATF2 electron beam optics and the magnet layout at the LWIP. To create the desired small electron beam focus, a dedicated set of electron beam optics are required that have to be specially implemented each time the laser-wire is used. This leads to a considerable amount of time being spent tuning the accelerator, which is for the most part undone at the end of the laser-wire operation period when the accelerator is reset to the nominal ATF2 optics and developed from there. Furthermore, the large spacing of the quadrupoles immediately after the LWIP mean that the electron beam expands to a very large size, particularly in the horizontal, which is the presumed cause of the large background observed. This is inevitable if a small electron beam size is desired at the LWIP.

To overcome these limitations, it was proposed by S. Boogert and A. Aryshev in summer 2011 that the LWIP be moved to a different location in the lattice [27]. Since then, the

LWIP has been relocated further along the extraction line approximately 13 m closer to the LW detector. This location was chosen as there is a mirror image of the final focus where the electron beam is predicted to have a vertical size of ~ 0.9 μm with the standard ATF2 electron beam optics and nominal emittance. The horizontal beam size is predicted to be approximately 100 μm.

This will provide two main advantages to the operation and development of the laser-wire. Firstly, the accelerator lattice was designed to make a < 1 μm vertical electron beam size at this location which should make demonstrating a 1 μm laser-wire scan achievable. Secondly, the well designed and developed ATF2 electron beam optics produce a negligible background in our detector improving the potential quality of the laser-wire scans and reducing the required laser pulse energy further. Since the laser-wire is essentially non-invasive and it will now use the same electron beam optics as all other users at the ATF2, the laser-wire can be used concurrently with other users of the facility. Although under development, it can be used as a diagnostic for the ATF2 tuning team.

With the increased proximity to the LW detector, alignment of the electron beam at the LWIP with corrector magnets should not be necessary, as for the typical angular variation in the orbit of the electron beam previously observed, the detector area is large enough to capture the signal irrespective of the electron beam direction making alignment and detection simpler.

A further hardware modification that could potentially improve the laser-wire further is the use of the spatial filter in the laser system. This was originally designed to change the near-Gaussian beam from the regenerative amplifier to a top-hat profile beam. A top-hat profile beam is more efficient at uniformly extracting energy from macroscopic gain media in the linear amplifiers and the uniform intensity minimises the risk of 'hot spots' that may lead to surface damage on various optical components. The spatial filter can potentially be modified to create a more Gaussian beam which would increase the spatial quality of the laser, lower the M^2 value and hence decrease the minimum focussed spot size available.

Further Studies

Irrespective of the planned hardware upgrades, several investigations remain that could potentially improve the laser-wire performance. A full characterisation of the LW lens would provide information on alignment tolerances and how the size of the focussed laser beam is affected by long range scanning.

To aid the characterisation of the laser-wire lens, it would be useful to measure the spectrum of the existing laser system at the ATF2. This measurement has not been made before and it is therefore unclear what is the minimum achievable spot size the lens can produce.

With the new LWIP, the aspect ratio of the electron beam has increased and is likely to be 100:1 or greater. For truly passive operation, the development of a technique to match the angle of the laser focus to the plane of the electron beam would prove useful. Even a small difference in angle would contribute a large increase in measured vertical beam size. This is potentially remedied by lowering the position of the input laser beam on the LW lens, but how this affects the focussed spot size is unknown. Although the angle between the two beams could be matched, if the focussed laser spot size is increased the result will be unmeasurable.

In a similar vein, varying the input beam size by altering the separation of the lenses in the telescope was not undertaken. This will be necessary if the smallest laser-wire scan possible is to be demonstrated.

7.2.2 Fibre Laser Development

Work remains to fully demonstrate the fibre laser system as a suitable laser source for a laser-wire. After developing the combined photodiode trace and burst energy measurement method as well as the software to determine the pulse energies, insufficient time remained within the scope of this research to compress the pulses and then frequency double them in a nonlinear crystal.

The output of the compressor will need to be characterised to ascertain the temporal profile of the pulses. After compression, the efficiency of conversion to the second harmonic in the nonlinear crystal will also need to be measured and optimised.

With the high degree of linear polarisation and the higher than expected pulse energies from the PCF amplifier, the frequency doubling is expected to be highly efficient. The frequency doubling process is proportional to the square of the incident intensity so the increased input energy will ensure even more efficient conversion. The spectral width of the laser pulses after frequency doubling is expected to be half that of the input but measurement is required to verify that chromatic aberrations will not be introduced by the LW lens.

After both compression and frequency conversion, the spatial quality of the laser system will need to be characterised and optimised. A very high spatial quality has been demonstrated from the PCF amplifier but this must be maintained through compression and frequency conversion if the best laser-wire resolution is to be achieved.

In addition to completion of the laser system, further studies can be undertaken. If another EOM was available, it could be used to accurately determine the pulse energies at the beginning of the laser pulse burst. The EOM could be used to isolate the first pulse and with the measured attenuation of the EOM, the pulse energy determined. The EOM switching point could then be delayed further into the amplified burst allowing an extra pulse through. With knowledge of the energy of the first pulse, the second could also be determined. This could be repeated for at least the first ten pulses and its scope only limited by the precision of the energy meter and the pulse energy stability from the PCF amplifier.

Similarly, this technique could also be used to measure the spectra of the initial pulses to ascertain whether the high energy initial pulses are experiencing any nonlinearities.

Upon completion, the laser system will be reconstructed at the ATF2 in Japan where it will be demonstrated. A simultaneous comparison of this laser system with the existing laser system will be undertaken. Furthermore, the fibre laser system could be used to scan several bunches at once, which has not been demonstrated before, potentially providing

characterisation of the multi-bunch performance of the ATF2 which is known to be different from single bunch operation. The $\sim$ 1 ps pulse length of the fibre laser system could be used to make longitudinal bunch profile measurements which has also not been demonstrated with a laser-wire before.

A further extension to the laser system would be to use a second PCF. This could be used as an additional or intermediate amplification stage to the PCF used. With a second PCF, higher output energies would be achievable, however achieving similar pulse energies with a greater stability would also be possible.

With a second PCF and potentially a second pump diode laser, the exponentially decaying pulses energies from the burst amplification could be counteracted. The timing of the pump in the first PCF could be delayed, turning on after the seed burst has entered the PCF. In this regime, the initial pulses are attenuated before the pump is turned on. Once the pump is turned on, the PCF first becomes transparent before amplifying the pulses. This would create a pulse train with an envelope that could be tailored to counteract the envelope from burst amplification in a single PCF.

As the gain from a fibre amplifier depends on the input pulse energy, the initial pules from the first PCF would not experience a high gain and much of the stored energy in the second PCF would remain. As the input pulse energies to the second PCF increase, the gain would also increase and more of the stored energy would be used. This would ideally provide a burst of pulses with the same energy and an energy greater than that achievable from the steady state of the two amplifiers working continuously. However, this has not been demonstrated before and it is unlikely that this technique would work for a period longer than $\sim$ 100 μs.

Bibliography

[1] A. Portone, W. Baker, E. Salpietro, A. Vostner, P. Bruzzone, F. Cau, A. della Corte, A. Di Zenobio, E. Theisen, A. Baldini, P. Testoni, J. Lucas, M. Pinilla and G. Samuelli. *IEEE Transactions on Applied Superconductivity*, **18**, 2 (2008) 499–504.

[2] O.S. Bruning, P. Collier, P. Lebrun, S. Myers, R. Ostojic, J. Poole and P. Proudlock. "LHC Design Report". CERN (2004).

[3] D. Iwanenko and I. Pomeranchuk. *Phys. Rev.*, **65** (1944) 343–343.

[4] Editors of the ILC RDR. "International Linear Collider Reference Design Report Volume 2: Physics at the ILC". Technical report (2007).

[5] R. Brinkmann, K. Flottmann, J. Rossbach, Peter Schmueser, N. Walker et al.

[6] I. Agapov, G.A. Blair and M. Woodley. *Physical Review Special Topics*, **10**, 112801 (2007) 1–20.

[7] Martin R. *Journal of Applied Physics*, **70**, 4 (1991) 1919–1923.

[8] I. Wilson et al. *Physics Reports*, **403-404** (2004) 365–378.

[9] Editors of the ILC RDR. "International Linear Collider Reference Design Report Volume 3: The Accelerator". Technical report (2007).

[10] CERN. "CERN Accelerator School: 5th General Accelerator Physics Course". CERN, Geneva (1994).

[11] E. Wilson. "An Introduction to Particle Accelerators". Oxford University Press (2001).

[12] H. Grote, F.C. Iselin, E. Keil and J. Niederer. "The MAD program". In "Particle Accelerator Conference, 1989. Accelerator Science and Technology., Proceedings of the 1989 IEEE", Volume 2, pages 1292 – 1294 (1989).

[13] A. Aspect. "Coherent and Collective Interactions of Particles and Radiation Beams". ISO Press (1997).

[14] W.S. Graves, E.D. Johnson and S. Ulc. *AIP Conference Proceedings*, **451**, 1 (1998) 206–213.

[15] P. Tenenbaum and T. Shintake. *Annual Review of Nuclear and Particle Science*, **49**, 1 (1999) 125–162.

[16] C. Field, D. McCormick, P. Raimondi and M. Ross. *AIP Conference Proceedings*, **451**, 1 (1998) 440–445.

[17] M. Ross, S. Anderson, J. Frisch, K. Jobe, D. McCormick, B. McKee, J. Nelson, T. Smith, H. Hayano, T. Naito and N. Terunuma. "A Very High Resolution Optical Transition Radiation Beam Profile Monitor". In "AIP Conference Proceedings", Volume 648, pages 237–247. IOP Institute of Physics Publishing Ltd. (2002).

[18] M. Ross, R. Alley, D. Arnett, E. Bong, W. Colocho, J. Frisch, S. Horton-Smith, S. Inman, K. Jobe, T. Kotseroglou, D. McCormick, J. Nelson, M. Scheeff and S. Wagner. *AIP Conference Proceedings*, **390**, 1 (1997) 281–289.

[19] T. Shintake. *Nuclear Instruments and Methods in Physics Research Section A: Accelerators, Spectrometers, Detectors and Associated Equipment*, **311**, 3 (1992) 453–464.

[20] A. Siegman. "Lasers". University Science Books (1990).

[21] ATF2 Group. "ATF2 Proposal-Volume". Technical report, CERN (2006).

[22] L. Deacon. "A Micron-Scale Laser-Based Beam Profile Monitor for the International Linear Collider". Ph.D. thesis, Royal Holloway, University of London (2009).

[23] S.T. Boogert, G.A. Blair, G. Boorman, A. Bosco, L. Deacon, P. Karataev, A. Aryshev, M. Fukuda, N. Terunuma, J. Urakawa, L. Corner, N. Delerue, B. Foster, D. Howell, M. Newman, R. Senanayake, R. Walczak and F. Ganaway. *Physical Review Special Topics - Accelerators and Beams*, **13**, 12 (2010) 1–16.

[24] S.T. Boogert, R. Ainsworth, G. Boorman, S. Molloy, M. Ross, A. Aryshev, Y. Honda, N. Terunuma, J. Urakawa, E.S. Kim et al. "Cavity Beam Position Monitor System for ATF2". In "IPAC 10 MOPE070", Number 227579, pages 1140–1142. Kyoto (2010).

[25] S. Hooker. "Laser Physics". Oxford University Press (2010).

[26] E. Hecht. "Optics". 4th edition (2001).

[27] S.T. Boogert. Private Communication (2011).

[28] C.B. Gutierrez, J.V. Civera, J. Cruz, D. Mccormick and G. White. "Multi Optical Transition Radiation System for the ATF2". In "IPAC 10 MOPE050", Kyoto (2010).

[29] M. Woodley. "EXT: Summary of Activities, Software Development, and Tuning Performance" (2011). 11th ATF2 Project Meeting.

[30] Y. Sintov, O. Katz, Y. Glick, S. Acco, Y. Nafcha, A. Englander and R. Lavi. *Journal of the Optical Society of America B*, **23**, 2 (2006) 218.

[31] G. Agrawal. "Nonlinear Fiber Optics". 3rd edition (2001).

[32] Nufern Speciality Fibers and Fiber Lasers. "SM-YDF-5-130".

[33] C.J. Koester and E. Snitzer. *Applied Optics*, **3**, 10 (1964) 1182.

[34] J. Limpert, F. Roser, S. Klingebiel, T. Schreiber, C. Wirth, T. Peschel, R. Eberhardt and A. Tiinnermann. *Selected Topics in Quantum Electronics, IEEE Journal of*, **13**, 3 (2007) 537 –545.

[35] Y. Takushima, S. Yamashita, K. Kikuchi and K. Hotate. *Journal of Lightwave Technology*, **16**, 4 (1998) 661–669.

[36] J. Noda, K. Okamoto and Y. Sasaki. *Journal of Lightwave Technology*, **4**, 8 (1986) 1071–1089.

[37] R. Paschotta, J. Nilsson, A.C. Tropper and D.C. Hanna. *IEEE Journal of Quantum Electronics*, **33**, 7 (1997) 1049–1056.

[38] J.D. Minelly, W.L. Barnes, R.I. Laming, P.R. Morkel, J.E. Townsend, S.G. Grubb and D.N. Payne. *Photonics Technology Letters, IEEE*, **5**, 3 (1993) 301–303.

[39] J. Sebastian, H. Schulze, R. Hulsewede, P. Hennig, J. Meusel, M. Schroder, D. Schroder and D. Lorenzen. "High-Brightness, High-Power 9XX-nm Diode Laser Bars: Developments at JENOPTIK Diode Lab". Volume 6456. SPIE (2007).

[40] J. Limpert, F. Roser, T. Schreiber and A. Tunnermann. *Selected Topics in Quantum Electronics, IEEE Journal of*, **12**, 2 (2006) 233–244.

[41] Y. Jeong, J. Sahu, D. Payne and J. Nilsson. *Optics Express*, **12**, 25 (2004) 6088–92.

[42] P. Parvin, M. Ilchi-Ghazaani, A. Bananej and Z. Lali-Dastjerdi. *Optics & Laser Technology*, **41**, 7 (2009) 885–891.

[43] D. Xue, Q. Lou and J. Zhou. *Optics & Laser Technology*, **39**, 4 (2007) 871–874.

[44] E. Desurvire, J.R. Simpson and P.C. Becker. *Optics Letters*, **12**, 11 (1987) 888–90.

[45] C.R. Giles and E. Desurvire. *Journal of Lightwave Technology*, **9**, 2 (1991) 147–154.

[46] D. Marcuse. *Journal of the Optical Society of America*, **68**, 1 (1978) 103.

[47] T.F. Johnston. *Appl. Opt.*, **37**, 21 (1998) 4840–4850.

[48] International Standards Organisation. "ISO Standard 11146".

[49] C. Finot. *Optics Communications*, **249**, 4-6 (2005) 553–561.

[50] F. Röser, J. Rothhard, B. Ortac, A. Liem, O. Schmidt, T. Schreiber, J. Limpert and A. Tünnermann. *Optics Letters*, **30**, 20 (2005) 2754.

[51] I. Martial, F. Balembois, J. Didierjean and P. Georges. *Optics Express*, **19**, 12 (2011) 11667–11679.

[52] J. Boullet, Y. Zaouter, R. Desmarchelier, M. Cazaux, J. Saby, R. Bello-doua and E. Cormier. *Optics Express*, **16**, 22 (2008) 17891–17902.

[53] L. Hanxuan, I. Chyr, D. Brown, X. Jin, F. Reinhardt, T. Towe, T. Nguyen, R. Srinivasan, M. Berube, R. Miller, K. Kuppuswamy, Y. Hu, T. Crum, T. Truchan and J. Harrison. *Proceedings of SPIE*, **6456** (2007) 64560C.

[54] B.L. Volodin, S.V. Dolgy, E.D. Melnik, E. Downs, J. Shaw and V.S. Ban. *Opt. Lett.*, **29**, 16 (2004) 1891–1893.

[55] Y. Huang, Y. Li, H. Wang, X. Yu, H. Zhang, W. Zhang, H. Zhu, S. Zhou, R. Sun and Y. Zhang. *Chin. Opt. Lett.*, **9**, 3 (2011) 031403.

[56] J.P. Koplow, D.A. Kliner and L. Goldberg. *Optics Letters*, **25**, 7 (2000) 442–444.

[57] P. Russell. *Science (New York, N.Y.)*, **299**, 5605 (2003) 358–62.

[58] J.C. Knight. *Nature*, **424**, 6950 (2003) 847–51.

[59] T. Sorensen, J. Broeng and A. Bjarklev. *Electronics*, **37**, 5 (2001) 287–289.

[60] T. Schreiber, F. Röser, O. Schmidt, J. Limpert, R. Iliew, F. Lederer, A. Petersson, C. Jacobsen, K. Hansen, J. Broeng and A. Tünnermann. *Opt. Express*, **13**, 19 (2005) 7621–7630.

[61] O. Schmidt, J. Rothhardt, T. Eidam, F. Röser, J. Limpert, A. Tünnermann, K. P. Hansen, C. Jakobsen and J. Broeng. *Opt. Express*, **16**, 6 (2008) 3918–3923.

[62] D.J. Richardson and J. Nilsson. *JOSA B*, **27**, 11.

[63] P. Maine, D. Strickland, P. Bado, M. Pessot and G. Mourou. *IEEE Journal of Quantum Electronics*, **24**, 2 (1988) 398–403.

[64] Y. Zaouter, E. Mottay, L. Corner and N. Delerue. *Proceedings of SPIE*, **6881**, 1 (2008) 68810J–68810J–5.

[65] Y. Zaouter. Private Communication (2010).

[66] NKT Photonics. "DC-200-70-PM-YB-ROD".

[67] T. Schreiber, F. Röser, O. Schmidt and J. Limpert. *Optics Express*, **13**, 19.

[68] S. Molloy, M. Torino, F. Pivi, G. White and Y. Renier. "Interfacing of Third-Party Accelerator Code with The Lucretia Flight Simulator". In "PAC 09", pages 4814–4816. Vancouver (2009).